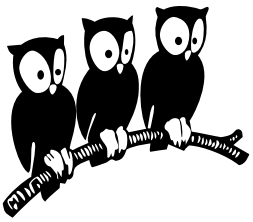
Département de physique
École Normale Supérieure

Laboratoire Kastler Brossel



THÉSE de DOCTORAT de l'UNIVERSITÉ PARIS VI

Spécialité : Physique Quantique

présentée par

Diogo RIO FERNANDES

pour obtenir le grade de Docteur de l'Université Pierre et Marie Curie (Paris VI)

Trapping and cooling of fermionic alkali atoms to quantum degeneracy. Sub-Doppler cooling of Potassium-40 and Lithium-6 in gray molasses.

Soutenue le 29 septembre 2014

devant le jury composé de :

Denis BOIRON	Rapporteur
Philippe BOUYER	Rapporteur
Frédéric CHEVY	Directeur de thèse
Roland COMBESCOT	Examinateur
Bruno LABURTHE-TOLRA	Examinateur
Giacomo ROATI	Examinateur
Christophe SALOMON	Membre invité

À minha avó Lilinha,
aos meus pais e à minha irmã

"[...]
Eles não sabem, nem sonham,
que o sonho comanda a vida,
que sempre que um homem sonha
o mundo pula e avança
como bola colorida
entre as mãos de uma criança."

António Gedeão

Contents

1 Introduction **15**

1.1 Prospects for ultracold fermionic mixtures 17

1.2 State of the art in Fermi-Fermi experiments 18

1.3 Outline of this thesis 20

2 Experimental apparatus **23**

2.1 Vacuum chamber 23

2.1.1 MOT chamber 25

2.1.2 Transport section 26

2.2 Laser systems 29

2.2.1 Atomic levels and cooling transitions 30

2.2.2 Setup for cooling in the D_2 and D_1 transitions 31

2.2.3 Optical setup around the science cell 32

2.3 Absorption imaging 33

2.3.1 Evaluation of the imaging data 34

2.3.2 Imaging optical setup 36

2.3.3 High magnetic field imaging 38

2.4 Computer control system 40

Appendix 2.A Vacuum parts 43

Appendix 2.B ^{40}K Laser table 45

Appendix 2.C ^{6}Li Laser table 46

Appendix 2.D Imaging detunings for high-field imaging 47

3 Dual-species MOT **49**

3.1 Double MOT current status and improvements 50

Appendix 3.A Publications 53

4 Gray molasses **81**
4.1 Introduction . . . 81
4.2 Principle . . . 82
4.3 The case of ^{40}K: semi-classical calculations . . . 86
4.4 Experimental setup . . . 89
4.5 Results and discussion . . . 90
4.5.1 Characterization of the ^{40}K gray molasses . . . 91
4.5.2 Role of the repumper: study of the Raman detuning . . . 95
4.6 Gray molasses cooling of ^{6}Li . . . 98
4.6.1 Experimental setup - offset lock . . . 98
4.7 Conclusions . . . 102
Appendix 4.A Publications . . . 103

5 Magnetic trapping and magnetic transport **123**
5.1 Principles of magnetic trapping of neutral atoms . . . 124
5.2 Optical pumping and transferring atoms into the magnetic quadrupole trap . . . 129
5.3 Magnetic transport . . . 135
5.3.1 Working principle . . . 136
5.3.2 Optimization and performance . . . 139
5.4 Conclusions . . . 148
Appendix 5.A Electromagnets . . . 151
5.A.1 Description of the coils . . . 151
5.A.2 Electronics . . . 156

6 Evaporative cooling in a plugged magnetic quadrupole trap **159**
6.1 Introduction . . . 159
6.2 Cold elastic collisions . . . 160
6.2.1 S-wave collisions . . . 162
6.2.2 P-wave collisions . . . 164
6.3 Loss mechanisms . . . 166
6.3.1 Majorana losses . . . 166
6.3.2 Spin-exchange collision rate . . . 167

6.4 Evaporation dynamics . . . 168
6.4.1 Evaporation rate . . . 169
6.4.2 Evaporation dynamics . . . 171
6.5 Experimental techniques . . . 173
6.5.1 Radio-frequency and micro-wave sources . . . 174
6.5.2 Probing density and energy distributions in a magnetic trap . . . 176
6.5.3 Optical plug . . . 178
6.5.4 Study of the plugged magnetic quadrupole trap . . . 180
6.6 Evaporation in the plugged trap . . . 181
6.7 Sympathetic cooling of ^{6}Li . . . 184
6.7.1 Thermalization of a gas of ^{6}Li with ^{40}K . . . 184
6.7.2 Thermalization experiments in the MOT chamber . . . 185
6.7.3 Sympathetic cooling of ^{6}Li . . . 186
6.7.4 Spin-exchange interspecies collision rate . . . 187
6.8 Summary . . . 190
Appendix 6.A Corrective factor for evaporation rate . . . 191
Appendix 6.B Construction of the antennae . . . 193
6.B.1 Potassium-40 hyperfine frequency (MW) antenna . . . 194
6.B.2 Radio-frequency antenna . . . 195
6.B.3 Lithium-6 hyperfine frequency (RF) antenna . . . 198
6.B.4 Stub technique . . . 198

7 Evaporative cooling in an optical dipole trap 201
7.1 Trapping in an ODT . . . 201
7.2 Experimental setup . . . 204
7.2.1 Laser setup . . . 205
7.2.2 Laser power control with a logarithmic amplifier . . . 206
7.3 Loading of the ODT . . . 207
7.3.1 Model . . . 207
7.3.2 Experimental results . . . 210
7.4 Axial confinement . . . 212
7.5 Evaporative cooling to quantum degeneracy . . . 215
7.5.1 Introduction . . . 215

7.5.2 Experimental results 216
7.5.3 Transfer to the lower Zeeman states 218
7.5.4 Degenerate Fermi gas 221
7.6 Cooling of the ^{6}Li-^{40}K mixture 223
7.7 Conclusions 225
Appendix 7.A Gravitational sag 227
Appendix 7.B Evaporation rate of a double atomic gas with interspecies collisions 227

8 Conclusions and outlook **229**
8.1 Summary of the results 229
8.2 Perspectives 232
Appendix 8.A Optical lattice for ^{40}K 235

Index **237**

Bibliography **239**

Abstract

This thesis describes the design, construction and characterization of an apparatus capable of trapping and cooling fermionic atoms of ^{6}Li and ^{40}K to ultracold temperatures. The study of mixtures of degenerate Fermi gases opens the door for the creation of new many-body quantum systems.

We present a novel laser cooling technique able to simultaneously cool ^{6}Li and ^{40}K to the sub-Doppler regime based on the gray molasses scheme operating on the D_1 atomic transition. This strategy enhances the phase space density of both atomic species to 10^{-4}, the highest value reported in the literature for laser cooled ^{6}Li and ^{40}K.

The optimization of a device able to transport a magnetically trapped atomic cloud from the MOT chamber to a science cell is described. In this cell evaporative cooling is performed first in a plugged magnetic quadrupole trap and then in an optical dipole trap. We report the production of a quantum degenerate Fermi gas of 1.5×10^5 atoms ^{40}K in a crossed dipole trap with $T/T_\mathrm{F} = 0.17$, paving the way for the creation of strongly interacting superfluids of ^{40}K.

Résumé

Ce mémoire décrit la conception, la construction et la caractérisation d'un appareil capable de piéger et refroidir des atomes fermioniques de ^{6}Li et ^{40}K à des températures ultrabasses. L'étude des mélanges des gazes de Fermi dégénérés ouvre la porte vers la création des nouveaux systèmes quantiques à N corps.

Nous présentons une nouvelle technique de refroidissement laser capable de refroidir simultanément ^{6}Li et ^{40}K à des températures sub-Doppler basée sur un schéma de molasses grises fonctionnant sur la transition atomique D_1. Cette stratégie améliore la densité dans le espace des phases des deux espèces atomiques à 10^{-4}, la valeur la plus élevée rapportée dans la littérature pour le refroidissement laser du ^{6}Li et du ^{40}K.

L'optimisation d'un dispositif capable de transporter un nuage atomique piégé magnétiquement de l'enceinte MOT à une cellule de science est décrite. Dans cette cellule on effectue du refroidissement évaporatif d'abord dans un piège magnétique quadripolaire dont le zéro du champ est interdit par un potentiel répulsif et après dans un piège optique dipolaire. Nous rapportons la production d'un gaz quantique de Fermi dégénéré de 1.5×10^5 atomes de ^{40}K dans un piège dipolaire croisé avec $T/T_F = 0.17$, ouvrant la voie à la création des superfluides de ^{40}K en interactions fortes.

Acknowledgements

I start by thanking Denis Boiron, Philippe Bouyer, Roland Combescot, Bruno Laburthe-Torla and Giacomo Roati, who have kindly accepted to be part of my thesis jury committee and gave very useful remarks that helped to improve this manuscript.

The work presented in this manuscript would not be successful without the help and support of many people, whom I would like to acknowledge here.

To start, I would like to thank my thesis supervisor Frédéric Chevy for constantly supporting the experimental effort during all its phases and for his very rational advice. He has the great ability of going beyond "the box" and impress us with smart and fruitful perspectives.

Equivalently, I thank my "second" supervisor Christophe Salomon, for his enthusiasm, deep knowledge and positive thinking that he brought to the experiment. When facing a problem in the laboratory, Christophe was extremely helpful to reach solutions. Not only we could profit from his vast experience, but he also knew which were the good questions to be asked and made us re-evaluate what we wrongly took for granted.

I would like to give a very special thanks to the first generation of people working in the experiment. It was a privilege working with them and I was fortunate to have such talented mentors during my first year of thesis. From the start, Armin Ridinger (*Armix*) thought me *everything* to be known about the experimental apparatus and impressed me with his outstanding scientific and social skills. Working or having a beer with him was always a pleasure. Besides the extensive scientific knowledge of Saptarishi Chaudhuri (*Wrishix*), he was a model of patience, tenacity and perseverance. For him a difficulty was challenge and his teachings guided me throughout my thesis. I had also the pleasure of working with Thomas Salez (*Tobomix*), specially when facing the challenging task of implementing the magnetic transport. I was impressed with his multi-faceted talents and his fascination with different aspects of Physics. Finally, Ulrich Eismann (*Ulle*), with whom I shared the office and I could benefit from technical expertise.

thank my *co-thésards* Franz Sievers, for his outstanding technical and engineering skills, and Norman Kretzschmar (*Normie*), for his calmness, patience and professionalism. Daniel Suchet joined the team in the later years of my thesis and it was a pleasure to work by his side. I admire and envy his numerous qualities, such as his extraordinary scientific and human

maturity. It is hard to mention all the great moments we shared: *apéros*, concerts, pop music contests and unicorn songs (PFUDOR!), to mention a few. I feel lucky to have Daniel as a friend. I wish plenty of exciting results with the Fermix apparatus, together with the newest members of the team, Michael Rabinovich and Thomas Reimann.

I also would like to thank Colin Parker for his collaboration with the project in the early days. We were all amazed with his outstanding intellectual and experimental skills. I am grateful for collaborating with Saijun Wu, who suggested cooling in the D_1 atomic transition and without whom the gray molasses project would never be realized. I was happy to work with Lev Khaykovich, who visited our laboratory for few months. I thank Paolo Chiggiato and Ivo Wevers from the CERN, who generously accepted to coat our vacuum parts with TiZrV getter.

I thank the Lithium team, Igor Ferrier-Barbut, Benno Rem, Andrew Grier, Marion Delehaye, Sébastien Laurent and Matthieu Pierce. I am indebted to Andrew, who was of great help during my thesis. I was impressed by his exceptional technical skills and his modesty. I also acknowledge Andrea Bergschneider and Tim Langen.

I thank the rest of the cold atoms groups, in particular for being sympathetic to my frequent requests of laboratory material. I was lucky to become friends with Christof Weitenberg, with whom I learned a lot and shared very good moments.

I express my gratitude to the LKB administrative services, namely to Christophe Bernard, Thierry Tardieu, Dominique Giafferi and Monique Granon. In particular, I thank Christophe for always being friendly, sharing many *pause café* and professionally carrying out our numerous demands. I thank the workshop staff, namely Thierry Bastien, Jean-Michel Isac and Saysavanh Sourasing. I equally thank the electric and electronic technicians and engineers, namely Toufik El Atmani, Lionel Pérenes and Bernard Trégon.

I greatly thank my closest friends Gabriel Gomes da Silveira [160], Renato Sousa and Augustin Brat for their continuous unconditional support and sympathy, specially in the most stressful times. I own you a lot.

Finally, I would like to thank my wonderful family to whom I dedicate my thesis. I am infinitely grateful for providing me with a open and stimulating environment in which I grew. I could never reach this far if it were not for you.

1 Introduction

The field of ultracold atoms has made a remarkable progress since the 1980s and is today an important subject in Physics on its own. One of the main motivations for development of the field in the early days was the quest for the observation of a quantum phase transition predicted by S. N. Bose and A. Einstein [23, 53]. Bose-Einstein condensation (BEC) occurs when the typical distance between bosonic particles becomes of the order of their thermal de Broglie wavelength. In this regime, the single-particle wavefunctions interfere, driving the macroscopic occupation the ground state of the system, giving rise to a "macroscopic wavefunction". This phenomenon was first observed in superfluid ^{4}He in 1937 [4, 95]. In the 1970s it was pointed out that dilute gases of neutral atoms were promising systems for achieving weakly interacting BEC.

The first system to be explored was polarized Hydrogen, which has a high critical temperature, due to its small mass. Cooling was performed in two stages: first by using a cryostat to load Hydrogen directly in a magnetic trap [86] and then by performing evaporative cooling in this trap [85, 125]. However, the quest for BEC was hindered by the small atom scattering cross-section and dipolar losses.

Starting in the 1980s, there was a spectacular development of powerful laser cooling techniques, such as magneto-optical trapping (MOT) [162] and sub-Doppler cooling [30, 38, 112]. It was the combination of laser cooling [128] and evaporative cooling [99] in a magnetic trap [131] that allowed the first observations of BEC in Rubidium [6] and Sodium [39] in 1995. Hydrogen followed few years later in 1998 [61], as well as many other bosonic isotopes: all alkali metals (except Francium), alkaline earth metals (Calcium and Strontium), a noble gas (metastable Helium), a transition metal (Chromium) and Lanthanides (Ytterbium, Erbium, Dysprosium).

Using the same techniques of laser and evaporative cooling, several groups tried to cool fermionic isotopes. While for bosons the occupation of the same quantum state is possible, for fermions this is not the case since they obey the Pauli exclusion principle.

In consequence, no phase transition was expected to occur when reaching the quantum regime, only the observation of a smooth transition to the degenerate Fermi sea. Moreover, the cooling of fermions is hindered by the Pauli principle, which does not allow indistinguishable fermions to collide at low energies, making evaporative cooling impossible[1]. This was circumvented by cooling two distinguishable spin-states of the fermionic atom [41, 42, 44] or by using a boson as a sympathetic coolant for the fermion [176]. The cooling of fermions to quantum degeneracy was first achieved with ^{40}K atoms in 1999 for the first time [43]. Since then, degeneracy was attained for several atoms: another alkali ^{6}Li [177, 202], metastable ^{3}He* [127], ^{87}Sr [45, 195], ^{173}Yb [64], ^{161}Dy [119] and ^{167}Er [3].

The discovery of Feshbach resonances was a key turning point in the field of ultracold Fermi gases. These resonances occur when two free atoms (open channel) are coupled to a molecular bound state belonging to a different molecular potential (closed channel). In this case, the scattering properties of the two free atoms can dramatically change. By tuning the energy difference between the open and closed channels, one can control their coupling and, consequently, the elastic scattering cross-section. Typically, this is achieved by choosing molecular states which have different magnetic moment, so that their coupling may be manipulated by simply tuning the magnetic field[2]. Feshbach resonances were first observed in bosons by measuring strong inelastic losses, which were triggered by the enhancement of interactions [89]. Few years later, resonances were also observed in fermionic atoms ^{6}Li [47, 94, 145] and ^{40}K [118]. Fortunately, it turns out that for fermions inelastic three-body losses are suppressed due to the Pauli exclusion principle [158]. The stability of strongly interacting Fermi gases opens the door for exciting experimental manipulations.

There were many ground-breaking achievements in the ultracold fermionic gas field, but it is out of the scope of the introduction of this thesis to do a complete review of those results (for this we refer the reader to refs. 70, 100). Instead we give few examples. 1. The observation of BEC of pairs of strongly bound fermions [73, 93, 217]. 2. The production of quantized vortices, which is a proof of superfluidity, throughout the BCS-BEC crossover [219]. This crossover can be studied by changing the

[1] A remarkable exception is Erbium, for which elastic collisions between atoms in the same state are possible due to the strong magnetic dipole-dipole interaction [2].

[2] We refer the reader to ref. 29 for a review on Feshbach resonances in ultracold atoms.

strength of the attractive interaction between two components of a Fermi gas. The gas smoothly alters between weakly attractive fermions (Cooper pairs, BCS phase) and strongly bound fermions (composite molecules, BEC phase). 3. The study of the phase diagram of a two-component Fermi gas [182]. 4. The measurement of the equation of state of a universal gas [136]. 5. The observation of ultracold fermionic polar diatomic molecules in the rovibrational ground state [139].

Besides having the possibility of tuning the interaction strength, ultracold atomic systems are versatile (one can tailor the confining potential practically at will), pure (as opposed to condensed matter systems, where impurities are always present) and controlled (all couplings to the exterior are manipulated by the experimentalist). All these attributes unravel a surprisingly broad class of interesting quantum many-body systems. By designing systems with the same Hamiltonian as systems from condensed matter, QCD or even astrophysics, ultracold atoms can be used as multi-faceted quantum simulators [18, 58, 68].

This thesis describes the design, construction and characterization of a new generation apparatus for the production of large samples of quantum degenerate gases of two different atomic fermionic species: ^{6}Li and ^{40}K. Mixtures of mass imbalanced fermions allied with the realization of species-selective potentials open the door to new classes of quantum many-body systems. In the following we will briefly review the existing theoretical proposals for mixtures of Fermi gases, present the state of art of the field and then describe the outline of this thesis.

1.1 Prospects for ultracold fermionic mixtures

A mixture of two different fermionic atomic species allows the observation and study of a wide range of new interesting phenomena. In recent years there were many exciting theoretical proposals [70, and references therein] of which we give here some account.

A consequence of having a fermionic mass imbalance system is the presence of unmatched Fermi surfaces, which do not allow symmetric pairing, resulting in a much richer phase diagram than the balanced case [11, 15, 37, 48, 69, 77, 83, 90, 124, 151, 207, 214]. For this system there is the prediction of exotic superfluids [11, 79, 148]. The asymmetric pairing can give rise to a superfluid with a spatially inhomogenous

density, which is a known topic in condensed matter physics (and QCD) [26]. Some exotic phases are predicted, such as the FFLO state [65, 88, 108, 132], the breached pair state [60, 116] and the Sarma state [174]. There is also the possibility of a link with baryonic phases of QCD [163, 211] and there are proposals for the observation of Anderson localization using atoms as random scatterers [66] and a transition to a stable crystalline phase [157].

From the few-body physics approach, studies were performed on the atom-dimer and dimer-dimer scattering [5, 8, 19, 113] and long-lived [114] and nonuniversal [170] trimers were predicted.

The fact that the two atoms have different energy level structures opens the possibility of tailoring selective potentials for each of the atomic species [117]. One exciting direction is to freeze the motion of one (or both) fermionic species in one (or more) directions of space, thereby creating a mixed-dimensional system. Many new exotic phases and phenomena are predicted in this regime [1, 34, 140–143].

Another possibility is the production of quantum degenerate dipolar molecules in the rovibrational ground state [40, 139], which in the case of ^{6}Li^{40}K possess a large dipolar moment [9, 10]. New phases of matter are expected to be observed with quantum gases with strong dipolar interactions [104].

The list of theoretical proposals is not exhaustive, but shows that ultracold fermionic mixtures are strong candidates for the observation of interesting new phenomena. In our group the planned research direction is the study of mixed-dimension systems, which will be described in more detail in section 8.2 (perspectives of this thesis).

1.2 State of the art in Fermi-Fermi experiments

There are five experimental apparatus in the world capable of cooling ^{6}Li and ^{40}K, of which two are pursuing the investigation of fermionic mixtures.

The pioneering steps were made by the group of K. Dieckmann in Munich (now in Singapore), which reported the triple magneto-optical trapping (MOT) of ^{6}Li, ^{40}K and ^{87}Rb [193]. They reported the cooling of the three species to quantum degeneracy by evaporative cooling of ^{87}Rb and letting the fermions being sympathetically cooled in a Ioffe-Pritchard trap [192]. The group is trying now to produce bosonic ^{6}Li^{40}K molecules in the rovibrational ground state and study the resulting dipolar gas.

The group of J. Walraven (Amsterdam) constructed two 2D-MOTs to produce cold atomic beams of both ^{6}Li [196] and ^{40}K. Potassium is evaporative cooled in an optically plugged magnetic trap, transferred in an optical dipole trap and transported into a science cell for further evaporation. Quantum degeneracy of ^{40}K was reported, but not of ^{6}Li [200]. Sadly, this experiment was recently shut down.

In Innsbruck, a group led by R. Grimm built an apparatus incorporating a single Zeeman slower for ^{6}Li and ^{40}K (and Strontium). After capturing and cooling the two species in a MOT, they load the mixture in a crossed optical dipole trap and perform forced evaporation of ^{6}Li on a Feshbach resonance to double degeneracy [187, 188].

At the MIT in Boston the group of M. Zwierlein cooled the fermionic mixture using ^{41}K, a bosonic isotope of Potassium, as coolant. Forced evaporation was performed in a optically plugged magnetic trap resulting in degenerate gas of the three species [213]. They reported Feshbach resonances between ^{6}Li and ^{41}K and between ^{40}K and ^{41}K. This machine is now devoted to the production of quantum degenerate NaK molecules in the rovibrational ground state.

Our experiment, in Paris, led by F. Chevy and C. Salomon, we built a Zeeman slower for ^{6}Li and a 2D-MOT for ^{40}K [167]. After transferring the mixture into a science cell with a dynamic magnetic trap, we evaporate ^{40}K and load it in an optical dipole trap, as explained in this thesis. The evaporation of two spin states of ^{40}K results in a quantum degenerate gas. Attaining the double degeneracy should be achieved in the near future.

Several Feshbach resonances were observed in the ^{6}Li-^{40}K system [198, 212]. At the present, these resonances are very well studied and understood. Thanks to a asymptotic-bound-state model [199], the positions and widths of all the ^{6}Li-^{40}K Feshbach resonances were numerically calculated and match very well with the existing experimental values [134]. Unfortunately, strong inelastic losses were observed and the universal regime is quite narrow (only few milli-Gauss wide), which increases the experimental challenge. The main experimental achievements with the ^{6}Li-^{40}K system include the observation of the enhancement of the interspecies collision rate close to the Feshbach resonance [35] and the production of ^{6}Li^{40}K Feshbach molecules [205], both reported by the group of K. Dieckmann. In Innsbruck, the group of R. Grimm studied the expansion of a strongly interacting gas of ^{6}Li-^{40}K [201], investigated the dressing of ^{40}K impurities by a sea of strongly interacting ^{6}Li atoms [101]

and, more recently, observed the predicted [5, 113] strong attractive interaction between a ^{6}Li-^{40}K dimer and ^{40}K atoms [91].

1.3 Outline of this thesis

This thesis reports the design, construction and characterization of an apparatus capable of cooling a mixture of ^{6}Li and ^{40}K. It started from an already designed and partially constructed experiment, with the laser sources ready for laser cooling on the D_2 atomic line. The main achievements of this thesis are the discovery of a sub-Doppler scheme for cooling ^{40}K and ^{6}Li, the implementation of a magnetic transport and the production of the first quantum degenerate gas of ^{40}K in France. The organization of this thesis follows the chronological order of the cooling sequence of the fermionic mixture.

Chapter 2

In this chapter, the presentation of the more technical aspects of the experimental apparatus will be made. We will describe the systems involving vacuum, laser cooling and laser trapping, imaging and experiment control.

Chapter 3

This chapter will be devoted to the presentation and characterization of the double MOT. A Zeeman slower was built to produce an atomic jet of ^{6}Li and a 2D-MOT was conceived to produce a cold atomic beam from a vapor of ^{40}K-enriched sample of natural Potassium. Atoms from both systems were collected in a double species MOT, yielding high number of collected atoms and high capture rates for both species [167]. The description of subsequent improvements of the setup will also be the subject of this chapter.

Chapter 4

We will present in this chapter one of the core results of the thesis, which is an efficient sub-Doppler cooling mechanism implemented on the D_1 atomic line. This novel

strategy relies on a gray molasses scheme, which we show to be able to cool an entire atomic cloud of ^{40}K to the sub-Doppler regime [168]. We also report the implementation of this strategy on ^{6}Li [184]. The described gray molasses scheme is the first efficient sub-Doppler cooling mechanism being reported for the fermionic alkalis and it is also being implemented in a increasing number of isotopes. Thanks to its success, gray molasses cooling on the D_1 atomic line is turning out to be a standard technique for sub-Doppler cooling of atomic gases.

Chapter 5

In this chapter we will explain the properties of a quadrupole magnetic trap and how to efficiently load it with an atomic cloud. In a second part, we will describe a magnetic transport which is able to efficiently transfer the atomic cloud from the MOT chamber into a science cell.

Chapter 6

We will describe the forced evaporation of a cloud of ^{40}K in a magnetic plugged trap and its transfer into an optical dipole trap. Calculations will be presented in order to understand the evaporative cooling dynamics and they will be compared to experimental results. We also show results of the sympathetic cooling of ^{6}Li in the plugged magnetic trap.

Chapter 7

The loading and evaporation of ^{40}K in the optical dipole trap to quantum degeneracy will be presented in this chapter. We will also report on the efforts done to obtain a strongly interacting superfluid of ^{40}K and on strategies to achieve a double degenerate gas.

Chapter 8

In the final chapter we will summarize the results of this thesis and discuss some concrete and exciting ideas to be realized in the near future with this apparatus.

2 Experimental apparatus

This chapter is devoted to the description of the main technical features of the Fermix machine. The apparatus in located in a laboratory room two levels below the ground floor, which is temperature stabilized by air conditioning with set point at 21°C (daily temperature stability $\sim \pm 0.5$°C). The room has weak reception of mobile and wifi signals and it is likely that the strongest electromagnetic contamination comes from an elevator located $\sim 5 - 10$m away.

When the author of this thesis started working in the Fermix apparatus the laser sources for cooling ^{40}K and ^{6}Li on the D_2 atomic line were already implemented and a preliminary ^{40}K MOT had already been tested. The following steps were to bake-out the vacuum chamber and then to assemble and align all the optics necessary to achieve the double MOT. The description of these tasks was already reported with detail by two fellow PhD students [166, 171] and was also the object of a publication [167]. To avoid repetition, in this chapter we shall only describe changes in the apparatus relative to those documents.

In this chapter we shall start by presenting the vacuum chamber and the improvements which were made. The different laser setups will only be enumerated, since their detailed description is made more pertinently in subsequent chapters. Finally, we will present the absorption imaging technique and the implemented computer control system. The electromagnetic coils used in the experiment are described in appendix 5.A. The radiofrequency/microwave sources and the antennae are presented in section 6.5.1 and appendix 6.B, respectively.

2.1 Vacuum chamber

Experiments with ultracold gases must be done under high quality vacuum. Since the standard traps for neutral atoms are rather shallow (the depth is typically of the order of 100mK), a collision of a trapped atom with a particle from the background

gas at room temperature will knock it from the trap [203]. The required pressure regime to perform experiments with ultracold atoms is the ultra-high vacuum (UHV, $< 10^{-9}$mbar), in which the background gas is so dilute that particles fly ballistically, bouncing only at the walls of the vacuum chamber (molecular flow). To be more accurate,, the typical background pressure in experiments is rather in the $10^{-11} - 10^{-12}$mbar regime[1], which requires a very careful design and building of the vacuum chamber and the pumping system[2]

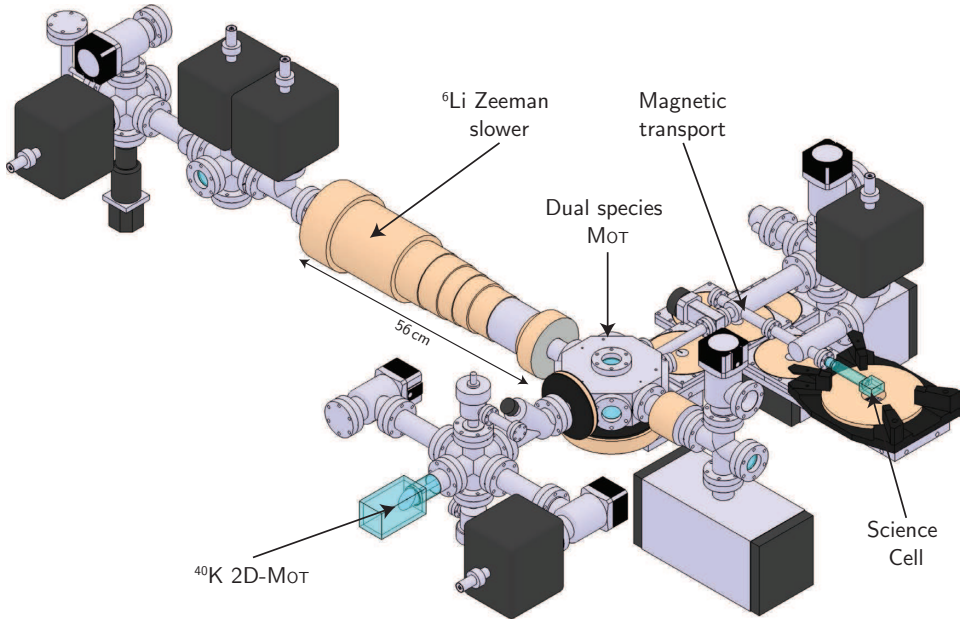


Figure 2.1.1: Vacuum chamber (scheme from ref. 183).

The structure of the vacuum chamber is depicted in fig. 2.1.1. It comprises the atomic sources: a 2D-MOT with enriched ^{40}K (4%) and a Zeeman slower for ^{6}Li; the MOT chamber; a (magnetic) transport in a "L" shape and a (science) glass cell. All components under vacuum are either made of glass or stainless steel. The majority of the components was bought from MDC Vacuum, which are made of type 304 stainless steel and UHV rated to 1×10^{-13}Torr. As explained in ref. 166, the global strategy is to implement a series of differential pumping stages. This technique consists in in-

[1]For comparison, the pressure at the interaction point of the LHC is $\sim 10^{-11}$mbar; the pressure at 10.000km of altitude is $\sim 10^{-13}$mbar.
[2]For building and baking-out UHV chambers the author found reference 22 very useful.

serting a physical constriction between a chamber with an elevated pressure and a second one where a lower pressure is required. By pumping the later, one can create an important gradient of pressure between the two chambers. This strategy was realized between the atomic sources (where the background pressure is very high), the MOT chamber (where a moderate pressure of $\sim 10^{-10}$mbar can be accepted) and the science cell (where experiments will be conducted and very low pressure $\sim 10^{-12}$ mbar is required).

The lifetime of the magnetically trapped atoms in the MOT chamber was determined to be $\approx$ 3.0s for both ^{40}K and ^{6}Li, which suggests that it was limited by the background pressure (as losses due to stray light and Majorana losses depend on the atomic species). At the time of the measurement, this value was found acceptable. By measuring the geometry of the vacuum tubbing between the MOT chamber and the science cell, it is possible to calculate the conductances and the pumping speed in this region. Using this calculation, one can estimate the pressure ratio induced by the differential pumping between the two chambers to be $\approx$ 9.8. The lifetime measured in the science cell was indeed of 30s, indicating that it is limited by the residual background gas bouncing from the MOT chamber to the science cell.

The situation reported in the previous paragraph was not ideal for performing experiments with ultracold gases. In particular, evaporative cooling in a magnetic trap typically requires a long lifetime (see section 6.3). Experiments confirmed that ^{40}K could not be evaporated efficiently due to the limiting lifetime. To improve the background pressure it was decided to increase the pumping speed in two different regions: in the MOT chamber and in the transport section. This approach did not require baking the full apparatus, which would imply removing all the optics from the main table, and took only about 1 month of work. The improvements resulted in very satisfactory lifetimes and made efficient evaporative cooling possible.

2.1.1 MOT chamber

The lifetime in the magnetic trap in the MOT chamber prior to the increase in pumping speed was of $\approx$ 3.0s. This value did not depend on the pressure of the atomic sources, which indicated that the MOT chamber had a small leak or a badly baked region outgassing. The strategy to reduce pressure was to insert a thin metallic strip

(Constantan) with a deposit of St 707, a non evaporable getter (NEG)[3]. This getter is fully activated when heated between $400 - 500$°C for $\sim$ 10min (or for longer times at lower temperatures) and efficiently pumps H_2, H_2O, CO, CO_2 and N_2 (especially H_2). Some $\approx$ 20cm of NEG strip were inserted into a CF40 90° elbow, which was connected to the valve close to the glass window for the Zeeman laser beam (see fig. 2.1.2). The termination was done with another all-metal valve.

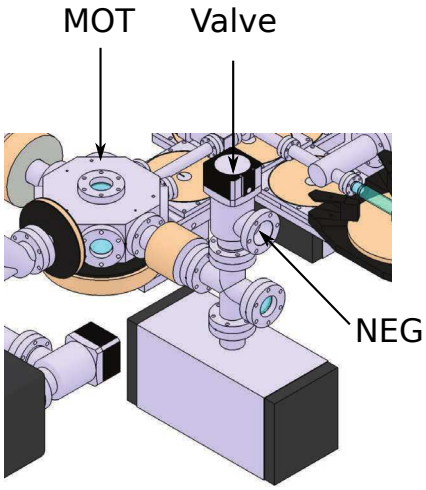


Figure 2.1.2: Detail of fig. 2.1.1 showing the intervention area.

Increasing the pumping speed in the MOT chamber improved the lifetime to $\approx$ 9s over one day. If needed, the NEG strip could be reactivated by closing the valve to the MOT chamber and by heating the strip again and pump desorbing H_2 (other molecules migrate to deeper layers of the getter). At the moment of writing, the lifetime in the magnetic trap in the MOT chamber is (16.5 ± 0.6)s, which is a factor 5 improvement compared to the previous situation. Interestingly, the reported lifetime was measured with the valve to the getter pump closed. This suggests that the actions undertaken to activate the getter and bake the transport region (reported in the following section) somehow helped solving the pressure problem existing in the MOT chamber.

2.1.2 Transport section

The region of the transport is decoupled from the rest of the apparatus by a valve about 20cm from the MOT chamber (see fig. 2.1.1). This gives the freedom to improve the pumping in the transport region without having to bake the whole experiment (or removing important parts of the optics). In the following we describe the important changes that were made to the vacuum parts in this region.

The transport section is schematized in fig. 2.1.3. It shows the MOT chamber, from which the atoms are magnetically transported to the science cell (depicted as

[3]St 707 is a getter alloy made of 70% Zirconium, 24.6% Vanadium and 5.4% Iron commercialized by SAES getters (reference St 707/CTAM/30D).

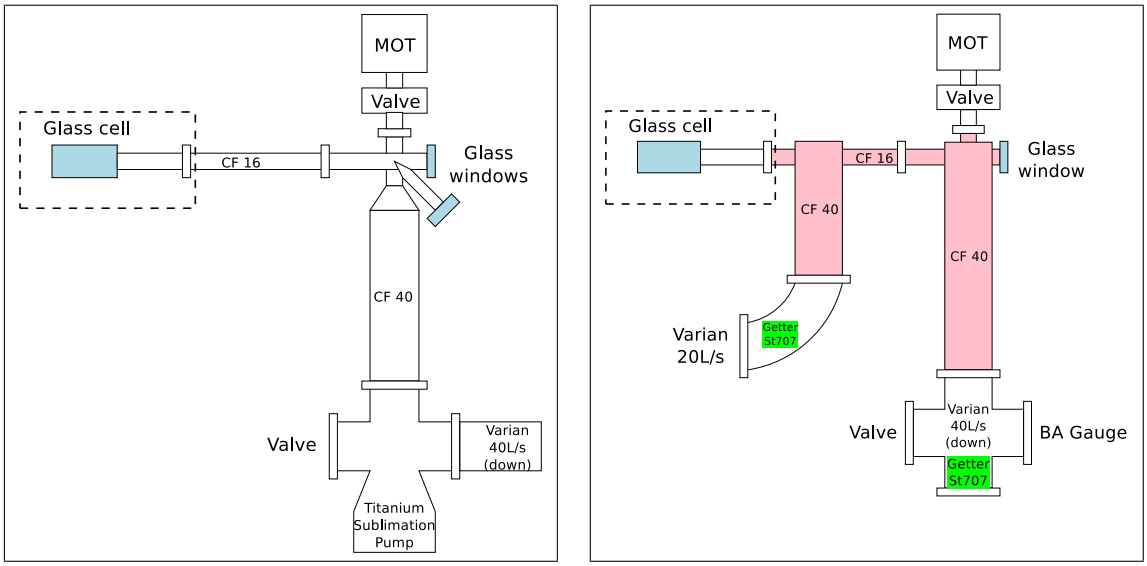


Figure 2.1.3: Scheme of the vacuum parts of the second transport part viewed from the above. In the left is depicted the previous setup (reported in refs. 166, 171, see fig. 4.25 and fig. A.8 of ref. 171) and in the right the current setup. The pink color refers to the parts coated with the TiZrV NEG and the green color the emplacement of St707 NEG strips.

"Glass cell") in a "L" shaped motion. The corner of the "L" is called *elbow* and is a pumping region. One of the major issues of the previous setup was that the pumping at this level was not optimal (see left scheme of fig. 2.1.3). The pumping rate at the elbow S_E is given by the relation $1/S_E = 1/S_{Pump} + 1/C_{Pump}$, where S_{Pump} is the nominal pumping rate of the installed pumps and C_{Pump} is the conductance of the tube between the elbow and the pumps. The conductance of a cylindrical tube is $C = 12.4D^3/L$ for N_2 (in L/s units), D being the diameter of the tube and L its length both in cm units. It turns out that the conductance C_{Pump} was very low $C_{Pump} \approx 6.6$L/s, simply due to the neck-shaped constriction of diameter 16mm between the elbow and the CF40 tube (see left scheme of fig. 2.1.3). This design problem rendered the Titanium sublimation pump useless, as the pumping speed at the elbow was limited by the tubbing conductance.

In the new design it was introduced a straight CF40 tube[4], which increased conductance C_{Pump} by a factor of 3 (see right scheme of fig. 2.1.3). The engineering drawing of the new designed part can be found in section 2.A (top scheme). The

[4]Due to the presence of the transport coils, it was not possible to have a tube with larger diameter.

cumbersome (and useless) Titanium sublimation pump was removed from the system and replaced by ≈ 20cm of St707 getter strip. A Bayard-Alpert ionization gauge was introduced in order to help diagnosing eventual problems[5] .

In addition, a second stage of differential pumping was introduced between the elbow and the science cell. A supplementary gradient of pressure is possible due to a constriction of diameter 16mm between the elbow and the new pumping region (see right scheme of fig. 2.1.3). The engineering drawing of this vacuum part can be found in section 2.A (bottom scheme). The pumping is assured by a 20L/s ion pump[6] and ≈ 20cm St707 strip. Notice that since NEGs do not capture noble gases it is preferable to combine them with ion pumps. Without taking into account the pumping power of the NEGs, the calculated improvement in pressure in the science cell was of factor 16, yielding a pressure ratio of 160 between the science cell and the MOT chamber.

Moreover, we decided to coat the interior of two of the new vacuum parts with a NEG (colored in pink in fig. 2.1.3). This technology was developed by a group at CERN, who managed to optimize a mixture of Titanium, Zirconium and Vanadium (TiZrV) that works as an efficient getter and has a low activation temperature of ≈ 180ºC [17]. In addition, they used magnetron sputtering to depose this NEG in the interior of vacuum parts, most notably in all the LHC vacuum chambers [28]. This group very kindly accepted to coat our vacuum parts (see fig. 2.A.2)[7]. We expect this NEG coating to pump very efficiently since it is not limited by any conductance. Molecules bouncing in the vacuum tubes from the MOT chamber will immediately stick in the coating.

The TiZrV coating was activated by baking it at 200ºC for 24h, while the St 707 strips were baked at 350ºC for 2h. The activation of the TiZrV coating was the last step of the bake-out of the transport to ensure maximum pumping efficiency. Both NEGs can be reactivated if needed: H_2 will be desorbed and pumped by the ion pumps, while other gases will migrate to lower layers of the getters. However, one as to act wisely since there are some reports of pealing off of the NEG coating.

At the moment of writing, the lifetime in the magnetic trap at the elbow region is

[5] Agilent UHV-24 P

[6] All ion pumps in the apparatus are Varian Vaclon Plus 20L/s or 40L/s. This particular ion pump was shielded using mu-metal due to its proximity to the science cell (Ateliers Soudupin).

[7] We acknowledge Paolo Chiggiato and Ivo Wevers for their contribution.

$\approx$ 130s for ^{40}K. It is not clear if this value is limited by the background pressure, but it is largely sufficient to evaporative cool down atomic gases to quantum degeneracy.

2.2 Laser systems

Light is a versatile and powerful method to manipulate atoms [75, 128]. In this experiment we dispose of several laser systems built with different purposes. The relevant atomic transitions are shown in section 2.2.1 and comprise a D_2 and a D_1 line for both ^{40}K ($\lambda = 766.701$nm and $\lambda = 770.108$nm) and ^{6}Li ($\lambda = 670.977$nm and $\lambda = 670.979$nm, respectively). The atomic properties of ^{6}Li and ^{40}K can be found in refs. 67, 197, respectively.

- The laser system for cooling on the D_2 atomic line is described in detail in section 2.3 of ref. 166 and it had already been already implemented when the author started his thesis. The updated scheme of this laser system is depicted in fig. 2.2.2 and the optical tables are depicted in sections 2.C and 2.B. The main changes are the paths for optical pumping (discussed in section 5.2) and for imaging in the high-field (see section 2.3).

- For the gray molasses cooling we implemented two different laser systems frequency locked to the D_1 line for ^{40}K and for ^{6}Li (see fig. 2.2.2). These systems are described in sections 4.4 and 4.6.1, respectively.

- We also implemented laser systems for an optical plug with $\lambda = 532$nm, an optical dipole trap at 1064nm and an optical lattice at 808nm. These systems are described in detail in sections 6.5.3, 7.2 and in the appendix 8.A, respectively. The laser setup around the science cell is explained in section 2.2.3.

2.2.1 Atomic levels and cooling transitions

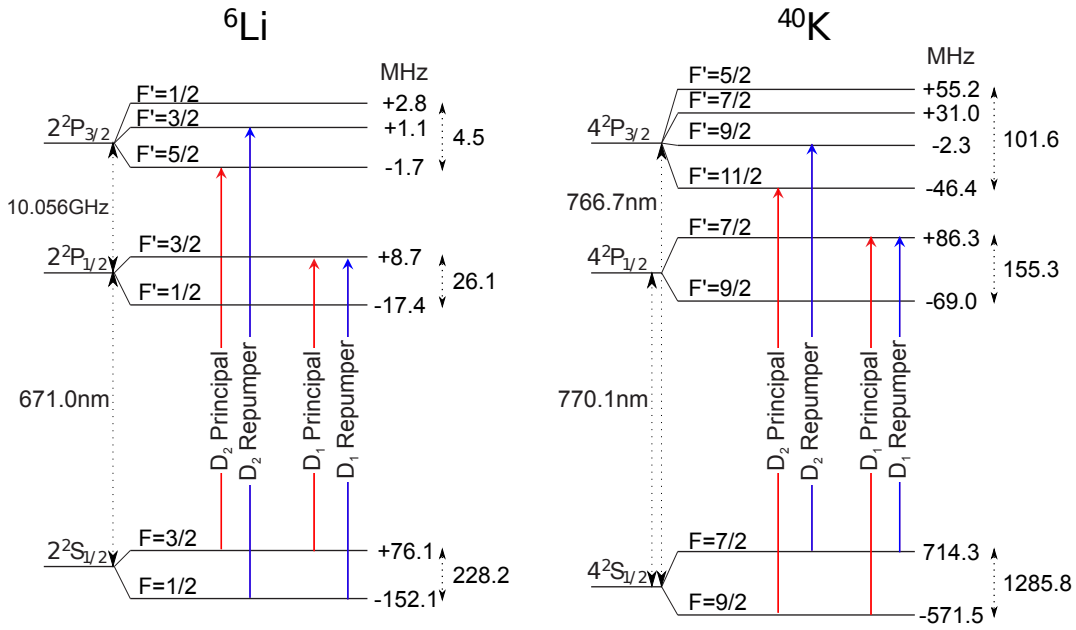


Figure 2.2.1: ^{6}Li and ^{40}K atomic transitions used for laser cooling.

^{6}Li Laser Beam	δ		^{40}K Laser Beam	δ		Transition
^{6}Li Crossover	+116 MHz		^{39}K Crossover	-593 MHz		D_2 Principal
Zeeman Cooling	-76Γ		2D-MOT Cooling	-3.0Γ		D_2 Principal
Zeeman Repumper	-76Γ		2D-MOT Repumper	-2.0Γ		D_2 Repumper
3D-MOT Cooling	-4.5Γ		3D-MOT Cooling	-2.9Γ		D_2 Principal
3D-MOT Repumper	-2.6Γ		3D-MOT Repumper	-5.2Γ		D_2 Repumper
Imaging	0		Imaging	0		D_2 Principal
D_1 Cooling	+4Γ		D_1 Cooling	+2.3Γ		D_1 Principal
D_1 Repumper	+4Γ		D_1 Repumper	+2.3Γ		D_1 Repumper

Table 2.2.1: Laser beams used for locking, cooling and imaging and their detunings δ respective to the atomic transitions signaled in fig. 2.2.1 ($\Gamma_{^6\mathrm{Li}}/2\pi \approx 5.87$MHz and $\Gamma_{^{40}\mathrm{K}}/2\pi \approx 6.04$MHz).

2.2.2 Setup for cooling in the D_2 and D_1 transitions

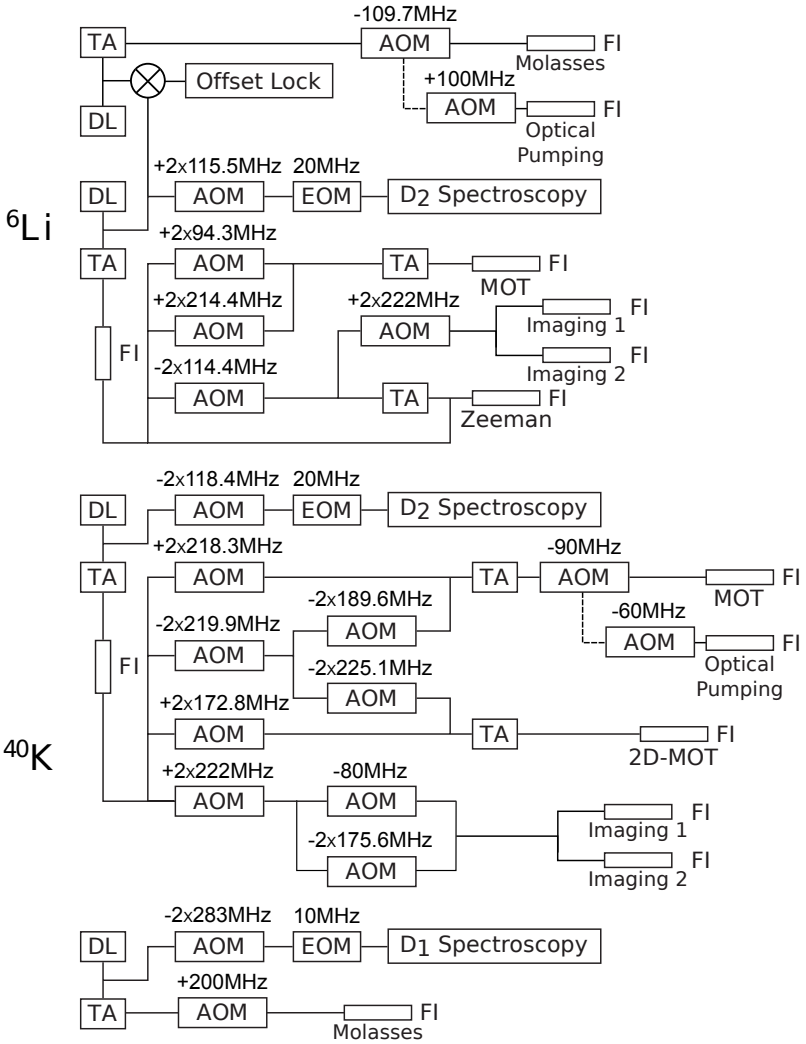


Figure 2.2.2: Laser setup for cooling of ^{6}Li (top) and ^{40}K (bottom) on the D_2 and in the D_1 atomic lines, adapted from ref. 167. AOMs diffract light and are used to tune laser frequency and power. The frequency shifts corresponding to the detunings of table 2.2.1 are indicated in the figure and can be single or double. Vertical dashed lines refer to light that passes through an AOM without diffraction (thus not frequency shifted). EOMs are used for phase modulation of a spectroscopic probe beam in order to generate a lock dispersive signal, following the Pound-Drever-Hall technique [49]. Single mode polarization maintaining fibers (FI) are used for spatial mode filtering and laser pointing stability.

2.2.3 Optical setup around the science cell

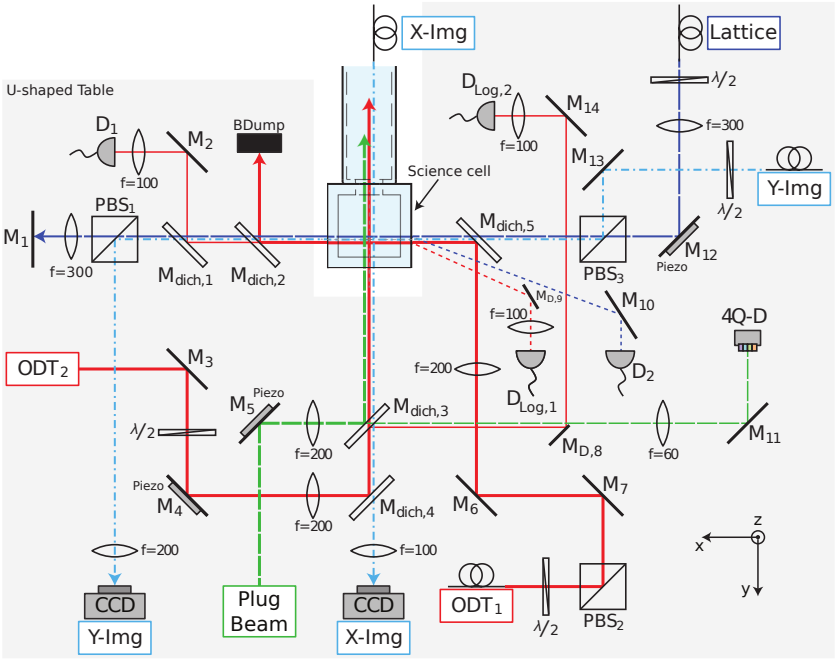


Figure 2.2.3: After the atom cloud being magnetically transported from the MOT chamber, it is trapped in the inner quadrupole coils of the science cell. This cell is made of Vycor glass (not coated) of 4mm thickness by Hellma and has inner size of $23 \times 23 \times 10$mm ($x \times y \times z$). The technical drawings can be found in previous thesis [166, 171]. The magnetic field center is in the center of the science cell, except in the y direction, for which it is ≈ 7mm from the glass wall. This asymmetry allows an improved optical access in the y direction ($\mathrm{NA}_{\mathrm{max}} \approx 0.52$) with reasonable working distance and allows having laser beams with incidence angle of 45°. In this setup, the beams along the x axis make an angle of 10° with the perpendicular of the science cell wall (not shown in the scheme to simplify). This avoids reflections in the cell walls to interfere with the incoming beam. The crossed optical dipole trap (ODT1 and ODT2) is depicted in red. The optical plug beam is depicted in green. The absorption imaging beam is depicted in light blue and is bichromatic since it has a component resonant with ^{40}K and another with ^{6}Li. The z direction (vertical) has the best optical access and there is an imaging system along this axis (not shown). The lattice beam is depicted in dark blue. Dichroic mirrors are Thorlabs DMLP1000, except for dichroic 3, which is Melles-Griot LWP-45-RP532-TU633-106. The optical breadboard has dimensions $640 \times 580 \times 60$mm and was custom made by Thorlabs. Scheme is adapted from ref. 183.

2.3 Absorption imaging

In order to probe the density profile of an atomic cloud in this apparatus, we use the standard absorption imaging, which is a destructive probing technique. It relies on impinging a resonant laser beam onto the atomic cloud and recording the transmitted light, which features a shadow cast by the atoms. This shadow in the transmitted beam is due to the absorption of resonant light by the atoms and subsequent rescattering in random directions (we assume negligible the scattered light measured by the detector). The detectors used in this apparatus are charge-coupled device (CCD)-based cameras[8] that through an optical imaging system are able to record an image of the atomic cloud $I(x,y)$[9].

In a typical detection sequence a first *imaging* laser pulse with 100μs duration is recorded $I_{\text{img}}(x,y)$ and, after letting the atomic cloud expand and fall for $\approx$ 50ms, a second *reference* picture is taken $I_{\text{ref}}(x,y)$[10]. This image has exactly the same characteristics as $I_{\text{img}}(x,y)$, except for the presence of atoms. Another pair of pictures is taken in the same conditions, but in the absence of laser light in order to measure the dark noise in the CCD camera $I_{\text{bg,img}}(x,y)$ and $I_{\text{bg,ref}}(x,y)$[11]. Using this data, the transmission profile $T(x,y)$ can be calculated

$$T(x,y) = \frac{I_{\text{img}} - I_{\text{bg,img}}}{I_{\text{ref}} - I_{\text{bg,ref}}},$$

which does not depend on the intensity profile of the laser beam. This function carries information about the *integrated* density profile of the atomic cloud along the imaging

[8] pco. Pixelfly QE 270XD, 1392 $\times$ 1024 pixels (px), 1px$\hat{=}$6.45μm. The quantum efficiency for λ = 767nm light is $\sim$ 25% and for λ=671nm is $\sim$ 43% (in the "high gain" mode).

[9] Since a CCD image sensor is made out of pixels of finite size, $I(x,y)$ is in reality a discrete function of position $I(x_n, y_m)$. For simplicity, we assume this function to be continuous, since in the images recorded in this thesis the atomic cloud features were always much bigger than the pixel size (6.45μm).

[10] The Pixelfly cameras in our apparatus operate in the double shutter mode, which allows an exposition time as short as 5μs and a time interval between subsequent images as short as 5μs. This allows to take a reference picture immune to mechanical vibrations of the imaging system. Another possibility is to use this double shutter mode to collect two different images of the atomic cloud (two hyperfine or Zeeman spin states) or images of the ^{6}Li and the ^{40}K cloud in the same experimental cycle.

[11] This is mandatory since in the double shutter mode the image and reference pictures have different exposure times.

direction. Assuming that the atomic absorption is homogeneous along the imaging direction z, we can use the Beer-Lambert law to obtain the integrated density profile:

$$n_{2D}(x,y) \equiv \int n(\mathbf{r})dz = -\frac{1}{m\sigma}\ln T(x,y). \tag{2.3.1}$$

In this equation m is the magnification of the imaging system and σ is the scattering cross-section, which is given by

$$\sigma = \frac{C^2\sigma_0}{1+\left(\delta_{\text{img}}/(\Gamma'/2)^2\right)^2}. \tag{2.3.2}$$

In this relation $\sigma_0 = 3\lambda^2/2\pi$ (λ is the wavelength of the atomic transition), δ_{img} is the frequency detuning of the imaging light in respect to the atomic transition, C is the Clebsch-Gordan coefficient of the imaging atomic transition and $\Gamma' = \Gamma\sqrt{1+2I/I_{\text{sat}}}$ is the broadened line-width of the excited state (here I is the intensity of the imaging light pulse). In this thesis we always work in the regime $I/I_{\text{sat}} \ll 1$ (and $\Gamma' = \Gamma$). A useful quantity readily obtained from the experimental data is the *optical density* $\text{OD}(x,y) = -\ln T(x,y)$, which is trivially related to the integrated density $n_{2D} = \text{OD}/\sigma$.

2.3.1 Evaluation of the imaging data

A very powerful measurement method is to directly probe the *in situ* atomic density distribution, while the trap is present. However, the non-trivial influence of the confinement[12] and/or the limited resolution of the imaging system[13] may hinder the analysis of the images. The alternative to *in situ* imaging is to abruptly switch off the trap, let the atoms expand freely for a time t_{TOF} and then perform absorption imaging. We call this the time-of-flight technique (TOF) and it is widely used in the cold

[12] An optical dipole trap induces a space-dependent light shift of the atomic ground-state $U(\mathbf{r})$, being maximum at the trap center $U(0) = U_0$. For a two-level system, the imaging resonance will be shifted by $2U(\mathbf{r})$ and, in consequence, the probe light absorption will be non-uniform. Exceptions occur when the cloud is confined to the trap center $k_B T \ll U_0$ or when the light shift is smaller than the imaging transition linewidth $2U_0 \ll \hbar\Gamma$. An interesting application of a non-uniform probe light absorption is the light-shift tomography in ^{87}Rb [24].

[13] The most notable exception is the ^{87}Rb quantum microscope [181].

atoms community. From these images one can extract the atom number and the temperature of the trapped cloud. The number of atoms N is given by integrating the signal

$$N = \int n_{2D}(x,y)dxdy$$

and does not depend on the value of t_{TOF}. For a classical atomic gas, the measured density distribution n_{2D} is simply given by the Maxwell-Boltzmann law and the temperature is directly related to the speed at which the gas expands[14]. The measured cloud size σ as a function of t_{TOF} is given by

$$\sigma^2(t_{TOF}) = \sigma_0^2 + \frac{k_B T}{m} t_{TOF}^2, \tag{2.3.3}$$

from which one can extract the temperature T of the cloud. Here we assume that the initial atomic distribution is gaussian with size σ_0. This is the case of the harmonic trap, for which the density distribution is always given by a gaussian function and $\sigma_0^2 = k_B T/m\omega^2$, ω being the trapping frequency. In contrast, in a linear trap the corresponding value of σ_0 is a complicated function of the size of the trapped cloud λ (see section 5.1 for the definition of λ and details). For a bosonic or a fermionic quantum gas this picture breaks down and the problem of measuring temperature can be rather complex. This issue will be addressed in section 7.5.4.

Typically, the accurate measurement of the atom number N is not a trivial task, mainly due to the imprecision in determining the scattering cross-section σ (see eq. 2.3.2). By varying the frequency of the imaging pulse, one can precisely determine the imaging resonance frequency and verify if there is no power broadening from the width of the experimental data curve. The most difficult term to evaluate is the Clebsch-Gordan factor C, which depends on the imaging transition. A notable case is the transition between stretched states $m_F = \pm(I + 1/2) \rightarrow m_{F'} = m_F \pm 1$ with $\sigma^{\pm}$-polarized light, in a presence of a small guiding homogenous magnetic field. For this particular case, the atom can be considered a two-level system while absorbing and emitting light and therefore $C^2 = 1$. When the guiding magnetic field is not

[14] We make the assumption that there is no variation of the kinetic energy when releasing the atoms from the trap. The assumption is valid if the trap is switched off fast enough and that the interaction energy is negligible compared to the kinetic energy.

present, the atomic magnetic moment will randomly rotate in space and its projection to the imaging light field will be arbitrary. In this case, for a closed imaging transition $F = I + 1/2 \rightarrow F' = F + 1$, we chose an averaged transition strength which is the average of all the different possible transitions, yielding $C^2 = 0.4$ for ^{40}K and $C^2 = 0.5$ for ^{6}Li [166, 200]. All the absorption imaging measurements reported in this thesis were done in this regime, except if mentioned otherwise. Notice that the case of ^{6}Li is more complicated due to its narrow excited structure (see level scheme in section 2.2.1), which allows important off-resonant excitations and decay to the dark $F = 1/2$ hyperfine level. To compensate for this effect, we shine a beam resonant with the transition $F = 1/2 \rightarrow F' = 1/2, 3/2$ in a direction perpendicular to the imaging one, in order to pump back the atoms back into the imaged state $F = 3/2$. Nevertheless, we admit that it might be possible that the atom number counting suffers from an unidentified systematic error. Another source of systematic error is the determination magnification of the imaging system, since the measured atom number and temperature depend quadratically on this value. The value of the magnification was carefully measured down to the 10% level or better with methods described in section 2.3.2.

2.3.2 Imaging optical setup

The frequency of the light needed for absorption imaging is controlled by AOMs installed in the optical tables of ^{40}K and ^{6}Li (see fig. 2.2.2). In each optical table, the imaging light is injected into two separate fibers: one for imaging in the MOT chamber another for imaging in the science cell (see section 2.2.3). In the main experimental table, the light from each atomic species is combined together using dichroic mirrors. For each species, the light power in each imaging direction can be controlled using $\lambda/2$ plates and PBS (polarization beam splitters) cubes.

For each imaging direction, a collimated resonant laser beam shines through the atomic cloud and is collected via an imaging system onto the CCD camera (for details concerning the camera see section 2.3). The waist of this beam can be found in table 2.3.1. The imaging system is in general composed of a series of lenses that image the object (the atomic cloud) onto the CCD plane. In our apparatus they are composed by one or two lenses, whose positions were found by using the standard the thin lens

equation and the imposed physical constraints.

In order to find the accurate position of the CCD camera (the imaging plane) we image a small atomic cloud ($\approx 4\mu m$ in the science cell). We find the imaging plane by determining the position of the camera for which the size of the imaged cloud is smallest. In general, for a gaussian object of size w_0 placed in the object plane, the size of its image will be $w(z) = mw_0\sqrt{1+z^2/L^2}$, where z is distance of the camera to the image plane and L is a length that depends on the image size mw_0, the numerical aperture NA and the light wavelength λ. The magnification was determined by letting this cloud of ^{40}K to free fall under gravity and using the fact that the acceleration is g[15]. In the MOT chamber we used a different strategy, which consisted in imaging a stainless steel mesh of $320 \times 320\mu m^2$ in opposite sides of the chamber. By determining the corresponding positions of the imaging plane and taking the average of those two measurements, one could estimate the position of the image of the center of the chamber and the corresponding magnification (see table 2.3.1).

Direction	w (mm)	m	PS (μm)	Optical system	NA	$d_r(\mu m)$
MOT [166]	13.8	0.44	15	$f = 60$mm (Gradium)	0.12	3.9
SC x-axis	4.0	1.6	4.0	$f = 200$mm (AC254-200-B)	0.039	12
SC y-axis	6.0	0.79	8.2	$f = 100$mm (AC254-100-B)	0.056	8.4
SC z-axis	2.7	2.55	2.53	$f = 75$mm (AC254-75-B) $f = 200$mm (AC508-200-A)	0.17	2.8

Table 2.3.1: Imaging systems in the MOT chamber and in the science cell (SC). m is the experimentally determined magnification, PS the pixel size, NA the numerical aperture calculated assuming the lens as aperture and d_r the calculated optical resolution (as given by the Rayleigh criterium for $\lambda = 767$nm). The AC lenses were acquired from Thorlabs.

The resolution the imaging systems has yet to be determined experimentally. The lower boundary can be estimated using the geometry of the optical system and the Rayleigh criterium:

$$d_r = 1.220\frac{s_o\lambda}{D} \approx 1.220\frac{\lambda}{2\text{NA}},$$

[15]Notice that we make the assumption that no other forces act on the atoms during the free fall. A stray magnetic gradient b on the vertical direction would add a contribution to the acceleration of $a = \mu_B b/m$ for the stretched state. While for ^{40}K we estimate that this contribute is not significant, for ^{6}Li this might not be the case due to its smaller mass.

with D being the diameter of the entrance pupil and s_o its distance to the object[16]. This value is only a lower bound since it does not take into account the effect of aberrations. In our apparatus we try to minimize their effect by using achromatic lens doublets.

For applications needing higher optical resolution we decided to acquire a commercial objective[17], which costed a factor 10 less than a custom made one. This objective has a high numerical aperture of NA=0.5 and a long working distance of 15.1mm (the physical constraints of the science cell are discussed in section 2.2.3). Also, it is corrected for a glass plate of BK7 ($n = 1.57$) with thickness 3.5mm, which is close to the wall of the science cell. The science cell is made of Vycor ($n = 1.46$) and its walls have thickness 4mm. The relative difference of the optical paths is 2.7% (instead of -61% without glass plate correction). This objective is optimized for a range of visible wavelengths ($436 - 656$nm), having a specified longitudinal chromatic aberration of $\sim 4\mu$m for $\lambda = 767$nm. The performance of this objective is yet to be tested, but it is a promising device.

Another strategy to improve the resolution is to image atoms using an atomic transition with lower wavelength, thereby reducing the resolution diffraction limit. A possible transition for ^{40}K has wavelength $\lambda = 404$nm [16, 166] and for ^{6}Li $\lambda = 323$nm.

2.3.3 High magnetic field imaging

Feshbach resonances are a powerful phenomenon that allow the manipulation of interactions in cold atoms, as it was explained in chapter 1. To access them one produces an homogeneous magnetic field in the $B = 150 - 250$G range for the ^{6}Li-^{40}K and the ^{40}K-^{40}K resonances and in the $B = 700 - 900$G range for the ^{6}Li-^{6}Li resonances. As it will be properly explained in section 5.1, the energy of the atomic states is shifted due to an external magnetic field (Zeeman effect). Consequently, the imaging transitions will shift in frequency. One solution to this problem is to switch off the magnetic field and image the atoms in the absence of a field, but this is not acceptable for some experiments. The purpose of this section is to calculate the frequency shifts for the most

[16] 1.220 is the first root of the Bessel function $J_1(x)$ divided by π
[17] Mitutoyo G plan APO 50x

relevant imaging transitions.

The magnetic coupling to an atom is given by $V = -\mu B$, μ being the projection of the atomic magnetic moment to the magnetic field direction and B the value of that field. As it will be better explained in section 5.1, for low magnetic fields $B \ll B_{\mathrm{hf}} = h\Delta\nu_{\mathrm{hf}}/2\mu_{\mathrm{B}}$, the total atomic angular momentum $\mathbf{F} = \mathbf{I} + \mathbf{J}$ is a good quantum number and the magnetic interaction energy is given by $E_{\mathrm{m}} = m_{\mathrm{F}} g_{\mathrm{F}} \mu_{\mathrm{B}} B$. Here m_{F} is the atomic Zeeman state, g_{F} the Landé factor, μ_{B} the Bohr magneton and $h\Delta\nu_{\mathrm{hf}}$ the ground-state hyperfine energy splitting. On the other hand, if $B \gg B_{\mathrm{hf}}$ the electron angular momentum $\mathbf{J}$ fully decouples from the nuclear angular momentum $\mathbf{I}$ and $\mathbf{F}$ is no longer a good quantum number. In this case, since the Wigner-Eckart theorem can not be used, one can not write the magnetic interaction as $V = \mu_{\mathrm{B}} g_F F_z B$. The case $B \gg B_{\mathrm{hf}}$ is called the *Paschen-Back regime* and the magnetic interaction energy is given by $E_{\mathrm{m}} = \mathrm{cte} + \mu_{\mathrm{B}}(g_{\mathrm{J}} m_{\mathrm{J}} + g_{\mathrm{I}} m_{\mathrm{I}})B$. Notice that since the electron is decoupled from the nucleus and since the light field is only coupled to the electron, the selection rule $\Delta m_{\mathrm{I}} = 0$ applies for electric dipolar transitions.

For the intermediate case $B \approx B_{\mathrm{hf}}$, one has to diagonalize the full atomic Hamiltonian to find the eigen-energies E_{m}. For orbital angular momentum $L = 0$, the diagonalization can be performed analytically and one can find an expression for the eigen-energies, which is given by the *Breit-Rabi* formula [189]. However, the excited $P_{3/2}$ manifold has $L = 1$ and the Breit-Rabi formula can not be applied. Fortunately, the hyperfine spacings of the excited state are much smaller than the ones of the ground state ($B_{\mathrm{hf}} = 14\mathrm{G}$ for $^{40}\mathrm{K}$ and $B_{\mathrm{hf}} = 1.4\mathrm{G}$ for $^{6}\mathrm{Li}$) and the Paschen-Back regime is attained for smaller magnetic fields. Therefore, one can apply the Breit-Rabi formula to accurately calculate the Zeeman shifts of the ground states and the Paschen-Back formula for the shifts of the excited states (provided that $B \gg B_{\mathrm{hf}} \sim 20\mathrm{G}$). This is confirmed by comparing this approximative approach with the diagonalization of the full Hamiltonian (see fig. 2.3.1).

The Zeeman states that have relevant Feshbach resonances for this experiment are $|m_{\mathrm{F}} = -9/2, -7/2, -5/2\rangle$ of the $F = 9/2$ manifold for $^{40}\mathrm{K}$ (that correspond to the states $|m_I = -4, -3, -2\rangle$ with $m_{\mathrm{J}} = -1/2$ in the Paschen-Back regime, respectively) and $|m_{\mathrm{F}} = -1/2, 1/2\rangle$ of the $F = 1/2$ manifold for $^{6}\mathrm{Li}$ (that correspond to the states $|m_I = 0, 1\rangle$ with $m_{\mathrm{J}} = -1/2$ in the Paschen-Back regime, respectively). Their imaging

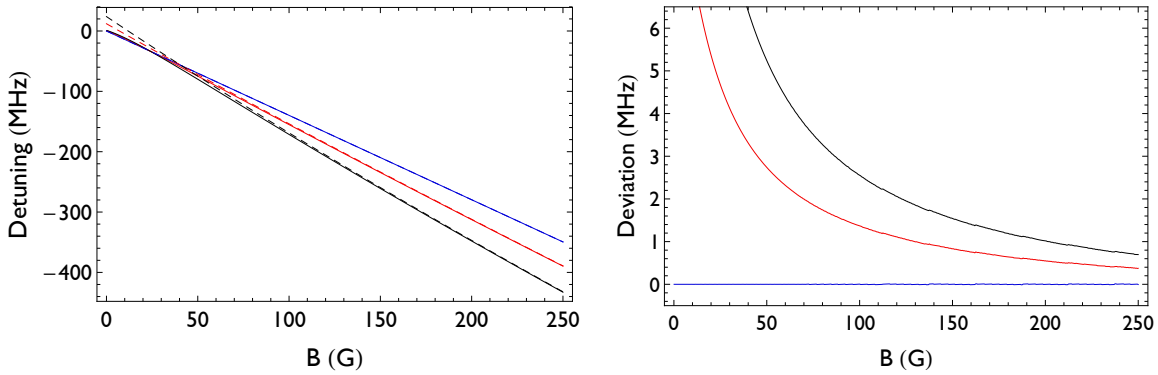


Figure 2.3.1: Detuning from the imaging transitions of ^{40}K $|m_F = -9/2\rangle \rightarrow |m_F = -11/2\rangle$ (blue), $|m_F = -7/2\rangle \rightarrow |m_F = -9/2\rangle$ (red) and $|m_F = -5/2\rangle \rightarrow |m_F = -7/2\rangle$ (black) from the $F = 9/2 \rightarrow F' = 11/2$ transition at $B = 0$. In the left we plot the numerical calculation of the detuning (solid lines) and the approximative approach (dashed lines) as explained in the main text. In the right we plot the absolute difference between the two calculations.

detunings were calculated around $B_0 = 200$G and are listed in tables 2.D.1 and 2.D.2 of appendix 2.D.

In order to shift the imaging laser frequency, we installed an additional AOM for ^{40}K, as depicted in fig. 2.2.2. This setup is flexible enough to image all three target states in the desired field range with σ^- or π polarization. For ^{6}Li the high-field imaging laser system has yet to implemented. One option, which would be the most versatile one, would be to have an independent laser diode[18] offset-locked to the ^{6}Li master diode laser, which in turn is spectroscopy-locked to the D_2 light. The offset frequency could be tuned using a voltage controlled oscillator (VCO) or a controllable frequency synthesizer.

2.4 Computer control system

In this apparatus we dispose of three desktop computers, *Bruxelles*, *Bamako* and *Asgard*, in order to control the experiment, acquire and process images and analyze data, respectively.

The control of the experiment is done by using the "Atticus Hardware Server", which communicates to the hardware via a series of National Instruments cards (3

[18]For example Opnext HL6756MG lases at 670nm with 15mw of output power.

digital cards PXI-6533 and 5 analog cards PXI-6713 at the present). The experimental sequence is generated and uploaded to Atticus by the "Cicero Word Generator", which provides a very intuitive graphical interface. We use a variable frequency clock synthesized by a FPGA module[19], which allows to have a variable timebase during the experimental sequence. We changed the code of Atticus and Cicero in order to communicate with our imaging acquisition software and with the synthesizers used for the evaporation ramps (described in section 6.5.1). Atticus and Cicero were developed by Aviv Keshet [96] and their implementation in our apparatus was done by Norman Kretzschmar.

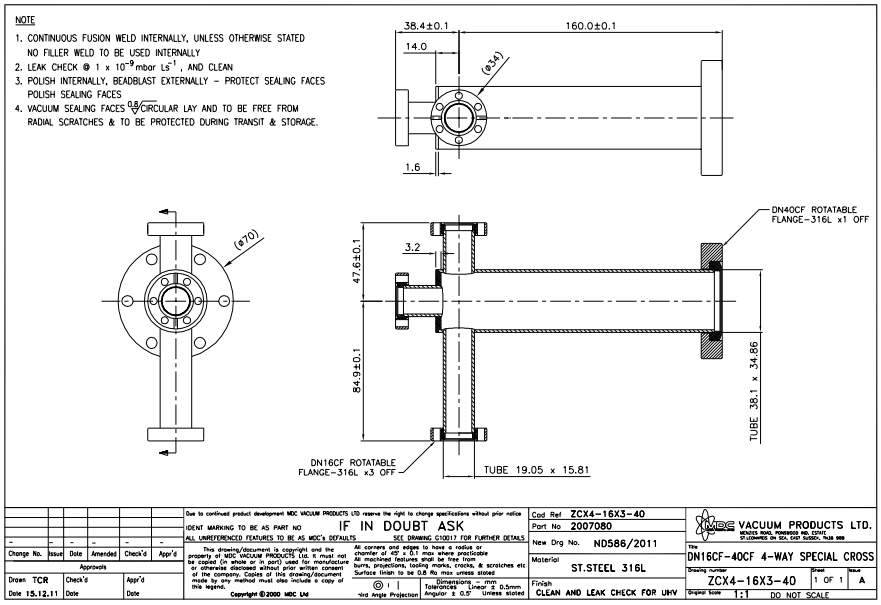
The imaging acquisition is done using a Python code originally written by Florian Schreck and modified by successive generations of students of the LKB Lithium machine. It communicates with Atticus, triggers the CCD cameras and downloads the images to *Bamako*.

The automatic processing of the images is done by an Octave code originally written by Colin Parker and modified by the author of this thesis. It is a robust program that finds the atomic cloud in the taken image, fits it to 1D/2D-dimensional gaussians and outputs all relevant fitting parameters to an external file. This data is analyzed in *Asgard* using Mathematica 8.

The temperature in several points of the lab can be monitored using thermistances, whose voltage drop is acquired using an inexpensive DAQ (Data Acquisition) card[20]. Using the same acquisition card we also monitor the position of the optical plug by measuring the voltages in a 4-quadrant photodiode (see details in section 6.5.3).

[19] Opal Kelly XEM 3001
[20] National Instruments USB-6009

Appendix 2.A Vacuum parts



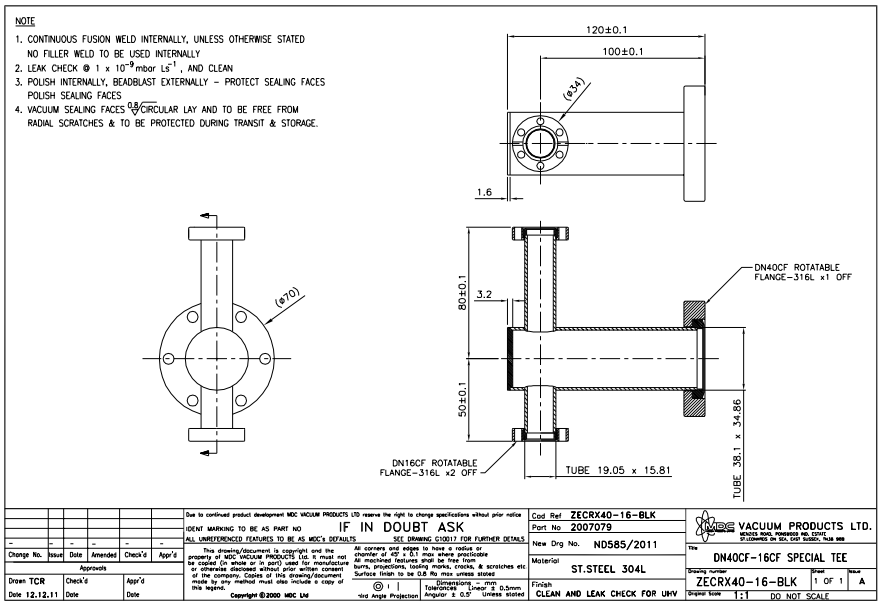


Figure 2.A.1: Engineering drawings of the new vacuum parts made by MDC Vacuum for the second transport section.



Figure 2.A.2: Vacuum parts being coated with the NEG of TiZrV at a facility in CERN (engineering schemes in fig. 2.A.1). Photo courtesy of Ivo Wevers.

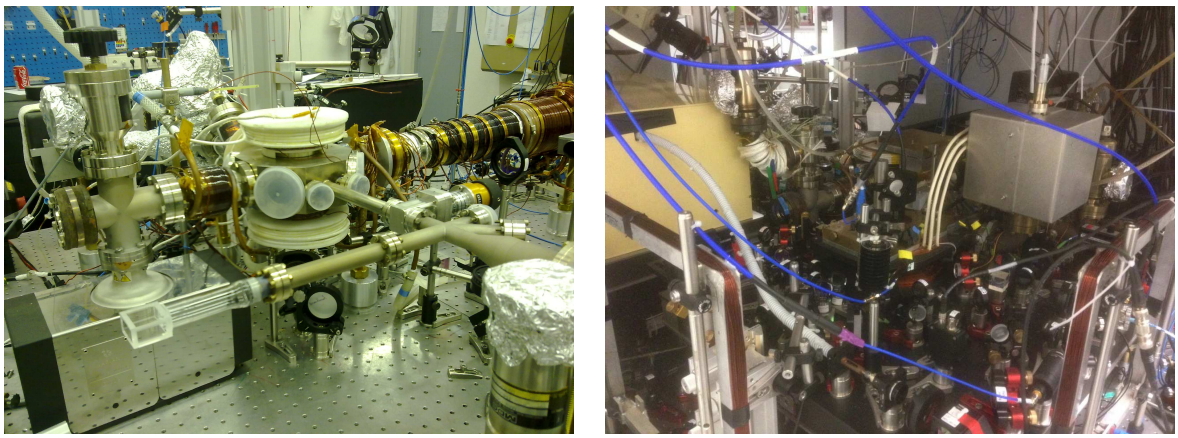
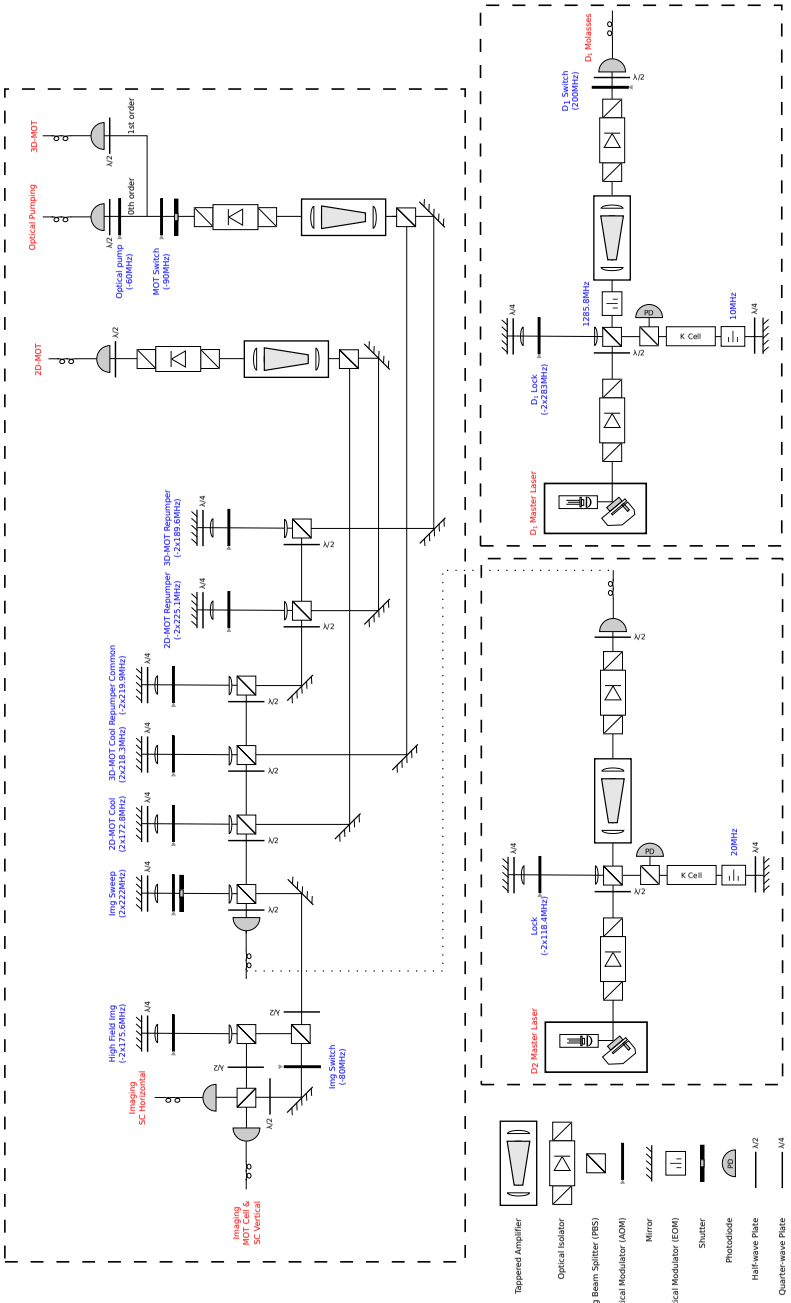
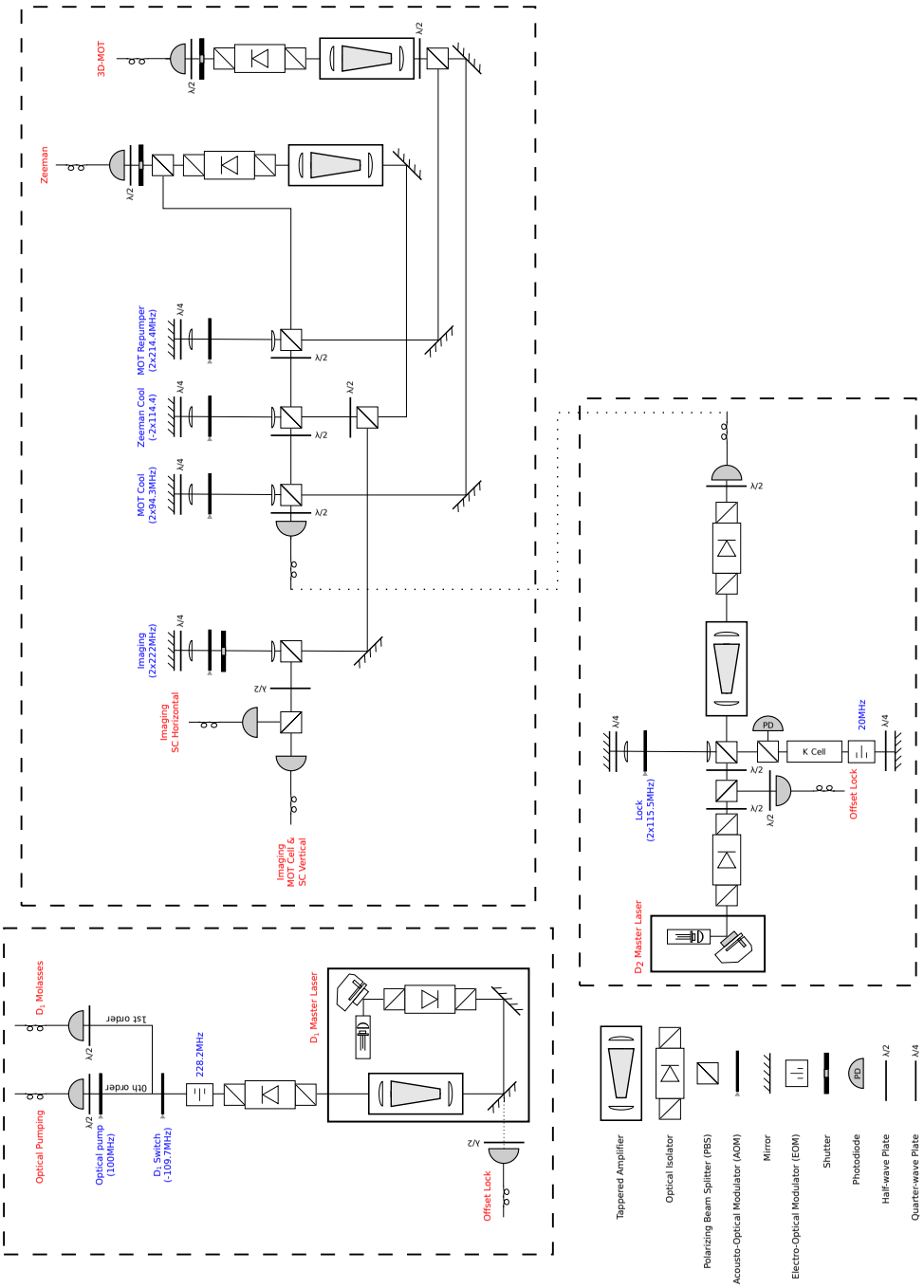


Figure 2.A.3: Photo of the vacuum chamber after baking-out in March 2010 (left). One can distinguish the science cell and the MOT chamber (compare with fig. 2.1.1). Equivalent photo taken in September 2014 (right), see section 2.2.3 for a scheme and a description.

Appendix 2.B ^{40}K Laser table



Appendix 2.C ^{6}Li Laser table



Appendix 2.D Imaging detunings for high-field imaging

$\lvert m_F\rangle \rightarrow \lvert m_{J'}, m_{I'}\rangle$ (σ^-)	$\delta_0(B_0)$ (MHz)	$\frac{h}{\mu_B}\delta'(B_0)(1/G)$
$\lvert -9/2\rangle \rightarrow \lvert -3/2, -4\rangle$	-279.6	-1.00
$\lvert -7/2\rangle \rightarrow \lvert -3/2, -3\rangle$	-312.0	-1.11
$\lvert -5/2\rangle \rightarrow \lvert -3/2, -2\rangle$	-347.0	-1.23

$\lvert m_F\rangle \rightarrow \lvert m_{J'}, m_{I'}\rangle$ (π)	$\delta_0(B_0)$ (MHz)	$\frac{h}{\mu_B}\delta'(B_0)(1/G)$
$\lvert -9/2\rangle \rightarrow \lvert -1/2, -4\rangle$	125.7	0.334
$\lvert -7/2\rangle \rightarrow \lvert -1/2, -3\rangle$	84.4	0.222
$\lvert -5/2\rangle \rightarrow \lvert -1/2, -2\rangle$	40.9	0.100

Table 2.D.1: Detuning of the imaging transitions of ^{40}K respective to the $F = 9/2 \rightarrow F' = 11/2$ resonance at $B = 0$, calculated around $B_0 = 200$G: $\delta(B) \approx \delta_0(B_0) + \delta'(B_0)(B - B_0) + \mathcal{O}(B - B_0)^2$. The calculation is done for σ^- and π light polarization excitations.

$\lvert m_J, m_I\rangle \rightarrow \lvert m_{J'}, m_{I'}\rangle$ (σ^-)	$\delta_0(B_0)$ (MHz)	$\frac{h}{\mu_B}\delta'(B_0)(1/G)$
$\lvert -1/2, 1\rangle \rightarrow \lvert -3/2, 1\rangle$	-107.0	-1.05
$\lvert -1/2, 0\rangle \rightarrow \lvert -3/2, 0\rangle$	-179.6	-1.09

$\lvert m_J, m_I\rangle \rightarrow \lvert m_{J'}, m_{I'}\rangle$ (π)	$\delta_0(B_0)$ (MHz)	$\frac{h}{\mu_B}\delta'(B_0)(1/G)$
$\lvert -1/2, 1\rangle \rightarrow \lvert -1/2, 1\rangle$	265.6	0.281
$\lvert -1/2, 0\rangle \rightarrow \lvert -1/2, 0\rangle$	194.0	0.247

$\lvert m_J, m_I\rangle \rightarrow \lvert m_{J'}, m_{I'}\rangle$ (σ^+)	$\delta_0(B_0)$ (MHz)	$\frac{h}{\mu_B}\delta'(B_0)$ (1/G)
$\lvert -1/2, 1\rangle \rightarrow \lvert 1/2, 1\rangle$	638.1	1.62
$\lvert -1/2, 0\rangle \rightarrow \lvert 1/2, 0\rangle$	567.7	1.58

Table 2.D.2: Detuning of the imaging transitions of ^{6}Li respective to the $F = 3/2 \rightarrow F' = 5/2$ resonance at $B = 0$, calculated around $B_0 = 200$G: $\delta(B) \approx \delta_0(B_0) + \delta'(B_0)(B - B_0) + \mathcal{O}(B - B_0)^2$. The calculation is done for σ^-, π and σ^+ light polarization excitations.

3 Dual-species MOT

The apparatus to create a quantum degenerate gas mixtures starts with a laser cooling and trapping phase. Atomic beams produced by a Zeeman slower for ^{6}Li and by a 2D-MOT for ^{40}K are cooled are trapped in a dual-species magneto-optical trap (MOT).

Large atom number dual-species magneto-optical trap for fermionic ^{6}Li and ^{40}K atoms

The design, implementation and characterization of a dual-species MOT for fermionic ^{6}Li and ^{40}K atoms with large atom numbers was reported in the following publication (in appendix 3.A):

- A. Ridinger, S. Chaudhuri, T. Salez, U. Eismann, D.R. Fernandes, K. Magalhães, D. Wilkowski, C. Salomon, and F. Chevy. *Large atom number dual-species magneto-optical trap for fermionic ^{6}Li and ^{40}K atoms*. Eur. Phys. J. D (The European Physical Journal D) **242**, 223-242 (2011).

The MOT simultaneously contains 5.2×10^9 ^{6}Li-atoms and 8.0×10^9 ^{40}K-atoms, which are continuously loaded by a Zeeman slower for ^{6}Li and a 2D-MOT for ^{40}K. The atom sources induce capture rates of 1.2×10^9 ^{6}Li-atoms/s and 1.4×10^9 ^{40}K-atoms/s. Trap losses due to light-induced interspecies collisions of $\sim 65\%$ were observed and could be minimized to $\sim 10\%$ by using low magnetic field gradients and low light powers in the repumping light of both atomic species. This system represents the starting point for the production of a large-atom number quantum degenerate fermi-fermi mixture.

Photoassociative creation of ultracold heteronuclear ^{6}Li^{40}K* molecules

At this point, we investigated the formation of weakly bound, electronically excited, heteronuclear ^{6}Li^{40}K* molecules by single-photon photoassociation in the dual-species

magneto-optical trap. The results of this study were reported in the following publication (in appendix 3.A):

- A. Ridinger, S. Chaudhuri, T. Salez, D. R. Fernandes, N. Bouloufa, O. Dulieu, C. Salomon, and F. Chevy. *Photoassociative creation of ultracold heteronuclear $^6Li^{40}K^*$ molecules*. EPL (Europhysics Letters) **96**, 33001 (2011).

We performed trap loss spectroscopy within a range of 325 GHz below the Li($2S_{1/2}$) + K($4P_{3/2}$) and Li($2S_{1/2}$) + K($4P_{1/2}$) asymptotic states and observed more than 60 resonances, which we identify as rovibrational levels of 7 of 8 attractive long-range molecular potentials. The long-range dispersion coefficients and rotational constants are derived. We find large molecule formation rates of up to $\sim 3.5 \times 10^7 \mathrm{s}^{-1}$, which are shown to be comparable to those for homonuclear $^{40}K_2^*$. Using a theoretical model we infer decay rates to the deeply bound electronic ground-state vibrational level $X^1\Sigma^+(v' = 3)$ of $\sim 5 \times 10^4 \mathrm{s}^{-1}$. Our results pave the way for the production of ultracold bosonic ground-state ^{6}Li^{40}K molecules which exhibit a large intrinsic permanent electric dipole moment.

3.1 Double MOT current status and improvements

In this section we report on the changes made to the MOT system in order to improve its functioning. At the present, we routinely load 1.5×10^9 ^{6}Li atoms and 3×10^9 ^{40}K atoms in the double MOT in 15s. The capture rates are 1.7×10^8 ^{6}Li atoms/s from the Zeeman oven and 2×10^8 ^{40}K-atoms/s from the 2D-MOT. These values are smaller than the ones reported before, in particular the capture rates. However, they are largely sufficient to create a double-species degenerate gas with high numbers.

One of the main improvements in the MOT chamber relative to the previously reported setup was the background pressure, which decreased by a factor of ≈ 5, as explained in section 2.1.1. By estimating the steady-state number of atoms in the MOT as $N \sim L/\gamma$ (neglecting light-induced collisions), we should expect an improvement of factor 5 ($1/\gamma$ is the lifetime of the MOT and L its capture rate). On the other hand, we measured a degradation of the capture rate L of a factor of ≈ 7. The number of atoms in the MOT (for a 15s loading) is a factor of ≈ 3 smaller compared to the re-

ported value (for the steady-state). We estimate that the main degradation occurred in the atom flux coming from the sources.

Zeeman slower

The Zeeman oven is routinely operated at 470ºC. In the Summer of 2011 we observed a sudden drop of the atomic flux. This was interpreted as the clotting of the collimation tube connecting the oven to the subsequent vacuum chamber. This tube has 6mm of internal diameter, according to fig. A.3 of ref. 171. In order to fix this problem, we installed heating bands in this region, increased its temperature to 400ºC and let it hot overnight. This partially solved the problem: the atomic flux increased considerably when returning to normal operation. This "clotting problem" occurs once or twice per year. We believe that the present atomic flux is limited by the deterioration of our control over the Lithium oven. However, we estimate that this limitation is not at all a problem for the experiment. In order to attain quantum degeneracy by sympathetic cooling with ^{40}K, only few 10^7 atoms of ^{6}Li are required in the MOT. Our current number is still two orders of magnitude higher than needed.

2D-MOT

It was found that maintaining a controlled pressure of Potassium in the 2D-MOT chamber for extended periods of time is a challenging task. We observed that Potassium quickly migrates inside the 2D-MOT chamber and we lose control over the position (and temperature) of the reservoir. The solution we found was to heat all the parts[1] (metal vacuum parts to $\approx$ 140ºC, ion pump to 80ºC and glass cell to $\approx$ 40ºC), while having a cold region with smaller and controlled temperature. For this purpose we wrapped 3 turns of a PVC tube around the glass part of the metal-to-glass junction of the 2D-MOT chamber (see fig. 7 of ref. 167). This tube is connected to a water chiller, which enables us to control the temperature of the cold point (the reservoir) by changing the temperature of the water. Overnight we set the water temperature to 16ºC, thus accumulating crystals of Potassium in the glass walls. This metallic crystals can be seen by naked eye, which is very useful to diagnose eventual problems.

[1] See section 2.5.2. of ref. 166 for a description of the 2D-MOT chamber.

By adjusting the temperature of the water to 40ºC we observe 50% absorption of a resonant beam along the cell, which corresponds to a vapor pressure of Potassium of $\approx 1.3 \times 10^{-7}$mbar (see appendix A of ref. 166 for details concerning the method for measuring the vapor pressure). In this case, the flux of the 2D-MOT should be of 1.2×10^{9}s^{-1}, as measured in fig. 10 of ref. 167, but we observe instead a flux ≈ 7 times smaller.

In order to improve the atom flux from the 2D-MOT we added an independent laser beam to push the atoms to the MOT chamber. This beam has waist $\approx$ 1.9mm and 4.6mW of power. Since it is derived from the 2D-MOT beams (1.2% of their power), it shares the same light frequencies and same ratio between cooling and repumper. After re-optimizing of the power balance in the 2D-MOT, we observed that the capture rate of the MOT increased by a factor 2 compared to the previous situation. Further improvement could eventually be obtained by independently tuning the frequencies of the pushing beam [27, 175, 191] or by having a combination of red- and blue-detuned pushing beams [152].

Although the 2D-MOT atomic flux is smaller than reported before, we show in this thesis that large quantum degenerate gases of ^{40}K could be produced. Furthermore, thanks to the reported improvements, we observe a stable number of atoms in the MOT over several months of continuous operation.

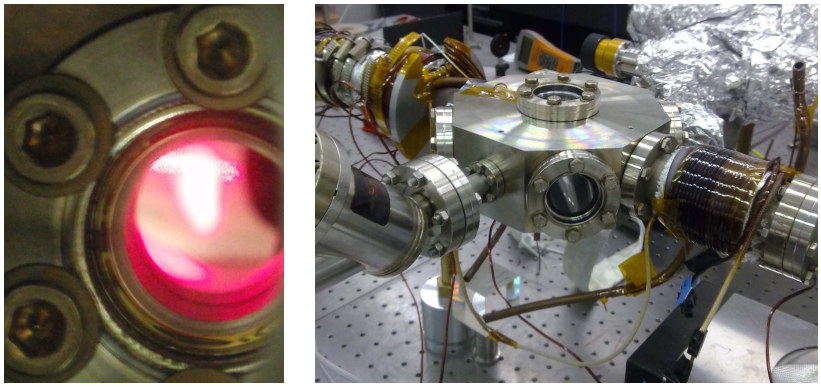


Figure 3.1.1: (Left) One of the first ^{6}Li MOTs. The emitted red fluorescence ($\lambda \approx$ 671nm) is visible to the naked eye. The diameter of the glass port is $\approx$ 1.5cm. (Right) MOT chamber right after baking-out (no optics nor electromagnetic coils). Picture taken in the same angle as scheme of fig. 2.1.1. The diameter of the glass ports is $\approx$ 4cm.

Appendix 3.A Publications

- A. Ridinger, S. Chaudhuri, T. Salez, U. Eismann, D.R. Fernandes, K. Magalhães, D. Wilkowski, C. Salomon, and F. Chevy. *Large atom number dual-species magneto-optical trap for fermionic ^6Li and ^{40}K atoms*. Eur. Phys. J. D (The European Physical Journal D) **242**, 223-242 (2011).

- A. Ridinger, S. Chaudhuri, T. Salez, D. R. Fernandes, N. Bouloufa, O. Dulieu, C. Salomon, and F. Chevy. *Photoassociative creation of ultracold heteronuclear $^6Li^{40}K^*$ molecules*. EPL (Europhysics Letters) **96**, 33001 (2011).

Eur. Phys. J. D **65**, 223–242 (2011)
DOI: 10.1140/epjd/e2011-20069-4

THE EUROPEAN PHYSICAL JOURNAL D

Regular Article

Large atom number dual-species magneto-optical trap for fermionic ^{6}Li and ^{40}K atoms

A. Ridinger[1,a], S. Chaudhuri[1], T. Salez[1], U. Eismann[1], D.R. Fernandes[1], K. Magalhães[2], D. Wilkowski[3,4], C. Salomon[1], and F. Chevy[1]

[1] Laboratoire Kastler Brossel, École Normale Supérieure, CNRS, Université Pierre et Marie-Curie, 24 rue Lhomond, 75231 Paris Cedex 05, France
[2] Instituto de Física de São Carlos, Universidade de São Paulo, Caixa Postal 369, 13560-970 São Carlos-SP, Brazil
[3] Centre for Quantum Technologies, National University of Singapore, 117543 Singapore, Singapore
[4] Institut Non Linéaire de Nice, Université de Nice Sophia-Antipolis, CNRS, 06560 Valbonne, France

Received 29 January 2011 / Received in final form 16 February 2011
Published online 27 April 2011 – © EDP Sciences, Società Italiana di Fisica, Springer-Verlag 2011

Abstract. We present the design, implementation and characterization of a dual-species magneto-optical trap (MOT) for fermionic ^{6}Li and ^{40}K atoms with large atom numbers. The MOT simultaneously contains 5.2×10^9 ^{6}Li-atoms and 8.0×10^9 ^{40}K-atoms, which are continuously loaded by a Zeeman slower for ^{6}Li and a 2D-MOT for ^{40}K. The atom sources induce capture rates of 1.2×10^9 ^{6}Li-atoms/s and 1.4×10^9 ^{40}K-atoms/s. Trap losses due to light-induced interspecies collisions of ∼65% were observed and could be minimized to ∼10% by using low magnetic field gradients and low light powers in the repumping light of both atomic species. The described system represents the starting point for the production of a large-atom number quantum degenerate Fermi-Fermi mixture.

1 Introduction

The study of ultracold atomic Fermi gases is an emerging research field aiming to understand many-body quantum phenomena occurring in various fields, such as condensed matter systems, disordered systems, quark-gluon plasmas or astrophysics (neutron stars) [1,2]. They provide a unique opportunity to create strongly correlated many-body systems with a high degree of experimental control. One intends to realize analog quantum simulators in Feynman's spirit [3], with which many-body Hamiltonians could be solved.

In the field of ultracold Fermi gases the study of mixtures of two different fermionic species with different mass is gaining interest. Both theoretical and experimental aspects motivate this study. Such mixtures are predicted to exhibit a rich phase diagram such as phase separation [4], crystalline phases [5], exotic pairing mechanisms [6] and long-lived trimers [7]. They further allow the creation of polar molecules, which have a long-range dipole-dipole interaction [8,9]. Two different atomic species yield additional tunable parameters, such as the mass imbalance and species-specific potentials. The mass-imbalance can be varied in an optical lattice, where the effective mass of each species depends on the optical lattice parameters.

The mixture ^{6}Li-^{40}K is a prime candidate for these studies. ^{6}Li and ^{40}K are the only stable fermionic alkali isotopes and thus belong to the experimentally best-mastered class of atoms. Moreover, both species have bosonic isotopes which can also be used to create boson-fermion gases. Furthermore, the mass difference between the two species is large leading to a large electric dipole moment for heteronuclear diatomic molecules (3.6 D) [10]. Finally, many of the above-mentioned predicted quantum phases require strong interspecies interactions and a universal behavior of the gas. It was recently reported [11] that it is possible to reach the universal regime for the ^{6}Li-^{40}K-mixture due to the existence of a 1.5 gauss-wide Feshbach resonance.

The starting point of most mixture experiments is a dual-species magneto-optical trap. It is desirable to capture a large number of atoms at this stage for the following reasons. First, large atom numbers allow to anticipate the losses induced by the subsequent evaporative cooling procedure, which needs to be applied to reach the quantum degenerate regime. Second, a large initial atom number makes the evaporation procedure more efficient. Third, the Fermi temperatures of the gas are larger for larger atom numbers and thus quantum phenomena can be observed at higher temperatures. Finally, a large atom number leads to better signal-to-noise ratios and a greater robustness in day-to-day operation.

A dual-species magneto-optical trap with large atom numbers also allows an efficient creation of ultracold heteronuclear molecules via photoassociation. Using this technique, we have been able to create excited

[a] e-mail: armin.ridinger@gmail.com

heteronuclear ^{6}Li-^{40}K* molecules with a formation rate of $\sim 5 \times 10^7 s^{-1}$. The results of this experiment will be the subject of a separate publication [12].

In this article we describe the design, implementation and characterization of a dual-species magneto-optical trap for ^{6}Li and ^{40}K with large atom numbers. In a dual-species MOT, the atom number is in general reduced compared to single-species MOTs due to additional interspecies collisions and to experimental constraints, such as the imperative to use the same magnetic field for both species or common optics. In other groups working with the ^{6}Li-^{40}K mixture the following atom numbers have been achieved: in the Munich group [13] the dual-species MOT is loaded from a Zeeman slower for ^{6}Li and a vapor for ^{40}K, resulting in atom numbers of $\sim 4 \times 10^7$ (^{6}Li) and $\sim 2 \times 10^7$ (^{40}K). In the Innsbruck group [14] the dual-species MOT is loaded from a multi-species Zeeman slower and atom numbers of $\sim 10^9$ (^{6}Li) and $\sim 10^7$ (^{40}K) are achieved. In the group in Amsterdam [15] two separate 2D-MOTs allow to load $\sim 3 \times 10^9$ (^{6}Li) and $\sim 2 \times 10^9$ (^{40}K). In our setup, the dual-species MOT is loaded from a Zeeman slower for ^{6}Li and a 2D-MOT for ^{40}K. It simultaneously contains 5.2×10^9 ^{6}Li-atoms and 8.0×10^9 ^{40}K-atoms, which represents a substantial atom number improvement.

For our application in particular a large atom number in the ^{40}K-MOT is of interest, since we intend to sympathetically cool ^{6}Li with ^{40}K, where ^{40}K will be prepared and cooled in two different spin states. This approach has been implemented by Tiecke et al. [11] and proved to be an efficient cooling method, as it can be realized in a magnetic trap. In this cooling process mostly ^{40}K-atoms will be lost.

In future experiments, the atoms stored inside the dual-species MOT will be polarized and magnetically transported to an ultra-high vacuum (UHV) environment with large optical access. There the atom cloud will be evaporatively cooled to quantum degeneracy in an optically plugged magnetic quadrupole trap. Finally it will be transferred into an optical trap to investigate many-body phenomena in lower dimensions.

This article is organized as follows. In Section 2 the experimental setup, including the vacuum assembly and the laser systems, is described. In Section 3 we present the design and the performance of the atom sources, which are used to load the dual-species MOT, i.e. a Zeeman slower for ^{6}Li and a 2D-MOT for ^{40}K. In Section 4, the dual-species MOT is characterized and a study of light-induced interspecies collisions is presented.

2 Experimental setup

2.1 Vacuum system

A three-dimensional view of the vacuum system is shown in Figure 1. It consists of two atom trap chambers and three flux regions. The first chamber is a central octagonal chamber where the ^{6}Li-^{40}K dual-species MOT is prepared.

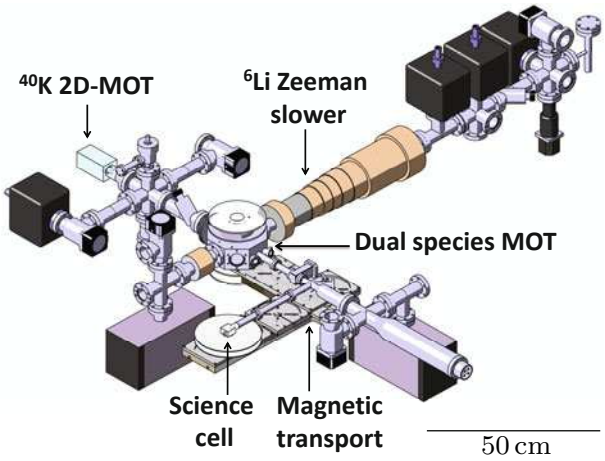


Fig. 1. (Color online) Schematics of the vacuum assembly. The dual-species MOT is loaded from a 2D-MOT for ^{40}K and a Zeeman slower for ^{6}Li. A magnetic transport allows to transfer the cloud to a UHV science cell with large optical access.

The second chamber is a glass science cell, in which we will evaporatively cool the mixture to quantum degeneracy.

The three flux regions are all connected to the octagonal chamber and are divided in two parts. First, the atom sources, namely a 2D-MOT for ^{40}K and a Zeeman slower for ^{6}Li. Second, a magnetic transport connecting the octagonal chamber to the final science cell. This magnetic transport consists of a spatially fixed assembly of magnetic coils which creates a moving trapping potential of constant shape by applying time-varying currents [16]. It has already been implemented in our system and will be described in a separate publication.

The octagonal chamber can be isolated from the source regions and the science cell by all-metal UHV valves, which allow for separate baking and trouble-shooting. The 2D-MOT and the Zeeman slower region are pumped by one and three 20 L/s ion pumps, respectively. The octagonal chamber is pumped by a 40 L/s ion pump and the science chamber by a 40 L/s ion pump and a titanium sublimation pump. Differential pumping tubes connect the source regions to the octagonal chamber in order to create a high vacuum environment in the octagonal cell. In a similar way, the science chamber is connected to the octagonal chamber via a combination of standard CF16- and homemade vacuum tubes of 1 cm diameter to further increase the vacuum quality. The glass science cell has a large optical access and permits the installation of an objective for high-resolution imaging.

2.2 Laser systems

The dual-species MOT requires separate laser systems and optics for the two different atomic transition wavelengths 671 nm (Li) and 767 nm (K). The laser systems provide several beams with different frequencies and intensities for slowing, trapping and probing each atomic species. A sketch of the energy levels of the atomic species and the

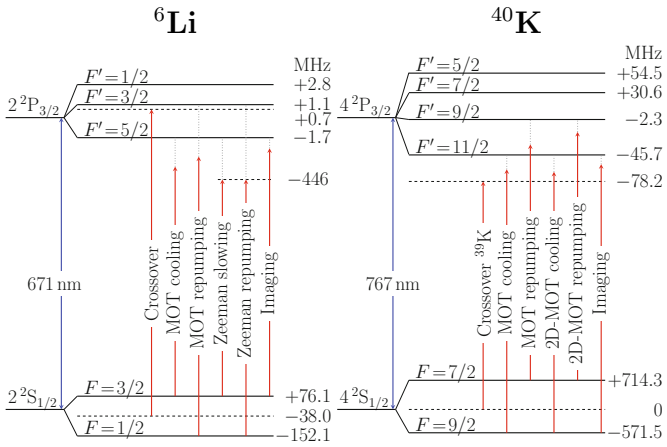


Fig. 2. (Color online) Level diagrams for the ^{6}Li and ^{40}K D_2-lines with their respective hyperfine structures, showing the frequencies required for the dual-species MOT operation. The diode lasers are locked to the indicated saturated absorption crossover signals $2S_{1/2}(F=1/2, F=3/2) \rightarrow 2P_{3/2}$ of ^{6}Li and $4S_{1/2}(F=1, F=2) \rightarrow 4P_{3/2}$ of ^{39}K.

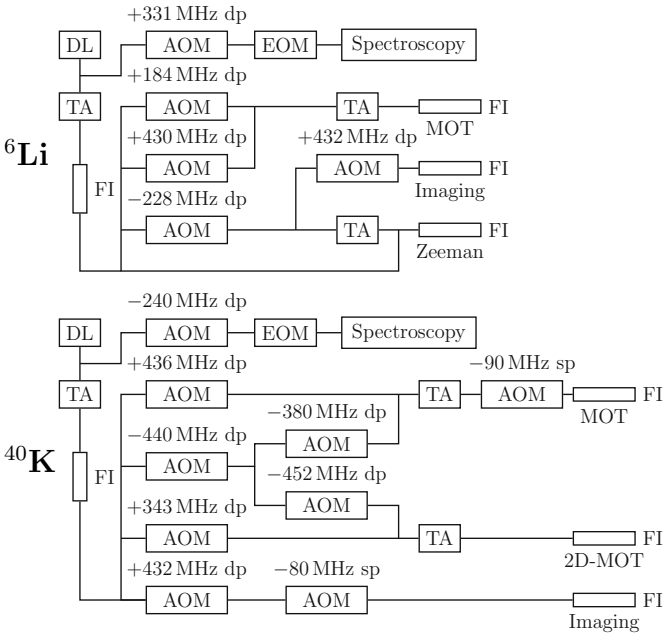


Fig. 3. Laser systems for ^{6}Li and ^{40}K. The frequencies and amplitudes of the various beams are controlled by AOMs in single pass (sp) or double pass (dp) configuration. The EOMs are used to phase modulate a part of the beam for the diode laser's frequency stabilization. Single mode polarization maintaining fibers (FI) are used for beam shaping and spatial filtering. The indicated AOM frequencies allow to generate the required beam frequencies (see Fig. 2).

frequencies of interest are shown in Figure 2. The laser systems are set up on separate optical tables and the generated laser beams are transferred to the main experimental table using optical fibers. A simplified scheme of the laser systems is shown in Figure 3. Each one consists of a single low output-power frequency-stabilized diode laser (DL) and three tapered amplifiers (TAs) used for light amplification. Due to the small hyperfine splittings of both ^{6}Li and ^{40}K, the required frequencies of the various laser beams are conveniently shifted and independently controlled by acousto-optical modulators (AOMs).

The diode lasers are homemade tunable external cavity diode lasers in Littrow configuration. The laser diode for Li (Mitsubishi, ref. ML101J27) is of low-cost due to its mass production for the DVD industry. Its central free running output wavelength at room temperature is 660 nm which can be shifted into the range of 671 nm by heating the diode to 80 °C. In external cavity configuration its output power is 40 mW at a driving current of 150 mA. Under these conditions the laser diode reaches a typical lifetime of 6 months. It can be mode hop-free tuned over a range of 5 GHz. The laser diode for K is an anti-reflection coated Ridge-Waveguide Laser (Eagleyard, ref. EYP-RWE-0790-0400-0750-SOT03-0000), whose central free running output wavelength at room temperature corresponds to the desired wavelength. In external cavity configuration its output power is 35 mW at 90 mA and it has a typical lifetime of one year. It can be mode hop-free tuned over a range of 10 GHz.

The tapered amplifiers are commercial semiconductor chips which are mounted on homemade supports. We developed compact support designs with nearly no adjustable parts, which allow for a quick temperature stabilization, do not require running water for heat dissipation and allow for an easy installation process. The support designs are described in detail in the appendix.

We have also developed an all-solid-state laser for lithium delivering more than 630 mW output power, with which we intend to increase further the number of laser-cooled Li atoms. The setup of this light source is described elsewhere [17].

The frequency of each diode laser is stabilized via saturated absorption spectroscopy for which a small part of the DL's output is used (see Fig. 3). A 20 MHz electro-optical modulator (EOM) is employed to modulate the phase of the spectroscopy laser beam yielding the derivative of the absorption signal through a lock-in detection. The resulting error signal is transferred to both the diode's current (via a high frequency bias-tee), and, via a PID-controller, to a piezo that adjusts the external cavity's length with a 4 kHz bandwidth. An AOM is used to offset the frequency of the diode laser with respect to the absorption line used for locking. It allows for fine adjustments of the frequency while the laser is locked.

The Li diode laser frequency is shifted by −331 MHz from the ^{6}Li $2S_{1/2}(F=1/2, F=3/2) \rightarrow 2P_{3/2}$ crossover signal and the K diode laser frequency is shifted by +240 MHz from the conveniently located $4S_{1/2}$ ($F=1$, $F=2$) $\rightarrow 4P_{3/2}$ crossover signal of ^{39}K. Note that the small excited state hyperfine structures of both ^{6}Li and ^{39}K are unresolved in the spectroscopy.

The saturated absorption spectroscopy for lithium is realized in a heat pipe of 50 cm length, in which a natural Li sample (with the isotopic abundances ^{7}Li: 92%,

^{6}Li: 8%) is heated to 350 °C to create a sufficiently high vapor pressure for absorption. The heat pipe consists of a standard CF40 tube with the Li-sample placed at its center. The tube is heated with a pair of thermocoax cables which are wound around the tube in parallel with opposite current directions in order to prevent magnetic fields to build up. Condensation of lithium atoms on the cell windows needs to be inhibited as Li chemically reacts with glass. This is achieved by adding an argon buffer gas at ∼0.1 mbar pressure, as Ar-Li collisions prevent Li to reach the cell windows in ballistic flight. The optimum argon pressure was chosen such that it provides enough collisions, but does not substantially collision-broaden the absorption spectrum. Water cooling of the metallic parts close to the windows leads to condensation of the diffusing lithium-atoms before those can reach the windows. To avoid that lithium slowly migrates to the colder surfaces, the inside of the tube is covered with a thin stainless steel mesh (Alfa Aesar, ref. 013477), which induces capillary forces acting on the condensed atoms. Since the surface tension of liquid lithium decreases with increasing temperature [18], the capillary forces cause the atoms to move back to the hotter surfaces.

The saturated absorption spectroscopy for potassium is realized in a cylindrical glass vapor cell of 5 cm length, in which a natural K-sample (with the isotopic abundances ^{39}K: 93.36%, ^{40}K: 0.012%, ^{41}K: 6.73%) is heated to 40 °C. Here, a small non-heated appendix of the cell serves as a cold point to prevent condensation of K-atoms on the surfaces crossed by the laser beam.

In both laser systems the frequency stabilized master laser beam is immediately amplified by a first TA and subsequently injected into a single-mode polarization maintaining optical fiber (FI) for beam shaping and spatial filtering (see Fig. 3). The output beam of the optical fiber is split by a series of polarizing beam splitters into several beams whose frequencies and intensities are independently shifted and controlled with AOMs in single or double pass configuration. The various beams are then recombined with a pair of polarizing beam splitters to linearly polarized bichromatic beams consisting of one cooling and one repumping frequency. Those are then either directly injected into a fiber or into another TA for further amplification. The fibers finally transfer the beams to the main experimental table.

The injection of a bichromatic beam into a TA, whose gain-medium is non-linear, is accompanied with the creation of sidebands [19]. The sideband creation is due to parametric amplification of the gain medium by the beating between the two injected frequencies. In general, sidebands represent a loss of the power available in the injected frequencies and can excite unwanted transitions. In our case, where the two injected beam components have significantly different powers and frequencies (differing by ∼228 MHz for ^{6}Li and by ∼1286 MHz for ^{40}K), the power losses are below 10%. No unwanted transitions are excited by the amplified bichromatic beams, except for the Zeeman slower beam, as that is detuned close to an integer multiple of 228 MHz and would thus perturb the atoms in the MOT. For this beam the injection of both frequency components into the same TA was thus avoided (see Fig. 3).

Acoustically isolated homemade mechanical shutters are placed in front of each fiber on the optical tables allowing to switch off the laser beams when required. The shutters consist of a low-cost solenoid-driven mechanical switch (Tyco Electronics, ref. T90N1D12-12) and a razor blade attached to it via a small rigid lever arm. These shutters typically have a closing time of ∼100 μs when placed in the focus of a laser beam and a sufficiently reproducible time delay of the order of 3 ms.

3 Atom sources

Magneto-optical traps can be loaded in different ways. The most efficient is the loading from a beam of slow atoms. This scheme allows isolating the MOT from the atom source region with a differential pumping tube, through which the beam is directed. The MOT thus can be located in a UHV chamber where collisions with the residual gas are minimized. Furthermore, the MOT will be quickly loaded when the atomic beam is cold and has a high flux. The most efficient methods to create such beams are Zeeman slowers and 2D-MOTs. For both atomic species ^{6}Li and ^{40}K, both, Zeeman slowers [14,20,21] and 2D-MOTs [22], have been realized in the past. In our setup we chose to implement a Zeeman slower for ^{6}Li and a 2D-MOT for ^{40}K.

3.1 ^{6}Li Zeeman slower

3.1.1 Introduction

Zeeman-tuned slowing represents one of the earliest and most widely used techniques to slow down atoms from an oven [23]. A Zeeman slower longitudinally decelerates an atomic beam using the radiative force of a counter-propagating resonant laser beam. The Doppler effect accumulated during the deceleration is compensated by the Zeeman effect, induced by an inhomogeneous magnetic field, which maintains the atoms on resonance and provides a continuous deceleration.

Two types of Zeeman slowers are commonly used: the positive-field and the sign-changing field ("spin-flip") Zeeman slower [24]. We have implemented a spin-flip Zeeman slower since it brings about several advantages. First, a smaller maximum absolute value of the magnetic field is required. Second, the Zeeman laser beam is non-resonant with the atoms exiting the slower and thus does not push them back into the slower, neither it perturbs the atoms trapped in the ^{6}Li-MOT. However, the spin-flip Zeeman slower requires repumping light in the region where the magnetic field changes sign and thus makes the optics system slightly more complicated.

3.1.2 Experimental setup

The Zeeman slower consists of two distinct parts: the oven, which creates an atomic beam of thermal atoms, and an assembly of magnetic field coils. In the oven a nearly pure ^{6}Li sample (5 g) is heated to 500 °C and an atomic beam is extracted through a collimation tube. The magnetic field coils create an inhomogeneous magnetic field along the flight direction of the atoms.

The oven consists of a vertical reservoir tube (diameter: 16 mm, length: 180 mm) and a horizontal collimation tube (diameter: 6 mm, length: 80 mm), which is attached to it (see Fig. 1). The upper end of the reservoir tube and the free end of the collimation tube are connected to CF40-flanges. The flange of the reservoir tube is sealed and allows connecting a vacuum pump for baking purposes. The flange of the collimation tube connects the oven to the rest of the vacuum chamber. All parts of the oven are made of stainless steel of type 302L and connected using nickel gaskets instead of copper gaskets as they stand higher temperatures and react less with lithium. The heating of the oven is realized with two high power heating elements (Thermocoax, ref. SEI 10/50-25/2xCM 10), wound around both, the reservoir and the collimation tube.

The temperature of the oven needs to be stabilized precisely, since the atomic flux critically depends on the temperature. This is accomplished by an active stabilization circuit and an isolation with glass wool and aluminum foil. Along the collimation tube a temperature gradient is maintained in order to recycle lithium atoms sticking to the inner tube walls through capillary action, as explained above. In order to amplify the effect of capillary action, a thin stainless steel mesh with a wire diameter of 0.13 mm (Alfa Aesar, ref. 013477) is placed inside the tube. This wire decreases the effective diameter of the collimation tube to ∼5 mm. For the operating temperature of 500 °C, the vapor pressure of lithium in the oven amounts to 4×10^{-3} mbar.

A computer controlled mechanical shutter (Danaher Motion, ref. BRM-275-03) in front of the oven allows to block the atomic beam during experiments or when the ^{6}Li-MOT is not in operation.

The oven is pumped through the collimation tube with a 20 L/s ion pump and isolated from the main chamber via three differential pumping stages and the tube of the Zeeman slower. The pumping efficiency through the collimation tube is ∼0.19 L/s resulting in a pressure drop of a factor ∼100. The second and third differential pumping tubes both have a length of 100 mm and a diameter of 5 mm and 10 mm, respectively. A 20 L/s ion pump is placed after each tube. In total a pressure drop of a factor of $\sim 2.5 \times 10^6$ between the oven and the main chamber is obtained.

The assembly of the oven is a three-step procedure. First, the metallic parts of the oven are pre-baked at 600 °C during 48 h. Then, the oven is filled with the lithium sample under air atmosphere and baked again at 600 °C during 12 h in order to eliminate the impurities in the lithium sample (mostly LiH). Typically 50% of the sample is lost during this procedure. Then, the oven is connected to the rest of the vacuum chamber under an argon atmosphere, since argon does not react with lithium. Since argon damages ion pumps, the vacuum chamber is first pumped by a turbo molecular pump during 12 h before the ion pumps are finally launched and the oven is operational.

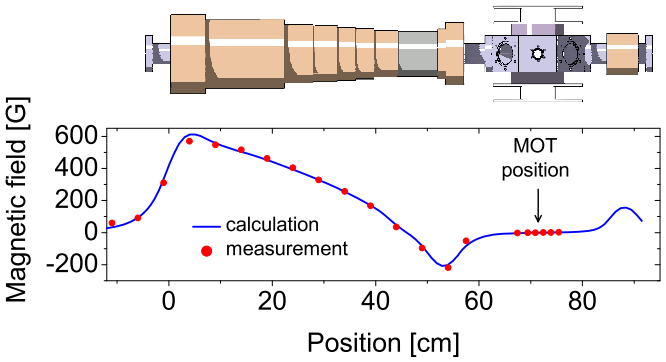


Fig. 4. (Color online) ^{6}Li Zeeman slower coil assembly and generated axial magnetic field profile. The thermal atoms coming from the ^{6}Li-oven enter the coil assembly at the position 0, and a fraction of them is slowed down and finally captured in the ^{6}Li-MOT, which is located at 71.4 cm. A compensation coil placed on the opposite side of the MOT (at 84.1 cm) ensures that the magnetic field is zero at the position of the MOT.

The Zeeman slower coils are mounted on a 65 cm long standard CF40 tube placed between the oven and the MOT chamber. A sketch of the coil assembly and the generated axial magnetic field profile are shown in Figure 4. The coil assembly extends over $L = 55$ cm and is separated from the position of the MOT by 16 cm. The coils are connected in series and were designed such that the desired magnetic field profile is generated for a moderate driving current of 12 A. The axial magnetic field of the slower along the flight direction of the atoms is measured to be 570 G at the entrance and −220 G at the exit.

The magnetic field of the Zeeman slower is non-zero at the position of the MOT and hence compensated by a coil placed opposite to the slower coils at a distance of 12.7 cm from the MOT (see Fig. 4). The compensation coil consists of 4 coil layers wound around a 10 cm long CF40 standard tube. They are powered by a separate power supply for fine adjustments. When compensated, the magnetic field has an axial gradient of 0.5 G/cm at the position of the MOT.

The cables of the Zeeman slower coils (APX France, ref. méplat cuivre émaillé CL H 1.60 × 2.50) stand bake out procedures up to 200 °C. One layer of a heating cable (Garnisch, ref. GGCb250-K5-19) is permanently placed underneath the magnetic field coils for these bake out procedures. To avoid heating of the vacuum parts during the Zeeman slower's operation, two layers of water coils were wound underneath the coil layers.

Slowing and repumping light for the Zeeman slower is derived from a bichromatic laser beam which is provided by an optical fiber originating from the laser system.

It has a total power of $P_{\text{fiber}} = 50$ mW and its frequencies are both red detuned by $\Delta\omega_{\text{slow}} = \Delta\omega_{\text{rep}} = 75\ \Gamma$ from the $2S_{1/2}(F = 3/2) \rightarrow 2P_{3/2}(F' = 5/2)$ slowing and the $2S_{1/2}(F = 1/2) \rightarrow 2P_{3/2}(F' = 3/2)$ repumping transition (see Fig. 2). The intensity I_{slow} of the slowing light is 8 times bigger than the intensity I_{rep} of the repumping light. Both beam components have the same circular polarization (σ^+ at the position where the atoms enter the slower).

The detuning of the slowing light and the axial magnetic field at the entrance of the coil assembly define the so-called capture velocity $v_{\text{cap}}^{\text{Zee}}$ of the Zeeman slower. All atoms with a velocity smaller than $v_{\text{cap}}^{\text{Zee}}$ are expected to be decelerated to the same final velocity $v_{\text{fi}}^{\text{Zee}}$ at the exit of the slower, provided that they initially populate the correct internal atomic state. The resonance condition for the atoms inside the slower yields $v_{\text{cap}}^{\text{Zee}} \sim 830$ m/s and $v_{\text{fi}}^{\text{Zee}} \sim 90$ m/s. The exit velocity of the slower is thus larger than the capture velocity of the ^{6}Li-MOT, which is estimated to be ∼50 m/s. However, the atoms are still decelerated significantly in the region between the slower exit and the MOT and are thus expected to be captured by the MOT. The capture velocity of the Zeeman slower is smaller than the most probable thermal speed of the atomic beam, which is given by $v_p = \sqrt{2k_{\text{B}}T/m} = 1464$ m/s at $T = 500$ °C, where k_{B} denotes the Boltzmann constant and m the mass of the ^{6}Li-atoms.

The bichromatic Zeeman slower beam is expanded and focused by a lens pair. The focusing of the beam accounts for the divergence of the atomic beam and the loss of beam power due to absorption and thus yields an efficient utilization of the available laser power. In addition, it induces a small cooling effect along the transverse direction [24]. The $1/e^2$-diameter at the position of the MOT is 31 mm and the focus is at a distance of 120 cm from the MOT, 10 cm behind the oven.

The divergence of the atomic beam is an important parameter characterizing the Zeeman slower. Three factors contribute to it: first, the geometry of the oven's collimation and the subsequent differential pumping tubes, second the atom's deceleration inside the slower, and third the transverse heating due to the scattered photons during the slowing process. In order to estimate the divergence of the atomic beam, we calculate the maximum possible deflection of an atom which exits the oven with a longitudinal velocity $v_{\text{cap}}^{\text{Zee}}$. An atom with this velocity needs ∼1.1 ms to reach the exit of the Zeeman slower and additional ∼1.8 ms to reach the MOT. Due to the geometry of the collimation and differential pumping tubes it can have a maximum transverse velocity of ∼16 m/s. The change in transverse velocity due to the heating is calculated to be ∼2.5 m/s [25] and is thus negligible with respect to the maximum transverse velocity determined by the tube geometry. The final transverse displacement of the atom with respect to the beam axis at the position of the ^{6}Li-MOT would thus be ∼5 cm, resulting in an effective beam divergence of ∼90 mrad. This divergence requires ^{6}Li-MOT beams of a large diameter.

Table 1. Optimized values for the parameters of the ^{6}Li Zeeman slower, yielding a ^{6}Li-MOT capture rate of $\sim 1.2 \times 10^9$ atoms/s at an oven temperature of 500 °C. The definition of the symbols is given in the text. The natural linewidth of ^{6}Li is $\Gamma/(2\pi) = 5.87$ MHz. The length of the Zeeman slower coil assembly is 55 cm.

	^{6}Li Zeeman slower
P_{fiber} (mW)	50
$\Delta\omega_{\text{slow}}$ (Γ)	–75
$\Delta\omega_{\text{rep}}$ (Γ)	–75
$I_{\text{rep}}/I_{\text{slow}}$	1/8
B_{max} (G)	570

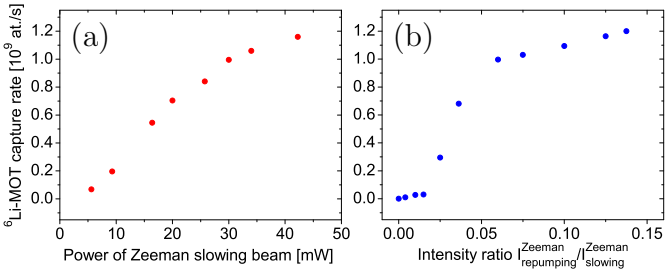


Fig. 5. (Color online) ^{6}Li-MOT capture rate as a function of (a) the power of the Zeeman slowing light for a constant repumping light power of 5.6 mW and (b) the intensity ratio between repumping and slowing light of the Zeeman slower for a constant slowing light power of 45 mW. The intensities of the superimposed beams depend on the position inside the slower, since the beams are focused toward the oven. At the position where the magnetic field changes sign, a power of 10 mW corresponds to an intensity of 2.5 I_{sat}, with the saturation intensity I_{sat} given in Table 3.

3.1.3 Experimental results

For our application the essential parameter which characterizes the performance of the Zeeman slower is the capture rate of the ^{6}Li-MOT. We studied its dependence as a function of several Zeeman slower parameters, such as: the temperature of the oven, the power of the slowing light, the magnitude of the magnetic field and the intensity ratios between the repumping and slowing light. The optimized values of these parameters are displayed in Table 1, leading to a ^{6}Li-MOT capture rate of $\sim 1.2 \times 10^9$ atoms/s. The capture rate was deduced from a very short loading of the MOT, for which atom losses can still be neglected (∼250 ms).

Figure 5a shows the dependence of the ^{6}Li-MOT capture rate on the power of the Zeeman slowing light. The curve increases with increasing beam power and indicates saturation for higher powers. In the experiment the slowing light power is 45 mW, for which the curve in Figure 5a starts to saturate, demonstrating that the size of the slowing beam is well chosen. In particular it shows that the beam is not absorbed significantly by the atoms inside the slower.

The dependence of the ^{6}Li-MOT capture rate on the intensity ratio between repumping and slowing light of the Zeeman slower is depicted in Figure 5b. The curve

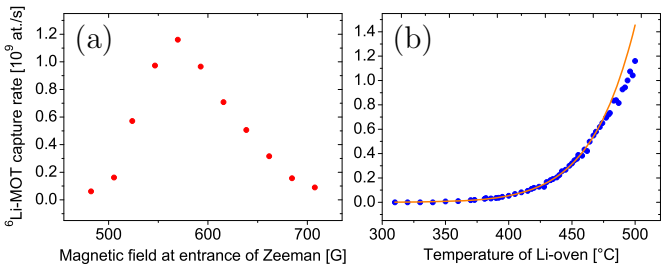


Fig. 6. (Color online) ^{6}Li-MOT capture rate as a function of (a) the axial magnetic field of the Zeeman slower and (b) the temperature of the Li-oven. Circles represent the experimental data and the solid curve the theoretical prediction from equation (3).

increases with increasing repumping intensity and saturates for higher intensities. For the intensity ratio $I_{\rm rep}/I_{\rm slow} \sim 0.1$ the repumping intensity in the region where the magnetic field of the Zeeman slower changes sign, is of the order of the saturation intensity. Therefore the transition probability of the repumping transition saturates at $I_{\rm rep}/I_{\rm slow} \sim 0.1$, explaining the behavior in Figure 5b. The graph shows that the Zeeman slower only requires a small repumping intensity. It is important that the repumping light has the same circular polarization as the slowing light, since it helps to optically pump the atoms to the cycling transition used for slowing.

Figure 6a shows the ^{6}Li-MOT capture rate as a function of the magnitude of the axial magnetic field of the Zeeman slower. The position of the maximum depends on the detuning of the slowing light.

Figure 6b shows the dependence of the ^{6}Li-MOT capture rate on the oven temperature T (circles) as well as a (scaled) theoretical prediction (solid curve) for the experimental data. The curve shows a nearly exponential increase of the capture rate with the temperature. The theoretical prediction is based on a model which assumes no collisions between the atoms (i.e., no intrabeam collisions and no collisions between the beam and the MOT atoms). It is derived as follows.

In the absence of collisions, the normalized velocity distribution of the Zeeman-slowed atoms exiting the slower does not depend on the temperature of the oven. Assuming that the ^{6}Li-MOT captures mainly atoms which have been slowed by the Zeeman slower, the capture rate $\dot{N}_{\rm M}$ of the ^{6}Li-MOT is a temperature-independent fraction of the flux $\dot{N}_{\rm Z}$ of the Zeeman-slowed atoms: $\dot{N}_{\rm M}(T) = \kappa_1 \dot{N}_{\rm Z}(T)$. The proportionality constant κ_1 depends on the divergence of the atomic beam and the capture velocity of the ^{6}Li-MOT. The flux of the Zeeman-slowed atoms $\dot{N}_{\rm Z}$ is given by the flux of the oven atoms which have a speed smaller than the Zeeman slower's capture velocity $v_{\rm cap}^{\rm Zee}$ and which are in the correct internal atomic state to be decelerated by the Zeeman slower (i.e. $F = 3/2$, $m_F = 3/2$). Assuming the oven to be in thermal equilibrium, $\dot{N}_{\rm Z}$ is given by [22,26]

$$\dot{N}_{\rm Z}(T) = \kappa_2 n_{\rm s}(T) A \int_0^{\Omega_{\rm Z}} d\Omega \frac{\cos\theta}{4\pi} \int_0^{v_{\rm cap}^{\rm Zee}} v f(v,T) dv, \quad (1)$$

with a temperature-independent constant κ_2, which equals the fraction of atoms which are in the correct internal atomic state. $n_{\rm s}(T)$ is the atomic density in the oven, $A = 2 \times 10^{-5}$ m^2 the aperture surface of the oven, $\Omega_{\rm Z} = A'/l^2 = 5 \times 10^{-4}$ the solid angle of the atomic beam (with A' the aperture surface of the last differential pumping tube and l the distance between the two aperture surfaces A, A') and $d\Omega = 2\pi \sin\theta d\theta$, with θ the emission angle with respect to the oven axis. $f(v,T)$ is the normalized speed distribution function given by

$$f(v,T) = \sqrt{\frac{2m^3}{\pi k_{\rm B}^3 T^3}} v^2 \exp\left(-\frac{mv^2}{2k_{\rm B}T}\right). \quad (2)$$

Since the solid angle of the atomic beam is small, it is $\cos\theta \approx 1$ and thus $\int_0^{\Omega_{\rm Z}} d\Omega \cos\theta \approx \Omega_{\rm Z}$.

The explicit temperature dependence of the ^{6}Li-MOT capture rate is then obtained via $\dot{N}_{\rm M}(T) = \kappa_1 \dot{N}_{\rm Z}(T)$ by substituting into equation (1) the ideal gas equation $n_{\rm s}(T) = p_{\rm s}/(k_{\rm B}T)$ and the relation $p_{\rm s} = p_{\rm a} \exp[-L_0/(k_{\rm B}T)]$ for the saturated vapor pressure $p_{\rm s}$, with $p_{\rm a} = 1.15 \times 10^8$ mbar and the latent heat of vaporization $L_0/k_{\rm B} = 18\,474$ K [27]. This relation applies to the temperature range 300–500 °C with an accuracy of 5%. Thus, we have

$$\dot{N}_{\rm M}(T) = \kappa A \Omega_{\rm Z} p_{\rm a} \sqrt{\frac{m^3}{8\pi^3 k_{\rm B}^5 T^5}} e^{-\frac{L_0}{k_{\rm B}T}} \int_0^{v_{\rm cap}^{\rm Zee}} v^3 e^{-\frac{mv^2}{2k_{\rm B}T}} dv, \quad (3)$$

with $\kappa = \kappa_1 \kappa_2$. Scaling equation (3) to the experimental data for a given (low) temperature ($T = 350$ °C) yields the theoretical prediction for the curve shown in Figure 6. The scaling yields $\kappa = 10^{-3}$, thus 0.1% of the atoms, which enter the Zeeman slower with a velocity smaller than $v_{\rm cap}^{\rm Zee}$, are captured by the ^{6}Li-MOT.

The main contribution to the small value of κ is the large divergence of the slowed atomic beam: κ is proportional to the ratio of the atomic beam cross section and the capture surface of the ^{6}Li-MOT, which is estimated to $\sim 10^{-2}$ (assuming the ^{6}Li-MOT capture surface to be a circle of 1.1 cm diameter). Two-dimensional transverse laser cooling of the atomic beam could vastly increase the value of κ. The remaining 10% are due to an inefficient capture of the ^{6}Li-MOT and to a significant fraction of oven atoms occupying the incorrect internal atomic states.

The obtained theoretical prediction agrees well with the experimental data for temperatures below 475 °C (see Fig. 6b). For temperatures above 475 °C, the experimental data deviate from the prediction indicating that intrabeam collisions or collisions between the atoms in the beam and the MOT become important. We found that for $T = 500$ °C collisions between the thermal ^{6}Li beam and the trapped ^{6}Li-MOT atoms indeed take place, which we verified by measuring the lifetime of the ^{6}Li-MOT in presence and absence of the thermal ^{6}Li beam, making use of the mechanical block placed at the exit of the oven. The lifetime was found 10% larger for the case where the thermal ^{6}Li beam was blocked. In a similar way the thermal ^{6}Li beam also affects the lifetime of the ^{40}K-MOT.

In order to avoid a reduction of the number of trapped ^{40}K atoms in the dual-species MOT, we therefore limit the ^{6}Li-oven temperature to 500 °C.

With the help of equation (1) the lifetime of the oven can be estimated. Assuming that the collimation tube of the oven recycles all atoms sticking to its wall and the vacuum pumps have no impact on the Li pressure in the oven, the total atomic flux through the collimation tube is obtained by replacing $A' = A$, $v_{\mathrm{cap}}^{\mathrm{Zee}} = \infty$ and $l = 8$ cm (the length of the collimation tube) in equation (1). For the working temperature $T = 500$ °C the lithium vapor pressure is $p_s = 4.8 \times 10^{-3}$ mbar, corresponding to a density $n_s = 4.5 \times 10^{19}$ m^{-3}. Thus, the atom flux through the collimation tube is $\dot{N}_{\mathrm{O}} = 3.5 \times 10^{14}$ s^{-1} $\hat{=}$ 3.5×10^{-12} kg/s. With 3 g of ^{6}Li this corresponds to an oven lifetime of $\tau_{\mathrm{oven}} \sim 25$ years. (The importance of the recycling becomes manifest when comparing this value to the hypothetical lifetime of the oven, would the collimation tube be replaced by an aperture of the same surface. In this case the atom flux through this aperture would be $\dot{N}_{\mathrm{O}}^{\mathrm{hyp}} = (\pi l^2/A)\dot{N}_{\mathrm{O}} \sim 1000\dot{N}_{\mathrm{O}}$ and thus $\tau_{\mathrm{oven}}^{\mathrm{hyp}} \sim 10$ days.)

3.2 ^{40}K 2D-MOT

3.2.1 Introduction

2D-MOTs have been widely used over the past years to produce high flux beams of cold atoms [14,22,28–31]. In some cases they offer advantages over the more common Zeeman slowers. Even though Zeeman slowers can produce higher fluxes and are more robust, they have the following disadvantages. They produce unwanted magnetic fields close to the MOT which need to be compensated by additional fields, they require a substantial design and construction effort and are space consuming. The atomic beam source of Zeeman slowers needs to be operated at higher temperatures than the vapor cell used as source for 2D-MOTs and the material consumption can be high. In the case of the rare isotope ^{40}K, this drawback is major: no pure source of ^{40}K exists and enriched ^{40}K samples are very expensive (4000 Euros for 100 mg of a 4% enriched sample). Therefore a ^{40}K Zeeman slower would be very costly. A 2D-MOT can be operated at lower pressures and is thus more economic. In addition it allows separating ^{40}K from the more abundant ^{39}K, since it produces an atomic beam which nearly only contains the slowed atoms (i.e. no thermal background). These considerations motivated us to implement a 2D-MOT for ^{40}K.

3.2.2 Principle of operation

In a 2D-MOT, an atomic vapor is cooled and confined transversally and out-coupled longitudinally through an aperture tube. The role of the aperture tube is two-fold. First, it isolates the 2D-MOT from the MOT chamber by differential pumping, and second, it acts as a geometric velocity filter, since only atoms with a small transverse velocity pass through. As the transverse cooling is more efficient for atoms which have a small longitudinal velocity – since those spend more time in the cooling region – most of the transversally cold atoms are also longitudinally cold. Thus, the filter indirectly filters atoms also according to their longitudinal velocity. A 2D-MOT thus produces an atomic beam which is transversally and longitudinally cold.

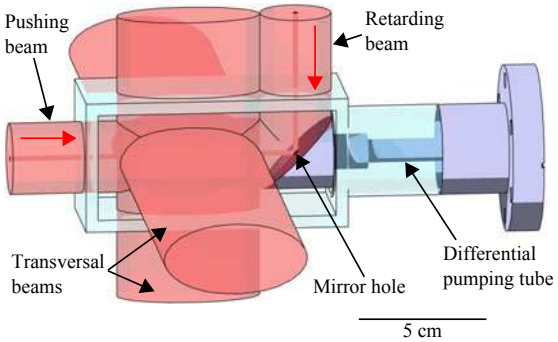


Fig. 7. (Color online) Sketch of the parallelepipedical glass cell used for the ^{40}K 2D-MOT. A mirror is placed inside the vacuum chamber to allow an independent control over the longitudinal beam pair. The mirror has a hole in its center and creates a dark cylindrical region in the reflected beams.

The flux of a 2D-MOT can be improved by adding a longitudinal molasses cooling to the 2D-MOT configuration [28]. Thus, the atoms spend more time in the transverse cooling region due to the additional longitudinal cooling. The longitudinal beam pair is referred to as the pushing and the retarding beam, where the pushing beam propagates in the direction of the atomic beam (see Fig. 7). We implemented such a configuration, making use of a 45°-angled mirror inside the vacuum chamber. This mirror has a hole at its center which creates a cylindrical dark region in the reflected retarding beam. In this region, the atoms are accelerated along the longitudinal direction by the pushing beam only, which allows an efficient out-coupling of the atomic beam.

3.2.3 Experimental setup

The vacuum chamber of the 2D-MOT consists of standard CF40 components and a parallelepipedical glass cell (dimensions 110 mm × 55 mm × 55 mm), which is depicted in Figure 7. Its long axis is aligned horizontally, parallel to the differential pumping tube and the direction of the produced atomic beam. The mirror inside the vacuum chamber is a polished stainless steel mirror with an elliptical surface (diameters 3.0 cm and 4.2 cm). It is attached to the differential pumping tube inside the vacuum. It allows to overlap the two longitudinal laser beams whose powers and orientations can thus be independently controlled externally. The mirror's material has a reflectivity of only 50%, but inhibits chemical reaction of potassium with its surface. The differential pumping tube intercepts the mirror at its center. The tube has a diameter of 2 mm over a distance of 1.5 cm and then stepwise widens up to 10 mm over a total distance of 22 cm. The ^{40}K-MOT

is located 55 cm away from the 2D-MOT center. Assuming a ballistic flight of the atoms, the geometry of the differential pumping tube defines an upper limit of the divergence of the atomic beam, which is calculated to be ∼35 mrad. The atomic beam thus is expected to have a diameter of ∼2 cm when it reaches the ^{40}K-MOT. The differential pumping tube has a conductance of 0.04 L/s. The generated pressure ratio between the 2D-MOT and the 3D-MOT chambers is $\sim 10^3$.

The potassium source is an isotopically enriched ^{40}K sample (containing 4 mg of ^{40}K, 89.5 mg of ^{39}K and 6.5 mg of ^{41}K, from Technical Glass Inc., Aurora, USA), placed at a distance of 20 cm from the glass cell. It was purchased in a small ampule which was broken under vacuum inside a modified stainless steel CF16 bellow. The small vapor pressure of potassium at room temperature (10^{-8} mbar) requires heating of the entire 2D-MOT chamber. We heat the source region to 100 °C, all intermediate parts to 80 °C and the glass cell to 45 °C. The gradient in temperature ensures that the potassium migrates into the cell and remains there. The resulting K-pressure in the glass cell was measured by absorption of a low intensity probe. We found 2.3×10^{-7} mbar, which implies a partial pressure of the ^{40}K-isotope of 1×10^{-8} mbar. In contrast to lithium, the source lifetime is mainly determined by the pumping speed of the ion pump. At the measured pressure the lifetime of the source is estimated to ∼2 years.

Four air-cooled rectangular shaped elongated racetrack coils (dimensions 160 mm × 60 mm) are placed around the glass cell to produce a 2D quadrupole field with cylindrical symmetry and a horizontal line of zero magnetic field. This racetrack coil geometry allows an independent control of the transverse position of the magnetic field zero, and minimizes finite coil fringe effects at the coil ends. The coils are controlled by four separate power supplies. For optimized operation, the transverse magnetic field gradients are $\partial_x B = \partial_y B = 11$ G/cm.

Cooling and repumping light for the 2D-MOT is derived from a bichromatic laser beam which is provided by an optical fiber originating from the laser system. It has a total power of $P_{\text{fiber}} = 450$ mW and its frequencies are red detuned by ∼3.5 Γ from the $4S_{1/2}(F = 9/2) \rightarrow 4P_{3/2}(F' = 11/2)$ cooling and by ∼2.5 Γ from the $4S_{1/2}(F = 7/2) \rightarrow 4P_{3/2}(F' = 9/2)$ repumping transition (see Fig. 2). The beam is separated into four beams and expanded by spherical and cylindrical telescopes to create the transverse and longitudinal 2D-MOT beams. The transverse beams have an elliptical cross section ($1/e^2$-diameters: 27.5 mm and 55 mm), are circularly polarized and retro-reflected by right-angled prisms, which preserve the helicity of the beams. The power losses in the surface of the glass cell and the prisms weaken the power of the retro-reflected beams by ∼17% (the loss contribution of the absorption by the vapor is negligible due to the high laser power). This power imbalance is compensated by shifting the position of the magnetic field zero. The longitudinal beams are linearly polarized and have a circular cross section ($1/e^2$-diameter: 27.5 mm). 75% of the fiber output power is used for the transverse beams, 25% for the longitudinal beams. The intensity ratio between pushing and retarding beam along the atomic beam axis is ∼6 (for reasons explained below).

Table 2. Optimized values for the parameters of the ^{40}K 2D-MOT, yielding a ^{40}K-MOT capture rate of $\sim 1.4 \times 10^9$ atoms/s. The definition of the symbols is given in the text. The natural linewidth of ^{40}K is $\Gamma/(2\pi) = 6.04$ MHz.

	^{40}K 2D-MOT
P_{fiber} (mW)	450
$\Delta\omega_{\text{cool}}$ (Γ)	–3.5
$\Delta\omega_{\text{rep}}$ (Γ)	–2.5
$I_{\text{rep}}/I_{\text{cool}}$	1/2
$I_{\text{push}}/I_{\text{ret}}$	6
$\partial_x B, \partial_y B$ (G/cm)	11
K vapor pressure (mbar)	2.3×10^{-7}

3.2.4 Experimental results

For our purpose the essential parameter which characterizes the performance of the 2D-MOT is the capture rate of the ^{40}K-MOT. We studied its dependence as a function of several 2D-MOT parameters, such as: the vapor pressure in the 2D-MOT cell, the total cooling light power, the detuning of the cooling frequency and the intensity ratios between the repumping and cooling light and between the pushing and retarding beam. The optimized values of these parameters are displayed in Table 2, leading to a ^{40}K-MOT capture rate of $\sim 1.4 \times 10^9$ atoms/s.

The mean velocity of the atoms in the atomic beam can be estimated as follows. It is approximately given by the average time required for the atoms of the 2D-MOT region to reach the 3D-MOT. This time was measured by recording the time delay of the onset of the ^{40}K-MOT loading after switching on the 2D-MOT beams. We measured a time delay of ∼23 ms and deduce a mean longitudinal velocity of the captured atoms of ∼24 m/s. At this velocity, the displacement due to gravity of the beam of atoms from the ^{40}K-MOT center is ∼2.6 mm, which is negligible compared to the size of the ^{40}K-MOT beams and the divergence of the atomic beam.

Figure 8a shows the dependence of the ^{40}K-MOT capture rate on the detuning $\Delta\omega_{\text{cool}}$ of the 2D-MOT cooling light. The curve has a maximum at $\Delta\omega_{\text{cool}} = -3.5\ \Gamma$ and a full width at half maximum (FWHM) of 2.7 Γ. The maximum is the result of two opposing effects: the scattering force of the 2D-MOT beams decreases with increasing detuning whereas the capture velocity increases [24]. The first effect implies a less efficient transverse cooling whereas the second leads to a more efficient capture of atoms. An additional effect might influence the shape of the curve: since the scattering force of the pushing beam depends on the detuning, also the mean-velocity of the atomic beam depends on it [28,29,31]. Since we measure the ^{40}K-MOT capture rate rather than the flux of the 2D-MOT, the mean-velocity might exceed the capture velocity of the ^{40}K-MOT. However, as shown in references [28,29,31], the mean-velocity of the beam only

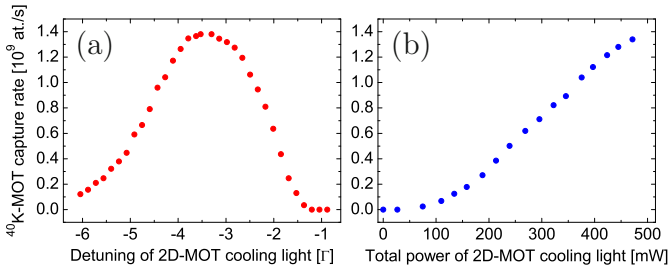


Fig. 8. (Color online) ^{40}K-MOT capture rate as a function of (a) the detuning and (b) the total power of the cooling light used for the 2D-MOT (for a constant intensity ratio between the cooling and repumping light). The total power refers to the sum of the powers in the six 2D-MOT beams, where a power of 470 mW corresponds to a total intensity of $\sim 47\, I_{\rm sat}$ at the center of the 2D-MOT, with the saturation intensity $I_{\rm sat}$ given in Table 3.

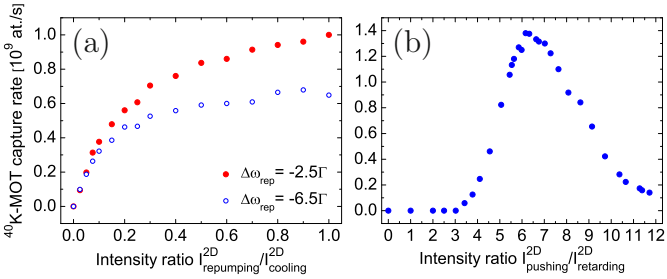


Fig. 9. (Color online) ^{40}K-MOT capture rate as a function of the intensity ratio between (a) repumping and cooling light of the 2D-MOT for two different repumping detunings $\Delta\omega_{\rm rep}$ and a constant total cooling light power of 300 mW (which corresponds to a total intensity of $\sim 30\, I_{\rm sat}$) and (b) the pushing and the retarding beams of the 2D-MOT. The intensities of the pushing and retarding beams refer to the intensities along the atomic beam axis.

Table 3. Characteristic parameters of the dual-species ^{6}Li-^{40}K-MOT.

	^{40}K-MOT	^{6}Li-MOT
$P_{\rm fiber}$ (mW)	220	110
$\Delta\omega_{\rm cool}$ (Γ)	–3	–5
$\Delta\omega_{\rm rep}$ (Γ)	–5	–3
$\Gamma/(2\pi)$ (MHz)	6.04	5.87
$I_{\rm cool}$ per beam ($I_{\rm sat}$)	13	4
$I_{\rm sat}$ (mW/cm^2)	1.75	2.54
$I_{\rm rep}/I_{\rm cool}$	1/20	1/5
$\partial_z B$ (G/cm)	8	8
$N_{\rm single}$ ($\times 10^9$)	8.9	5.4
$N_{\rm dual}$ ($\times 10^9$)	8.0	5.2
$n_{\rm c}$ ($\times 10^{10}$ at./cm^3)	3	2
T (μK)	290	1400

slightly changes with the detuning, such that we expect this effect to only weakly influence the curve. From the shape of the curve we conclude that the ^{40}K-MOT capture rate is not very sensitive to changes of $\Delta\omega_{\rm cool}$.

The dependence of the ^{40}K-MOT capture rate on the total power of the 2D-MOT cooling light is depicted in Figure 8b. The total power refers to the sum of the powers in the six 2D-MOT beams. According to the chosen beam sizes, the maximum power of 470 mW corresponds to a total intensity of $\sim 47\, I_{\rm sat}$ (for zero detuning) at the center of the 2D-MOT, with the saturation intensity $I_{\rm sat}$ given in Table 3. The curve almost linearly increases with light power without a clear indication of saturation. The increase is due to two effects. First, the 2D-MOT capture velocity increases with laser power due to the power broadening of the atomic spectral lines. Second, the scattering force increases, resulting in a steeper transverse confinement, which facilitates the injection of the atoms into the differential pumping tube. At some point, the curve is expected to saturate, since the temperature of the cooled atoms and light-induced collisions between them increase with light power. These effects, however, are less limiting in a 2D-MOT as compared to a 3D-MOT, since the atomic density in a 2D-MOT is typically three orders of magnitude smaller due to the absence of a three-dimensional confinement. Thus, in a 2D-MOT a high light power would be required to reach the regime of saturation.

Figure 9a shows the dependence of the ^{40}K-MOT capture rate on the intensity ratio between the cooling and repumping light of the 2D-MOT for the two different repumping detunings $\Delta\omega^{(1)}_{\rm rep} = -2.5\ \Gamma$ and $\Delta\omega^{(2)}_{\rm rep} = -6.5\ \Gamma$ and for a constant total cooling light power of 300 mW. The graph shows that for both frequencies the ^{40}K-MOT capture rate increases with increasing repumping intensity and that it saturates at high intensities. It also shows that the maximum capture rate is bigger for the smaller detuning. The intensity dependence of the curves results from the likewise intensity dependence of the transition probability for an atomic transition. The maximum capture rate is bigger for the smaller detuning, since this detuning contributes more efficiently to the cooling process. In our experiment, a fixed total laser power is available for both repumping and cooling light. It is distributed such that the resulting capture rate is maximized. It was found to be maximum for an intensity ratio of $I_{\rm rep}/I_{\rm cool} \sim 1/2$. For that ratio the detuning $\Delta\omega^{(2)}_{\rm rep} = -2.5\ \Gamma$ also yields the maximum capture rate.

The dependence of the ^{40}K-MOT capture rate on the intensity ratio between pushing and retarding beam is depicted in Figure 9b. The curve has a maximum at $I_{\rm push}/I_{\rm retard} \sim 6$. It is zero for values of $I_{\rm push}/I_{\rm retard}$ between 0 and 3, then increases until the maximum and falls off again with a smaller slope. From the curve we can extract information about the importance of the reflectivity of the mirror inside the vacuum and of the size of its hole. For a given intensity ratio $I_{\rm push}/I_{\rm retard}$ along the (horizontal) direction of the atomic beam, the mirror's reflectivity determines the intensity ratio $I^*_{\rm push}/I^*_{\rm retard}$ along the vertical direction above the reflecting surface of the mirror (see Fig. 7). If $I^*_{\rm push}/I^*_{\rm retard}$ differs from 1, the atomic beam can experience a vertical deflection in this region. The hole inside the mirror creates a dark cylinder in the pushing beam after its reflection, so that in the region above the hole only light from the retarding beam has a

vertical direction, which can also give rise to a vertical deflection of the atomic beam.

In the following we estimate the deflection of the atomic beam, which is induced by the unbalanced retarding beam in the small region above the hole. Assuming the atomic beam to have reached its final longitudinal velocity of 24 m/s when entering into the hole, the atoms spend 85 μs in the region above the hole. Neglecting Doppler shifts and the presence of the pushing beam along the horizontal direction (no transverse beams are present in the region above the mirror), the atoms will scatter $N_{\mathrm{ph}} = R_{\mathrm{sc}} \times (85\ \mu s) \sim 75$ photons, with R_{sc} being the scattering rate [24] for the given detuning $\Delta\omega_{\mathrm{cool}} = -3.5\ \Gamma$ and peak intensity $I^*_{\mathrm{retard}} = 2.5 I_{\mathrm{sat}}$. The recoil velocity of ^{40}K being given by $v_{\mathrm{rec}} = 0.013$ m/s, each atom will accumulate a transverse velocity of $v_{\mathrm{dev}} \sim 1$ m/s. This leads to a downwards deflection of the atomic beam by an angle of ~40 mrad, which is more than a factor two bigger than the maximum deflection angle allowed by the differential pumping tubes. The atoms will thus not reach the ^{40}K-MOT.

This deflection needs to be anticipated by an intensity imbalance $I^*_{\mathrm{push}} > I^*_{\mathrm{retard}}$ in the region above the reflecting surface of the mirror, as that results in an upwards deflection of the atomic beam. For the given mirror reflectivity of 50%, $I^*_{\mathrm{push}} > I^*_{\mathrm{retard}}$ is equivalent to $I_{\mathrm{push}}/I_{\mathrm{retard}} > 4$, which corresponds to the experimental observation depicted in Figure 9b. The deflection of the atomic beam in the region above the hole could be avoided using a beam block which creates a dark cylinder in the region above the mirror which overlaps with the one in the pushing beam. In this configuration the position of the curve optimum in Figure 9b would change from $I_{\mathrm{push}}/I_{\mathrm{retard}} = 6$ to $I_{\mathrm{push}}/I_{\mathrm{retard}} = 4$. For mirrors with a reflectivity close to 100% the position of the curve optimum could thus even be changed to $I_{\mathrm{push}}/I_{\mathrm{retard}} = 1$, for which the longitudinal optical molasses cooling would be most efficient leading to a maximum 2D-MOT flux. Due to the polarization gradients generated by the transverse 2D-MOT beams the longitudinal optical molasses cooling is, however, still very efficient even in case of an intensity imbalance of 6 along the atomic beam axis.

We now study the dependence of the ^{40}K-MOT capture rate on the vapor pressure of potassium (all isotopes) in the 2D-MOT cell, which is shown in Figure 10 (circles) together with a fit to a theoretical model (solid curve). The vapor pressure was measured by recording the absorption profile of a low intensity probe. The curve in Figure 10 has a maximum at a vapor pressure of 2.3×10^{-7} mbar. In the absence of collisions, the curve should increase linearly with pressure, which is indeed observed for low pressures. For high pressures, collisions become important and limit the ^{40}K-MOT capture rate. The dependence of the ^{40}K-MOT capture rate L on the pressure p can be described by the function [31]

$$L = L_0 \exp\left[-\left(\Gamma_{\mathrm{coll}} + \beta \int n^2(\mathbf{r}) d^3r\right) \langle t_{\mathrm{cool}} \rangle\right], \qquad (4)$$

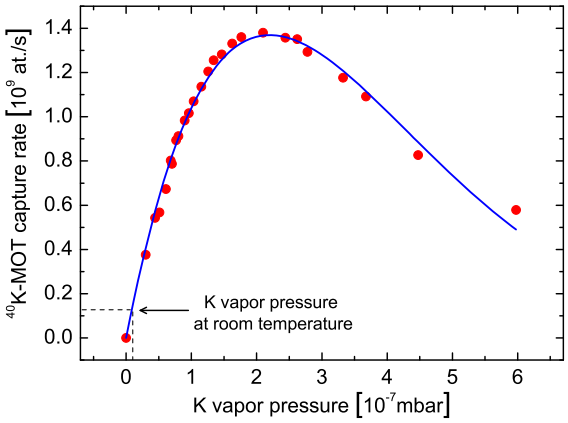


Fig. 10. (Color online) ^{40}K-MOT capture rate as a function of the potassium vapor pressure (all isotopes). Circles: experimental data, solid curve: fit of the experimental data by equation (5). Due to the low abundance of the ^{40}K-isotope in our potassium sample (4%), the ^{40}K-MOT capture rate is limited by collisions between the ^{40}K-atoms and the other K-isotopes in the 2D-MOT cell. At room temperature the potassium vapor pressure is 1×10^{-8} mbar.

where L_0 denotes the hypothetical capture rate of the ^{40}K-MOT in the absence of collisions in the 2D-MOT chamber, Γ_{coll} denotes the collisional loss rate due to collisions in the 2D-MOT chamber between the cooled atoms and the background atoms, $\langle t_{\mathrm{cool}} \rangle$ is the average time which the atoms spend inside the 2D-MOT cooling region, $n(\mathbf{r})$ is the position-dependent atomic density in the atomic beam, and β is the two-body loss rate coefficient which describes the cold collisions between the ^{40}K atoms in the atomic beam. L_0 is proportional to the atomic density n_{K} in the vapor cell, and $\Gamma_{\mathrm{coll}} = n_{\mathrm{K}} \sigma_{\mathrm{eff}} \langle v \rangle$, where σ_{eff} is the effective collision cross section, and $\langle v \rangle \sim 400$ m/s the mean velocity of the thermal potassium atoms. The term describing the cold collisions is approximately proportional to n_{K}^2 due to the small density obtained in the 2D-MOT. For the investigated pressure range, the ratio p/n_{K} only changes slightly with temperature and can thus be considered constant. Therefore equation (4) can be written as

$$L(p) = \kappa_1 p \exp\left(-\kappa_2 p - \kappa_3 p^2\right), \qquad (5)$$

with the constants $\kappa_1, \kappa_2, \kappa_3$, which are obtained from the fit shown in Figure 10. At the curve's maximum, the fit yields $\kappa_2 p/\kappa_3 p^2 = 8$, showing that the collisions which limit the ^{40}K-MOT capture rate are mainly the collisions with the hot background atoms, consisting mostly of ^{39}K.

The background atoms are predominantly potassium atoms. These can collide either with the excited or the non-excited ^{40}K-atoms of the atomic beam. Depending on the isotopes of the colliding partners, these collisions have different cross sections. Collisions between an excited and a non-excited atom of the same isotope usually have a very large cross section due to the strong resonant dipole-dipole interaction, described by a C_3/R^3-potential. In 2D-MOT systems of other atomic species these collisions have been identified as the ones which limit the

flux of the 2D-MOT [28,29,31]. In the case of ^{40}K, the scattering rate for these collisions is reduced by the small abundance of ^{40}K in the vapor. Therefore other collisions might limit the flux. In order to identify the flux-limiting collisions we calculate the cross section of different possible collisions and deduce the corresponding collision rates. The cross sections can be calculated using the approach described in reference [32] for losses out of a cold atom cloud. The cross section for collisions involving an excited and a non-excited ^{40}K-atom is given by [32]

$$\sigma_{\mathrm{eff}}^{40,40^*} = \pi \left(\frac{4C_3}{m v_{\mathrm{esc}} \langle v \rangle} \right)^{2/3}, \tag{6}$$

where m is the mass of the ^{40}K-atom, $v_{\mathrm{esc}} \sim 1$ m/s is the estimated transverse velocity kick needed to make an atom miss the ^{40}K-MOT, and $C_3 = 5.4 \times 10^{-48}$ J m^3 is the dispersion coefficient for the resonant dipole-dipole interaction [33]. The cross section for collisions involving a non-excited ^{40}K-atom and a non-excited K-atom of the different isotopes is given by [32]

$$\sigma_{\mathrm{eff}}^{40,39} \sim \sigma_{\mathrm{eff}}^{40,41} \sim \sigma_{\mathrm{eff}}^{40,40} = \pi \left(\frac{15\pi C_6}{8 m v_{\mathrm{esc}} \langle v \rangle} \right)^{1/3}, \tag{7}$$

where $C_6 = 3.7 \times 10^{-76}$ J m^6 is the dispersion coefficient for the underlying van der Waals interaction [33]. Substituting the experimental parameters, one obtains: $\sigma_{\mathrm{eff}}^{40,40^*} = 2.7 \times 10^{-16}$ m^2 and $\sigma_{\mathrm{eff}}^{40,39} \sim \sigma_{\mathrm{eff}}^{40,41} \sim \sigma_{\mathrm{eff}}^{40,40} = 1.3 \times 10^{-17}$ m^2. The resulting collision rates are proportional to the atomic densities n_{39}, n_{40} and n_{41} of the corresponding isotopes in the vapor and the relative number of excited ^{40}K-atoms in the atomic beam, which was estimated to $P \sim 0.1$ for the given beam detunings and intensities. One obtains

$$\Gamma_{\mathrm{coll}}^{40,40^*} = P n_{40} \sigma_{\mathrm{eff}}^{40,40^*} \langle v \rangle = 4.4 \times 10^{-16} n_{\mathrm{K}}, \tag{8}$$

$$\Gamma_{\mathrm{coll}}^{40,39} = (1-P) n_{39} \sigma_{\mathrm{eff}}^{40,39} \langle v \rangle = 4.4 \times 10^{-15} n_{\mathrm{K}}, \tag{9}$$

$$\Gamma_{\mathrm{coll}}^{40,40} = (1-P) n_{40} \sigma_{\mathrm{eff}}^{40,40} \langle v \rangle = 2.0 \times 10^{-16} n_{\mathrm{K}}, \tag{10}$$

$$\Gamma_{\mathrm{coll}}^{40,41} = (1-P) n_{41} \sigma_{\mathrm{eff}}^{40,41} \langle v \rangle = 3.0 \times 10^{-16} n_{\mathrm{K}} \tag{11}$$

(n_{K} denoting the atomic density of potassium in the vapor cell). The dominant collision rate here is $\Gamma_{\mathrm{coll}}^{40,39}$ (Eq. (9)) for collisions involving a non-excited ^{40}K-atom and a non-excited ^{39}K-atom from the background. The largest collision rate for collisions between two ^{40}K-atoms, $\Gamma_{\mathrm{coll}}^{40,40^*}$, is by a factor of 10 smaller than $\Gamma_{\mathrm{coll}}^{40,39}$. Therefore, collisions involving two ^{40}K-atoms are not the collisions which limit the flux of the 2D-MOT. This is in contrast to 2D-MOT systems of other species. From the difference between $\Gamma_{\mathrm{coll}}^{40,40^*}$ and $\Gamma_{\mathrm{coll}}^{40,39}$ we conclude that the flux of the 2D-MOT for ^{40}K could still be improved by about a factor of 10 by using a potassium sample of a higher isotopic enrichment.

4 ^{6}Li-^{40}K dual-species MOT

4.1 Introduction

Previously, several groups have studied samples of two atomic species in a magneto-optical trap [13–15,34–37]. Here we report on the implementation and performance of our ^{6}Li-^{40}K dual-species MOT and on the study of collisions between atoms of the different species. After a description of the experimental setup, we start with a characterization of the single-species MOTs and then focus on the collisions in the dual-species MOT.

4.2 Principle of operation

In a magneto-optical trap six counter-propagating red-detuned overlapping laser beams cool and magneto-optically confine atoms in a magnetic quadrupole field around its zero [24]. MOTs for alkali-atoms require laser light of two frequencies, namely the cooling and the repumping frequency. The latter ensures that the atoms stay in the cycling transition used for cooling. Typically the repumping light has a much lower power than the cooling light as the atoms principally occupy the states belonging to the cooling transition. For ^{6}Li, however, the power of the repumping light needs to be relatively high, since ^{6}Li has a very small hyperfine structure in the excited state manifold (of the order of the linewidth). When laser cooled, ^{6}Li-atoms thus very likely quit the cooling transition. Therefore, the repumping light needs to contribute to the cooling process. As a consequence it needs to be present in all six directions with the same polarization as the cooling light. Therefore, we use bichromatic MOT-beams containing both cooling and repumping frequencies. We adapt the same strategy also for ^{40}K.

4.3 Experimental setup

Light for the dual-species MOT is derived from two bichromatic laser beams, containing each a cooling and a repumping frequency, which are provided by two separate optical fibers originating from the respective laser systems. The beams are superimposed using a dichroic mirror and then expanded by a telescope to a $1/e^2$-diameter of 22 mm. All subsequent beam reflections are realized by two-inch sized broadband mirrors (Thorlabs, ref. BB2-E02-10). The beam is separated by three two-inch sized broadband polarization cubes (Lambda Optics, ref. BPB-50.8SF2-550) into four arms that form a partially retro-reflected MOT, in which only the vertical beam pair is composed of independent counter-propagating beams. Each retro-reflected MOT beam is focused with a lens of focal length 10 cm, placed at a distance of ∼11 cm in front of the retro-reflecting mirror, in order to increase the intensity and therefore compensate for the losses in the optics and the light absorption by the trapped atoms. The distribution of the light power over the MOT beams is independently

adjusted for the two wavelengths using a pair of custom-made wave plates, placed in front of each broad-band splitting cube. The wave plate pair consists of a $\lambda/2$ plate of order 4 for the wavelength 767 nm and a $\lambda/2$ plate of order 4 for the wavelength 671 nm. To a very good approximation each of these wave plates can turn the polarization direction for one wavelength without affecting the polarization for the other one (since it is $4.5 \times 767 \approx 5 \times 671$ and $4.5 \times 671 \approx 4 \times 767$). The circular polarization of the MOT beams is produced by first order $\lambda/4$ plates for 767 nm, which work sufficiently well also for 671 nm. All four frequency components thus have the same circular polarizations in each beam. A mechanical shutter is placed in the focus of the telescope allowing to produce total extinction of the MOT light in addition to the partial and fast switching by the AOMs.

The bichromatic beam for the ^{40}K-MOT has a total power of $P_{\text{fiber}} = 220$ mW and its frequencies are red-detuned by $\sim 3\ \Gamma$ from the $4S_{1/2}(F = 9/2) \rightarrow 4P_{3/2}(F' = 11/2)$ cooling and by $\sim 5\ \Gamma$ from the $4S_{1/2}(F = 7/2) \rightarrow 4P_{3/2}(F' = 9/2)$ repumping transition (see Fig. 2). The intensity of the cooling light is $\sim$20 times bigger than that of the repumping light. The bichromatic beam for the ^{6}Li-MOT has a total power of $P_{\text{fiber}} = 110$ mW and its frequencies are red-detuned by $\sim 5\ \Gamma$ from the $2S_{1/2}(F = 3/2) \rightarrow 2P_{3/2}(F' = 5/2)$ cooling and by $\sim 3\ \Gamma$ from the $2S_{1/2}(F = 1/2) \rightarrow 2P_{3/2}(F' = 3/2)$ repumping transition (Fig. 2). The power of the cooling light is $\sim$5 times bigger than that of the repumping light.

The magnetic field for the dual-species MOT is created by a pair of coils in anti-Helmholtz configuration. The magnetic field gradient along the vertically directed symmetry axis is $\partial_z B = 8$ G/cm. This gradient yields an optimum atom number for the ^{40}K-MOT.

The atoms in the dual-species MOT are probed by absorption imaging. In order to obtain a two-dimensional density profile of the atom cloud, three pictures are taken and recorded by a CCD-camera (PCO imaging, ref. Pixelfly qe). The first picture is taken with the imaging beam tuned near resonance and thus records the shadow cast by the atom cloud on the CCD-chip of the camera. The second picture is taken with the imaging beam tuned far off resonance (by $-10\ \Gamma$) and records the intensity profile of the imaging beam. The third picture is taken in absence of the imaging beam and records the background signal. The change of frequency of the imaging beam allows to take the first two pictures with a short time delay (2 ms), while keeping the imaging beam at the same frequency would require to wait for the atom cloud to disappear before the second picture could be recorded. Thus, the intensity fluctuations of the imaging beam during the recording process are minimized and both pictures can be taken with the same intensity.

Each atomic species requires its own imaging beam, which is provided by a separate optical fiber originating from the respective laser system (see Fig. 3). The two imaging beams are superimposed using a dichroic mirror and expanded by a telescope to a $1/e^2$-diameter of 27.5 mm. The imaging beams have low intensity ($I_{\text{img}} \sim 0.01 I_{\text{sat}}$ in the beam center), are circularly polarized and pass through the MOT along the horizontal direction, perpendicular to the axis of the quadrupole magnetic field of the MOT. No bias magnetic field is applied when absorption pictures are taken. The best atom number estimate from the measured absorption pictures is thus given by using an averaged squared Clebsch-Gordan coefficient, which is $C^2 = 0.5$ for ^{6}Li and $C^2 = 0.4$ for ^{40}K. Both beams are red detuned by $2\ \Gamma$ from the $4S_{1/2}(F = 9/2) \rightarrow 4P_{3/2}(F' = 11/2)$ and the $2S_{1/2}(F = 3/2) \rightarrow 2P_{3/2}(F' = 5/2)$ cooling transitions of ^{40}K and ^{6}Li, respectively (see Fig. 2), so as to reduce saturation effects. For the chosen length of the imaging pulses (100 μs) no repumping is required during the imaging process (we verified for ^{6}Li that even in the case of a resonant imaging beam, the presence of a repumping beam would yield an increase of the detected atom number of only 8%, which would be even less for ^{40}K). In order to image the total number of atoms in the MOTs the atom clouds are exposed for 500 μs to only the repumping light before the image is taken in order to optically pump all atoms to the hyperfine ground state which is imaged. The overall uncertainty of the absolute atom number determination is estimated to be 50%.

4.4 Experimental results

In single-species operation we characterized the MOTs using the parameters for the optimized dual-species operation. We determined the atom numbers, the atomic densities in the cloud center, the loading times and the temperatures. Furthermore, we studied for each atomic species the dependence of the steady-state MOT atom number on the following parameters: the power and detuning of the cooling light and the intensity ratio between the repumping and cooling light. In dual-species operation, we studied the dependence of heteronuclear light-induced cold collisions on the laser power used for the MOT-beams. The optimum parameters, which lead to atom numbers of $N_{\text{single}} \sim 8.9 \times 10^9$ in the ^{40}K-MOT and $N_{\text{single}} \sim 5.4 \times 10^9$ in the ^{6}Li-MOT, are displayed in Table 3 together with the characteristics of the MOTs (in dual-species operation, the atom numbers only slightly change due to the additional interspecies collisions to $N_{\text{dual}} \sim 8.0 \times 10^9$ in the ^{40}K-MOT and $N_{\text{dual}} \sim 5.2 \times 10^9$ in the ^{6}Li-MOT). The $(1 - 1/e)$-loading times of the MOTs are $\sim$5 s for ^{40}K and $\sim$6 s for ^{6}Li.

Magneto-optical traps with large atom numbers have a high optical density and are optically dense for weak resonant laser beams. Therefore, when determining the atom number via absorption imaging, the frequency of the imaging beam has to be detuned, so not to "black out" the image.

Figures 11a, 11b depict the *detected* atom number of the two MOTs (circles) as a function of the detuning of the imaging beam. The detected atom number was derived from the measured optical density assuming the imaging beam to be resonant. The curves are expected to have the shape of a Lorentzian with the peak centered around zero detuning. The experimental data shown in

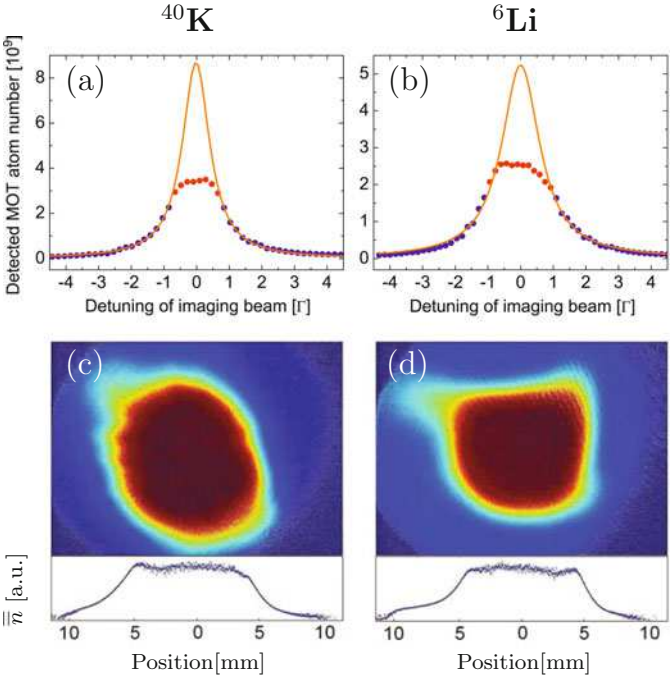


Fig. 11. (Color online) (a), (b) Detected atom number in the MOTs as a function of the detuning of the imaging beams. Circles correspond to the experimental data and solid curves to Lorentzian fits of the curve wings with an imposed width, which was determined by another measurement. (c), (d) Absorption images of the MOTs and the doubly-integrated optical density profile $\overline{\overline{n}}$, recorded with a resonant imaging beam. The graphs (a, c) relate to the ^{40}K-MOT and (b), (d) to the ^{6}Li-MOT. The flat top of $\overline{\overline{n}}$ in the graphs (c), (d) and the saturation of the detected atom number for small magnitudes of the detuning in the graphs (a), (b) demonstrate that the MOTs are optically dense for the imaging beam when the detuning is small. Their (extrapolated) central optical densities for a resonant imaging beam are ∼20 for ^{40}K and ∼15 for ^{6}Li.

Figures 11a, 11b clearly deviate from a Lorentzian behavior – they saturate for small magnitudes of the detuning. This deviation demonstrates that the MOTs are optically dense for small detunings. A correct estimate of the atom number is obtained from an extrapolation of the experimental data to zero detuning based on a Lorentzian fit of the curve wings (solid curves). A reliable extrapolation, however, requires imposing the width of the Lorentzian fit. In order to determine this width, an additional experiment was done (not shown): the data in Figures 11a, 11b were again recorded and fitted by a Lorentzian for a MOT with a small atom number and a low optical density (obtained by a short loading of 250 ms). The widths found by this additional measurement were 1.05 Γ for ^{40}K and 1.5 Γ for ^{6}Li. For ^{40}K this width corresponds to the natural linewidth of the exited state addressed by the imaging transition. For ^{6}Li the width is larger than the natural linewidth, since the small excited hyperfine structure is unresolved and thus its width (∼0.5 Γ) and the natural linewidth add up (this line broadening does not occur when a bias magnetic field is applied and a closed transition is used for imaging). The peak values of the Lorentzian fits in Figures 11a, 11b finally yield the atom numbers in the MOTs, given in Table 3.

Figures 11c, 11d show images of the MOTs and their doubly-integrated optical density profiles $\overline{\overline{n}}$ for the case of a resonant imaging beam. The flat top of $\overline{\overline{n}}$ as a function of position shows that the MOTs are optically dense. Their central optical densities for the resonant imaging beam are determined to be ∼20 for ^{40}K and ∼15 for ^{6}Li by the extrapolation technique described above. In addition, the density profiles in Figures 11c, 11d show that the MOTs have spatial extensions of the order of 1 cm.

The atomic density in the MOT center is extracted from the recorded two-dimensional density profile as follows. The recorded profile is proportional to the atomic density $n(x, y, z)$ integrated along the imaging beam direction z: $g(x, y) \propto \int n(x, y, z)dz$. When assuming that the MOT has cylindrical symmetry (with the symmetry axis along the x-direction), the local atomic density n_c at the MOT center is given by the maximum of the inverse Abel transform of $g(x_c, y)$, where x_c is the x-coordinate of the MOT center

$$n_c = \max_r \left(-\frac{1}{\pi} \int_r^\infty \left(\frac{\partial g(x_c, y)}{\partial y} \right) \frac{dy}{\sqrt{y^2 - r^2}} \right), \qquad (12)$$

with $r = \sqrt{y^2 + z^2}$ denoting the distance to the MOT center [38]. Since the derivative $\partial g/\partial y$ is very sensitive to noise, the density profile g is smoothened before its derivative is calculated. We obtain $n_c^K \sim 3\times10^{10}$ atoms/cm^3 and $n_c^{Li} \sim 2 \times 10^{10}$ atoms/cm^3, respectively.

The temperature of the MOTs in single-species operation was determined by the time-of-flight method [24]. The ^{40}K-MOT has a temperature of 290 μK and the ^{6}Li-MOT of 1.4 mK. Both temperatures are higher than the Doppler cooling limit, because of the high intensity in the MOT beams. In addition, for ^{6}Li, the unresolved excited hyperfine structure (see Fig. 2) inhibits sub-Doppler cooling effects. The same temperatures are found in dual-species operation. The measured temperatures and atomic densities yield the peak phase space densities $D_K = n_c^K \Lambda_K^3 \sim 1.2\times10^{-7}$ and $D_{Li} = n_c^{Li} \Lambda_{Li}^3 \sim 1.3\times10^{-7}$ with the thermal de Broglie wavelength $\Lambda = \sqrt{2\pi\hbar^2/(mk_BT)}$, respectively.

The dependence of the MOT atom number on the detuning of the cooling light is depicted in Figures 12a, 12b. The atom number is maximum at $\Delta\omega_{cool}^K = -3\ \Gamma$ for ^{40}K and at $\Delta\omega_{cool}^{Li} = -5\ \Gamma$ for ^{6}Li, and has a FWHM of 2.3 Γ and 4.1 Γ, respectively.

Figures 12c, 12d show the dependence of the MOT atom number on the power of the cooling light per MOT beam. In the figures, a power of 10 mW corresponds to an on-resonance peak intensity of ∼3 I_{sat} (Fig. 12c) and ∼2 I_{sat} (Fig. 12d) in each of the six MOT beams. The atom number increases with increasing light power and saturates for higher powers. The saturation is due to several effects. First, the absorption probability for the cooling light saturates for high intensities. Second, the repulsive forces between the atoms due to rescattered photons and the temperature of the cloud increase with increasing light

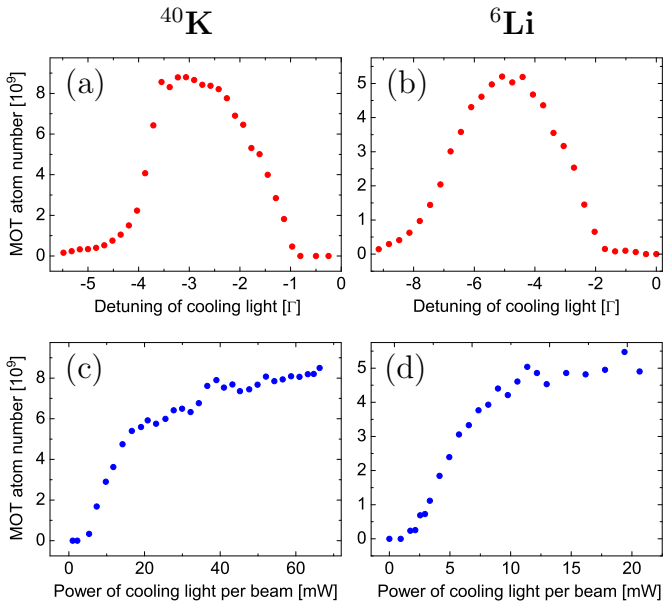


Fig. 12. (Color online) MOT atom number as a function of (a), (b) the detuning and (c), (d) the power of the cooling light per MOT beam for a constant intensity ratio between the cooling and repumping light. The graphs (a), (c) relate to the ^{40}K-MOT and (b), (d) to the ^{6}Li-MOT. For ^{40}K a power of 45 mW corresponds to an intensity of 13 I_{sat}, for ^{6}Li a power of 20 mW corresponds to an intensity of 4 I_{sat}, with the respective saturation intensities I_{sat} given in Table 3.

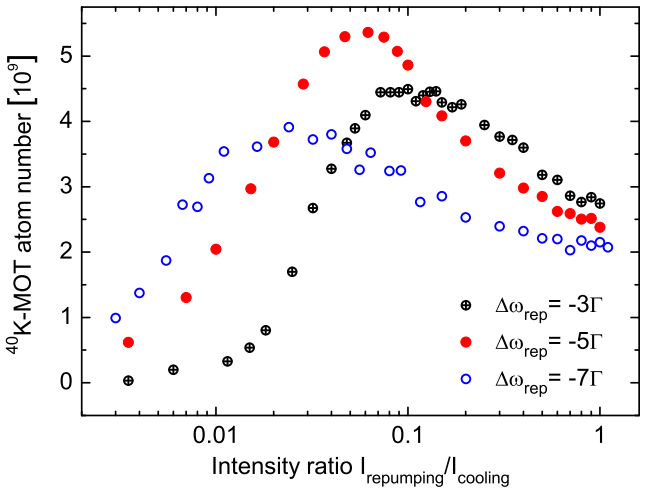


Fig. 13. (Color online) ^{40}K-MOT atom number as a function of the intensity ratio between repumping and cooling light for three different repumping detunings $\Delta\omega_{\mathrm{rep}}$ and a constant cooling light power of 18 mW per MOT beam (which corresponds to an intensity of 6 I_{sat}).

power [32]. Finally the scattering rate for light-induced cold collisions increases with increasing light power.

Figure 13 shows the dependence of the ^{40}K-MOT atom number on the intensity ratio $I_{\mathrm{rep}}/I_{\mathrm{cool}}$ between repumping and cooling light for three different repumping detunings $\Delta\omega_{\mathrm{rep}}^{(1)} = -3\ \Gamma$, $\Delta\omega_{\mathrm{rep}}^{(2)} = -5\ \Gamma$ and $\Delta\omega_{\mathrm{rep}}^{(3)} = -7\ \Gamma$ and a constant cooling light power of 18 mW per MOT beam. The curves have a maximum at different ratios $I_{\mathrm{rep}}/I_{\mathrm{cool}}$, the position of the maxima lying at higher ratios for lower detunings. Furthermore, the maxima have different values for the three curves. The maximum is biggest for the detuning $\Delta\omega_{\mathrm{rep}}^{(2)} = -5\ \Gamma$. The shape of the curves can be understood as follows. Each curve increases between $I_{\mathrm{rep}}/I_{\mathrm{cool}} = 0$ and the position of the maximum, because the transition probability of the repumping transition increases with increasing repumping intensity. Thus the atoms are more efficiently cooled by the cooling light, as they are more efficiently repumped into the cycling transition. However, when the intensity of the repumping light becomes too large, the curve decreases again. Then, due to the strong repumping, the atoms are exposed to the more intense near-resonant cooling light, which causes light-induced cold collisions, leading to trap loss. At the maximum, the repumping is sufficiently strong to allow for an efficient cooling, and it is sufficiently weak to preserve the atoms from cold collisions induced by the strong cooling light. The value of the curve maximum is biggest for the detuning $\Delta\omega_{\mathrm{rep}}^{(2)} = -5\ \Gamma$. It is situated at $I_{\mathrm{rep}}/I_{\mathrm{cool}} \sim 1/20$, for which, as one can see below, only ~20% of the ^{40}K-MOT atoms occupy the cooling cycle states $F = 9/2$ or $F' = 11/2$ (see Fig. 14), the others occupying the "dark" hyperfine ground state $F = 7/2$.

For very small intensity ratios $I_{\mathrm{rep}}/I_{\mathrm{cool}} \leq 0.01$ the atom number in the ^{40}K-MOT is larger for higher repumping detunings (Fig. 13). This behavior might be a consequence of the fact that the ^{40}K-MOT is loaded from a slow atomic beam. The beam atoms, which have a negative Doppler shift of more than 5 Γ with respect to the counter-propagating MOT beams, might absorb the repumping light more likely when it has a higher detuning.

Figure 14 shows the fraction of atoms in the ^{40}K-MOT (circles) which populate the states $F = 9/2$ or $F' = 11/2$ (i.e. the cooling cycle states, see Fig. 2) as a function of the intensity ratio $I_{\mathrm{rep}}/I_{\mathrm{cool}}$ between repumping and cooling light. In the experiment, the cooling light power was fixed to 18 mW per MOT beam, and the repumping detuning was $\Delta\omega_{\mathrm{rep}} = -5\ \Gamma$. The graph was recorded as follows. The absolute population of the states $F = 9/2$ and $F' = 11/2$ was measured by simultaneously switching off both the repumping and cooling light of the ^{40}K-MOT 600 μs before taking the image (with the imaging beam being near-resonant with the $F = 9/2 \rightarrow F' = 11/2$-transition). During the 600 μs time delay, all excited atoms relax to one of the ground states. For the used detunings and intensities of the MOT-beams ~90% of the excited atoms occupy the state $F' = 11/2$ and thus relax to the ground state $F = 9/2$, which is imaged. Therefore, the image approximately yields the sum of the populations of the states $F = 9/2$ and $F' = 11/2$. The total population of all states (i.e. the total number of trapped atoms) was measured as described in the previous paragraph.

The curve in Figure 14 is increasing with increasing ratios $I_{\mathrm{rep}}/I_{\mathrm{cool}}$ and it saturates for high ratios. For the ratio $I_{\mathrm{rep}}/I_{\mathrm{cool}} = 1/5$ about 60% of the ^{40}K-MOT atoms occupy the cooling cycle states. For this ratio the fluorescence

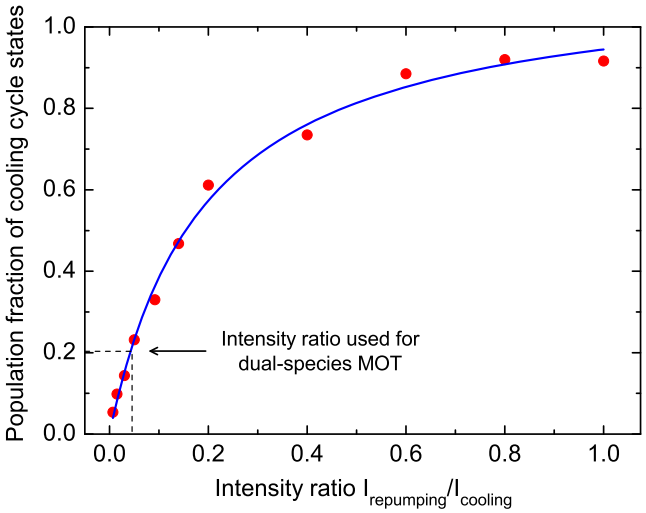


Fig. 14. (Color online) Circles: measured fraction of atoms in the ^{40}K-MOT populating the states $F = 9/2$ or $F' = 11/2$ (cooling cycle states) as a function of the intensity ratio between repumping and cooling light for the repumping detuning $\Delta\omega_{\rm rep} = -5\ \Gamma$ and a constant cooling light power of 18 mW per MOT beam (which corresponds to an intensity of $6\,I_{\rm sat}$). For the ratio which maximizes the total atom number in the ^{40}K-MOT, $I_{\rm rep}/I_{\rm cool} \sim 1/20$, only 20% of the trapped atoms occupy the cooling cycle states. Solid curve: a fit based on Einstein's rate equations.

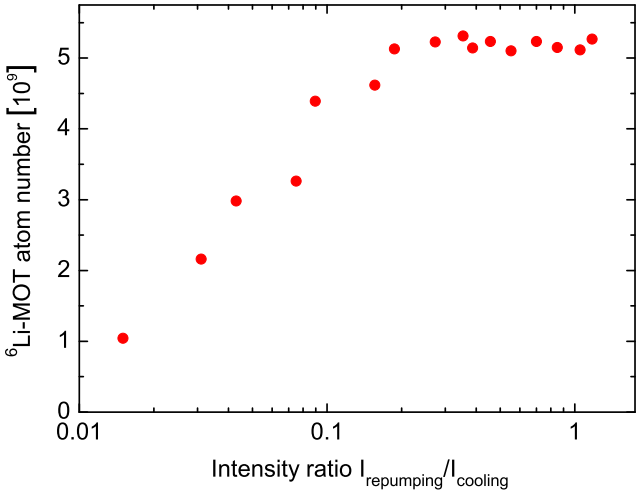


Fig. 15. (Color online) ^{6}Li-MOT atom number as a function of the intensity ratio between repumping and cooling light for a constant cooling light power of 11 mW per MOT beam (which corresponds to an intensity of 2 $I_{\rm sat}$). In comparison to ^{40}K (Fig. 13), the optimum atom number requires a larger intensity in the repumping light, which is a consequence of the unresolved excited hyperfine structure of ^{6}Li.

emitted by the ^{40}K-MOT is found to be maximum. For the ratio $I_{\rm rep}/I_{\rm cool} = 1/20$, which is used in the experiment, only ∼20% of the atoms occupy the cooling cycle states. Atom losses due to light-induced collisions are thus minimized.

The solid curve in Figure 14 shows a fit of the experimental data, based on a simple model, assuming ^{40}K to be a four-level atom (with the states $F = 9/2$, $F = 7/2$, $F' = 11/2$ and $F' = 9/2$). Einstein's rate equations yield that the curve obeys the law $P_{\rm ccs} = 1/(1 + a + b/(I_{\rm rep}/I_{\rm cool}))$, with the fitting parameters $a = -0.11$ and $b = 0.17$, which depend on the transition probabilities and the used intensities and detunings.

Figure 15 shows the dependence of the ^{6}Li-MOT atom number on the intensity ratio $I_{\rm rep}/I_{\rm cool}$ between repumping and cooling light for the repumping detuning $\Delta\omega_{\rm rep} = -3\ \Gamma$ and a constant cooling light power of 11 mW per MOT beam. In contrast to Figure 13, the curve does not have a maximum but rather increases with increasing $I_{\rm rep}/I_{\rm cool}$ and saturates. This behavior is a result of the important contribution of the repumping light to the cooling process, particular to ^{6}Li, as it has an unresolved excited state hyperfine structure.

In a dual-species MOT, inelastic collisions between atoms of the two different species can occur and represent important loss mechanisms. Previous studies have shown that the principal loss mechanisms for heteronuclear collisions in dual-species MOTs involve one ground-state and one excited atom of different species [35,36]. Such atom pairs can undergo radiative escape or fine-structure changing collisions [39]. Both these loss processes require the two atoms to approach each other sufficiently close such that a large enough interaction energy is gained to make the atoms leave the trap. The long-range behavior of the scattering potentials determines if the atoms can approach each other sufficiently. For LiK, the scattering potentials for a singly-excited heteronuclear atom pair are all attractive for the case where the K atom is excited and all repulsive for the case where the Li atom is excited [40]. As a consequence, a ground-state K atom and an excited Li atom repel each other and are prevented from undergoing inelastic collisions (optical shielding). Inelastic collisions involving singly-excited heteronuclear atom pairs thus always contain an excited K atom. In order to minimize the rate of heteronuclear collisions in the LiK-MOT, the density of excited K atoms must therefore be reduced. Furthermore, the atomic density in the trap as well as the relative speed of the colliding atoms, i.e. the temperature of the cloud, need to be minimized.

In our ^{6}Li-^{40}K dual-species MOT the following strategy is applied in order to minimize inelastic heteronuclear collisions. First the use of very low magnetic field gradients (8 G/cm), which decreases the atomic densities ($n_{\rm c}^{\rm K} \sim 3{\times}10^{10}$ atoms/cm^3 and $n_{\rm c}^{\rm Li} \sim 2{\times}10^{10}$ atoms/cm^3). Second, low intensities in the repumping light for both, ^{6}Li and ^{40}K, are used in order to decrease the number of excited atoms. Decreasing the number of excited ^{6}Li atoms here a priori serves to decrease the temperature of the ^{6}Li-cloud. Since that is much larger than the temperature of the ^{40}K-cloud, the relative speed of two colliding atoms and thus the collision rate can be efficiently decreased by minimizing the temperature of the ^{6}Li-cloud. Finally a small mutual influence of the MOTs is obtained: the atom numbers in the MOTs decrease by ∼4% in the

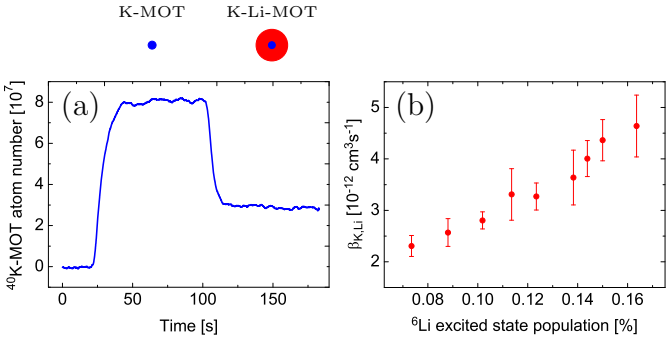


Fig. 16. (Color online) (a) Evolution of the atom number in the ^{40}K-MOT in the absence ($t < 100$ s) and presence ($t > 100$ s) of the ^{6}Li-MOT for an increased magnetic field gradient of 16 G/cm. (b) Trap loss coefficient β_{KLi} for heteronuclear collisions as a function of the relative excited state population of the trapped ^{6}Li atoms.

^{6}Li-MOT and ∼10% in the ^{40}K-MOT due to the presence of the other species.

The importance of decreasing the magnetic field gradients in order to minimize the heteronuclear collision rate in the dual-species MOT is demonstrated in Figure 16a, which depicts the effect of the ^{6}Li-MOT on the ^{40}K-MOT atom number when a two-times larger magnetic field gradient (16 G/cm) is used. At this gradient the atomic density in the ^{6}Li-MOT is by a factor of 4 larger than at the gradient used for the optimized MOT. In the experiment, the ^{40}K-MOT was intentionally reduced in size (by decreasing the 2D-MOT flux) to ensure a better inclosure in the ^{6}Li-MOT. The curve shows that ∼65% of the ^{40}K-MOT atoms leave the trap due to the enhanced heteronuclear collisions. Using a low magnetic field gradient is therefore helping significantly to decrease the heteronuclear collisions.

In the following we determine the trap loss coefficients for the (optimized) dual-species MOT in order to quantify the heteronuclear collisions. The rate equation for the atom number in a dual-species MOT (with species A and B) reads [35]

$$\frac{dN_{\mathrm{A}}}{dt} = L_{\mathrm{A}} - \gamma N_{\mathrm{A}} - \beta_{\mathrm{AA}} \int n_{\mathrm{A}}^2 dV - \beta_{\mathrm{AB}} \int n_{\mathrm{A}} n_{\mathrm{B}} dV, \quad (13)$$

where L_{A} is the loading rate, γ the trap loss rate due to collisions with background gas atoms and $n_{\mathrm{A}}, n_{\mathrm{B}}$ the local atomic densities. β_{AA} and β_{AB} denote the cold collision trap loss coefficients for homo- and heteronuclear collisions, respectively. L_{A} and γ are determined from the loading and decay curves of the single-species MOTs. The obtained values for L_{A} are given in Table 3 and γ is found to be 1/7.5 s^{-1}. The homonuclear trap loss coefficients β_{AA} are determined from the steady state atom numbers in single-species operation using the measured density profiles. For the experimental conditions indicated in Table 3, we obtain

$$\beta_{\mathrm{LiLi}} = (8 \pm 4) \times 10^{-12}\,\mathrm{cm}^3\ \mathrm{s}^{-1}, \quad (14)$$

$$\beta_{\mathrm{KK}} = (6 \pm 3) \times 10^{-13}\,\mathrm{cm}^3\ \mathrm{s}^{-1}. \quad (15)$$

The determination of the heteronuclear trap loss coefficients β_{AB} for the optimized dual-species configuration would require the knowledge of the mutual overlap of the MOTs, which is difficult to estimate when absorption images are taken only along one direction. We therefore choose a configuration, which makes the determination of β_{AB} less dependent on assumptions about the mutual overlap (but which does not change the value of β_{AB}). We reduce the atom flux of species A, in order to decrease the spatial extension of the trapped cloud of species A and to place it in the center of the cloud of species B. A video camera which records the fluorescence of the MOTs from a different direction than that of the absorption imaging verifies that this configuration is indeed achieved. Then, in equation (13) it is $\int n_{\mathrm{A}} n_{\mathrm{B}} dV \sim n_{\mathrm{c}}^{\mathrm{B}} N_{\mathrm{A}}$. Comparing the steady-state atom numbers for the different configurations then yields

$$\beta_{\mathrm{LiK}} = (1 \pm 0.5) \times 10^{-12}\,\mathrm{cm}^3\ \mathrm{s}^{-1}, \quad (16)$$

$$\beta_{\mathrm{KLi}} = (3 \pm 1.5) \times 10^{-12}\,\mathrm{cm}^3\ \mathrm{s}^{-1}, \quad (17)$$

for the experimental conditions indicated in Table 3. Comparing all four trap loss coefficients, the dominant is β_{LiLi} (Eq. (14)) for light-induced homonuclear ^{6}Li-^{6}Li collisions. This is a consequence of the large temperature of the ^{6}Li-MOT and the unresolved hyperfine structure of ^{6}Li which prohibits the creation of a dark MOT, leading to a large excited state population. The much smaller homonuclear trap loss coefficient β_{KK} for ^{40}K (Eq. (15)) is consistent with Figure 13 which shows that, for ^{40}K, small repumping intensities are favorable. The heteronuclear trap loss coefficients $\beta_{\mathrm{LiK}}, \beta_{\mathrm{KLi}}$ (Eqs. (16) and (17)) are also much smaller than β_{LiLi}, indicating that our applied strategy for decreasing the heteronuclear collisions is good. In the Amsterdam group the heteronuclear trap loss coefficients were found by a factor of about 2 larger than ours [15]. A dark SPOT MOT has been implemented in order to reduce the excited state population of the ^{40}K atoms. In the next paragraph we show, however, that it is also important to reduce the excited state population of the ^{6}Li atoms.

Figure 16b depicts the dependence of the trap loss coefficient β_{KLi} on the relative excited state population of the ^{6}Li atoms. The graph was obtained by recording the influence of the ^{6}Li-MOT on the ^{40}K-MOT as the power of the ^{6}Li-MOT beams was varied. For each power it was verified that the ^{40}K-MOT was placed in the center of the ^{6}Li-MOT and the atomic density of the ^{6}Li-MOT was recorded. In the experiment a magnetic field gradient of 16 G/cm was used. The central atomic density of the ^{6}Li-MOT was found to be approximately constant, when the power was varied ($n_{\mathrm{c}}^{\mathrm{Li}} \sim 8 \times 10^{10}$ atoms/cm^3). The relative excited state population for a given beam power was estimated using Einstein's rate equations. In addition the variation of the excited state population was measured by recording the fluorescence emitted by the ^{6}Li-MOT and by measuring the number of captured atoms. The latter changed by a factor of 1.5 in the considered range of beam powers. The graph in Figure 16b shows that the trap loss coefficient increases by more than a factor of 2

as the relative excited state population is increased from ∼7% to ∼16%. The error bars shown in the figure refer to statistical errors. The uncertainty due to systematic errors is estimated to be 50%. The significant increase of β_{KLi} demonstrates the importance of minimizing the number of excited ^{6}Li atoms (and not only that of the excited ^{40}K atoms). One reason for this increase is the increase of temperature of the ^{6}Li-MOT, which changes from ∼1 mK to ∼1.6 mK when the beam power is increased. Another reason could be the occurence of collisions involving doubly-excited Li*K* atom pairs, the rate of which increases with the excited state populations. The scattering potentials for these collisions are known to be of a long-range, as they scale with the internuclear separation as $1/R^5$ [41], whereas they scale as $1/R^6$ for collisions involving a singly-excited heteronuclear atom pair [33].

5 Conclusions

We have produced a dual-species magneto-optical trap for fermionic ^{6}Li and ^{40}K with large atom numbers. Two strategies have been applied in order to achieve this result. First, the dual-species MOT is placed in an ultra-high vacuum environment, being continuously loaded from cold atomic beams. The atomic beams originate from separate atom sources – a Zeeman slower for ^{6}Li and a 2D-MOT for ^{40}K – which both yield a large flux of cold atoms. Second, the homo- and heteronuclear collisions have been minimized by using small magnetic field gradients and low light powers in the repumping light. The atom loss in each MOT due to the presence of the other species decreases by only 4% (^{6}Li) and 10% (^{40}K) due to the heteronuclear collisions.

We have given a detailed description of the implemented apparatus, which we hope serves as a guideline for the construction of next generation experiments with fermionic ^{6}Li and ^{40}K.

The produced dual-species MOT represents the starting point for the production of a large-atom number quantum degenerate Fermi-Fermi mixture. The atoms trapped in the dual-species MOT have already been transferred into the magnetic trap and magnetically transported to the science chamber with large optical access and low background pressure. The large depth of magnetic traps as compared to optical traps allows for a large transfer efficiency, leading to smaller losses of atoms. In the science cell, the dual-species cloud will be evaporatively cooled in a plugged magnetic trap to quantum degeneracy and then transferred into an optical trap for investigation.

The authors acknowledge support from ESF Euroquam (FerMix), SCALA, ANR FABIOLA, Région Ile de France (IFRAF), ERC Ferlodim and Institut Universitaire de France. A.R. acknowledges funding from the German Federal Ministry of Education and Research and D.R.F. from Fundação para a Ciência e Tecnologia (FCT) through grant SFRH/BD/68488/2010 and from Fundação Calouste Gulbenkian.

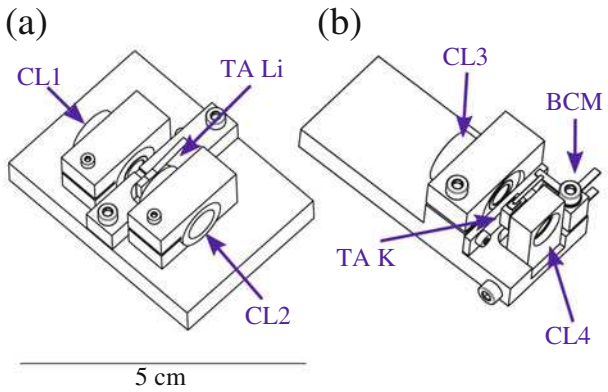


Fig. 17. (Color online) Sketch of the tapered amplifier supports for (a) Li and (b) K. In the figure, TA Li and TA K refer to the respective tapered amplifier chips, CL1, CL2, CL3 and CL4 to the (only longitudinally adjustable) collimation lens supports and BCM to the isolated mount for the blade connectors used to power the chip for K. The supports for the output collimation lenses are CL2 and CL4.

Appendix: Tapered amplifier mounts

We developed compact support designs for our tapered amplifier chips, in order to minimize the costs of the laser sources of our experimental setup. The TAs are commercial semiconductor chips which are mounted on homemade compact mechanical supports with nearly no adjustable parts. The support designs allow for an easy installation process, which does not require any gluing or the help of micrometric translation stages for the alignment of the collimation optics, as that can be accomplished by free hand. Furthermore, the design minimizes the heat capacity of the support and the produced temperature gradients, allowing for a quick temperature stabilization that makes the TAs quickly operational after switch-on. The temperature stabilization is accomplished using a Peltier element (Roithner Lasertechnik GmbH, ref. TEC1-12705T125) connected to a PID control circuit. The heat of(the chip is dissipated via an aluminum base plate which is economically cooled by air rather than running water (the base plate reaches a maximum temperature of 28 °C for diode currents of 2 A).

The commercial TA chips are sold on small heat sinks which have different dimensions for the two different wavelengths. We thus had to design slightly different supports for the Li- and K-TAs, which are both schematically shown in Figure 17.

For lithium the semiconductor chip (Toptica, ref. TA-670-0500-5) is delivered on a heat dissipation mount of type "I". It is placed between two axially aligned cylindrical lens tubes (CL1 and CL2 in Fig. 17a), each of which containing an aspheric collimation lens of focal length 4.5 mm (Thorlabs, ref. C230TME-B). The support of the tubes and the chip are precisely machined such that the chip's output beam falls on the center of the respective collimation lens (CL2 in Fig. 17a). The tubes are supported by cylindrically holed tightenable hinges in which

they can move only longitudinally, along the direction of the amplified laser beam. This restriction of the tube's motion facilitates the alignment of the collimation lenses. The support design does not allow for a transverse alignment of the collimation lenses. Since this alignment is not very critical for the performance of the TA, we found it needless to allow this degree of freedom and relied on precise machining (possible imperfections could be compensated utilizing the mechanical play of the large attachment screw holes of the commercial heat sinks of the chips). When tightened by a screw, the hinges fix the position of the tubes. Since the tightening applies a force perpendicular to the longitudinal direction, it does not move the tubes along this (critical) direction. They might only move slightly along the transverse direction, which does not affect the final performance of the TA.

For potassium, the semiconductor chip (Eagleyard, ref. EYP-TPA-0765-01500-3006-CMT03-0000) is delivered on a heat dissipation mount of type "C". Placing this mount between two hinges as for the case of lithium is less convenient since the heat dissipation mount has to be attached by a screw in the longitudinal direction which requires access from one side. Therefore one hinge is replaced by a rail which guides a parallelepipedically formed mount for the second (output) collimation lens (CL4 in Fig. 17b). The motion of this mount is also fixed by tightening a screw applying forces perpendicular to the rail direction, which does not move the collimation lens along the critical longitudinal direction. For all our TAs, the positioning of the collimation lenses never had to be adjusted again once they were aligned.

The commercial heat dissipation mount of the potassium chip is inconvenient for a simple powering of the chip. The very fragile gold wire, which has to be connected to the negative source of the current supply, has to be protected by a mechanical support before being connected to a cable. Therefore we soldered it to a blade connector that is fixed by an isolated plastic mount (BCM Fig. 17b) and which is connected to the current supply. To avoid an overheating of the chip during the soldering process we permanently cooled the gold wire by blowing cold dry air from a spray can on it.

The output beams of the TA chips are astigmatic and thus require additional collimation. The choice of the collimation optics needs to be adapted to the specifications of the subsequent optical fiber, which in our case requests a collimated circular Gaussian beam of 2.2 mm $1/e^2$-diameter for optimum coupling efficiency. The mode-matching was found optimum for a pair of lenses consisting of one spherical lens (with $f = 15$ cm for Li and $f = 4$ cm for K) and a cylindrical lens (with $f = 8$ cm for Li and $f = 2.54$ cm for K), which are placed outside the TA's housing. The cylindrical lenses are supported by rotatable mounts, in order to facilitate the mode-matching into the fibers. For all our TAs we achieve fiber-coupling efficiencies larger than 50% (Li) and 60% (K).

When injected with 20 mW, the Li-TAs yield an output power of 500 mW at 1 A driving current and the K-TAs yield an output power of 1500 mW at 2.5 A driving current. In order to increase the lifetime of the chips, we limit the driving currents to smaller values and we switch the chips on only for periods of experimentation. When switched on, the TAs quickly reach a stable functioning (usually within 10 min) due to the compactness of the mechanical support, which allows for a quick temperature stabilization.

References

1. *Proceedings of the International School of Physics Enrico Fermi on Ultracold Fermi Gases*, edited by M. Inguscio, W. Ketterle, C. Salomon (Societa Italiana di Fisica, Bologna, Italy, 2006)
2. S. Giorgini, L.P. Pitaevskii, S. Stringari, Rev. Mod. Phys. **80**, 1215 (2008)
3. R.P. Feynman, Int. J. Theor. Phys. **21**, 467 (1982)
4. A.F. Ho, M.A. Cazalilla, T. Giamarchi, Phys. Rev. A **79**, 033620 (2009)
5. D.S. Petrov, G.E. Astrakharchik, D.J. Papoular, C. Salomon, G.V. Shlyapnikov, Phys. Rev. Lett. **99**, 130407 (2007)
6. M.M. Forbes, E. Gubankova, W.V. Liu, F. Wilczek, Phys. Rev. Lett. **94**, 017001 (2005)
7. J. Levinsen, T.G. Tiecke, J.T.M. Walraven, D.S. Petrov, Phys. Rev. Lett. **103**, 153202 (2009)
8. J. Deiglmayr, A. Grochola, M. Repp, K. Mörtlbauer, C. Glück, J. Lange, O. Dulieu, R. Wester, M. Weidemüller, Phys. Rev. Lett. **101**, 133004 (2008)
9. K.-K. Ni, S. Ospelkaus, M.H.G. de Miranda, A. Péer, B. Neyenhuis, J.J. Zirbel, S. Kotochigova, P.S. Julienne, D.S. Jin, J. Ye, to be published
10. M. Aymar, O. Dulieu, J. Chem. Phys. **122**, 204302 (2005)
11. T.G. Tiecke, M.R. Goosen, A. Ludewig, S.D. Gensemer, S. Kraft, S.J.J.M.F. Kokkelmans, J.T.M. Walraven, Phys. Rev. Lett. **104**, 053202 (2010)
12. A. Ridinger, S. Chaudhuri, T. Salez, N. Bouloufa, L. Pruvost, O. Dulieu, F. Chevy, C. Salomon, to be published
13. M. Taglieber, A.-C. Voigt, F. Henkel, S. Fray, T.W. Hänsch, K. Dieckmann, Phys. Rev. A **73**, 011402 (2006)
14. F.M. Spiegelhalder, A. Trenkwalder, D. Naik, G. Kerner, E. Wille, G. Hendl, F. Schreck, R. Grimm, Phys. Rev. A **81**, 043637 (2010)
15. T. Tiecke, Ph.D. thesis, University of Amsterdam, 2009
16. M. Greiner, I. Bloch, T.W. Hänsch, T. Esslinger, Phys. Rev. A **63**, 031401 (2001)
17. U. Eismann, F. Gerbier, C. Canalias, G. Trénec, J. Vigué, F. Chevy, C. Salomon, to be published
18. K.A. Yakimovich, A.G. Mozgovoi, High Temp. **38**, 657 (2000)
19. G. Ferrari, M.-O. Mewes, F. Schreck, C. Salomon, Opt. Lett. **24**, 151 (1999)
20. M.-O. Mewes, G. Ferrari, F. Schreck, A. Sinatra, C. Salomon, Phys. Rev. A **61**, 011403 (1999)
21. Z. Hadzibabic, S. Gupta, C.A. Stan, C.H. Schunck, M.W. Zwierlein, K. Dieckmann, W. Ketterle, Phys. Rev. Lett. **91**, 160401 (2003)
22. T.G. Tiecke, S.D. Gensemer, A. Ludewig, J.T.M. Walraven, Phys. Rev. A **80**, 013409 (2009)

23. W.D. Phillips, H. Metcalf, Phys. Rev. Lett. **48**, 596 (1982)
24. H.J. Metcalf, P. van der Straten, *Laser cooling and trapping* (Springer, Berlin, 1999)
25. A. Joffe, W. Ketterle, A. Martin, D.E. Pritchard, J. Opt. Soc. Am. B **10**, 2257 (1993)
26. N.F. Ramsey, *Molecular Beams* (Oxford University Press, Oxford, 1986)
27. C.B. Alcock, V.P. Itkin, M.K. Horrigan, Can. Metall. Quart. **23**, 309 (1984)
28. K. Dieckmann, R.J.C. Spreeuw, M. Weidemüller, J.T.M. Walraven, Phys. Rev. A **58**, 3891 (1998)
29. J. Schoser, A. Batär, R. Löw, V. Schweikhard, A. Grabowski, Yu.B. Ovchinnikov, T. Pfau, Phys. Rev. A **66**, 023410 (2002)
30. J. Catani, P. Maioli, L. De Sarlo, F. Minardi, M. Inguscio, Phys. Rev. A **73**, 033415 (2006)
31. S. Chaudhuri, S. Roy, C.S. Unnikrishnan, Phys. Rev. A **74**, 023406 (2006)
32. A.M. Steane, M. Chowdhury, C.J. Foot, J. Opt. Soc. Am. B **9**, 2142 (1992)
33. A. Derevianko, W.R. Johnson, M.S. Safronova, J.F. Babb, Phys. Rev. Lett. **82**, 3589 (2002)
34. M.S. Santos, P. Nussenzveig, L.G. Marcassa, K. Helmerson, J. Flemming, S.C. Zilio, V.S. Bagnato, Phys. Rev. A **52**, R4340 (1995)
35. U. Schlöder, H. Engler, U. Schünemann, R. Grimm, M. Weidemüller, Eur. Phys. J. D **7**, 331 (1999)
36. G.D. Telles, W. Garcia, L.G. Marcassa, V.S. Bagnato, D. Ciampini, M. Fazzi, J.H. Müller, D. Wilkowski, E. Arimondo, Phys. Rev. A **63**, 033406 (2001)
37. J. Goldwin, S.B. Papp, B. DeMarco, D.S. Jin, Phys. Rev. A **65**, 021402 (2002)
38. V. Dribinski, A. Ossadtchi, V.A. Mandelshtam, H. Reisler, Rev. Sci. Instrum. **73**, 2634 (2002)
39. M. Weidemüller, C. Zimmermann, *Interactions in Ultracold Gases* (Wiley-VCH, Weinheim, 2003)
40. B. Bussery, Y. Achkar, M. Aubert-Frécon, Chem. Phys. **116**, 319 (1987)
41. M. Marinescu, H.R. Sadeghpour, Phys. Rev. A **59**, 390 (1999)

A Letters Journal Exploring the Frontiers of Physics

November 2011

EPL, **96** (2011) 33001
doi: 10.1209/0295-5075/96/33001

www.epljournal.org

Photoassociative creation of ultracold heteronuclear $^6Li^{40}K^*$ molecules

A. Ridinger[1(a)], S. Chaudhuri[1(b)], T. Salez[1], D. R. Fernandes[1], N. Bouloufa[2], O. Dulieu[2], C. Salomon[1] and F. Chevy[1]

[1] *Laboratoire Kastler Brossel, École Normale Supérieure, CNRS, Université Pierre et Marie-Curie 24 rue Lhomond, F-75231 Paris Cedex 05, France, EU*
[2] *Laboratoire Aimé Cotton, CNRS, Université Paris-Sud 11 - F-91405 Orsay, France, EU*

received 2 August 2011; accepted in final form 7 September 2011
published online 14 October 2011

PACS 33.20.-t – Molecular spectra
PACS 37.10.Mn – Slowing and cooling of molecules
PACS 34.20.Cf – Interatomic potentials and forces

Abstract – We investigate the formation of weakly bound, electronically excited, heteronuclear $^6Li^{40}K^*$ molecules by single-photon photoassociation in a magneto-optical trap. We performed trap loss spectroscopy within a range of 325 GHz below the $Li(2S_{1/2}) + K(4P_{3/2})$ and $Li(2S_{1/2}) + K(4P_{1/2})$ asymptotic states and observed more than 60 resonances, which we identify as rovibrational levels of 7 of 8 attractive long-range molecular potentials. The long-range dispersion coefficients and rotational constants are derived. We find large molecule formation rates of up to $\sim 3.5 \times 10^7 s^{-1}$, which are shown to be comparable to those for homonuclear $^{40}K_2^*$. Using a theoretical model we infer decay rates to the deeply bound electronic ground-state vibrational level $X^1\Sigma^+(v' = 3)$ of $\sim 5 \times 10^4 s^{-1}$. Our results pave the way for the production of ultracold bosonic ground-state $^6Li^{40}K$ molecules which exhibit a large intrinsic permanent electric dipole moment.

Copyright © EPLA, 2011

Introduction. – The recent realization of gases of ultracold polar molecules in their rovibrational ground state [1,2] has opened a new frontier in atomic and molecular physics [3,4]. Due to their long-range anisotropic dipole-dipole interactions and the possibility to trap and manipulate these molecules with external electric fields, they offer fascinating prospects for the realization of new forms of quantum matter [5,6]. Applications to quantum information processing [7,8], precision measurements [9,10] and ultracold chemistry [3] have been proposed.

The heteronuclear alkali dimer LiK is an excellent candidate for these studies. It has a large dipole moment of 3.6 D [11] in its singlet rovibrational ground state and both of its constituents, Li and K, possess stable fermionic and bosonic isotopes with which dipolar gases of different quantum statistics can be realized.

While atoms are routinely laser cooled to ultracold temperatures, the complex internal structure of molecules makes this direct method difficult (although possible [12]). So far the most efficient way to produce ultracold molecules has been to associate pre-cooled atoms. Two techniques have been established, namely magnetically tunable Feshbach resonances and photoassociation. Feshbach resonances allow the production of vibrationally excited molecules in the electronic ground state. In this way, ultracold heteronuclear $^6Li^{40}K$ molecules could recently be produced [13,14]. A combination of Feshbach resonances with a multi-photon state transfer may give access to the collisionally stable rovibrational ground state [1,15]. Photoassociation can directly give access to this state either via single-photon photoassociation and subsequent spontaneous decay [2] or by multi-color photoassociation [16].

In this letter we report on the production of ultracold heteronuclear excited $^6Li^{40}K^*$ molecules by single-photon photoassociation (PA) in a dual-species magneto-optical trap (MOT). We detect the molecule creation by a loss in the number of trapped atoms, which results from the molecules' spontaneous decay into either a pair of free untrapped atoms or a bound ground-state molecule.

Heteronuclear PA has so far been demonstrated for $RbCs^*$ [17], KRb^* [18], $NaCs^*$ [19], $LiCs^*$ [2] and $YbRb^*$ [20]. As compared to homonuclear molecules, the

(a) E-mail: armin.ridinger@gmail.com
(b) Current address: LENS and Dipartimento di Fisica, Università di Firenze - Via Nello Carrara 1, 50019 Sesto Fiorentino, Italy, EU.

PA rate for heteronuclear molecules is typically smaller due to the different range of the excited-state potentials. Whereas two identical atoms in their first excited state interact via the resonant dipole interaction at long range (with potential $V(R) \propto -C_3/R^3$), two atoms of different species interact via the van der Waals interaction ($V(R) \propto -C_6/R^6$), leading, for the heteronuclear case, to molecule formation at much shorter distances where fewer atom pairs are available. Besides, it has been argued that among the heteronuclear dimers, LiK* would be particularly difficult to photoassociate due to its small reduced mass and C_6 coefficients, which should lead to small PA rates of, *e.g.*, two orders of magnitude less than for the heavier dimers RbCs* and KRb* [21]. However, the PA rates we observe in our experiment are similar to those of the comparable experiment with RbCs* [17] and those found for homonuclear K_2^*. Our theoretical calculations are able to predict the large rates observed.

We perform PA spectroscopy in order to determine the long-range part of the excited-state molecular potentials. Previously, several molecular potentials of LiK have been determined by molecular [22–24] and Feshbach resonance spectroscopy [14,25]. Our measurements give access to previously undetermined spectroscopic data of high precision and will allow the derivation of more precise molecular potential curves facilitating the search for efficient pathways to produce LiK molecules in the rovibrational ground state.

Figure 1(a) shows the molecular potentials dissociating to the three lowest electronic asymptotes $2S+4S$, $2S+4P$ and $2P+4S$ of the LiK molecule. They have been calculated as described in ref. [11] and connected to the asymptotic form given in ref. [26] at large distances ($R > 40\,a_0$). Note that, as usual in alkali dimers, a strong spin-orbit coupling is expected between the $1^3\Pi$ and the $2^1\Sigma^+$ states due to the crossing of their potential curves around $7.5\,a_0$. Relevant for our experiment are the eight Hund's case c potential curves dissociating to the $2S_{1/2}+4P_{1/2,3/2}$ asymptotes. Figure 1(b) displays their long-range part, which is obtained by diagonalizing the atomic spin-orbit operator in the subspace restricted to the Hund's case a states correlated to $2S+4P$, for each of the symmetries $\Omega^\sigma = 0^+, 0^-, 1, 2$ (where Ω denotes the quantum number of the projection of the total electronic angular momentum on the molecular axis and σ the parity of the electronic wave function through a symmetry with respect to a plane containing the molecular axis). These potentials are all attractive at long range, whereas the curves which dissociate to the asymptotes $2P_{1/2,3/2}+4S_{1/2}$ are all repulsive [21]. For the relevant asymptotes the dispersion coefficients C_6 assume only three different values due to the small atomic fine structure of the Li atom [27]. They have been calculated theoretically [26,27] and they are determined experimentally in this work.

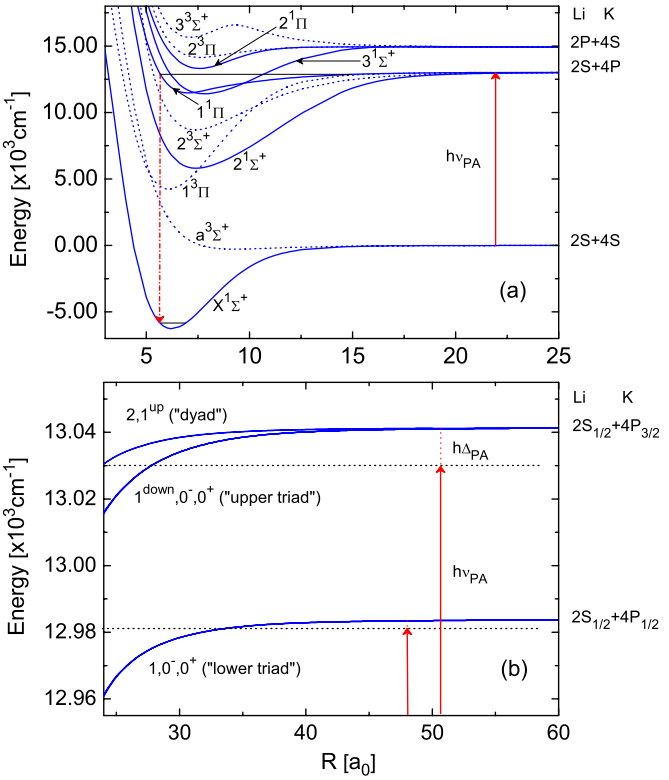


Fig. 1: (Colour on-line) (a) Molecular potentials of the LiK molecule for short interatomic separations R ($a_0 = 0.0529177\,\mathrm{nm}$). The upward arrow represents the energy delivered by the PA laser and the downward the spontaneous decay to electronic ground-state molecules. The vibrational state $X^1\Sigma^+(v'=3)$ shown in the figure has a favorable overlap with the addressed excited states due to spatially coincident classical inner turning points. (b) Detailed view of the excited-state potentials, labeled by their Hund's case c quantum numbers Ω^σ and an additional classification ("up/down") for unambiguous distinction. At short range, each of these potentials approaches one of those shown in (a) as illustrated in ref. [30].

Experimental setup. – The ^{6}Li^{40}K* molecules are created by a PA beam which is superimposed with the atoms trapped in the dual-species MOT. The MOT is continuously loaded from a Zeeman slower for ^{6}Li and a 2D-MOT for ^{40}K, as described in ref. [28]. We record PA spectra by scanning the PA beam in frequency, simultaneously recording the steady-state atom number of each species via the emitted trap fluorescence. The signature of ^{6}Li^{40}K* formation is a decrease of both the ^{6}Li and the ^{40}K fluorescence. The PA laser is scanned red detuned with respect to one of the atomic transitions of ^{40}K (see fig. 1(b)) and has no effect on a single-species ^{6}Li-MOT. The ^{6}Li fluorescence signal thus represents a pure heteronuclear PA spectrum, whereas the ^{40}K fluorescence signal represents the sum of a heteronuclear (^{6}Li^{40}K*) and homonuclear ($^{40}K_2^*$) PA spectrum. The frequency of the PA laser is recorded by a wavelength meter (High Finesse, ref. WS-6) with an absolute accuracy of $\pm 250\,\mathrm{MHz}$[1].

[1] A higher accuracy could be obtained using a more precise wavelength meter or an optical frequency comb. However, a significantly

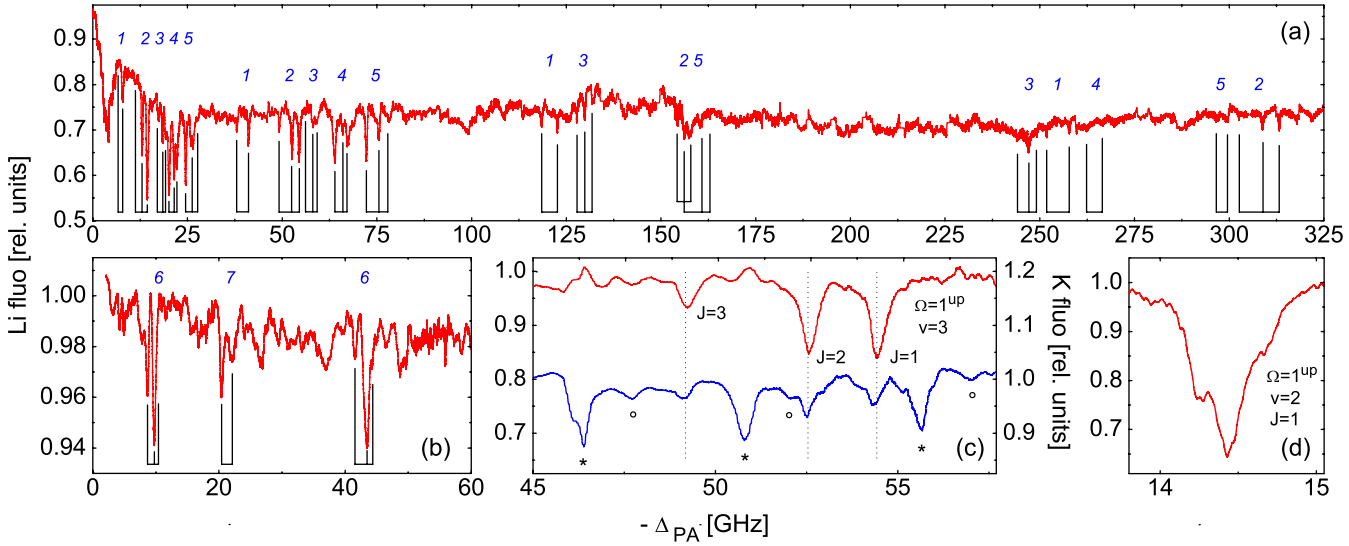


Fig. 2: (Colour on-line) Heteronuclear PA trap loss spectra of ^{6}Li^{40}K* below the asymptotes $2S_{1/2}+4P_{3/2}$ (a) and $2S_{1/2}+4P_{1/2}$ (b). The spectra contain seven vibrational series (labeled $N=1,\ldots,7$) with resolved rotational structure, whose assignment is given in table 1. (c) Zoom on the heteronuclear (upper trace, left axis) and heteronuclear+homonuclear (lower trace, right axis) PA spectrum below the $2S_{1/2}+4P_{3/2}$ asymptote showing the rotational structure of the $\Omega=1^{\rm up}$, $v=3$ vibrational state of ^{6}Li^{40}K* (v denoting the vibrational quantum number counted from dissociation) and three vibrational $0_{\rm u}^+$ levels of ^{40}K$_2^*$, which show a resolved hyperfine ($*$ and $\circ$) but no rotational structure. (d) Zoom on the $\Omega=1^{\rm up}, v=2, J=1$ resonance of ^{6}Li^{40}K*, showing a nearly resolved hyperfine structure. The PA detuning $\Delta_{\rm PA}$ is specified relative to the ^{40}K atomic transitions $4S_{1/2}(F=9/2)\rightarrow 4P_{3/2}(F'=11/2)$ (a,c,d) and $4S_{1/2}(F=9/2)\rightarrow 4P_{1/2}(F'=9/2)$ (b).

Additionally, a Fabry-Perot interferometer is used to verify the laser's single-mode operation.

The PA light is derived from a homemade diode laser-tapered amplifier system. It has a wavelength of 767 nm and a power of 660 mW at the output of a single-mode polarization-maintaining fiber. It is collimated and passes four times through the center of the MOT with a total peak intensity of $\sim$100 W/cm^2. The beam diameter of 2.2 mm ($1/e^2$) was chosen to match the size of the ^{6}Li-MOT. Using the feed-forward technique [29], the laser's mode hop free continuous tuning range extends over $\sim$35 GHz.

For optimum experimental conditions, the PA-induced trap loss needs to be maximized and all other intrinsic losses that compete with it minimized [30]. Besides, the frequency of the PA beam needs to be scanned slowly enough ($\sim$15 MHz/s) to allow the trap loss to reach a quasi-steady state. To achieve these conditions the ^{6}Li-MOT is reduced to a small atom number and volume (by lowering the loading rate) and placed at the center of the larger ^{40}K-MOT. Further, light-induced cold collisions are reduced by using small intensities for the MOT cooling and repumping light ($I_{\rm cool}^{\rm Li}\sim 1.5 I_{\rm sat}^{\rm Li}$, $I_{\rm rep}^{\rm Li}\sim 0.5 I_{\rm sat}^{\rm Li}$, $I_{\rm cool}^{\rm K}\sim 10 I_{\rm sat}^{\rm K}$, $I_{\rm rep}^{\rm K}\sim 3 I_{\rm sat}^{\rm K}$ per beam, respectively). The detunings are $\Delta\nu_{\rm cool}^{\rm Li}=\Delta\nu_{\rm rep}^{\rm Li}\sim -3\Gamma$, $\Delta\nu_{\rm cool}^{\rm K}=\Delta\nu_{\rm rep}^{\rm K}\sim -4\Gamma$ and the axial magnetic field gradient is 20 G/cm. These parameters result in $N_{\rm Li}\sim 5\times 10^8$ and $N_{\rm K}\sim 2.5\times 10^9$ trapped atoms with central atomic densities of $n_{\rm Li}\sim 7\times 10^{10}\,{\rm cm}^{-3}$ and $n_{\rm K}\sim 5\times 10^{10}\,{\rm cm}^{-3}$ and temperatures of $T_{\rm Li}\sim 1.2$ mK and $T_{\rm K}\sim 300\,\mu$K, respectively. At these temperatures only heteronuclear collisions of s- and p-wave character (*i.e.*, $\ell=0,1$, where ℓ is the rotational angular momentum of the atom pair) reach sufficiently short internuclear distances to allow for PA (the height of the d-wave rotational barrier being 13.4 mK). If J is the total angular-momentum quantum number of the atom pair (including electronic angular momentum and rotation), molecule formation is thus restricted to the rotational levels $J=0,1,2$ for electronic states with $\Omega=0$, $J=1,2,3$ for $\Omega=1$ and $J=2,3$ for $\Omega=2$.

more precise determination of the resonance positions could not be gained due to the large widths of the resonances.

Results. – Figure 2(a)–(d) shows a compilation of our recorded spectroscopic data. Figures 2(a) and (b) depict the heteronuclear PA spectra near the dissociation limits $2S_{1/2}+4P_{3/2}$ and $2S_{1/2}+4P_{1/2}$ for PA detunings $\Delta_{\rm PA}$ between 0 and -325 GHz and between 0 and -60 GHz, respectively. The graphs represent, respectively, an average of $\sim$6 and $\sim$20 recorded spectra for noise reduction and have been recorded in pieces and stitched together. The spectra contain 68 resonances whose contrasts decrease and whose mutual separations increase with increasing detuning. The maximum contrast amounts to $\sim$35% and is obtained for a detuning of $\Delta_{\rm PA}=-14.4$ GHz (see fig. 2(d)). The observed resonance widths (FWHM) vary between 80 and 300 MHz, primarily due to unresolved molecular hyperfine structure [31].

We have also recorded the heteronuclear+homonuclear PA spectra appearing on the K fluorescence signal, which contain all the resonances of fig. 2(a,b) as well. A comparison between the two spectra is shown for a small part in fig. 2(c). This figure shows comparable contrasts for the heteronuclear ^{6}Li^{40}K* and homonuclear ^{40}K$_2^*$ PA signals. We identify the observed ^{40}K$_2^*$ resonances as excitations to 0_u^+ states [32].

In the heteronuclear spectra of fig. 2(a), (b) we identify seven vibrational series (labeled with numbers), corresponding to seven of the eight molecular potentials dissociating to the $2S_{1/2}+4P_{1/2,3/2}$ asymptotes (see fig. 1(b)). Each series contains up to five resonances, which appear in doublets or triplets due to resolved rotational structure. This structure is shown more clearly in fig. 2(c) for a particular vibrational state. Some of the observed rovibrational resonances have a further substructure resulting from hyperfine interactions, which is shown for a particular resonance in fig. 2(d).

In fig. 2(a), (b) and table 1 we present an assignment of the observed resonances, which was obtained by the combination of different assignment rules: the first is the rotational progression law $E_{\rm rot}=B_v[J(J+1)-\Omega^2]$, with $J=\Omega,\Omega+1,\ldots$ for Hund's case c molecules [30] combined with our theoretical calculations of the rotational constants B_v. It allowed us to identify rotational progressions and to assign some J and Ω based on the rotational spacing. The identification of the $\Omega=2$ vibrational series (series 1 in fig. 2(a)) is particularly easy, because only two rotational lines per vibrational level are expected, as opposed to three for all other series. The second is the semi-classical LeRoy-Bernstein (LRB) law [33,34] (see eq. (1)) combined with the available calculated C_6 coefficients [26,27]. It allowed us to identify vibrational progressions and to assign some v and Ω based on the vibrational spacing. The third is the hyperfine structure law $E_{\rm hfs}\propto\Omega/[J(J+1)]$ for $\Omega=1$ and $E_{\rm hfs}\approx 0$ for $\Omega=0$ [31,35]. It predicts small widths for resonances with $\Omega=0$ and particularly large widths for those with $\Omega=1, J=1$ making their identification possible. The fourth is the expected similar contrast pattern of the rotational lines of the same vibrational series, which helped us to identify vibrational progressions.

An application of the assignment rules allowed us to identify the observed vibrational series and to assign their quantum numbers except the parity σ of the $\Omega=0$ electronic states. σ can be determined from an analysis of the relative strength of the rotational lines: due to the selection rules, the parity of the total wave function of the system, *i.e.* the product of σ and $(-)^\ell$ for the rotational part, changes sign during the transition. Further, σ is conserved, namely only $X^1\Sigma^+(0^+)\to 0^+$ and $a^3\Sigma^+(0^-)\to 0^-$ are allowed for parallel transitions. In our experiment, s-wave collisions dominate, such that the total parity is + (−) for the former (the latter) initial state. The parallel transition $X^1\Sigma^+(0^+,\ell=0)\to(0^+,\ell=1)$ is thus allowed enhancing then the $J=1$ line, while the parallel transition $a^3\Sigma^+(0^-,\ell=0)\to(0^-,\ell=1)$ is forbidden. Under the same approximation, the perpendicular transition $a^3\Sigma^+(1,\ell=0)\to(0^-,\ell=0)$ is allowed and enhances the $J=0$ line in the spectrum. Therefore we assign the $\Omega=0$ series with pronounced (reduced) $J=1$ line to the excited 0^+ (0^-) states.

Table 1: PA resonances of ^{6}Li^{40}K* observed below the $2S_{1/2}+4P_{1/2,3/2}$ asymptotes and their contrasts. N denotes the number of the vibrational series given in fig. 2(a), (b).

N	Ω	v	J	$-\Delta_{\rm PA}$ [GHz]	Contr. [%]	N	Ω	v	J	$-\Delta_{\rm PA}$ [GHz]	Contr. [%]
1	2	1	2	0.37	1.1	4	0^-	2	2	3.03	21.4
			3	6.60	2.3				1	3.66	22.7
		2		7.88	9.4			3	2	20.11	25.0
		3	3	38.00	5.6				1	21.48	20.4
			2	41.08	10.6				0	22.16	17.4
		4	3	118.49	6.3			4	2	63.99	14.7
			2	122.67	6.3				1	66.06	5.0
		5	3	251.80	3.7				0	67.13	7.6
			2	257.81	4.3			6	2	262.37	1.9
2	$1^{\rm up}$	1	2	0.37	1.1				0	266.75	1.9
			1	1.34	6.1	5	$1^{\rm down}$	2	3	4.12	23.9
		2	3	11.27	2.4				2	4.85	14.9
			2	13.01	18.5				1	5.90	4.6
			1	14.40	35.0			3	3	24.52	19.8
		3	3	49.20	6.5				2	26.15	9.8
			2	52.47	14.1				1	27.72	3.0
			1	54.53	14.8			4	3	72.26	15.4
		4	2	154.35	5.4				2	75.55	10.0
			1	157.40	4.7				1	77.87	5.0
		5	3	302.50	2.0			5	3	156.12	6.1
			2	308.75	3.9				2	160.20	1.4
			1	313.26	4.6				1	162.91	1.9
3	0^+	2	2	1.34	6.1			6	2	296.51	1.8
			1	2.35	11.0				1	299.57	1.8
			0	3.03	21.4	6	0^+	2	2	8.66	3.9
		3	2	17.23	6.2				1	9.74	5.8
			1	18.51	10.6				0	10.37	0.8
			0	19.25	8.4			3	2	41.56	1.6
		4	2	56.30	2.0				1	43.40	5.1
			1	58.17	6.6				0	44.31	2.0
			0	59.21	5.6	7	1	2	2	20.42	3.6
		5	2	127.76	4.0				1	21.93	2.0
			1	129.91	7.8						
			0	131.80	5.0						
		6	2	244.13	2.0					Accuracy	
			1	247.07	5.2					± 0.25	± 1.0
			0	249.01	2.2						

Discussion. – Having assigned all observed resonances, the parameters of the different molecular potentials can be derived. We infer the C_6 coefficients from the measured vibrational binding energies $D-E_v=-(h\Delta_{\rm PA}-E_{\rm rot})$ (D denoting the dissociation energy and E_v the energy of the vibrational level v), using the LRB formula [33,34]

$$D-E_v=A_6(v_D-v)^3, \tag{1}$$

with $A_6=64\pi^3\hbar^3C_6/\left[B(2/3,1/2)\sqrt{2\mu C_6}\right]^3$, where B denotes the Beta-function ($B(2/3,1/2)\approx 2.587$), μ is the

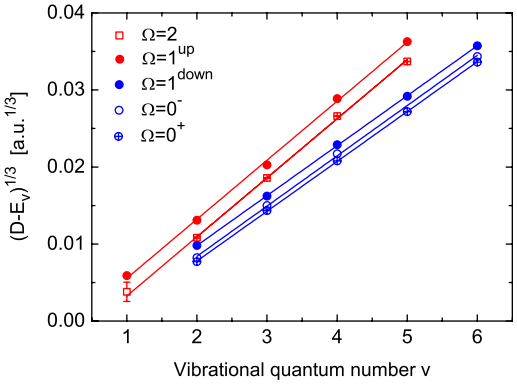


Fig. 3: (Colour on-line) Plot of the one-third power of the measured binding energies $D - E_v = -(h\Delta_{\rm PA} - E_{\rm rot})$ (symbols) as a function of the vibrational quantum number counted from the dissociation limit for the five vibrational series dissociating to the $2S_{1/2} + 4P_{3/2}$ asymptote. The slopes of the linear fits (solid lines) yield the dispersion coefficients C_6 according to eq. (1). The nearly identical slopes of the triad and dyad potentials demonstrate the equality of the respective C_6 coefficients.

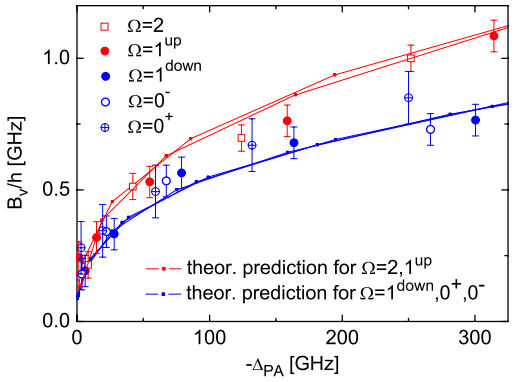


Fig. 4: (Colour on-line) Measured rotational constants (symbols) for the observed excited molecular states below the $2S_{1/2} + 4P_{3/2}$ asymptote and their theoretical predictions for computed vibrational levels (dots, the lines serve to guide the eye), derived from the potential curves of fig. 1.

reduced mass, and v_D the vibrational quantum number at dissociation (a constant between 0 and 1 so that the most weakly bound state has $v = 1$). Figure 3 shows the plots of the 1/3-rd power of the binding energies as a function of the vibrational quantum number for the five vibrational series dissociating to the $2S_{1/2} + 4P_{3/2}$ asymptote. The plots are predicted to follow straight lines whose slopes yield: $C_6 = 9170 \pm 940$ a.u. and $C_6 = 9240 \pm 960$ a.u. for the dyad potentials $\Omega = 2, 1^{\rm up}$, $C_6 = 25220 \pm 600$ a.u., $C_6 = 25454 \pm 720$ a.u. and $C_6 = 24310 \pm 1710$ a.u. for the upper triad potentials $\Omega = 1^{\rm down}, 0^+, 0^-$ and $C_6 = 12860 \pm 660$ a.u. for the lower triad potential $\Omega = 0^+$ (not shown in fig. 3), respectively, where the uncertainties represent statistical uncertainties for the fits. These values are in good agreement with the respective theoretical values $C_6 = 9800$ a.u., $C_6 = 25500$ a.u. and $C_6 = 13830$ a.u. predicted by Bussery *et al.* [26]. The agreement with the values $C_6 = 9520$ a.u., $C_6 = 22000$ a.u. and $C_6 = 15420$ a.u. predicted by Movre *et al.* [27] is not as good. The two predictions differ in their treatment of the interaction between the two asymptotes $2S + 4P$ and $2P + 4S$, which is taken into account in ref. [26] only, hinting its significance.

The uncertainty of the derived C_6 coefficients results from the following effects. First, the heteronuclear nature of LiK and its small C_6 coefficients lead to molecule formation at small internuclear separations (of $R_{\rm eff} = \hbar/\sqrt{2\mu B_v} \sim 18\, a_0$ at $\Delta_{\rm PA} = -300$ GHz) at which the exchange interaction and higher-order terms in the long-range multipole expansion of the molecular potential become important, which are neglected by the LRB law. Second, the small reduced mass of LiK leads to a low density of vibrational states and thus to a small number of states with long-range character available for fitting.

The measured rotational splittings allow us to infer the rotational constants and to confirm the assignments above. They are shown in fig. 4 for the five vibrational series below the $2S_{1/2} + 4P_{3/2}$ asymptote, together with their theoretical predictions, which we have derived from the potential curves of fig. 1. The agreement between the measured and predicted values is reasonable. The error bars account for the imprecision of the wavelength determination and of the resonance positions due to the unresolved hyperfine structure. Deviations from the theoretical predictions are likely to be due to the multichannel character of the vibrational levels.

We have determined the ^{6}Li^{40}K* molecule formation rate from the steady-state depletion of the ^{6}Li atom number induced by PA. For the resonance shown in fig. 2(d) we obtain a lower bound of $\beta_{\rm PA} n_{\rm K} N_{\rm Li}^{\rm PA} \sim 3.5 \times 10^7\,{\rm s}^{-1}$ and a PA rate coefficient $\beta_{\rm PA} = (2.2 \pm 1.1) \times 10^{-12}\,{\rm cm}^3/{\rm s}$. This coefficient is larger by about a factor of two than the one found in the experiment with RbCs* [17], showing that PA rates for LiK* are much more favorable than previously expected [21], confirming the trend discussed in ref. [36]. Using the approach described in ref. [37] we estimate the total PA rate coefficient for a computed $1^{\rm up}$ level with -21 GHz detuning to $1.6 \times 10^{-12}\,{\rm cm}^3/{\rm s}$ [32], in agreement with our measured value. The associated ^{6}Li^{40}K* molecule formation rate is also found to be comparable to that for ^{40}K$_2^*$, which is derived from fig. 2(c) to be $\sim 5.3 \times 10^7\,{\rm s}^{-1}$, despite the much longer range of the excited ^{40}K$_2^*$ molecular potential. Using our model, which reproduces the observed rovibrational structure, we infer the rates for decay into bound levels of the $X^1\Sigma^+$ state. The rates are found largest for the decay into the most weakly bound level, but are still significant for the decay into deeply bound levels such as the $X^1\Sigma^+(v' = 3)$ level (v' counted from the potential bottom) for which it is $5 \times 10^4\,{\rm s}^{-1}$ (see fig. 1). Since the ^{6}Li^{40}K* molecule formation rate saturates in our experiment at moderate PA intensities of

$\sim 80\,\mathrm{W/cm^2}$, efficient coherent multi-photon population transfers to the molecular rovibrational ground state can be expected.

Conclusion. – In summary, we have investigated single-photon photoassociation of excited heteronuclear $^6Li^{40}K^*$ molecules. We have recorded photoassociation spectra and assigned all observed resonances. We have derived the long-range dispersion coefficients and rotational constants, which agree with the theoretical predictions of ref. [26] and our calculations, respectively. In particular, we have observed large formation rates for the heteronuclear $^6Li^{40}K^*$ molecules which are comparable to those found for homonuclear $^{40}K_2^*$. These rates promise efficient creation of rovibrational ground-state molecules and show that photoassociation is an attractive alternative to Feshbach resonances, since those have a very small width for $^6Li^{40}K$ and are thus difficult to control [14].

For future research it will be interesting to combine ours and previously recorded data on LiK and to refine the molecular potentials. Spectroscopic data is available for the potential $1^1\Pi$ [38], which correlates with the $\Omega = 1^{\mathrm{up}}$ potential, for which we measured the binding energies of the five previously undetermined least-bound vibrational states, such that a complete set of vibrational levels is now available for a high-precision refinement of this potential.

* * *

The authors thank L. Pruvost and J. Deiglmayr for insightful discussions, U. Eismann for assistance with the experiment and M. Aymar for providing us with unpublished LiK potential curves and transition dipole moments. Support from ESF Euroquam (FerMix), SCALA, ANR FABIOLA, Région Ile de France (IFRAF), ERC Ferlodim and Institut Universitaire de France is acknowledged. AR acknowledges funding from the German Federal Ministry of Education and Research and DRF from Fundação para a Ciência e Tecnologia and Fundação Calouste Gulbenkian.

REFERENCES

[1] Ni K.-K. *et al.*, *Science*, **322** (2008) 231.
[2] Deiglmayr J. *et al.*, *Phys. Rev. Lett.*, **101** (2008) 133004.
[3] Carr L. D., DeMille D., Krems R. V. and Ye J., *New J. Phys.*, **11** (2009) 055049.
[4] Dulieu O. and Gabbanini C., *Rep. Prog. Phys.*, **72** (2009) 086401.
[5] Damski B. *et al.*, *Phys. Rev. Lett.*, **90** (2003) 110401.
[6] Yi S. and You L., *Phys. Rev. A*, **61** (2000) 041604.
[7] DeMille D., *Phys. Rev. Lett.*, **88** (2002) 067901.
[8] Rabl P. *et al.*, *Phys. Rev. Lett.*, **97** (2006) 033003.
[9] Hudson E. R., Lewandowski H. J., Sawyer B. C. and Ye J., *Phys. Rev. Lett.*, **96** (2006) 143004.
[10] Shelkovnikov A., Butcher R. J., Chardonnet C. and Amy-Klein A., *Phys. Rev. Lett.*, **100** (2008) 150801.
[11] Aymar M. and Dulieu O., *J. Chem. Phys.*, **122** (2005) 204302.
[12] Shuman E. S., Barry J. F. and DeMille D., *Nature*, **467** (2010) 820.
[13] Voigt A.-C. *et al.*, *Phys. Rev. Lett.*, **102** (2009) 020405.
[14] Wille E. *et al.*, *Phys. Rev. Lett.*, **100** (2008) 053201.
[15] Danzl J. G. *et al.*, *Science*, **321** (2008) 1062.
[16] Sage J. M., Sainis S., Bergeman T. and DeMille D., *Phys. Rev. Lett.*, **94** (2005) 203001.
[17] Kerman A. J. *et al.*, *Phys. Rev. Lett.*, **92** (2004) 033004.
[18] Wang D. *et al.*, *Phys. Rev. Lett.*, **93** (2004) 243005.
[19] Haimberger C., Kleinert J., Bhattacharya M. and Bigelow N. P., *Phys. Rev. A*, **70** (2004) 021402.
[20] Nemitz N. *et al.*, *Phys. Rev. A*, **79** (2009) 061403.
[21] Wang H. and Stwalley W. C., *J. Chem. Phys.*, **108** (1998) 5767.
[22] Rousseau S. *et al.*, *Chem. Phys.*, **247** (1999) 193.
[23] Jastrzebski W., Kowalczyk P. and Pashov A., *J. Mol. Spectrosc.*, **209** (2001) 50.
[24] Salami H. *et al.*, *J. Chem. Phys.*, **126** (2007) 194313.
[25] Tiemann E. *et al.*, *Phys. Rev. A*, **79** (2009) 042716.
[26] Bussery B., Achkar Y. and Aubert-Frécon M., *Chem. Phys.*, **116** (1987) 319.
[27] Movre M. and Beuc R., *Phys. Rev. A*, **31** (1985) 2957.
[28] Ridinger A. *et al.*, to be published in *Eur. Phys. J. D* (2011) DOI: 10.1140/epjd/e2011-20069-4.
[29] Führer T. and Walther T., *Opt. Lett.*, **33** (2008) 372.
[30] Krems R. V., Stwalley W. C. and Bretislav F. (Editors), *Cold Molecules: Theory, Experiment, Applications* (CRC Press, Boca Raton, Fla.) 2009.
[31] Williams C. J., Tiesinga E. and Julienne P. S., *Phys. Rev. A*, **53** (1996) R1939.
[32] Ridinger A., *Towards Ultracold Polar $^6Li^{40}K$ Molecules* (SVH, Saarbrücken, Germany) 2011, ISBN 978-3-8381-2895-5.
[33] LeRoy J. R. and Bernstein R. B., *J. Chem. Phys.*, **52** (1970) 3869.
[34] Stwalley W. C., *Chem. Phys. Lett.*, **6** (1970) 241.
[35] Grochola A. *et al.*, *J. Chem. Phys.*, **131** (2009) 054304.
[36] Azizi S., Aymar M. and Dulieu O., *Eur. Phys. J. D*, **31** (2004) 195.
[37] Pillet P. *et al.*, *J. Phys. B*, **30** (1997) 2801.
[38] Pashov A., Jastrzebski W. and Kowalczyk P., *Chem. Phys. Lett.*, **292** (1998) 615.

4 Gray molasses

In the previous chapter we described the setup responsible for the trapping and cooling of ^{6}Li and ^{40}K atoms in a double magneto-optical trap (MOT). At this point, the measured phase-space density (PSD) is of the order of $\sim 10^{-7}$ [166], meaning that further steps of cooling have to be implemented in order to achieve the quantum regime (PSD$\gtrsim 1$). One possibility is to perform evaporative cooling in a magnetic trap, but our experiments showed that the initial elastic collision rate was too small for the evaporation to be efficient. By implementing an intermediate cooling step such as sub-Doppler cooling, one can enhance the initial collision rate. Due to the inexistence of efficient sub-Doppler cooling for ^{6}Li and ^{40}K, we implemented a novel mechanism based on a gray molasses scheme [21, 76]. We show that using this cooling technique the PSD was enhanced by almost three orders of magnitude compared to the MOT, which provides excellent conditions for performing fast evaporation of ^{6}Li and ^{40}K.

We start this chapter by presenting the state of the art of laser cooling of ^{6}Li and ^{40}K. This will be followed by an introduction to the principle of our gray molasses cooling scheme and a discussion of the particular case of ^{40}K based on semi-classical calculations. The optical setup used for cooling will be presented, followed by the experimental results and their discussion. A separated section will be devoted to the gray molasses cooling of ^{6}Li. At the end of the chapter we will summarize the main results and point out that this novel technique was successfully implemented to other isotopes by other groups and is at the present well-established technique for sub-Doppler cooling.

4.1 Introduction

When shining coherent light to an ensemble of atoms, one can cool them down to very low temperatures by using clever strategies. Until the end of the 1980s, it was expected that the limit for laser cooling would be the Doppler temperature. This limit

would be attained by shinning light on atoms from all directions of space, frequency red-detuned by $\delta = -\Gamma/2$ from an atomic resonance, where $1/\Gamma$ is the lifetime of the excited state. In this case, each atom would perform a random walk in the momentum space due to the spontaneous emission, resulting an atomic ensemble at equilibrium temperature of $T_{\mathrm{D}} = \hbar\Gamma/2k_B$ (e.g. 145μK for ^{40}K and 141μK for ^{6}Li). In reality, experiments showed that the temperature attained in this configuration was lower than expected by one to two orders of magnitude. This effect was later explained as being consequence of another cooling mechanism: the Sisyphus or polarization gradient cooling [38]. This mechanism relies on the fact that two red-detuned counter-propagating beams give rise to a periodic modulation of the polarization or the intensity of light, which can play a crucial role for a multilevel atom. If there is a favorable positive correlation between light shift and optical pumping of the different internal levels, cooling can occur and temperature can decrease to the scale of the recoil energy $T_{\mathrm{R}} = \hbar^2 k_{\mathrm{L}}^2/2mk_{\mathrm{B}}$ (e.g. 0.41μK for ^{40}K and 3.5μK for ^{6}Li). In the case of the fermionic alkaline isotopes ^{40}K and ^{6}Li, the hyperfine structure of the $\mathrm{P}_{3/2}$ excited state is too narrow to allow efficient Sisyphus cooling. Indeed, strong off-resonant excitations disrupt the positive correlation between light shift and optical pumping, washing out the Sisyphus cooling effect. In the case of ^{40}K, it was observed that sub-Doppler cooling is possible, since temperatures of 15μK were reported, but only a small fraction of the atomic sample were cooled, typically $\sim 10^7$ atoms [71, 133].

Interestingly, the hyperfine structure of the $\mathrm{P}_{1/2}$ state is more resolved than its $\mathrm{P}_{3/2}$ counterpart. One can thus use the D_1 transition $\mathrm{S}_{1/2} \rightarrow \mathrm{P}_{1/2}$ and perform efficient sub-Doppler cooling. There are several Sisyphus-like mechanisms reported, most of them discovered in the 1990s. One of them is the gray molasses cooling, which can be performed with blue-detuned light respective to a $F \rightarrow F' = F$ or a $F \rightarrow F' = F - 1$ transition. This mechanism was successfully implemented on the D_1 transition of ^{40}K and will be described in the following sections. The results of subsequent works that demonstrated efficient cooling for ^{6}Li will be presented at the end of the chapter.

4.2 Principle

Gray molasses cooling was proposed by Grynberg and Courtois [76], Weidemüller et al. [209], following previous schemes involving a Λ transition [7], and was ex-

perimentally realized in a three dimensional configuration on the D_2 transitions of Cesium and Rubidium [20, 21, 55].

This cooling mechanism relies on the existence of dark and bright states when atoms are shinned with light, on a coupling between them induced by motion and on Sisyphus cooling. When an atom is in a non-coupled (dark) state its energy does not change with its position, but it can be excited to a coupled (bright) state. The energy of this state is positive for a positive light detuning and spatially variable since the light shift depends on the light intensity (and polarization) variations. Since coupling is more likely to occur at the bottom of the bright state potential, the atom will subsequently climb this potential and lose kinetic energy. As the atom approaches the top of the potential, it is optically pumped way back into the dark state. Repeated cooling cycles decrease the temperature of the atomic ensemble to the sub-Doppler regime (see fig. 4.2.1).

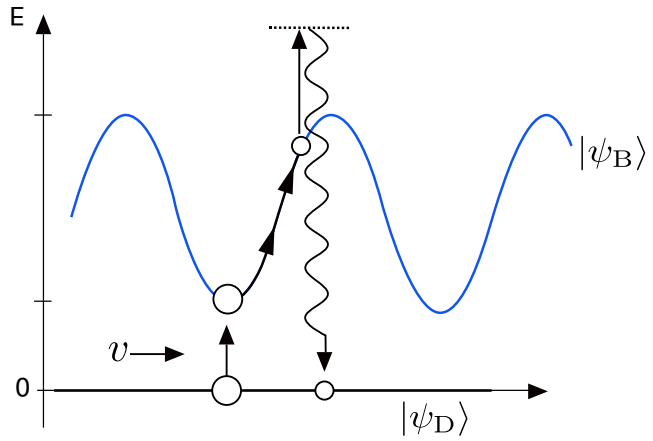


Figure 4.2.1: Gray molasses cooling scheme. An atom in the dark state $|\psi_D\rangle$ can be excited to the bottom of the bright state $|\psi_B\rangle$ potential by motion coupling. While climbing the potential the atom loses kinetic energy. After a cycle of absorption and spontaneous emission the atom returns to the dark state.

A toy model useful to understand the gray molasses cooling mechanism is the Λ system, which includes two (degenerate) ground states $|g_1\rangle$ and $|g_2\rangle$ coupled by light to an excited state $|e\rangle$. Let us consider an atom in one-dimension with Λ-type energy levels and two counter-propagating transition-dependent laser fields Ω_1 and Ω_2, as

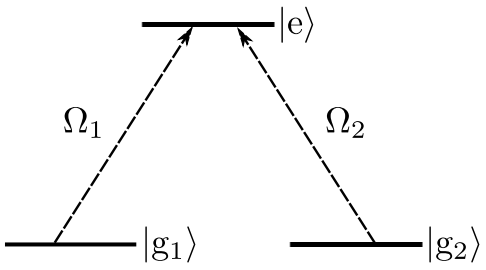


Figure 4.2.2: Scheme of three atomic levels coupled to light in a Λ configuration.

shown in fig. 4.2.2. For this system, the semi-classical light coupling is given by the interaction operator $\hat{V} = \hbar\Omega_1/2\,|e\rangle\langle g_1| + \hbar\Omega_2/2\,|e\rangle\langle g_2| + \text{h.c.}$ and can be derived from first principles from the dipolar interaction. We can then introduce a new basis for the ground state

$$\begin{aligned} |\psi_D\rangle &= \frac{1}{\Omega}\left(\Omega_2\,|g_1\rangle - \Omega_1\,|g_2\rangle\right) \\ |\psi_B\rangle &= \frac{1}{\Omega}\left(\Omega_1\,|g_1\rangle + \Omega_2\,|g_2\rangle\right), \end{aligned}$$

with $\Omega = \sqrt{\Omega_1^2 + \Omega_2^2}$.

We name the $|\psi_D\rangle$ the *dark or* the *uncoupled state*, since it is unaffected by light $\hat{V}\,|\psi_D\rangle = 0$ and we name the $|\psi_B\rangle$ the *bright* or the *coupled state*, since it is coupled to the excited state $\langle e|\,\hat{V}\,|\psi_D\rangle = \hbar\Omega/2$. These states give an intuitive picture of the system, but they are actually not stationary if we consider the complete hamiltonian $\hat{H} = \hat{H}_{at} + \hat{V}$, $\hat{H}_{at}$ being the atomic hamiltonian which includes the kinetic term $\hat{p}^2/2m$. In this case, there is coupling between the dark and the bright states, due to the atomic motion. It is not the purpose of this thesis to give a complete account of the problem, which can be found in section 2 of ref. 150 or refs. 31, 32, but one can obtain that

$$\langle\psi_B(p)|\,\frac{\hat{p}^2}{2m}\,|\psi_D(p)\rangle = -\frac{2\Omega_1\Omega_2}{\Omega^2}\hbar k\frac{p}{m},$$

which is the frequency at which the atomic state oscillates between the dark and the

bright state, where $v = p/m$ is the atomic speed. An atom in the dark state has thus a lifetime of $\tau_D \propto 1/(vk)^2$ before being transferred to the bright state (cf. Fermi rule). In consequence, atoms with low speed (colder) will be kept in the dark state, while atoms with high speed will be transferred to the bright state. The action of a cooling mechanism (e.g. Sisyphus) will decrease the velocity of the atoms and those which have lower speeds will accumulate in the dark state.

The seminal experimental study of this Λ system was done by Aspect et al. [7]. Atoms of metastable ^{4}He* were exposed to $\sigma^+\sigma^-$ light resonant with the $F = 1 \rightarrow F' = 1$ transition. The selection rules impose that the only possible couplings are $|F = 1, m_F = -1\rangle \equiv |g_1\rangle \rightarrow |F' = 0, m_F = 0\rangle \equiv |e\rangle$ (by means of σ^+ photons) and $|F = 1, m_F = +1\rangle \equiv |g_2\rangle \rightarrow |F' = 0, m_F = 0\rangle \equiv |e\rangle$ (by means of σ^- photons)[1]. The authors showed that atoms were pumped to the dark state $|\psi_D(p = 0)\rangle$ after a certain interaction time, resulting in a net cooling of the atomic ensemble. This is the principle of the so-called VSCPT mechanism (velocity-selective coherent population trapping) and applies to the particular of the case $F = 1 \rightarrow F' = 1$.

The second ingredient of the gray molasses is Sisyphus cooling, which can occur in the coupled state for a *positive detuning*. If the detuning between the light frequency and the atomic transition is $\delta = \omega - \omega_0$, the bright state will suffer a light shift given by $E_B = \hbar\Omega^2/\delta$ (proportional to the light intensity), while the dark state will not be affected by light $E_D = 0$. As argued above, an atom in the dark state with some kinetic energy can be transferred to the the bright state. The probability of this non-adiabatic passage can be calculated perturbatively

$$P = \left| \frac{\langle \psi_B(p) | \frac{\hat{p}^2}{2m} | \psi_D(p) \rangle}{E_B - E_D} \right|^2 = 2 \left(\frac{\Omega_1 \Omega_2}{\Omega^3} \delta k \frac{p}{m} \right)^2 .$$

The probability of non-adiabatic passage increases with the atomic speed $v = p/m$, decreases with light shift Ω^2/δ and increases with the detuning δ [209]. For a stationary wave the coupling from the dark to the bright state will be maximum at the valleys of the bright state potential, where $E_B - E_D = E_B$ is minimal (see fig. 4.2.1). When the atom is transferred to the bottom of this potential, it climbs the potential

[1] Notice that $J \equiv F$, since ^{4}He* has no nuclear angular momentum I.

hill and loses kinetic energy. At the top of the hill it may absorb a photon and decay to the dark state after a spontaneous emission. At the end of one cooling cycle, the kinetic energy of the atom will reduce and therefore the probability for non-adiabatic coupling also decreases. After many cooling cycles, atoms will be cold and stocked in the dark state. In a Sisyphus-type cooling mechanism, cooling becomes inefficient when the kinetic energy of the atom is too small to climb the potential hill. This leads to a final equilibrium temperature that scales with the light shift $k_B T \propto I/\delta$ (for $T \gg T_{\text{Recoil}} = \hbar^2 k^2/2mk_B$). We turn now to the question of the capture velocity of the gray molasses v_{cap}. If $\Gamma' \propto I/\delta^2$ is the optical pumping rate from the bright states to the dark states, then the capture velocity is given by $v_{\text{cap}} \sim \lambda/\tau' = \Gamma'/k$, with $\tau' = \Gamma'/2\pi$ being the optical pumping time and λ being the wavelength of the cooling light.

The analysis of the gray molasses cooling mechanism made so far was restricted to a Λ configuration in *one dimension*. In general, for transitions of the type $F \to F'$ and $F \to F' - 1$ one can always find dark states, which obey the relation $\hat{V}\,|\psi_D\rangle = 0$ for elliptically polarized light[2] [150, 185]. The idea is that one can always arrange the Zeeman states in a series of coupled Λ systems. In a three-dimensional configuration this is not always true. For the $F = 1 \to F' = 1$ case it was shown that the dark states survive in a three-dimensional arrangement of $\sigma^+\sigma^-$ polarized light [146][3]. However, for the relevant case of half-integer F and F' the dark states are localized in space.

4.3 The case of ^{40}K: semi-classical calculations

The relevant level structure of ^{40}K can be seen in section 2.2.1. It comprises a ground state manifold $^2S_{1/2}$ (with hyperfine states $F = 7/2$ and $F = 9/2$) and two excited manifolds $^2P_{1/2}$ (with hyperfine states $F' = 7/2$ and $F' = 9/2$) and $^2P_{3/2}$ (with hyperfine states $F' = 5/2, 7/2, 9/2, 11/2$). We decided to perform cooling on the D_1 transition (transition between the ground state $^2S_{1/2}$ to the $^2P_{1/2}$ manifold) for two reasons. First, the two states of the $^2P_{1/2}$ manifold are much better resolved than their $^2P_{3/2}$ counterparts. Second, by having a cooling beam blue detuned from the

[2] Notice that in the absence of magnetic field the quantification axis is given by the direction of light $\vec{k}$ and therefore light can only by elliptically polarized.

[3] See a simple argument in ref. 109.

$^2P_{1/2}$ manifold, the two possible transitions both result in gray molasses cooling.

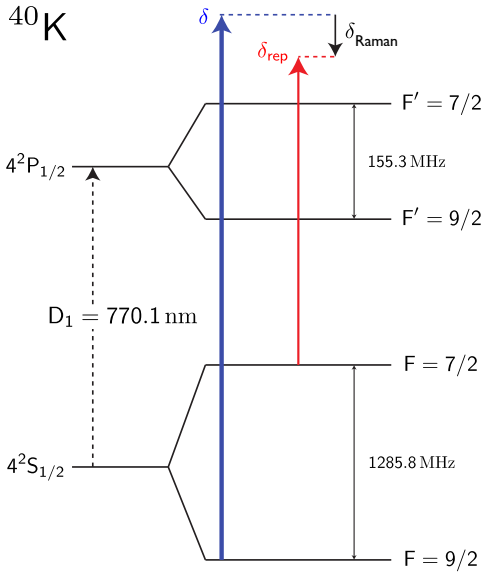


Figure 4.3.1: Level scheme of the transitions used for D_1 gray molasses cooling of ^{40}K. In blue is depicted the cooling laser frequency (positive detuning δ from the $F = 9/2 \rightarrow F' = 7/2$ transition) and in red the repumper frequency (detuning δ_{rep} from the $F = 7/2 \rightarrow F' = 7/2$ transition).

In fig. 4.3.1 we plot a scheme of the transitions used for cooling. The *cooling light* is blue detuned of δ from the $F = 9/2 \rightarrow F' = 7/2$ transition. Since depumping to the $F = 7/2$ state will occur, we also introduce *repumping light*, which is blue detuned of δ_{rep} from the $F = 7/2 \rightarrow F' = 7/2$ transition. We denote δ_{Raman} the difference between the detuning of the cooling light and the detuning of the repumper light. Notice that the effect of off-resonant excitations to the $F' = 9/2$ should be small, since this state is separated from $F' = 7/2$ by 155.3MHz $\widehat{=}$ 25.7Γ.

There are $2 \times (10 + 8)$ Zeeman levels of ^{40}K which are important to describe the cooling mechanism. Due to the complexity of the problem we performed a full computational calculation of the coupled optical Bloch equations in order to obtain the light shifts and the (de)pumping rates[4]. This calculation was performed for the one dimensional lin$\perp$lin configuration and for an atom at rest. The light intensities are $I_{\text{cool}}/I_{\text{sat}} = 13$ and $I_{\text{repump}} = I_{\text{cool}}/8$ per beam, with global detuning $\delta = +3\Gamma$ from the $F' = 7/2$ state and $\delta_{\text{Raman}} = 0$. The cooling and the repumper light fields are in phase. The results of these calculations are presented in figure 4.3.2.

When examining the plot of the light shift as a function of the position in the molasses one counts 9 bright states (labeled $m_F = -9/2, \ldots, 5/2$ at $z/\lambda = 1/8$), 2 weakly coupled states (labeled $m_F = 7/2$ and $m_F = 9/2$) and 9 very weakly coupled states ($F = 7/2$ manifold). This is in apparent contradiction with the conclusions of the

[4]The Matlab code for this calculation was kindly provided by Saijun Wu and is based on the Quantum Optics Toolbox made by Sze Meng Tan[194].

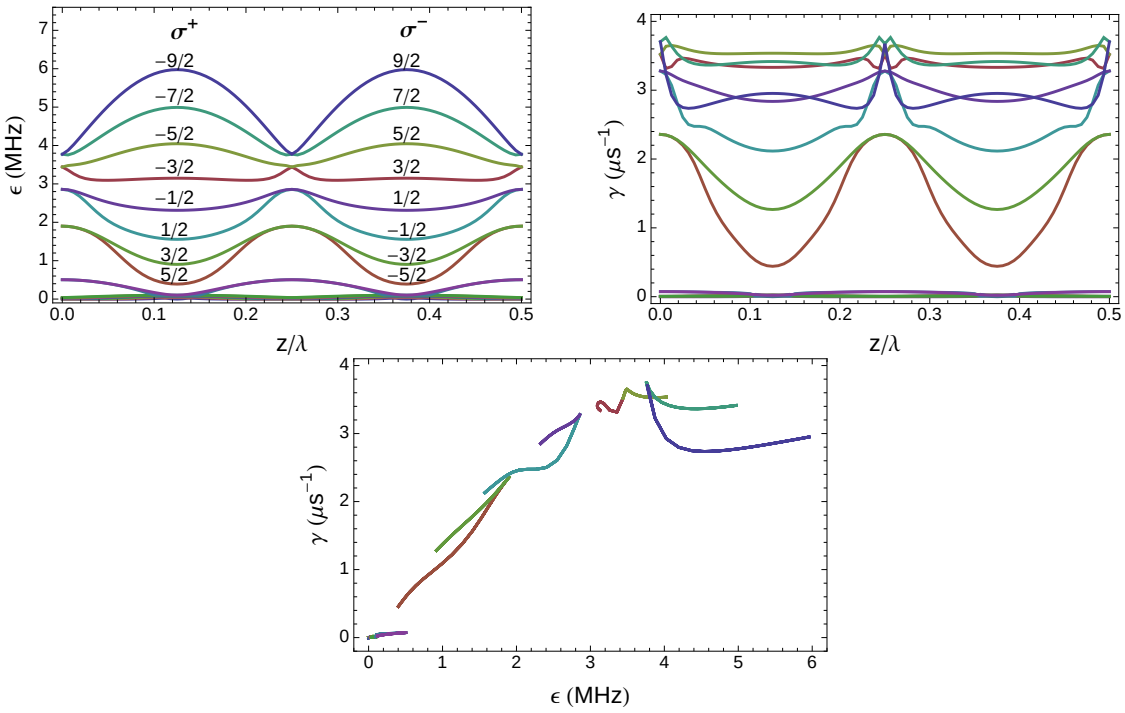


Figure 4.3.2: Light shift (top left) and depumping rate (top right) as a function of position in the molasses and light shift as a function of depumping rate (bottom). One dimensional lin⊥lin configuration with $I_{\text{cool}}/I_{\text{sat}} = 13$, $I_{\text{repumper}}/I_{\text{cool}} = 1/8$, $\delta = 3\Gamma$ and $\delta_{\text{Raman}} = 0$. The cooling and the repumper light fields are in phase.

previous section, that there should be 2 dark states all over the space z/λ. Actually, the existence of the excited level $F' = 9/2$ has a non-negligible contribution, giving rise to the 2 weakly coupled states mentioned before[5]. In fig. 4.3.2 there is also a plot of the departure rates γ for each state as a function of the position. This plot shows that the weakly coupled states are long-lived, while the bright states have a much smaller lifetime, as expected. Let us now turn to the interesting combined plot of γ and the light shift. It displays a set of long-lived weakly coupled states and a set of bright states, whose departure rate globally increases with light shift. In other words, an atom that climbed the bright state potential is more likely to be depumped than the one that is it still at the bottom of the potential. This behavior enables efficient

[5]This was confirmed by running the computational calculation for a 10 fold increased separation between the excited states $F' = 7/2$ and $F' = 9/2$ (10×155.3MHz). The light shift of the weakly coupled states was reduced to negligible values for all z/λ.

Sisyphus cooling.

4.4 Experimental setup

The D_1 system for ^{40}K operates at λ =770nm and is composed of a master diode laser which is frequency-locked to an atomic spectroscopic signal, an electro-optical modulator (EOM) that generates the repumping light and a tapered amplifier (TA). This system is depicted in a scheme in sections 2.2.2 and appendix 2.B and is described in the following paragraphs. The master diode laser is a commercial tunable diode in the Littrow configuration[6]. Using a polarization beamsplitter cube we divert part of the laser power to the spectroscopy setup ($\sim$ 1mW) and the main part to the EOM ($\sim$ 20mW) followed by the TA.

The spectroscopy setup is composed by an AOM in the cat-eye configuration (+2 $\times$ 260MHz), a homemade heated glass cell with natural Potassium ($\sim$ 50ºC) and an EOM that creates sidebands at $\pm$10MHz on the probe beam. This beam is focused in a fast photodiode[7] and the electric signal is demodulated by mixing it with the (dephased) reference signal fed to the EOM, following the Pound-Drever-Hall scheme. The resulting signal is dispersive [49] and by feeding it into the voltage of piezoelectric element voltage of the laser grating one can lock the light frequency to the chosen atomic transition[8]. For this we chose the strongest line we observed, which corresponds to the difference of energy between the ground-state crossover and the $F' = 2$ state of the $^2P_{1/2}$ manifold of ^{39}K.

The main part of the output of the laser diode goes through an EOM[9], which is fed by the amplified[10] signal of a synthesizer[11] tuned to the ground state hyperfine splitting of ^{40}K (1285.8MHz). The output beam of the EOM is injected into a TA[12] installed in a homemade mount [166].

The output of the TA is beam shaped with cylindrical and spherical lenses in order

[6] Toptica DL pro 770nm
[7] Newport model 1801-FS
[8] Toptica PDD110, SC110 and PID110.
[9] Qubig EO-K40-3M
[10] Mini Circuits ZHL-5W-2G+
[11] Winfreak Technologies SynthNV
[12] Eagleyard EYP-TPA-0765-01500-3006-CMT03-0000

to maximize fiber injection efficiency. Before the fiber injection there is a single pass AOM[13] (+200MHz) that serves to control the light power in the experiment. On the output side of the polarization maintaining fiber, the light is polarization cleaned with a polarization beamsplitter cube and then "combined" with the MOT light by means of a small angle, achieved by using a D-shaped mirror[14]. The waist size is 1.1cm and is the same as waist size of the MOT beams. We could in principle have reduced the beam size in order to improve the laser intensity: Indeed during the molasses phase the atomic cloud as only $\sim$ 3mm diameter. However we verified experimentally that the capture efficiency was 100% for the available laser power. Just like the MOT beam, the molasses laser beam is split into two vertical beams and two retro-reflected horizontal beams in a three-dimensional $\sigma^+\sigma^-$ configuration. A small fraction of this beam is injected into a Fabry-Perot[15] in order to determine the repumper fraction.

4.5 Results and discussion

In this section the experimental results concerning the ^{40}K D_1 gray molasses will be presented. The experimental cycle starts with the loading of the MOT, as described in the previous chapter. After this phase, the magnetic field gradient is ramped from 9G/cm to 60G/cm in 5ms without changing the detunings of the D_2 light. This process increases the spatial density of the cloud at the expense of temperature, which rises from 200μK to $\sim$ 3mK. The magnetic field gradient is then switched off abruptly by means of an IGBT[16]. We estimate that the field decreases with a time constant of $\sim$ 100μs due to Foucault currents. The magnetic field bias was compensated by installing a coil on each spatial axis and optimizing their currents by minimizing the molasses temperature. The diameter of the coils is about $\sim$ 1m in order to guarantee a very weak gradient over the atomic cloud. This bias coils are kept on since the beginning of the MOT loading until the magnetic transport sequence.

The measurement of the density profile of the atomic cloud was done by absorption imaging, as described in a previous section 2.3. The number of atoms is measured af-

[13]Crystal Technology 3200-124
[14]Thorlabs BBD1-E02
[15]Thorlabs SA200-5B
[16]Mitsubishi CM200HA-24H, see appendix 5.A for details.

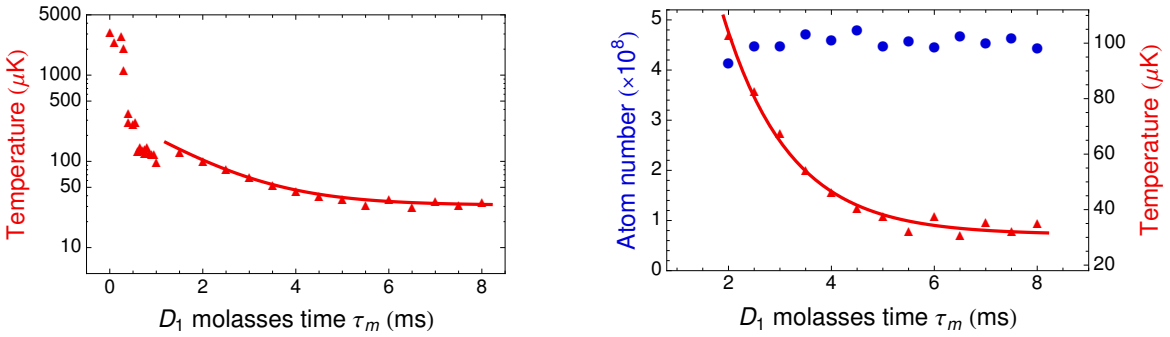


Figure 4.5.1: Atom number (in blue) and temperature (in red) of the atomic cloud after a pulse of molasses beams of duration τ_m. The cooling intensity was $I_{cool}/I_{sat} = 14$ per beam, the detuning was $\delta = 2.3\Gamma$, $I_{repump} = I_{cool}/8$ and the Raman detuning $\delta_{Raman} = 0$.

ter a short pulse of D_2 repumper light (in order to pump the atoms into the imaging transition) and the temperature is measured by taking several pictures at different time-of-flight (TOF) values. The laser power intensities are written as a function of $I_{sat} = 1.75\text{mW/cm}^2$, which corresponds to the saturated intensity of a ^{40}K closed transition. The ratio between the repumper and the cooling power is calculated by measuring the ratio between the amplitude of the corresponding peeks observed using the Fabry-Perot analyzer.

4.5.1 Characterization of the ^{40}K gray molasses

In a first experiment we pulsed the molasses beams for a certain duration τ_m and measured the atom number and the temperature of the cloud. The cooling intensity was set to the maximum $I_{cool}/I_{sat} = 14$ per beam, the detuning to $\delta = 2.3\Gamma$, $I_{repump} = I_{cool}/8$ and the Raman detuning δ_{Raman} was set to zero. As presented in fig. 4.5.1, we observe that all the atoms are captured in the molasses and are quickly cooled down. The cooling dynamics has two time scales: First there is a very fast drop of temperature from 3mK to 100μK in less than 1ms; Then a further drop from 100μK to 30μK in 4ms. This dynamics can be compared to the fluorescence light emitted during the D_1 molasses phase showed in fig. 4.5.2. Indeed, we observe a very fast decay of the molasses light emission in $\sim 1\mu$s to the 40% level and then a slow decay,

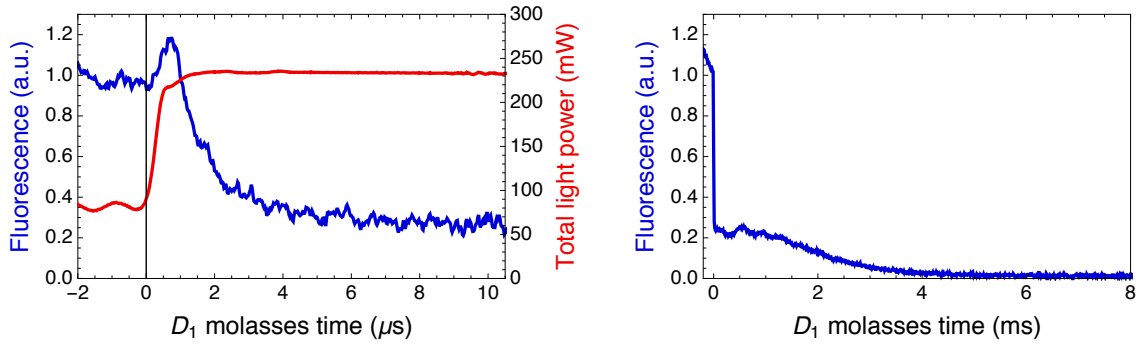


Figure 4.5.2: Measured fluorescence (in blue) and total cooling power (in red) during the MOT and the D_1 molasses phase as a function of time. Left: Detailed plot of the first $10\mu s$ of molasses. The vertical line is a help to the eye. In the interval $t \in [0, 2]\mu$s MOT and D_1 light may coexist due to finite time response of the AOMs, which might explain the initial positive "bump" in the fluorescence. Right: Measurement for complete molasses phase.

reaching 5% in $\sim$ 3ms.

In a second experiment we pulsed the molasses beams for a fixed time $\tau_m = 6$ms for different values of the D_1 laser intensity and measured the number of atoms captured in the molasses and their temperature (fig. 4.5.3). In order to measure the number of atoms captured in the molasses pictures at large time-of-flight (20ms) were taken. In this situation, atoms which are not captured by the molasses quickly fly off (due to their high energy) and their contribution to the measured signal is negligible. Indeed, without molasses light no atoms were measured after the time-of-flight. By decreasing the laser intensity we observed that the number of captured atoms decreases with the laser intensity, which is expected, since the molasses capture velocity decreases with laser intensity in the Sisyphus picture [168]. The capture efficiency saturates at $\sim$ 100% for $I_{cool}/I_{sat} \gtrapprox 11$. Notice that this saturation value depends on many variables such as the initial velocity distribution: For a less compressed/colder MOT the saturation intensity would be smaller. Concerning the temperature, we observed that it decreases monotonically with the cooling light intensity. This behavior is expected from a Sisyphus cooling mechanism, as discussed in section 4.2.

The results from the previous paragraphs suggests implementing the D_1 molasses cooling in two distinct phases. In the first one, the laser intensity is kept at maximum in order to have full capture efficiency; In the second one, the intensity is linearly

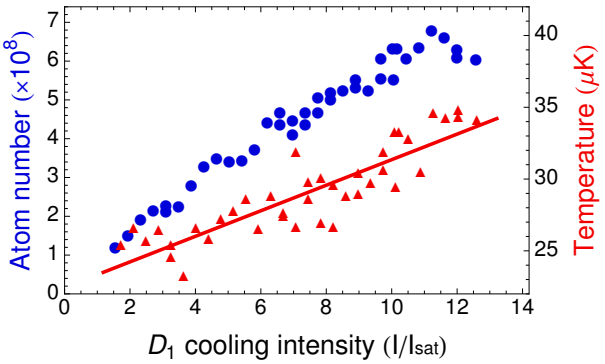


Figure 4.5.3: Atom number (in blue) and temperature (in red) of the atomic cloud after a pulse of molasses beams of duration $\tau_m = 6$ms. The cooling intensity was varied, the detuning was $\delta = 2.3\Gamma$, $I_{repump} = I_{cool}/8$ was kept constant and the Raman detuning $\delta_{Raman} = 0$. The capture efficiency is 100% for $I_{cool}/I_{sat} \gtrapprox 11$.

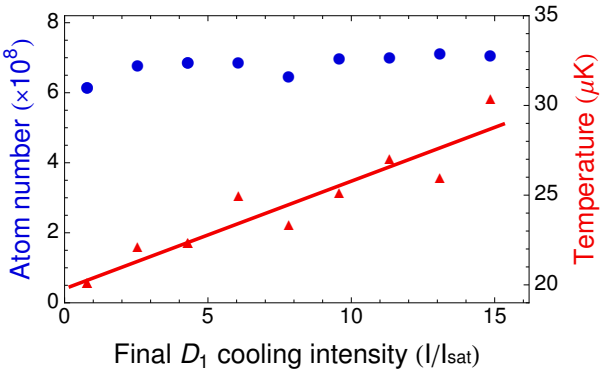


Figure 4.5.4: Atom number (in blue) and temperature (in red) of the atomic cloud after a pulse of molasses beams of duration 6ms with maximum cooling intensity $I_{cool}/I_{sat} = 14$ and a linear intensity ramp of 2ms to an adjustable value. The detuning was $\delta = 2.3\Gamma$, $I_{repump} = I_{cool}/8$ was kept constant and the Raman detuning $\delta_{Raman} = 0$.

ramped down in order to further cool down the captured atoms. To test this strategy the laser intensity was kept at high value $I_{cool}/I_{sat} = 14$ for 6ms and then linearly ramped down to an adjustable value for 2ms. We observed a drop of temperature from 30μK to 20μK without any loss of atoms (fig. 4.5.4).

In another experiment, the global laser detuning was varied for the full 8ms sequence (see fig. 4.5.5). For the interval $\delta \in [1.5, 3.5]\Gamma$ the temperature and the number

of captured atoms is essentially constant. For $\delta > 3.5\Gamma$ the number of atoms decreases due to inverse dependence of the capture velocity with detuning, while temperature stays constant. When detuning is too close of resonance $\delta < 1.5\Gamma$ the molasses stop working efficiently.

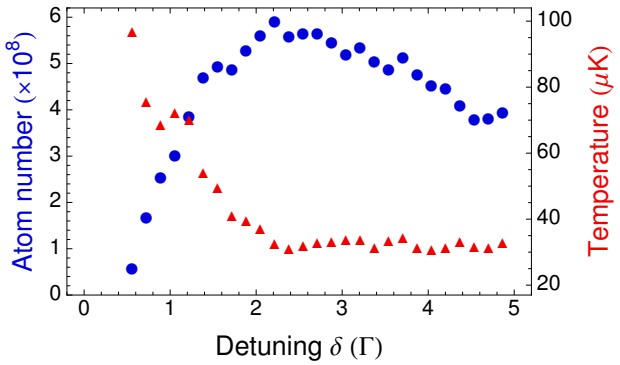


Figure 4.5.5: Atom number (in blue) and temperature (in red) of the atomic cloud after a molasses sequence of 8ms (described in the text). The global detuning δ was varied, the initial intensity was $I_{\text{cool}}/I_{\text{sat}} = 14$, $I_{\text{repump}} = I_{\text{cool}}/8$ was kept constant and the Raman detuning $\delta_{\text{Raman}} = 0$.

Discussion of the lowest attainable temperature

A relevant question that emerges at this point is which is the lowest temperature one can achieve with this cooling strategy. A semi-classical simulation of the movement of a ^{40}K atom in the three-dimensional molasses appears to show that the temperature can reach very low temperatures. In metastable ^{4}He*, Lawall et al. [110] managed to cool down 10^4 atoms to the sub-recoil regime $T = 180\text{nK} \approx T_R/22$. In ^{133}Cs it was reported that temperature was limited by atomic density. Indeed, for densities smaller than 10^9 atoms/cm^3 the measured temperature was of $T = 1.1\mu\text{K} \approx 2.4T_R$, while for higher values of density it was observed that temperature increased with a slope of $0.6\mu\text{K}/(10^{10}\text{atoms/cm}^3)$ [21]. The authors attributed this effect to "photon multiple scattering within the [gray molasses] atomic cloud". This effect is strong in "standard" bright molasses, but it is weak in gray molasses since atoms are accumulated in dark states and therefore light induced collisions are suppressed. In the

^{40}K setup the smallest temperature obtained was 20μK and the estimated density is of 2×10^{10} atoms/cm^3. By changing the atomic density there was no clear experimental evidence that there was a temperature variation. On the other hand, it was verified that temperature depends on the magnetic field bias B as $\Delta T \sim 80B^2\mu$K/G^2 and for that reason all the experiments reported in this thesis were done with cancelled stray magnetic fields to less than 100mG. Recent experiments done on ^{39}K, which has a even narrower D_1 excited state splitting (55.5MHz) than ^{40}K, show gray molasses cooling down to 6μK of an atomic cloud with density 1.3×10^{11} atoms/cm^3 [172]. This encourages the conclusion that probably the coldest temperature achieved on the ^{40}K setup was actually limited by technical imperfections. One possibility is the lack of fine control of the laser power balance between the different axes of the three-dimensional molasses[17].

Measurement of the molasses diffusion coefficient

Finally, we increased substantially the molasses time up to 0.5s in order to measure the molasses lifetime and the diffusion coefficient. The lifetime was determined to be $\sim$ 0.6s, probably limited by small misalignments of the beams and/or beam power imbalance. The spatial diffusion coefficient D_x was determined from the cloud size after a time-of-flight[18] of 10ms for different molasses times τ_m and the relation $\sigma^2 = \sigma_0^2 + 2D_x\tau_\mathrm{m}$. We estimate the spatial diffusion coefficient to be $D_\mathrm{x} \approx 1.2$ mm^2/s (results shown in fig. 4.5.6). In other experiments, with standard bright molasses and different conditions (cooling transition, light intensity, polarizations and detuning) higher (^{39}K [107]) and lower values (^{85}Rb [87]) for the spatial diffusion coefficient have been found.

4.5.2 Role of the repumper: study of the Raman detuning

Due to the open nature of the D_1 transition, one intuitively concludes that there is a need of a repumper to pump back the atoms accumulated in the $F = 7/2$ state

[17] Indeed we observed a drift of the molasses with speed $\sim$ 5mm/s in one of the axes during the molasses phase.

[18] Assuming that the temperature is the same for all data points, the squared cloud size after time-of-flight only differs from the squared *initial* cloud size by a constant.

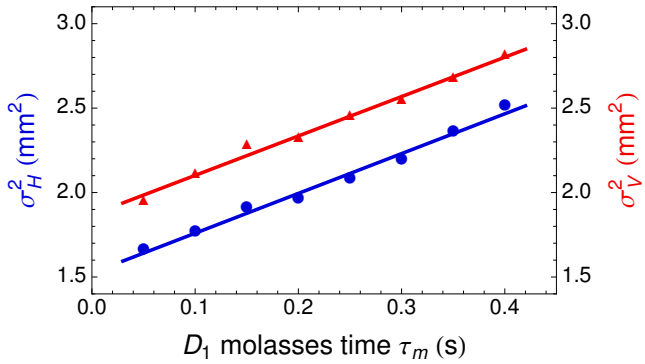


Figure 4.5.6: Squared cloud size after fixed time of flight as a function of the molasses duration τ_m. In blue we plot the data for the horizontal axis and in red the data for the vertical axis (gravity direction). The slopes of each axis are identical to the 10^{-2} level.

in the cooling transition. This was already realized in the pioneering studies of the gray molasses mechanism [20, 21, 55]. Actually it was discovered in this work that the repumper can have a more subtle and complex effect than just repumping the atoms back into the cooling transition: It can actually have a cooling effect of its own. Indeed, if one looks closely to scheme 4.3.1 one can see that if the cooling and repumper light fulfill the Raman condition, they form exactly the Λ structure discussed in section 4.2. Indeed this configuration will provide a new dark state manifold and a new bright state manifold in which gray molasses cooling can occur. For the sake of clarity we shall call this the *hyperfine gray molasses*, in order to distinguish from the cooling discussed in previous sections, which we shall call the *Zeeman gray molasses*. By varying the frequency of the repumper light (and consequently the Raman detuning) it was observed that these two molasses mechanisms can strongly interact between each other [74].

It was observed that when the Raman detuning was negative $\delta_{\text{Raman}} < 0$ (repumper light slightly blue or even red detuned from the repumper transition $F = 7/2 \rightarrow F' = 7/2$) the variation of the detuning had almost no effect on the temperature and the capture efficiency (see fig. 4.5.7). Comparing to the $\delta_{\text{Raman}} = 0$ case, the temperature was higher (around 45μK) and the capture efficiency lower (around 80%). Around the Raman condition, the system responded quite strongly with the Raman detuning, dis-

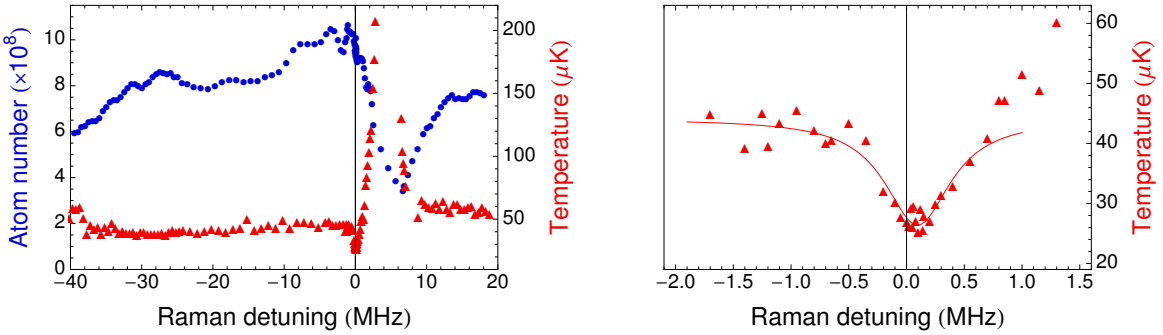


Figure 4.5.7: Number of atoms captured in the molasses (blue) and temperature (red) as a function of the Raman detuning (for a fixed cooling detuning). The plot at the right is an enlarged view close to the Raman resonance condition.

playing a resonance feature (fig. 4.5.7). By fitting this feature with a Lorentzian profile the minimal temperature observed was 26μK at $\delta = (0.10 \pm 0.02)$MHz and the width of the resonance was (0.7 ± 0.1)MHz (FWHM). The enhancement of cooling can be understood as a *cooperative* cooling interaction between the hyperfine and Zeeman cooling mechanisms. For red Raman detuning $\delta_{\text{Raman}} < 0$ (far from resonance) the two mechanisms decouple: the Zeeman gray molasses are sole responsible for the cooling, which is less performant without the combined action of the hyperfine cooling mechanism. Actually, one might expect that a detuned Λ configuration would induce heating, but it seems that it is prevented by the strong power imbalance between cooling and repumper. Indeed, we observed considerable heating for ^{6}Li and $\delta_{\text{Raman}} < 0$ when $I_{\text{cool}} \approx I_{\text{repumper}}$ compared to the imbalanced case [184]. In the balanced case, the effect of changing the Raman detuning on the hyperfine gray molasses is analogous to the effect of changing the magnetic field bias on the Zeeman gray molasses. In the imbalanced case, the heating effect is suppressed and the role of the repumper is mainly to repump atoms back into the cooling transition.

For blue Raman detuning $\delta_{\text{Raman}} > 0$ the situation is apparently very different from the one described above. Indeed, we observe a sharp peak of heating at $\delta = +(4.24 \pm 0.05)$MHz. This could be interpreted as a *destructive* effect of the repumper light on the Zeeman gray molasses. When the repumper detuning is such that the atoms in the $F = 7/2$ state are pumped to the top of a hill of the bright state potential (see fig. 4.2.1), they accelerate by falling down the optical potential, increasing their kinetic

energy and generating heating. To test this explanation we measured the position of the heating peak for two values of intensity (maintaining the ratio $I_{\text{repumper}}/I_{\text{cool}}$ constant) for ^{6}Li. It was observed that: The heating peak position displaced by a positive amount proportional to the laser intensity; The width of the heating peak also increased with intensity. This is consistent with the simple explanation put forward above since the light shift of the bright states is proportional to the light intensity.

We did not try to study the role of the phase of the repumper laser field relative to the one of the cooling in the molasses performance [80]. We estimate that in the three-dimensional configuration the relative phase is modulated in space and only has an averaged effect [74].

4.6 Gray molasses cooling of ^{6}Li

Due to the very narrow excited state structure of the $P_{3/2}$ level of ^{6}Li (compared with the linewidth Γ), it is not possible to attain efficient sub-Doppler cooling, as argued in the introduction of this chapter. The same gray molasses cooling strategy described for ^{40}K was employed for ^{6}Li, with identical results concerning the behavior of the capture fraction and the temperature as a function of the different experimental parameters. The gray molasses were operated with a cooling intensity per beam of $I_{\text{cool}}/I_{\text{sat}} = 15$, a cooling/repumper ratio of $I_{\text{repump}}/I_{\text{cool}} = 1/20$, a detuning of $\delta = 4\Gamma$ on the Raman resonance $\delta_{\text{Raman}} = 0$ (see fig. 4.6.1). After the CMOT phase there were 2×10^9 atoms at 800μK. For a gray molasses cooling sequence of 5ms, one could capture 1.2×10^9 atoms in the molasses (60% capture efficiency) and cool them down to 44μK. This cooling phase enhanced the PSD of factor ≈ 30. When performing the molasses cooling for ^{40}K simultaneously, no interspecies interaction was observed. This was expected since the cooling phase is fast and light-induced collisions are highly suppressed due to the accumulation of the atoms in the dark states. For a detailed study of the performance of the ^{6}Li gray molasses we refer the reader to ref. 184. Recently, Sisyphus cooling of ^{6}Li was observed in Berkeley [82] and related studies were reported by a team in Florence [25].

4.6.1 Experimental setup - offset lock

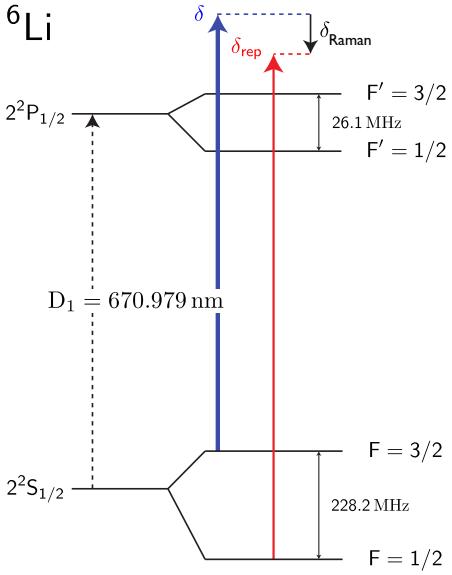


Figure 4.6.1: Level scheme of the transitions used for D_1 gray molasses cooling of ^{60}Li. In blue is depicted the cooling laser frequency (positive detuning δ from the $F = 3/2 \rightarrow F' = 3/2$ transition) and in red the repumper frequency (detuning δ_{rep} from the $F = 1/2 \rightarrow F' = 3/2$ transition).

The ^{6}Li system for D_1 gray molasses cooling (see section 2.2.2 and appendix 2.C) is identical to the one of ^{40}K described above, but with some differences worth mentioning. The light source is a compact tunable diode laser system amplified by a TA integrated in a single unit[19]. A small portion of the diode laser power is used for locking, which will be described in a following paragraph. The amplified output ($\sim$ 450mW) is beam shaped to optimize fiber injection and passes through an EOM[20] for the generation of the repumper sideband. The signal fed to the EOM is produced by a synthesizer[21] tuned to the ground state hyperfine splitting of ^{6}Li (228.2MHz) and then amplified[22]. The laser beam passes through an AOM[23] in single pass (-110MHz) before being injected to a polarization maintaining fiber. Around 40% of the power of the initial beam from the TA is measured at the output of the fiber.

To lock the laser light frequency to the D_1 line it was decided to implement an offset lock based on the setup of ref. 169. The idea is to beat the D_1 laser light with a D_2 reference, which is locked to an atomic absorption line by saturated absorption spectroscopy, and lock the beating signal to a precise offset frequency. The signal is first mixed down using as reference a stable (and tunable) signal at high frequency and then goes through the circuit that produces the error signal. In this circuit the signal (now at some tens of MHz) has its power divided in two: The first arm has a high pass filter at a cut frequency f_c and a diode that clips negative voltages; The second arm

[19] Toptica TA pro 670nm
[20] Qubig EO-Li6-3M
[21] Windfreak Technologies MixNV
[22] Mini Circuits ZHL-1-2W
[23] AA Opto-electronic MT110-B50A1-VIS

serves at reference and has a attenuator and a diode that clips positive voltages. These signals are then converted into DC and summed up. If $f > f_c$, the power is not attenuated in the first arm and the resulting DC sum signal is positive, since there is an attenuation in the reference arm. If $f < f_c$, the signal is attenuated in the first arm due to the high pass filter and the resulting DC is negative. This way one can have a dispersive signal around f_c with a rather steep slope (depending on the filter) and a good capture range. This contrasts with the "standard" delay-line technique [179], in which the output signal displays several dispersive signals and compromises have to be made in order to a good capture range and a steep error signal.

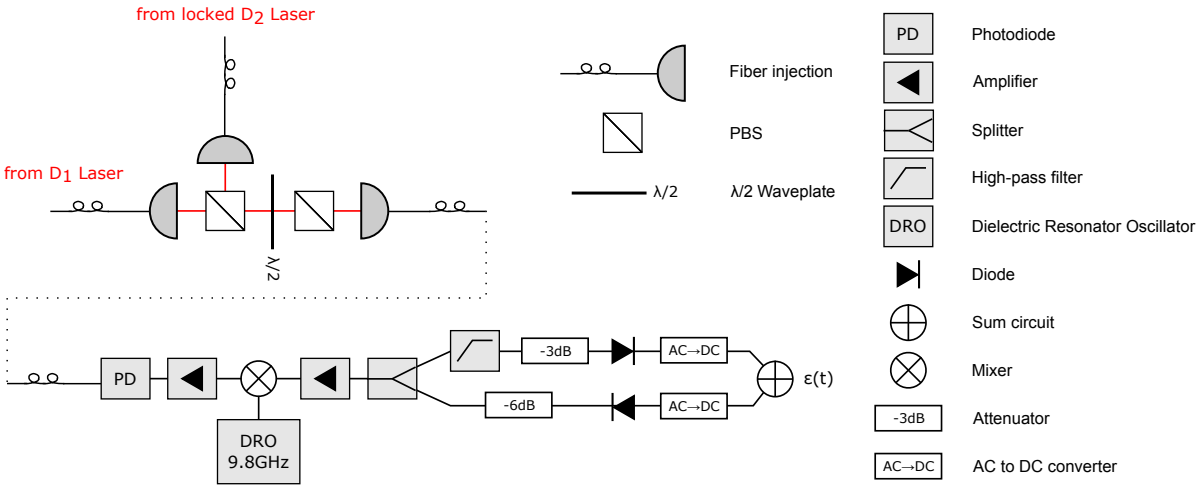


Figure 4.6.2: Scheme of the offset lock circuit described in the text.

The setup is depicted in fig. 4.6.2. A small portion of the diode laser beam is injected into a single mode fiber and a small portion of the spectroscopy locked D_2 diode laser beam is injected into a second fiber. The outputs of these fibers are combined spatial and polarisation-wise and injected into a third fiber which is connected to fast photodiode[24]. The power measured at the level of the photodiode is of 520μW for each individual beam. The electronic signal of the beating is then amplified[25]

[24]Newport 1580-A
[25]Mini-Circuits ZX60-183-S+

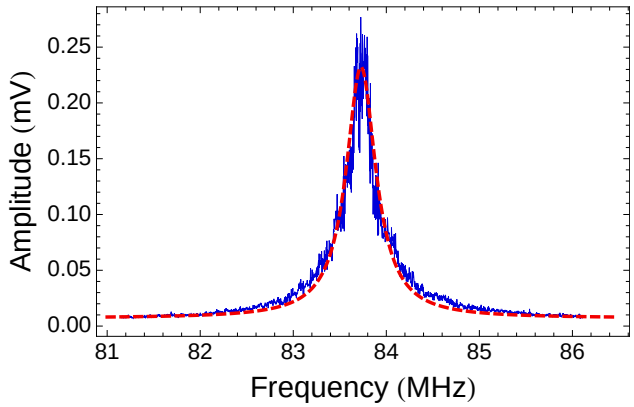


Figure 4.6.3: Spectrum of the mixed-down signal (bandwidth 10 kHz, integration time 1s, average of 10 shots). The red curve is a Lorentzian fit with central frequency 83.73 MHz and FWHM 0.39 MHz.

and mixed[26] with a stable reference at 9.783GHz[27]. The mixed down signal is then amplified[28] and the output power is divided in two[29] (a small fraction of the signal is picked up before the splitter by a coupler[30] for diagnostic purposes). After the splitter, the reference arm has two -3dB attenuators[31] and the filter arm has a -3dB attenuator and a high-pass filter[32]. The signal is then processed by a circuit similar to the one indicated in ref. 169, resulting in a dispersive signal, as explained above. This signal is fed into a PID circuit that feeds the piezoelectric element driving the grating of the ECDL for low frequency corrections and the current of the laser diode for the high frequency corrections. When locked, the mixed down signal was read by spectrum analyzer and the result outputted using the video output (see fig. 4.6.3 and its caption for details concerning the data acquisition). By fitting the signal with a Lorentzian we obtain the central frequency 83.73 MHz and the FWHM 0.39 MHz. The central frequency is close to the expected value for the used filter (82MHz). Without the fast

[26] Mini-Circuits ZX05-153LH-S+
[27] Dielectric Resonator Oscillator (DRO) made by CTI Inc. The specified thermal stability is 5ppm/°C$\widehat{=}$ 50kHz/°C and the mechanical tunability is $\pm$50MHz.
[28] Mini-Circuits ZFL-500+
[29] Mini-Circuits Z99SC-62-S+
[30] Mini-Circuits ZFDC-20-1H-S+
[31] Mini-Circuits VAT-3
[32] Mini-Circuits SHP-100+, nominal cut frequency at 82MHz (-3dB)

correction of the lock the FWHM was approximately 5 times higher. After several months of daily operation of the molasses, no drifts were observed in its performance, which validates the long-term stability of the lock.

4.7 Conclusions

The gray molasses cooling mechanism was implemented with success on ^{40}K and ^{6}Li on the D_1 transition. By having the cooling and the repumper light satisfying a Raman configuration enhanced cooling was observed. Compared with other reported cooling methods [50, 126], the gray molasses method yielded higher phase space density and the implementation of this scheme was fairly easy. Indeed, the light sources and techniques are the same as the ones used for the standard cooling, since the D_1 and the D_2 lines have very close wavelengths. The performance of the D_1 gray molasses is summarized in table 4.7.1.

	^{40}K	^{6}Li
I_{cool}	$13I_{\text{sat}}$	$15I_{\text{sat}}$
$I_{\text{rep}}/I_{\text{cool}}$	1/8	1/20
δ	2.3Γ	4Γ
N ($\times 10^9$)	3.2 (100%)	1.2 (60%)
T (μK)	20	44
PSD ($\times 10^{-5}$)	9.4	7

Table 4.7.1: Summary of the gray molasses parameters and resulting number of atoms, capture efficiency, temperature and phase space density (PSD).

The good performance and robustness of the gray molasses cooling attracted interest in the scientific community. This scheme was successfully implemented in other isotopes that do not display efficient sub-Doppler cooling: ^{7}Li [74], ^{39}K [138, 172] and ^{41}K (unpublished results of our group). Moreover, this technique allowed the implementation of efficient all-optical schemes for the production of quantum gases of ^{6}Li [25], ^{39}K [173] and ^{7}Li [98]. Gray molasses are at present a well-established technique for sub-Doppler cooling of atomic gases. In addition, this scheme could open the door for the implementation of single-atom resolved imaging [181, 210] of fermions in a pinning lattice, for which an efficient cooling mechanism is needed.

Appendix 4.A Publications

The work presented in this chapter was reported in the following articles:

- D. Rio Fernandes, F. Sievers, N. Kretzschmar, S. Wu, C. Salomon, and F. Chevy. *Sub-Doppler laser cooling of fermionic ^{40}K atoms in three-dimensional gray optical molasses*. EPL (Europhysics Letters) **100**, 63001 (2012).

- F. Sievers, S. Wu, N. Kretzschmar, D. Rio Fernandes, D. Suchet, M. Rabinovic, C. V. Parker, L. Khaykovich, C. Salomon, F. Chevy. *Simultaneous sub-Doppler laser cooling of fermionic ^{6}Li and ^{40}K: Theory and Experiment*. arXiv:1410.8545 (2014) (submited to Phys. Rev. A).

A Letters Journal Exploring the Frontiers of Physics

December 2012

EPL, **100** (2012) 63001
doi: 10.1209/0295-5075/100/63001

www.epljournal.org

Sub-Doppler laser cooling of fermionic ^{40}K atoms in three-dimensional gray optical molasses

D. Rio Fernandes[1(a),(b)], F. Sievers[1(a),(c)], N. Kretzschmar[1], S. Wu[2], C. Salomon[1] and F. Chevy[1]

[1] *Laboratoire Kastler-Brossel, École Normale Supérieure, CNRS and UPMC - 24 rue Lhomond 75005 Paris, France, EU*
[2] *Department of Physics, College of Science, Swansea University - Swansea, SA2 8PP UK, EU*

received 4 October 2012; accepted in final form 23 November 2012
published online 20 December 2012

PACS 37.10.De – Atom cooling methods
PACS 37.10.Gh – Atom traps and guides
PACS 67.85.-d – Ultracold gases, trapped gases

Abstract – We demonstrate sub-Doppler cooling of ^{40}K on the D_1 atomic transition. Using a gray-molasses scheme, we efficiently cool a compressed cloud of 6.5×10^8 atoms from $\sim 4\,$mK to $20\,\mu$K in 8 ms. After transfer to a quadrupole magnetic trap, we measure a phase space density of $\sim 10^{-5}$. This technique offers a promising route for fast evaporation of fermionic ^{40}K.

editor's choice Copyright © EPLA, 2012

Introduction. – Cooling of fermionic atomic species has played a fundamental role in the study of strongly correlated Fermi gases, notably through the experimental exploration of the BCS-BEC crossover, the observation of the Clogston-Chandrasekhar limit to superfluidity, the observation of the Mott-insulator transition in optical lattices, and the study of low-dimensional systems (see for instance [1,2] for a review). When the temperature is further decreased, new exotic phases are predicted (*p-wave* superfluids for spin imbalanced gases, antiferromagnetic order... [1,3,4]) and, as a consequence, intense experimental effort is currently under way to push the temperature limit achieved in ultracold fermionic samples in order to enter these novel regimes.

Most experiments on quantum degenerate gases begin with a laser cooling phase that is followed by evaporative cooling in a non-dissipative trap. Achieving quantum degeneracy depends critically on the collision rate at the end of the laser cooling phase and sub-Doppler cooling [5] is often a key ingredient for initiating efficient evaporation. In the case of fermionic lithium-6 and potassium-40, the narrow hyperfine structure of the $P_{3/2}$ excited level does not allow for efficient Sisyphus sub-Doppler cooling to the red of a $F \to F' = F + 1$ atomic transition [6,7].

Experiments for producing quantum degenerate gases of ^{40}K typically start with $\sim 10^8$ atoms laser-cooled to the Doppler limit ($145\,\mu$K) [8]. More refined laser-cooling schemes have produced ^{40}K temperatures of $\sim 15\,\mu$K, but with only reduced atom numbers ($\sim 10^7$) [7,9,10]. This relatively poor efficiency is due to the combination of the fairly narrow and inverted hyperfine level structure of the $P_{3/2}$ excited state which results in the washing out of the capture velocity of the molasses when the laser detuning is increased [11]. To overcome these limitations, two groups recently realized Magneto-Optical Traps (MOT) in the near-UV and blue regions of the spectrum to cool ^{6}Li [12] and ^{40}K [13], respectively. The associated transitions, being narrower than their D_2 counterparts, lead to a smaller Doppler temperature and were used to improve the final phase space density typically by one order of magnitude.

In this letter, we report efficient sub-Doppler cooling of ^{40}K atoms using gray molasses on the D_1 atomic transition at 770 nm. Thanks to the much reduced fluorescence rate compared to standard bright sub-Doppler molasses, we could produce cold and dense atomic samples. The temperature of a tightly compressed cloud of 6.5×10^8 atoms was decreased from $\sim 4\,$mK to $20\,\mu$K in 8 ms without significant change of the density in the process. After transfer to a quadrupole magnetic trap, we achieved a phase space density of $\sim 2 \times 10^{-5}$.

Gray molasses. – Sub-Doppler cooling using gray molasses was proposed in ref. [14] and realized in the mid 1990s on the D_2 atomic transition of cesium and rubidium, allowing one to cool atomic samples close to 6 times the

(a) These authors contributed equally to this work.
(b) E-mail: diogo.fernandes@lkb.ens.fr
(c) E-mail: franz.sievers@lkb.ens.fr

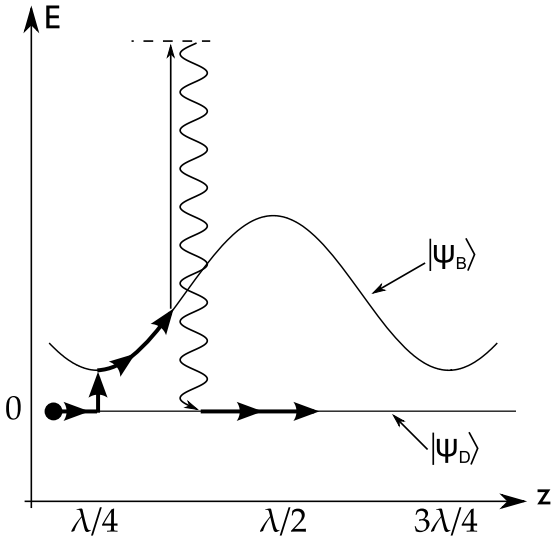


Fig. 1: Gray-molasses scheme. On a $F \to F' = F$ or $F \to F' = F-1$ optical transition with positive detuning, the ground state splits into a dark and a bright manifold with positive energy, shown as $|\psi_D\rangle$ and $|\psi_B\rangle$, respectively. In the presence of a polarization gradient, the bright-state energy is spatially modulated. Like in Sisyphus cooling, energy is lost when an atom in $|\psi_B\rangle$ climbs a potential hill before being pumped back into the dark state $|\psi_D\rangle$. Motional coupling between $|\psi_D\rangle$ and $|\psi_B\rangle$ occurs preferentially at the potential minima.

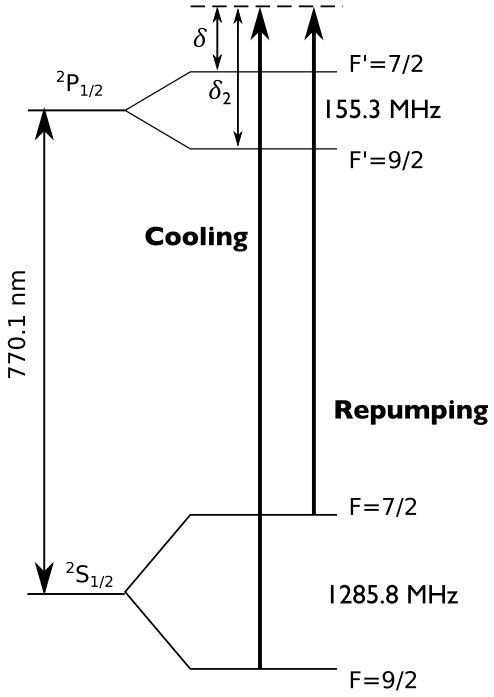


Fig. 2: Level scheme for the D_1 transition of ^{40}K and transitions used for gray-molasses cooling. The laser detuning from the cooling/repumping transitions is δ and the detuning from the off-resonant excited hyperfine state $F' = 9/2$ is δ_2 (see text).

single-photon recoil energy [15–17]. For an atomic ground state with angular momentum F, gray molasses operate on the $F \to F' = F$ ($F \to F' = F-1$) optical transition. For any polarization of the local electromagnetic field, the ground-state manifold possesses one (two) dark states which are not optically coupled to the excited state by the incident light [14,18]. When the laser is detuned to the blue side of the resonance, the ground-state manifold splits into dark states which are not affected by light and bright states which are light-shifted to positive energy by an amount which depends on the actual polarization and intensity of the laser field (see fig. 1).

When the atom is in a bright state, it climbs up the hill of the optical potential before being pumped back to the dark state near the top of the hill. The kinetic energy of the atom is thus reduced by an amount of the order of the height of the optical potential barrier. The cooling cycle is completed near the potential minima by a combination of motional coupling and optical excitation to off-resonant hyperfine states.

We implement 3D gray-molasses cooling in ^{40}K on the D_1 transition (see fig. 2). In alkali atoms, the $P_{1/2}$ excited level manifold has only two hyperfine states, which are better resolved than their $P_{3/2}$ counterparts. These facts allow for less off-resonant excitation and a good control of the cooling mechanism. A first laser beam (cooling beam) is tuned to the $|^2S_{1/2}, F = 9/2\rangle \to |^2P_{1/2}, F' = 7/2\rangle$ transition with a detuning $\delta > 0$. A second laser beam (repumping beam) is tuned to the $|^2S_{1/2}, F = 7/2\rangle \to |^2P_{1/2}, F' = 7/2\rangle$ transition with the same detuning δ.

As mentioned above, two mechanisms can lead to the departure from the dark state. The first one is the motional coupling V_{mot} due to the spatial variations of the dark state internal wave function induced by polarization and intensity gradients. The second one is the dipolar coupling V_{off} via off-resonant excited hyperfine states. A rough estimate shows that $V_{\mathrm{mot}} \simeq \hbar k v$, where v is the velocity of the atom and k the wave vector of the cooling light, while $V_{\mathrm{off}} \simeq \hbar\Gamma\,(\Gamma/\delta_2)\,I/I_{\mathrm{sat}}$, where Γ^{-1} is the lifetime of the excited state, I the light intensity, I_{sat} the saturation intensity and δ_2 the detuning to off-resonant excited state. Comparing the two couplings, we see that the motional coupling is significant in the high velocity regime $v \gtrsim \Gamma/k\,(\Gamma/\delta_2)\,I/I_{\mathrm{sat}}$. In our case, the off-resonant level $F' = 9/2$ (see fig. 2) is detuned by $\delta_2 = 155.3\,\mathrm{MHz} + \delta$ from the cooling transition $|^2S_{1/2}, F = 9/2\rangle \to |^2P_{1/2}, F' = 7/2\rangle$. For $I \simeq I_{\mathrm{sat}}$, motional coupling dominates for $T \gtrsim 50\,\mu$K, meaning that both processes are expected to be present in our experiments. In general, the transition rate between $|\psi_{\mathrm{D}}\rangle$ and $|\psi_{\mathrm{B}}\rangle$ induced by motional coupling V_{mot} and the off-resonant coupling V_{off} are both maximal when the distance between the dark and bright manifolds is smallest, which favors transitions near the bottom of the wells of the optical lattice.

In ^{40}K, the simplified discussion presented so far must be generalized to the case involving many hyperfine states $(10+8)$. However, the essential picture remains valid.

Indeed, by numerically solving the optical Bloch equations for the ^{40}K system in the presence of the cooling and repumping laser fields, we obtain the light shifts ϵ and the total optical pumping rates γ of all the dressed states for an atom at rest (see fig. 3). This is done for the particular case of a one-dimensional optical lattice in the lin⊥lin configuration and with a low repumping intensity (1/8 of the cooling beam intensity, typical for our experiments). In fig. 3a) we see 8 bright states, 2 weakly coupled states and 8 dark states combining both hyperfine manifolds. In fig. 3b) we plot the optical pumping rates of the corresponding dressed states. We find that the optical pumping rate is low for the weakly coupled states and it practically vanishes for the dark states. In fig. 3c) the optical pumping rates display a good correlation with the light shift magnitude, which favors efficient sub-Doppler cooling. Note also the long-lived dark states. This correlation shows that the gray-molasses picture remains valid for this more complex level scheme.

We now turn to the question of the capture velocity of the gray-molasses scheme. Let Γ' be the optical pumping rate from bright to dark states. The atom is pumped efficiently towards dark states if it stays a time $\tau \gtrsim \Gamma'^{-1}$ near the top of the hill. If the atom moves at a velocity v in the lattice, then $\tau \simeq 1/kv$ and the optical pumping to dark states is efficient when $kv \lesssim \Gamma'$. $v_c \simeq \Gamma'/k$ thus defines the capture velocity of the gray molasses. For a beam with detuning δ to the main cooling transition, $\Gamma' \propto I/\delta^2$ and thus v_c increases with laser intensity. On the other hand, the cooling efficiency is reduced when the atom cannot climb the potential hill anymore, which leads to an equilibrium temperature that scales as $k_B T \propto I/\delta$, when $T \gg T_{\mathrm{Recoil}} = \hbar^2 k^2/2mk_{\mathrm{B}}$ [5,19].

Experimental results. – Our setup is based on the apparatus presented in [20]. In the experiments presented here, 6.5×10^8 ^{40}K atoms are loaded from a two-dimensional magneto-optical trap (2D-MOT) into a three-dimensional magneto-optical trap (MOT) operating on the D_2 line. The initial temperature of the cloud is 200 μK, not far from the Doppler temperature $T_D = \hbar\Gamma/2k_{\mathrm{B}} = 145\,\mu$K, with $\Gamma/2\pi \approx 6.035$ MHz. In the MOT, the cooling and repumping laser intensities are $I_{\mathrm{cool}} = 13 I_{\mathrm{sat}}$ and $I_{\mathrm{repump}} = I_{\mathrm{cool}}/20$ per beam, with $I_{\mathrm{sat}} = 1.75$ mW/cm^2. After the loading phase, we ramp the magnetic field gradient from 9 G · cm^{-1} to 60 G · cm^{-1} in 5 ms without changing the laser detunings in order to compress the cloud. This process yields a cloud with high density, but with a much higher temperature of ~ 4 mK. At this point the magnetic field is switched off in $\simeq 100\,\mu$s and the D_1 molasses beams are switched on for a time τ_{m}.

The D_1 cooling and repumping beams are detuned by the same amount δ in the range of 2Γ–5Γ as shown in fig. 2. The repumping beam is detuned from the main cooling beam by 1285.8 MHz using an electro-optical modulator. Its intensity is typically 1/8 of the cooling beam intensity. After propagation through an optical fiber, the total D_1 optical power is 240 mW and the beam is magnified to a waist of 1.1 cm. We then split the beam into two vertical beams and two retro-reflected horizontal beams in a three-dimensional σ^+/σ^- configuration. The maximum D_1 cooling intensity per beam attained in our experiments is 25 mW/cm^2 or $I = 14 I_{\mathrm{sat}}$.

We first measure the atom number and temperature of the D_1 molasses as a function of the cooling beam

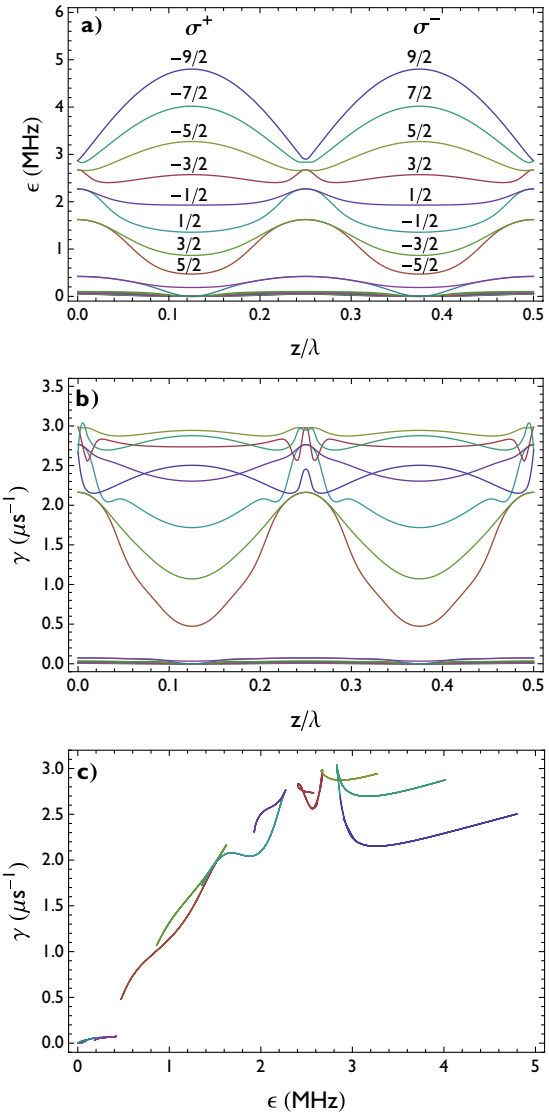


Fig. 3: (Color online) Semi-classical calculation of the effect of dual frequency counterpropagating laser beams in a 1D lin⊥lin configuration on a ^{40}K atom at rest. a) Light shifts ϵ *vs.* position; b) optical pumping rates γ; c) optical pumping rates *vs.* light shifts. The laser intensities are $I_{\mathrm{cool}} = 20 I_{\mathrm{sat}}$ and $I_{\mathrm{repump}} = I_{\mathrm{cool}}/8$ per beam, with $\delta = +3\Gamma$. The different lines correspond to the 18 dressed states of the $^2S_{1/2}$ ground state. At $z = \lambda/8$ the local polarization is σ^+ and here each curve corresponds to a pure m_F state. At this position the light shift increases with $-m_F$. The $|^2S_{1/2}, F = 7/2\rangle$ manifold interacts only weakly with light since the repumping beam is kept at low intensity. Consequently, the light shifts and optical pumping rates are small.

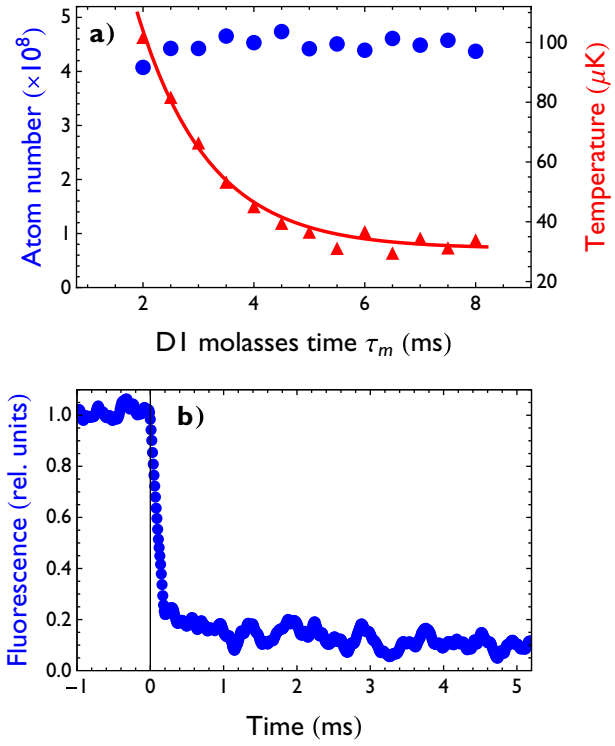


Fig. 4: (Color online) a) Number of atoms captured in the D_1 molasses (circles) and their temperature (triangles) as a function of molasses duration. The number of atoms in the compressed MOT was 4.5×10^8. b) Measured fluorescence during the MOT and the D_1 molasses phase. Both experiments were performed with $I_{\rm cool} = 14 I_{\rm sat}$, $\delta = 2.3\Gamma$ and $I_{\rm repump} = I_{\rm cool}/8$.

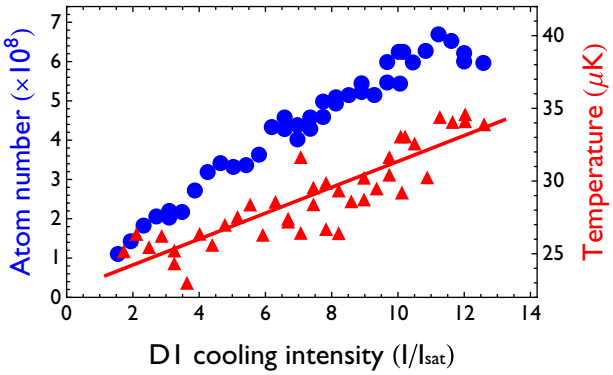


Fig. 5: (Color online) Number of atoms captured in the D_1 molasses (circles) and their temperature (triangles) as a function of the D_1 cooling beam intensity for $\delta = 2.3\Gamma$ and $I_{\rm repump} = I_{\rm cool}/8$. The number of atoms in the compressed MOT was 6.5×10^8 and the capture efficiency reaches $\sim$ 100% for $I \geqslant 11 I_{\rm sat}$.

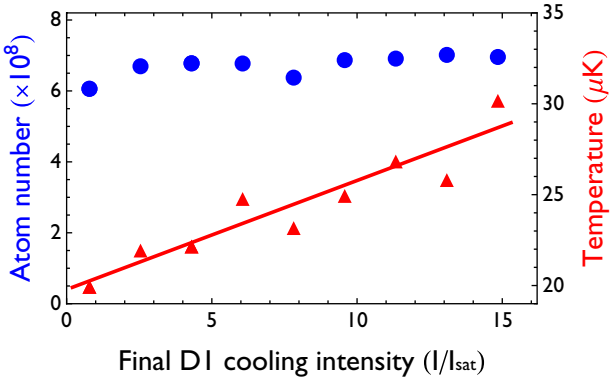


Fig. 6: (Color online) Number of atoms captured in the D_1 molasses (circles) and their temperature (triangles) after a 6 ms capture phase at high intensity $I_{\rm cool} = 14 I_{\rm sat}$ followed by a 2 ms linear intensity ramp to adjustable value. The detuning is fixed to $\delta = 2.3\Gamma$. The number of atoms in the compressed MOT was 7×10^8.

duration $\tau_{\rm m}$ (fig. 4). The temperature is determined by time of flight. At high intensity $I_{\rm cool} = 14 I_{\rm sat}$ and detuning $\delta = 2.3\Gamma$, all 4.5×10^8 compressed MOT atoms are cooled to a temperature of 30 μK in 6 to 8 ms. Although the initial temperature of the compressed MOT is rather high, D_1 cooling occurs rapidly. As shown in fig. 4a), the temperature drops from $\sim$ 4 mK to 100 μK in 2 ms, and reaches its asymptotic value in about 6 ms. These dynamics are confirmed by direct measurement of the fluorescence light emitted during the D_1 molasses phase, as displayed in fig. 4b). The fluorescence exhibits a fast decay in $\sim$ 200 μs to about 20% of the MOT light followed by a slower decay in $\sim$ 3 ms to 10%, which indicates the accumulation of atoms in weakly coupled states.

When repeating the experiment for lower D_1 laser intensities for a fixed time of 6 ms, we observe both a decrease of the number of atoms cooled by gray molasses and a further lowering of the temperature down to 24 μK (fig. 5). The number of atoms is measured after a time of flight of 20 ms, after which we would not detect any atoms in the absence of D_1 molasses. The capture efficiency increases with the cooling intensity indicating a higher capture velocity at higher laser intensity and it reaches $\sim$ 100% for $I \geqslant 11 I_{\rm sat}$. Similarly, the equilibrium temperature increases with laser intensity in the explored range in agreement with Sisyphus-type cooling mechanisms.

The results of fig. 4 and fig. 5 suggest implementing a cooling sequence with two successive phases. A first phase lasting 6 ms at high D_1 cooling intensity takes advantage of the high capture velocity. This phase is followed by a 2 ms stage in which the intensity is linearly reduced by an adjustable amount to further lower the temperature. As illustrated in fig. 6, this supplementary cooling phase allows the sample to reach a temperature of 20 μK by reducing the intensity by one order of magnitude and without any atom loss. No significant change of the atomic cloud volume was observed during this 8 ms sequence.

In fig. 7, we show the number of atoms captured in the D_1 molasses and their temperature as a function of the laser detuning δ for the complete 8 ms sequence. For $\delta \in [0.5\Gamma, 2\Gamma]$, we observe a steep decrease of the temperature from 100 μK to 30 μK, as expected from Sisyphus cooling,

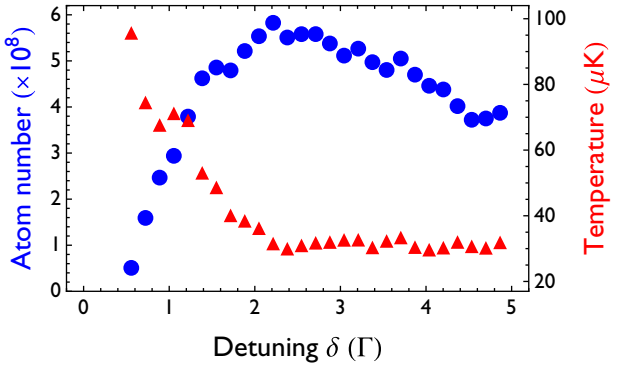


Fig. 7: (Color online) Number of atoms captured in the D_1 molasses (circles) and their temperature (triangles) for the dynamic 8 ms cooling sequence as a function of the detuning δ. The number of atoms in the compressed MOT was 6×10^8.

followed by a plateau near $30\,\mu$K for detunings above 2Γ. The capture efficiency raises sharply to $\sim 100\%$ at $\delta \sim 2.3\Gamma$, displays a broad maximum and slowly decreases above 4Γ, indicating a decrease of the capture velocity.

We have also scanned the intensity and the detuning of the repumping laser. We observe a very weak dependence of the molasses temperature and capture fraction upon repumping intensity. On the other hand, when scanning the repumper detuning, we observe that cooling is optimal within 300 kHz from the exact Raman condition. This points to the existence of long-lived coherences between the two hyperfine manifolds $|^2S_{1/2}, F = 9/2\rangle$ and $|^2S_{1/2}, F = 7/2\rangle$, resulting in the formation of new inter-manifold dark states. Finally, optimal parameters for ^{40}K gray molasses are summarized in table 1.

We checked that the minimum temperature of $20\,\mu$K is not limited by residual magnetic fields nor by atomic density. We found that the residual magnetic field during the D_1 molasses should be minimized. Indeed, introducing a small tunable bias magnetic field B in the vertical direction, the D_1 molasses temperature increased quadratically as $\Delta T \approx 80 B^2 \mu\mathrm{K/G}^2$. For this reason, the stray magnetic field was cancelled to less than 100 mG in three directions using compensation coils. We also searched for a density dependent temperature limitation and observed no significant temperature change when the density was reduced by a factor of 4 from $n_0 \sim 2 \times 10^{10}\mathrm{cm}^{-3}$. Modeling gray-molasses cooling in three dimensions in order to understand the temperature limit remains today an open problem.

Magnetic trapping. – After the D_1 molasses phase, the atoms are optically pumped to the $|^2S_{1/2}, F = 9/2, m_F = 9/2\rangle$ stretched state and then transferred into a quadrupole magnetic trap. The σ^+ polarized optical pumping laser beams are pulsed for $120\,\mu$s in the presence of a bias magnetic field. After this phase, the trap axial magnetic field gradient is raised from 0 to $37\,\mathrm{G \cdot cm}^{-1}$ in 3 ms, followed by a compression

Table 1: Optimized parameters for ^{40}K D_1 gray molasses. Using these parameters, all the 6.5×10^8 atoms from a compressed MOT are cooled to $20\,\mu$K in D_1 gray molasses.

	Duration (ms)	$I_{\mathrm{cool}}(I_{\mathrm{sat}})$	$\delta(\Gamma)$
Capture phase	6	14	+2.3
Cooling phase	2	14→1	+2.3

to 76 $\mathrm{G \cdot cm}^{-1}$ in 147 ms and a thermalization stage lasting 350 ms during which the field gradient remains constant. At this point we detect 2.5×10^8 atoms at a temperature of $80\,\mu$K. Assuming that all atoms are in the $|F = 9/2, m_F = 9/2\rangle$ stretched state, the central phase-space density is $\mathrm{PSD} = n_0 \lambda_{\mathrm{dB}}^3 \approx 2 \times 10^{-5}$. In the absence of gray-molasses phase, the central phase-space density is about 100 times lower. From the *p-wave* cross-section $\sigma \approx 2 \times 10^{-11}\,\mathrm{cm}^2$ at a temperature of $80\,\mu$K measured in [21], we estimate the trap averaged initial collision rate to be $\gamma_{\mathrm{coll}} = n_0 \sigma \bar{v}/8\sqrt{2} \approx 23\,\mathrm{s}^{-1}$. This rate is quite favorable for initiating evaporative cooling.

Conclusion. – We have shown that gray molasses operating on the D_1 optical transition is a very simple and powerful method to increase the phase space density of laser-cooled ^{40}K alkali gases to $\sim 10^{-5}$. This phase space density leads to excellent starting conditions for evaporative cooling in magnetic or optical dipole traps. For ^{40}K, this is particularly useful as the low temperature allows direct transfer into an optical trap and magnetic tuning to a Feshbach resonance for efficient evaporation. Moreover, our results open the way for sub-Doppler cooling of other atoms with narrow $P_{3/2}$ excited states, such as ^{6}Li and ^{7}Li. We already have experimental evidence for sub-Doppler D_1 cooling of ^{6}Li and ^{7}Li and this will be the subject of a future publication.

* * *

We acknowledge useful discussions with J. V. Porto, J. Dalibard, L. Khaykovich and D. Suchet. We acknowledge support from Région Ile de France (IFRAF), EU (ERC advanced grant Ferlodim) and Institut Universitaire de France. DRF acknowledges the support of Fundação para a Ciência e Tecnologia (FCT-Portugal), through the grant number SFRH/BD/68488/2010.

REFERENCES

[1] Inguscio M., Ketterle W. and Salomon C. (Editors), *Ultracold Fermi gases*, in *Proceedings of the International School of Physics "Enrico Fermi"*, Course CLXIV (IOS Press, Società Italiana di Fisica) 2006.

[2] Bloch I., Dalibard J. and Zwerger W., *Rev. Mod. Phys.*, **80** (2008) 885.

[3] Bulgac A., Forbes M. M. and Schwenk A., *Phys. Rev. Lett.*, **97** (2006) 020402.
[4] Werner F., Parcollet O., Georges A. and Hassan S. R., *Phys. Rev. Lett.*, **95** (2005) 056401.
[5] Dalibard J. and Cohen-Tannoudji C., *J. Opt. Soc. Am. B*, **6** (1989) 2023.
[6] Lin Z., Shimizu K., Zhan M., Shimizu F. and Takuma H., *Jpn. J. Appl. Phys.*, **30** (1991) L1324.
[7] Modugno G., Benkö C., Hannaford P., Roati G. and Inguscio M., *Phys. Rev. A*, **60** (1999) R3373.
[8] DeMarco B. and Jin D. S., *Science*, **285** (1999) 1703.
[9] Taglieber M., Voigt A.-C., Aoki T., Hänsch T. W. and Dieckmann K., *Phys. Rev. Lett.*, **100** (2008) 010401.
[10] Gokhroo V., Rajalakshmi G., Easwaran R. K. and Unnikrishnan C. S., *J. Phys. B: At. Mol. Opt. Phys.*, **44** (2011) 115307.
[11] Landini M., Roy S., Carcagn L., Trypogeorgos D., Fattori M., Inguscio M. and Modugno G., *Phys. Rev. A*, **84** (2011) 043432.
[12] Duarte P., Hart R., Hitchcock J., Corcovilos T., Yang T.-L., Reed A. and Hulet R., *Phys. Rev. A*, **84** (2011) 063420.
[13] McKay D., Jervis D., Fine D., Simpson-Porco J., Edge G. and Thywissen J., *Phys. Rev. A*, **84** (2011) 063420.
[14] Grynberg G. and Courtois J.-Y., *Europhys. Lett.*, **27** (1994) 41.
[15] Boiron D., Meacher D. and Verkerk P., *Phys. Rev. A*, **52** (1995) 3425.
[16] Esslinger T., Sander F., Hemmerich A., Hänsch T. W., Ritsch H. and Weidemüller M., *Opt. Lett.*, **21** (1996) 991.
[17] Boiron D., Michaud A., Lemonde P., Castin Y., Salomon C., Weyers S., Szymaniec K., Cognet L. and Clairon A., *Phys. Rev. A*, **53** (1996) R3734.
[18] Ol'shani M. and Minogin V., *Opt. Commun.*, **89** (1992) 393.
[19] Castin Y. and Dalibard J., *Europhys. Lett.*, **14** (1991) 761.
[20] Ridinger A., Chaudhuri S., Salez T., Eismann U. Fernandes D., Magalhaes K., Wilkowski D., Salomon C. and Chevy F., *Eur. Phys. J. D*, **242** (2011) 223.
[21] DeMarco B., Bohn J. L., Burke J. P., Holland M. and Jin D. S., *Phys. Rev. Lett.*, **82** (1999) 4208.

arXiv:1410.8545v1 [physics.atom-ph] 30 Oct 2014

Simultaneous sub-Doppler laser cooling of fermionic ^{6}Li and ^{40}K on the D_1 line: Theory and Experiment

Franz Sievers,[1,*] Saijun Wu,[2,†] Norman Kretzschmar,[1] Diogo Rio Fernandes,[1] Daniel Suchet,[1] Michael Rabinovic,[1] Colin V. Parker,[3] Lev Khaykovich,[4] Christophe Salomon,[1] and Frédéric Chevy[1]

[1] *Laboratoire Kastler Brossel, École Normale Supérieure, CNRS, UPMC, 24 rue Lhomond, 75005 Paris, France*
[2] *State Key Laboratory of Surface Physics and Department of Physics, Fudan University, 200433 Shanghai, P. R. China*
[3] *James Franck Institute, Enrico Fermi Institute and Department of Physics, University of Chicago, Chicago, IL 60637, USA*
[4] *Department of Physics, Bar-Ilan University, Ramat-Gan 52900, Israel*

(Dated: November 3, 2014)

We report on simultaneous sub-Doppler laser cooling of fermionic ^{6}Li and ^{40}K using the D_1 optical transitions. We compare experimental results to a numerical simulation of the cooling process applying a semi-classical Monte Carlo wavefunction method. The simulation takes into account the three dimensional optical molasses setup and the dipole interaction between atoms and the bichromatic light field driving the D_1 transitions. We discuss the physical mechanisms at play, we identify the important role of coherences between the ground state hyperfine levels and compare D_1 and D_2 sub-Doppler cooling. In 5 ms, the D_1 molasses phase largely reduces the temperature for both ^{6}Li and ^{40}K at the same time, with a final temperature of 44 μK and 11 μK, respectively. For both species this leads to a phase-space density close to 10^{-4}. These conditions are well suited to directly load an optical or magnetic trap for efficient evaporative cooling to quantum degeneracy.

PACS numbers: 37.10.De, 32.80.Wr, 67.85.-d

CONTENTS

Introduction 1

I. D_1 cooling mechanism 2
A. Semi-classical Monte Carlo simulation 2
B. Raman-detuning dependence for ^{6}Li 3
C. Raman-detuning dependence for ^{40}K 5
D. The D_1 cooling mechanism 5
E. Physical picture of the Raman-detuning effect 7

II. Simultaneous ^{6}Li and ^{40}K D_1 cooling 8

III. Conclusion 9

Acknowledgments 9

Appendix: Experimental details 9
1. ^{6}Li D_1 molasses 10

References 11

INTRODUCTION

The road towards quantum degeneracy in atomic gases usually starts with a laser cooling and trapping phase. The resulting initial phase-space density of the atomic ensemble and the initial collision rate should be as large as possible for initiating efficient evaporative cooling to quantum degeneracy. Sub-Doppler cooling has proven to be a powerful technique to increase the phase-space density of most alkali atoms and other atoms with multiple level structure [1–3]. However, in the case of lithium and potassium, the narrow excited-state structure of the D_2 transition compromises the efficiency of this cooling scheme [4, 5]. Both species possess stable fermionic and bosonic isotopes, and they play an important role in recent experimental studies of strongly correlated quantum gases. Thus, important efforts have been devoted to search for alternative laser cooling schemes.

For instance, it has recently been shown that three dimensional Sisyphus cooling for ^{7}Li, some GHz red detuned from the D_2 line, can lead to temperatures as low as 100 μK with up to 45 % of the atoms in the cooled fraction [6]. A second option is to operate the magneto-optical trap (MOT) on a transition with smaller linewidth to reduce the Doppler temperature [7–9]. Such transitions exist for ^{6}Li and ^{40}K in the near-UV and blue regions of the spectrum, respectively, leading to temperatures of 33 μK for ^{6}Li and 63 μK for ^{40}K. Yet, special optics and a coherent source at 323 nm for ^{6}Li and 405 nm for ^{40}K are needed for this approach. Additionally, at these wavelengthes the available power is still a limiting factor.

* franz.sievers@lkb.ens.fr
† saijunwu@fudan.edu.cn

More recently a simpler sub-Doppler cooling scheme using blue detuned molasses operating on the D_1 line was proposed and demonstrated on ^{40}K [10] and has been extended to other atomic species such as ^{7}Li [11], ^{39}K [12, 13] and ^{6}Li [14]. Using this technique, temperatures as low as 20 μK (^{40}K), 50 μK (^{7}Li), 6 μK (^{39}K) and 40 μK (^{6}Li) were reached.

Even though the main ingredients of the D_1 cooling scheme are now understood at a qualitative level, in particular the role of the coherences between hyperfine ground-state levels [11], a complete picture, taking into account the full level-structure of the atoms, is still missing. In this paper, we present a three-dimensional semi-classical solution of the optical Bloch equations that takes into account the full set of relevant energy levels of alkali atoms and we apply it to the case of ^{6}Li and ^{40}K. The model fully confirms the experimentally observed cooling behaviour and its robustness with respect to changes in experimental parameters. The model is validated by a good match between the simulation and the experimentally measured temperature and fluorescence rate. We recover the important role of the Raman-detuning between the main cooling laser and the repumping laser on the achievable temperature. We show here for both ^{6}Li and ^{40}K, that the gain in temperature of a factor of $\sim$3 at the exact Raman-resonance is well reproduced by the theoretical model and that the amount of coherence between both hyperfine states shows a pronounced resonance behavior. Beyond individual studies of the two species, we also show experimentally that simultaneous cooling of ^{6}Li and ^{40}K does not lead to any severe trade-off and is technically easy to implement. We are able to capture more than 1×10^9 atoms of each species, with a capture efficiency exceeding 60 % from a compressed magneto-optical trap (CMOT), and reach temperatures as low as 44 μK for ^{6}Li and 11 μK for ^{40}K within 5 ms.

I. D_1 COOLING MECHANISM

In a typical D_1 cooling setup (Fig. 1), all the D_1 hyperfine levels are involved in the interaction. The sub-Doppler cooling effects include a mix of Sisyphus cooling, motion-induced and off-resonant light coupling from gray to bright levels, and coherent population trapping of slow atoms in nearly decoupled states. In this section we first introduce our semi-classical laser cooling model. We then present and compare the results from experimental observations and numerical simulations, and finally discuss the physical mechanism of D_1 cooling.

A. Semi-classical Monte Carlo simulation

The level diagrams of our bichromatic cooling scheme for both ^{6}Li and ^{40}K are depicted in Fig. 1. The D_1 molasses is composed of a 3D lattice whose polarization configuration is the same as that of a six-beam standard MOT, but with two sidebands to address the $|F = 3/2\rangle$ and $|F = 1/2\rangle$ hyperfine ground states of ^{6}Li (resp. $|F = 9/2\rangle$ and $|F = 7/2\rangle$ for ^{40}K) in the D_1 Λ-system at positive detunings.

Here, by convention, we refer to the $|F = 3/2\rangle \rightarrow |F'_h\rangle$ and $|F = 1/2\rangle \rightarrow |F'_h\rangle$ transitions as cooling/repumping transitions. It is however important to notice that neither the cooling nor the repumping D_1 transitions are actually closed.

Our numerical simulation of the cooling process is based on a semi-classical Monte Carlo wavefunction method. The simulation takes into account the three dimensional optical molasses setup and the dipole interaction between the single atoms and the polarized light driving the transitions of the D_1 manifold, which is spanned by the $4(2I+1)$ hyperfine Zeeman sub-levels ($I > 0$ is the nuclear spin). We treat the external states of the atom classically and update its position $\mathbf{r}(t)$ and velocity $\mathbf{v}(t)$ according to the calculated expectation value of the light force

$$\mathbf{f}(t) = \frac{\langle\psi(t)| - \nabla H_{\text{eff}}(\mathbf{r}(t))\,|\psi(t)\rangle}{\langle\psi(t)|\psi(t)\rangle}. \tag{1}$$

The atomic internal states $|\psi(t)\rangle$ evolve in a dressed basis with respect to the cooling laser (Fig. 1), according to the Monte Carlo wave function method [15, 16] with the effective rotating-wave Hamiltonian

$$H_{\text{eff}} = H_0 + H_{F=I-1/2} + H_{F=I+1/2} - i\hat{\Gamma}/2, \tag{2}$$

where

$$H_0 = \sum_m |F = I - 1/2, m\rangle\, \hbar\Delta\, \langle F = I - 1/2, m| - \sum_{F'm'} |F', m'\rangle\, \hbar(\delta_{\text{cool}} + \delta_{\text{hfs},F'})\, \langle F', m'|\,. \tag{3}$$

Here H_0 operates over the whole D_1 manifold, δ_{cool} is the detuning of the cooling laser with respect to the $F = I + 1/2 \rightarrow F'_h$ transition, where F'_h (Fig. 1) corresponds to the excited hyperfine level that is higher in energy, e.g. $F'_h = 3/2$ for ^{6}Li and $F'_h = 7/2$ for ^{40}K. $\Delta = \delta_{\text{rep}} - \delta_{\text{cool}}$ is the two-photon detuning for the $F = I - 1/2 \rightarrow F = I + 1/2$ Raman-transition, and $\delta_{\text{hfs},F'}$ the hyperfine splitting of the excited state for F'_l and zero for F'_h.

The light-atom coupling Hamiltonian

$$H_{F=I\pm1/2} = \hbar \sum_{m,\sigma,F',m'} \Omega_{F,\sigma}\; c_{F,m,\sigma,F',m'} \times |F, m\rangle\, \langle F', m'| + h.c. \tag{4}$$

describes the cooling ($F = I + 1/2$) and repumping ($F = I - 1/2$) interactions [17]. Here $\Omega_{F,\sigma}$ are the Rabi frequencies of the repumping and cooling laser beams for $F = I - 1/2$, $I + 1/2$ respectively. $c_{F,m,\sigma,F'm'}$ represent the Clebsch-Gordan coefficients associated with the transitions coupled by σ polarized light. To take into account the radiation damping we include the spontaneous emission rate $\hat{\Gamma} = \Gamma\hat{P}_{ee}$ where Γ is the excited-state linewidth

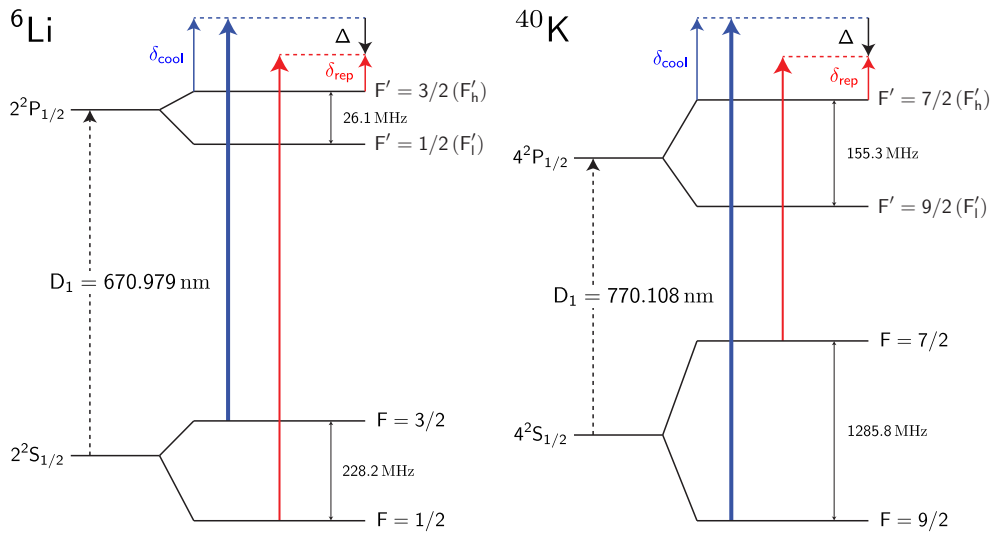


FIG. 1. (Color online) Cooling scheme on the ^{6}Li and ^{40}K D$_1$ lines. The cooling beam (blue) is blue detuned by $\delta_{\rm cool}$ from the $|F = 3/2\rangle \rightarrow |F'_h = 3/2\rangle$ ($|F = 9/2\rangle \rightarrow |F'_h = 7/2\rangle$) transition where F'_h (F'_l) is the upper (lower) excited state level. The repumping beam (red) is blue detuned by $\delta_{\rm rep}$ from the $|F = 1/2\rangle \rightarrow |F'_h = 3/2\rangle$ ($|F = 7/2\rangle \rightarrow |F'_h = 7/2\rangle$) transition. The detuning from the Raman-condition is denoted by $\Delta = \delta_{\rm rep} - \delta_{\rm cool}$.

and $\hat{P}_{ee} = \sum_{F',m'} |F'm'\rangle \langle F'm'|$. This leads to a decay of the internal state wave function norm $\langle\psi(t)|\psi(t)\rangle$. The speed of this decay probabilistically dictates the collapse of the internal quantum states in the numerical simulation, which corresponds to spontaneous emission. We take into account the polarization of the spontaneous scattering photon and follow the standard quantum jump procedure to project the atomic states to ground states with its norm reset to unity [15]. A recoil momentum shift is then assigned to $\mathbf{v}(t)$ before continuing to evolve $|\psi(t)\rangle$ via $H_{\rm eff}(\mathbf{r}(t))$.

The simulations are performed with parameters matching the experimental setup by properly introducing the spatially-dependent $\Omega_{F,\sigma}(\mathbf{r})$, the detunings Δ, $\delta_{\rm cool}$, and atomic initial conditions. To reproduce experimental conditions, we fix the relative phases for all the 12 cooling and repumping laser beams at values randomized for each simulation trial. We record the evolution of the 3D atomic velocity, the time-stamped fluorescence events corresponding to quantum jumps, as well as internal states properties such as state population and coherence. The observables are averaged over multiple simulation trials for comparison with the experiment.

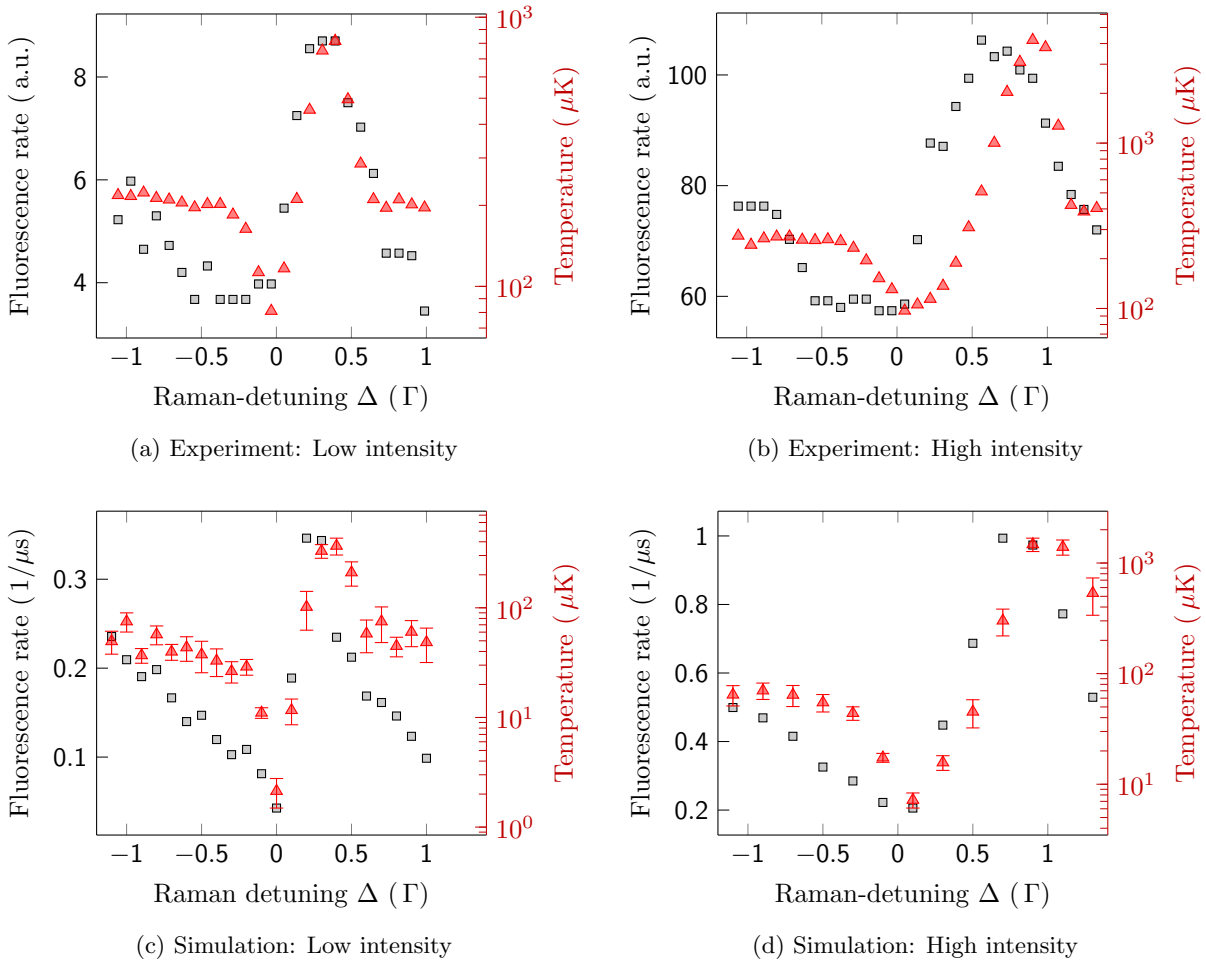
B. Raman-detuning dependence for ^{6}Li

A critical parameter in the D$_1$ molasses scheme is the Raman-detuning Δ (Fig. 1). In the following we investigate the Raman-detuning dependence of the ^{6}Li molasses temperature and fluorescence rate both theoretically and experimentally, for various cooling and repumping laser intensities.

Our ^{6}Li-^{40}K machine is described in [18]. We first load a lithium MOT using a laser slowed atomic beam (Zeeman slower). After a compressed MOT phase the magnetic field and the D$_2$ light are switched off and the D$_1$ molasses is applied (a more detailed description of the sequence is presented in the Appendix). To probe the Raman-detuning dependence we apply a 100 μs D$_1$ molasses pulse with variable Δ to an atomic cloud precooled to 100 μK. Figures 2a and 2b show the fluorescence rate and the temperature after the pulse as functions of the Raman-detuning Δ for the intensities used in the simulations. We observe a temperature dip at zero Raman-detuning and a heating/fluorescence peak at positive Δ whose position and amplitude are correlated to the molasses intensity.

In the simulations we set the initial velocity of lithium to 0.2 m/s ($T \sim 30$ μK). The simulation time is set to 200 μs. In the first 100 μs we allow the cooling dynamics to equilibrate, and during the second 100 μs we record the velocity $\mathbf{v}(t)$ as well as the time-stamped quantum jump events to calculate the equilibrium temperature and fluorescence rate. At each Raman-detuning we average over 25 trajectories. The simulation results for two different intensities $I_{\rm cool} = 2.7\, I_{\rm sat}$, $I_{\rm rep} = 0.13\, I_{\rm sat}$ and $I_{\rm cool} = 9\, I_{\rm sat}$, $I_{\rm rep} = 0.46\, I_{\rm sat}$ are shown in Figs. 2c and 2d, respectively (here $I_{\rm sat}$ refers to the saturation intensity of the D$_2$ line).

The simulated heating/fluorescence peak positions for low and high intensities (Fig. 2) agree well with the experimental findings. Also the shift between the heating and fluorescence peak, which increases with the molasses intensity, is numerically reproduced without any freely adjustable parameters.



(a) Experiment: Low intensity

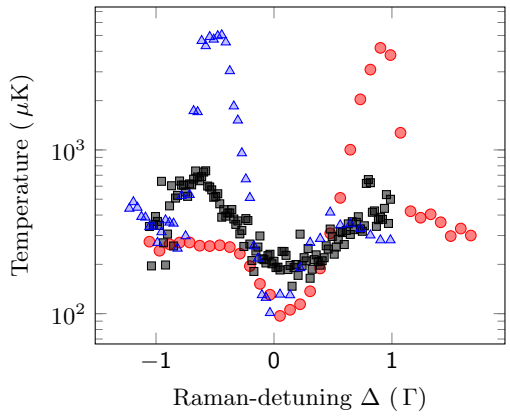
(b) Experiment: High intensity

(c) Simulation: Low intensity

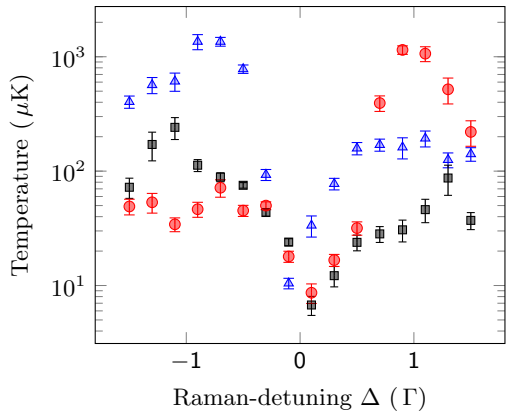
(d) Simulation: High intensity

FIG. 2. (Color online) Fluorescence (squares) and temperature (triangles, logarithmic scale) of the ^{6}Li atomic cloud after a 100 μs pulse of D_1 light with variable Raman-detuning Δ. (a) and (c) show the experimental and simulation results for $I_{\rm cool} = 2.7\, I_{\rm sat}$, $I_{\rm rep} = 0.13\, I_{\rm sat}$, (b) and (d) for $I_{\rm cool} = 9\, I_{\rm sat}$, $I_{\rm rep} = 0.46\, I_{\rm sat}$ per beam.

We next study the same Raman-detuning dependent effects, but for different cooling/repumping ratios. Typical experimental and simulation results are presented in Fig. 3. Here again, the simulation parameters are chosen according to the experimental values. The simulation and experiments match fairly well. In particular, for the usual configuration with $I_{\rm cool}/I_{\rm rep} > 1$ ($I_{\rm cool} = 9\ I_{\rm sat}$ and $I_{\rm rep} = 0.45\ I_{\rm sat}$), we observe a heating peak at $\Delta > 0$. When inverting the roles of the cooling and repumping light, i.e. $I_{\rm cool}/I_{\rm rep} < 1$ ($I_{\rm cool} = 0.18\ I_{\rm sat}$ and $I_{\rm rep} = 1.2\ I_{\rm sat}$), the heating peak appears for $\Delta < 0$ instead. In all cases, cooling is most efficient at the Raman-resonance ($\Delta = 0$). Finally, for $I_{\rm cool}$ equal to $I_{\rm rep}$, both as large as 9 $I_{\rm sat}$, we observe less efficient cooling at $\Delta = 0$ with moderate heating at blue and red detunings. Despite the nice match between simulations and experiments in Figs. 2 and 3, we observe that the semi-classical simulations provide temperatures that are systematically lower than the measured ones, particularly near the Raman-resonance condition $\Delta = 0$. The reason for this is not fully understood and may come both from theory and experimental limitations. In the semi-classical simulation, we observe that slow atoms are likely trapped within sub-wavelength regions, where the light shift is minimal and the atom is nearly decoupled from light over a long time without quantum jump. This coherent population trapping effect enhances the cooling at both large and small Δ, although it is most pronounced at the Raman-resonance ($\Delta = 0$) since more choices of decoupled states emerge. The semi-classical picture clearly exaggerates the cooling effect since the wave nature of the atom's external motion is not included in the model. In fact, the wave function of the slow atoms will sample a larger volume of the sub-wavelength traps and will shorten the lifetime of the dark periods. Another reason for shortening the lifetime of dark periods of the slow atoms is re-absorption of photons emitted by other atoms. We have indeed seen a density dependent excess temperature which we measured to be $4.6\,\mu{\rm K} \times 10^{11}$ at./cm^3 for ^{40}K. A careful simulation of cooling including photon re-absorption processes is far more complex and is beyond the scope of this work.



(a) Experiment



(b) Simulation

FIG. 3. (Color online) Temperature of the ^{6}Li D_1 molasses after a 100 μs pulse with variable Raman-detuning Δ for different cooling and repumping intensities. Standard intensities (red circles): $I_{\mathrm{cool}} = 9\,I_{\mathrm{sat}}$, $I_{\mathrm{rep}} = 0.46\,I_{\mathrm{sat}}$. Equal cooling/repumping ratio (black squares): $I_{\mathrm{cool}} = I_{\mathrm{rep}} = 9\,I_{\mathrm{sat}}$. Inverted cooling/repumping ratio (blue triangles): $I_{\mathrm{cool}} = 0.18\,I_{\mathrm{sat}}$, $I_{\mathrm{rep}} = 1.2\,I_{\mathrm{sat}}$.

C. Raman-detuning dependence for ^{40}K

Typical simulation results for ^{40}K are shown in Fig. 5a. Compared to ^{6}Li, simulations for ^{40}K require significant higher computational power due to larger internal state dimensions as well as a larger atomic mass and therefore slower cooling dynamics. To save computation time, we start at a velocity of 0.2 m/s ($T \sim 50$ μK), and set the simulation time to 2 ms. We record the velocity $\mathbf{v}(t)$ as well as the time-stamped quantum jump events for $t > 1$ ms to calculate the fluorescence rate. For each Raman-detuning Δ, 13 trajectories are simulated.

Experimental results for ^{40}K are presented in Fig. 4, showing the temperature and atom number of the D_1 molasses as functions of the Raman-detuning Δ. The total molasses duration $t_{\mathrm{m}} = 5$ ms. In the last 2 ms a linear intensity ramp to $I_{\mathrm{cool}} = 6\,I_{\mathrm{sat}}$ is performed. Just like ^{6}Li, we observe a sharp temperature drop at the Raman-condition, a heating resonance at $\sim$0.7 Γ and constant temperature regions below $-0.1\,\Gamma$ and above $2\,\Gamma$. For the constant temperature regions the temperature $T \sim 45$ μK is small compared to the Doppler-temperature $T_{\mathrm{Doppler,K}} = 145$ μK. On the Raman-condition the temperature decreases to 23 μK. In carefully optimized conditions we measured temperatures as low as 11 μK.

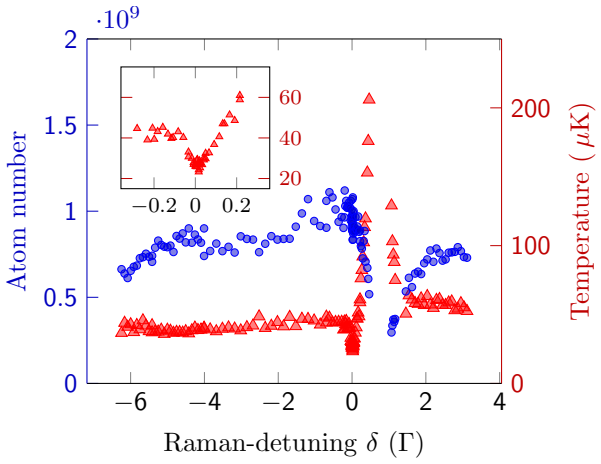


FIG. 4. (Color online) Experiment: Atom number and equilibrium temperature of the ^{40}K D_1 molasses as functions of the Raman-detuning Δ. $\delta_{\mathrm{cool}} = 3\,\Gamma$, $I_{\mathrm{cool}} = 6\,I_{\mathrm{sat}}$, $I_{\mathrm{rep}}/I_{\mathrm{cool}} = 7.6\,\%$, $t_{\mathrm{m}} = 5$ ms. In the constant temperature regions below $-0.1\,\Gamma$ and above $2\,\Gamma$ gray molasses cooling involves coherences between Zeeman states in a given hyperfine state but not between hyperfine states. At the exact Raman-condition $\Delta = 0$, long-lived coherences between hyperfine states are established, as can be seen in the simulation in Fig. 5. In a narrow detuning range, the temperature (red triangles) drops to 20 μK (inset: expanded scale).

As for ^{6}Li, the comparison between Fig. 4 and Fig. 5a again demonstrates the qualitative agreement between simulations and experimental results and that the heating peak position is reproduced by the simulation without adjustable parameters. Interestingly the inverted hyperfine structure in the ground and excited states of ^{40}K and the different $F \to F' = F - 1$ transition for the cooling laser and $F \to F' = F$ repumping transition does not significantly modify the D_1 cooling scheme as compared to ^{6}Li.

D. The D_1 cooling mechanism

The agreement between simulation and experiment suggests that the semi-classical picture is able to catch the essential physics behind the D_1 molasses cooling. In particular, the mechanisms behind the cooling dips and

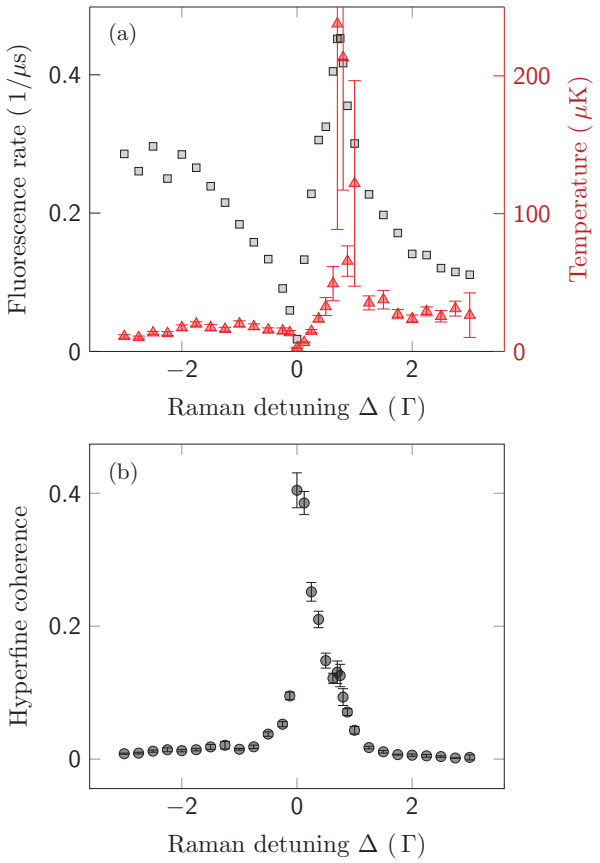


FIG. 5. (Color online) Hyperfine coherence and Λ-enhanced cooling for the ^{40}K D_1 molasses. Simulation time 2 ms, $\delta_{\rm cool} = 3\,\Gamma$, $I_{\rm cool} = 6\,I_{\rm sat}$, $I_{\rm rep}/I_{\rm cool} = 7.6\,\%$. (a) Fluorescence (squares) and temperature (triangles) as functions of the Raman-detuning Δ. (b) Coherence $4\cdot\langle\rho^2_{F=7/2,F=9/2}\rangle$ between the two hyperfine ground states $F = 7/2$ and $F = 9/2$ (see Section I E). The coherence is peaked at the Raman-resonance condition, with a width matching the temperature dip.

heating peaks in Figs. 2 to 4, previously interpreted using the dressed atom picture with a simplified three-level model [11], survive in the full level scheme of the D_1 transition.

It is well known that efficient D_2 sub-Doppler cooling requires isolated excited hyperfine levels for alkaline atoms [4, 5]. In contrast, the D_1 gray molasses operates well even when all D_1 levels are excited (as is the case of ^{6}Li) and even at zero excited-state hyperfine splitting as confirmed numerically. The robustness of D_1 molasses is also seen in its insensitivity to the relative phase between the "cooling" and "repumping" lattices, a critical parameter for D_2 bichromatic cooling where no polarization gradient was introduced [19].

In the following we discuss the physics behind the robustness of the D_1 sub-Doppler cooling. We then revisit the cooling dips and heating peaks in Figs. 2 to 4.

We notice all the dipole allowed D_1 transitions (Fig. 1) are "open": when addressed with weak off-resonant light, the probability of inelastic (m_F- or F-changing) photon scattering is comparable to or larger than that of elastic scattering. When blue detuned from the D_1 transitions, an off-resonant bichromatic lattice can establish a correlation between the spatially varying light shift (due to virtual elastic scattering) and decay (due to real inelastic scattering) for the dressed ground states, since a larger light shift is accompanied with a stronger light-atom coupling and typically a larger inelastic scattering cross-section.

We verify this idea with the full D_1 model for ^{6}Li atoms subjected to a 1D lattice with orthogonal linear polarizations (lin⊥lin configuration) with typical cooling parameters. The spatially varying light shifts ϵ of the six dressed ground states of ^{6}Li are plotted in Fig. 6a. The decay of the dressed states, due to inelastic light scattering, are characterized by the decay rate γ that is plotted versus ϵ in Fig. 6d. We see a correlation between ϵ and γ for $\epsilon < 1.5$ MHz. Such correlation is robustly established for the D_1 transitions, as verified numerically in the more complicated 3D lattices and for other atomic species. The correlation even persists for a fictitious atom with vanishing D_1 hyperfine splitting and thus suppressed m_F-changing light scattering [20].

Such a correlation between the spatially dependent light shift ϵ and decay rate γ has two consequences: First, atoms with $kv < \gamma$ tend to accumulate in dressed states with low light shifts, which facilitates cooling through motion-induced coupling to higher energy dressed states [21]. Second, for a slowly moving atom that adiabatically follows a particular dressed state, the atom tends to leave the dressed state when the light shift is high, leading to Sisyphus cooling. In addition, at locations where $\epsilon, \gamma \sim 0$, slow atoms can be confined near the local dark states such as those in Fig. 6a near $x = 0$, $\lambda/8$, $\lambda/4$, $3\lambda/8$ [22]. The resulting optical cooling force is plotted in Fig. 6g and is negative (cooling effect) over a broad range. We emphasize that this simplified 1D analysis remains valid in the more complex 3D beam geometry and is not restricted to ^{6}Li atoms. The D_1 laser cooling mechanism applies to all alkalis even those amenable to efficient D_2 sub-Doppler cooling such as cesium or rubidium. As D_1 laser cooling involves dark states it is less affected by density dependent photon multiple scattering and heating than D_2 sub-Doppler cooling. Therefore it would be interesting to quantify the gain in phase-space density by applying D_1 sub-Doppler cooling for these atoms.

In comparison, sub-Doppler cooling on the D_2 lines is significantly different. While the $F = I \pm 1/2 \rightarrow F' = I \pm 1/2$ transitions are as "open" as in D_1, the $F = I + 1/2 \rightarrow F' = I + 3/2$ and $F = I - 1/2 \rightarrow F' = I - 3/2$ have both "closed" and "open" transitions. Here the "closed" transitions are characterized by a greater-than-unity elastic-to-inelastic scattering ratio. If the $F = I + 1/2 \rightarrow F' = I + 3/2$ transitions can be

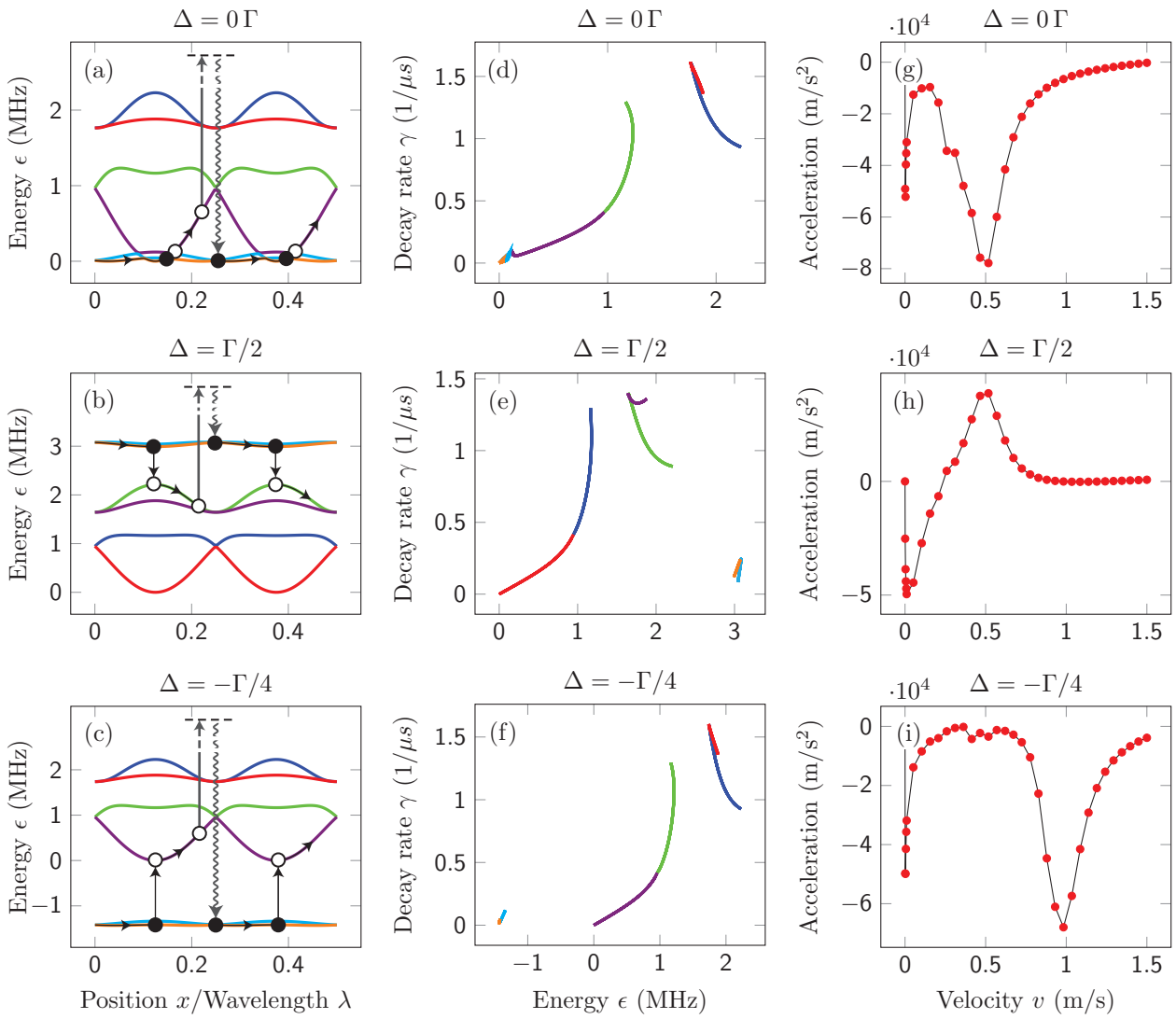


FIG. 6. (Color online) Cooling mechanism around Raman-condition in a simplified model. Optical Bloch equation simulation for ^{6}Li subjected to a 1D bichromatic lattice with linear orthogonal polarizations near D_1 resonance. The cooling lattice and repumping lattice are displaced by π ($\lambda/4$). $I_{\rm cool} = 15\, I_{\rm sat}$, $I_{\rm rep} = 0.75\, I_{\rm sat}$, $\delta_{\rm cool} = 4\,\Gamma$. (a)(b)(c) dressed states as functions of the position in units of the D_1 optical wavelength. The two dressed $F = 1/2$ levels (light blue and orange) are nearly flat in all the graphs due to the small $I_{\rm rep}$. (d)(e)(f) show the decay rate of dressed states as a function of their energy shifts. Here the two dressed $F = 1/2$ levels span a very small energy range and are with low decay rate. (g)(h)(i) show the velocity-dependent optical force for an atom dragged with velocity v. Figs. (a)(d)(g) are for $\Delta = 0$; Figs. (b)(e)(h) are for $\Delta = \Gamma/2$. Figs. (c)(f)(i) are for $\Delta = -\Gamma/4$. Note the negative sign of the force in (g) and (i) implying cooling, and the anti-cooling force for velocities near 0.5 m/s in (h).

isolated, then by taking advantage of the nearly closed $m_F - m_{F'}$ transitions, a correlation between the light shift and decay rate can be established with (instead) a red detuned lattice, as in standard sub-Doppler cooling [1–3]. However, in case of small hyperfine splitting the "open" hyperfine transitions are as well addressed at red detuning, leading to short-lived potential minima and degraded correlations, contributing to the inefficiency of the sub-Doppler cooling [23].

E. Physical picture of the Raman-detuning effect

We now extend the three-level picture of Ref. [11] to understand the details of the experiment. The cooling dips observed both experimentally and numerically at the Raman-resonance condition are also fairly easy to understand in the full model: At $\Delta = 0$ the resonant Raman-coupling splits the $F = I \pm 1/2$ hyperfine ground states into a bright and a dark manifold. The dark manifold is weakly coupled to the molasses. More precisely,

the coupling strength of the Raman dark manifold is even weaker than those due to individual cooling/repumping couplings. Therefore the emergence of the Raman dark manifold enhances all sub-Doppler cooling effects.

Since the dark manifold is a coherent superposition of the two hyperfine states $F_1 = I - 1/2$ and $F_2 = I + 1/2$, we expect that laser cooled atoms mostly occupy the dark manifold and therefore display a hyperfine coherence ρ_{F_1,F_2} with significant amplitude. To test this picture, we record the time-dependent off-diagonal density matrix quantity $4 \cdot \langle \rho^2_{F_1,F_2}(t) \rangle$ for all the quantum trajectories of the numerical simulations. The factor 4 ensures the normalization to one for the maximally coherent situation. To compute the two-photon detuning Δ dependent quantity $4 \cdot \langle \rho^2_{F_1,F_2} \rangle$ we average over both the equilibrium time and many quantum trajectories at fixed Δ. Typical results for ^{40}K are given in Fig. 5 with the cooling parameters corresponding to Fig. 4. We see that the coherence $4 \cdot \langle \rho^2_{F_1=7/2,F_2=9/2} \rangle$ is peaked at the Raman-resonance condition and becomes significant with a width matching the temperature dip.

As in Figs. 2 to 4 and [11] we now explain the heating peaks with the full D_1 model. We first focus on the case of $I_{\rm cool} \gg I_{\rm rep}$ so that at large $|\Delta|$ the dressed $F = I - 1/2$ hyperfine level is relatively long-lived and populated. As in Figs. 6b,c, the Raman-detuning Δ determines the energy level of the dressed $F = I - 1/2$ hyperfine level, and it is clear that when $\Delta < 0$, the motion-induced-coupling to the dressed $F = I + 1/2$ level should still contribute to cooling (as in Figs. 6c,f,i) [21], apart from Sisyphus cooling. On the contrary, for $\Delta > \max[\epsilon_{F=I+1/2}]$, e.g. a Raman-detuning beyond the maximum light shift of the dressed $F = I + 1/2$ manifold (as in Fig. 6b,e,h), motion-induced coupling to the lower energy dressed $F = I + 1/2$ manifold would lead to heating. In addition, the Sisyphus effect at the $F = I + 1/2$ manifold also contributes to heating, since atoms coupled from $F = I - 1/2$ are more likely to start at the anti-trap positions. The corresponding heating peak is located at $\Delta \sim \max[\epsilon_{F=I+1/2}] > 0$.

When $I_{\rm cool} \ll I_{\rm rep}$, the heating peak is shifted to $\Delta \sim -\max[\epsilon_{F=I-1/2}] < 0$, as in Fig. 3. This is straightforward to understand as the role of the two hyperfine ground states are now inverted with respect to the previous case. Finally, for $I_{\rm cool} \sim I_{\rm rep}$, the two hyperfine ground states have similar lifetimes and therefore similar steady-state populations. As the heating effects are balanced by cooling effects, the corresponding heating peaks in Fig. 3 (black squares) at $\Delta \sim \max[\epsilon_{F=I+1/2}]$, $\Delta \sim -\max[\epsilon_{F=I-1/2}]$ are substantially suppressed.

II. SIMULTANEOUS ^{6}Li AND ^{40}K D_1 COOLING

Finally, we discuss the simultaneous operation of the ^{6}Li and ^{40}K D_1 molasses. We found that this simultaneous operation is required for subsequent efficient thermalization between both species in a quadrupole magnetic trap. The timing sequence and parameters are the same as for single-species operation. Experimental details are given in the Appendix and in [10]). The D_1 molasses phase is composed of a 3 ms capture phase and a 2 ms cooling phase. Table I summarizes the optimal parameters of the dual-species molasses. The presence of the other species reduces the atom numbers in the MOTs by 4 % for ^{6}Li and by 10 % for ^{40}K. However, we observe no mutual influence during the CMOT and the D_1 molasses phase. The temperatures and relative atom numbers in dual-species operation do not differ from single-species operation. This has several reasons. First, the D_1 resonances and lasers are ∼100 nm apart in wavelength. Second, the CMOT and molasses phases are short in duration (5ms) and the light-induced inter-species collision losses or heating are minimized as atoms are accumulated in dark states. Table II summarizes the performance of the different experimental phases in dual species-operation. For both ^{6}Li and ^{40}K the D_1 molasses phase largely reduces the temperature while the cloud-size after the CMOT phase is conserved. For both species this leads to a phase-space density close to 10^{-4}.

	Potassium	Lithium
P (mW)	230	300
$\delta_{\rm cool}$ (Γ)	2.3	4
$\delta_{\rm rep}$ (Γ)	2.3	4
$I_{\rm cool}$ per beam ($I_{\rm sat}$)	14	14
$I_{\rm cool}/I_{\rm rep}$	8	20
D line properties	^{40}K	^{6}Li
$\Gamma/(2\pi)$ (MHz)	6.04	5.87
$I_{\rm sat}$ (mW/cm^2)	1.75	2.54

TABLE I. Parameters of the simultaneous ^{6}Li and ^{40}K D_1 cooling phase.

	T (μK)	N ($\times 10^9$)	n ($\times 10^{10}$ cm^{-3})	$\phi^{\rm a}$ ($\times 10^{-5}$)
Lithium				
MOT	1000	2	2.6	0.03
CMOT	800	2	18	0.29
Molasses	48	12	7.6	8.2
Potassium				
MOT	240	3.2	7	0.02
CMOT	2000	3.2	37	0.06
Molasses	11	3.2	30	10.7

[a] The given phase-space density does not take into account the different internal states and is calculated as $\phi = n\lambda_{\rm B}^3$, where $\lambda_{\rm B}$ is the thermal de Broglie wavelength.

TABLE II. Performance of the different experimental phases for ^{6}Li and ^{40}K, in dual species operation. We show the optimum temperature T, the atom number N, the density n and the phase-space density ϕ.

III. CONCLUSION

In this study we have investigated the properties of D_1 laser cooling both experimentally and with numerical simulations. The simulations take into account all relevant Zeeman and hyperfine levels as well as the three dimensional bichromatic lattice geometry. Simulations and experimental results match fairly well for both lithium and potassium. Various sub-Doppler cooling effects [10] are recovered in the full model. We have outlined the importance of coherences between the ground-state hyperfine levels [11].

We discussed the robustness of the D_1 cooling scheme, in particular its insensitivity to the excited state hyperfine splitting and to the relative phase between the cooling and repumping lattices, which is in sharp contrast to its D_2 counterpart [4, 5, 19]. We suggest and numerically verify that in a blue detuned bichromatic D1 lattice, the dressed ground states exhibit a robust correlation between light-shift and decay, responsible for efficient sub-Doppler cooling. Because of a smaller absorption cross-section for atoms cooled in weakly coupled states, D_1 gray molasses should also be less affected by the density dependent heating than their D_2 counterparts [24].

Experimentally, using commercial semiconductor laser sources delivering ∼200 mW of CW power, we achieve efficient, simultaneous cooling of ^{6}Li and ^{40}K, resulting in a phase space density close to 10^{-4} for both species. This D_1 cooling scheme enables efficient direct loading of a dipole or magnetic trap because of the large gain in temperature. As recently shown in [12, 14] these conditions are well suited to directly load an optical dipole trap and to perform all-optical evaporation to quantum degeneracy. In our own experiments, we load a magnetic trap, transport the atoms to a separate science cell, and perform evaporative cooling of ^{40}K in two Zeeman states with a combined magnetic/optical trap scheme introduced in [25]. Deep quantum degeneracy ($T/T_F = 0.14$) in the dipole trap has been achieved and will be the subject of a future publication.

Finally we have also used the D_1 gray molasses scheme to cool the bosonic ^{41}K isotope. All of 5×10^9 ^{41}K atoms from a CMOT were cooled to a final temperature of 20 μK leading to a phase-space density of 1.1×10^{-4}. This confirms the generality of this D_1 sub-Doppler cooling method.

ACKNOWLEDGMENTS

We acknowledge useful discussions with A. T. Grier, I. Ferrier-Barbut, B. S. Rem, M. Delehaye, S. Laurent, and J. V. Porto, and support from Région Ile de France (DIM Nano-K and IFRAF), EU (ERC grants Ferlodim and Thermodynamix), Institut de France (Louis D. Award), and Institut Universitaire de France. D.R.F. acknowledges the support of Fundação para a Ciência e Tecnologia (FCT-Portugal), through the grant number SFRH/BD/68488/2010. S.W. acknowledges the support of the Physics Department at Swansea University when part of this research was carried out.

APPENDIX: EXPERIMENTAL DETAILS

In this section we describe the experimental details, as well as results of additional measurements on the D_1 molasses scheme, in particular, the single species operation of ^{6}Li.

Our experimental setup has been already described previously [18]. A Zeeman-slower for ^{6}Li and a 2D$^+$-MOT for ^{40}K load the three-dimensional dual-species MOT in the MOT-chamber. The D_2 laser systems for ^{6}Li and ^{40}K comprise master oscillator power amplifiers (MOPAs) to produce light at 671 nm and 767 nm respectively. Beamsplitters and acousto-optic modulators (AOMs) generate the cooling and repumping beams, which are combined before injecting tapered amplifiers for the Zeeman-slower and 3D-MOT for ^{6}Li and accordingly the 2D$^+$-MOT and 3D-MOT for ^{40}K.

The D_1 laser system for ^{40}K operates at 770 nm and is composed of a MOPA and an electro-optic modulator (EOM) to produce the repumping frequency. The total power used for the ^{40}K cooling is 240 mW, with an intensity per molasses beam of $14\, I_{\mathrm{sat}}$.

The source for the ^{6}Li D_1 light at 671 nm, used in this work, is a home-made solid-state laser, the next generation of [26, 27], with up to 5 W output power. AOMs allow to independently tune the frequencies and powers of the cooling and repumping beams, before recombination and injection into an optical fiber. We typically use 300 mW total power for the ^{6}Li D_1 cooling. The waist of the ^{6}Li D_1 beam after the telescope (Fig. 7) is 8.6 mm. We have also used a commercial 671 nm tapered amplifier system (MOPA) with 130 mW available power impinging on the atoms and obtained similar performances for the capture efficiency and sub-Doppler temperatures.

Our optical scheme superimposes the D_1 and D_2 light for both ^{6}Li and ^{40}K and produces the molasses and 3D-MOT beams (Fig. 7). D-shaped mirrors (M_{D}) superpose the D_1 cooling light and the 3D-MOT light of each species before a dichroic mirror (M_{dichroic}) combines the lithium and potassium light. The beam containing all eight frequencies is expanded and distributed to the three pairs of σ^+–σ^- counter-propagating beams of the 3D-MOT and the D_1 molasses. The two horizontal axes are retroreflected, the vertical axis consists of two independent beams. The $\lambda/2$ plates of order four for lithium ($\lambda/2^*_{\mathrm{Li}}$) and potassium ($\lambda/2^*_{\mathrm{K}}$) allow for independent control of the ^{6}Li and ^{40}K MOT power distribution.

The experiment starts with loading the dual-species MOT. In 10 s we typically load 8×10^8 ^{6}Li atoms with an initial temperature of 1 mK and 3×10^9 ^{40}K atoms at 200 μK. Then a CMOT phase [28] increases the density of the atom cloud. The magnetic gradient is linearly ramped from 9 G/cm to 60 G/cm in 5 ms. Meanwhile the

Pas, M. Inguscio, M. Zaccanti, and G. Roati, Physical Review A **90**, 043408 (2014).
[15] J. Dalibard, Y. Castin, and K. Mø lmer, Phys. Rev. Lett. **68**, 580 (1992).
[16] H. Carmichael, *An Open Systems Approach to Quantum Optics*, Lecture Notes in Physics Monographs, Vol. 18 (Springer Berlin Heidelberg, 1993).
[17] By assuming the ground-state hyperfine splitting to be large enough, the $F = I + 1/2$ ($F = I - 1/2$) is dark to the repumping (cooling) laser and the associated couplings are ignored in the Hamiltonian. This approximation allows us to write down the Hamiltonian in the time-independent form.
[18] A. Ridinger, S. Chaudhuri, T. Salez, U. Eismann, D. R. Fernandes, K. Magalhães, D. Wilkowski, C. Salomon, and F. Chevy, The European Physical Journal D **65**, 223 (2011).
[19] R. Gupta, C. Xie, S. Padua, H. Batelaan, and H. Metcalf, Phys. Rev. Lett. **71**, 3087 (1993).
[20] W. Happer, Reviews of Modern Physics **44**, 169 (1972).
[21] C. Cohen-Tannoudji, *Atomic Motion in Laser Light*, edited by J. Dalibard, J. Raimond, and J. Zinn Justin (Les Houches, Session LIII, 1990) pp. 1–164.
[22] Exact locations of the dark states depend on the relative phase between the cooling and repumping lattices.
[23] For the D_2 transitions the complication is also Δ-dependent. A complete comparison of D_1 and D_2 cooling will be the subject of a future publication.
[24] M. Drewsen, P. Laurent, A. Nadir, G. Santarelli, A. Clairon, Y. Castin, D. Grison, and C. Salomon, Applied Physics B **59**, 283 (1994).
[25] Y.-J. Lin, A. Perry, R. Compton, I. Spielman, and J. Porto, Physical Review A **79**, 063631 (2009).
[26] U. Eismann, F. Gerbier, C. Canalias, A. Zukauskas, G. Trénec, J. Vigué, F. Chevy, and C. Salomon, Applied Physics B **106**, 25 (2011).
[27] U. Eismann, A. Bergschneider, F. Sievers, N. Kretzschmar, C. Salomon, and F. Chevy, Opt. Express **21**, 9091 (2013).
[28] M.-O. Mewes, G. Ferrari, F. Schreck, A. Sinatra, and C. Salomon, Physical Review A **61**, 011403 (1999).

5 Magnetic trapping and magnetic transport

The typical phase space density achieved after the gray molasses cooling phase described in the previous chapter is $\sim 10^{-4}$. In order to achieve quantum degeneracy one has to reconfine the atoms and perform evaporative cooling. One possibility is to directly load the atoms into an optical dipole trap (the so-called all optical approach), which was the strategy pursued by the Innsbruck team with success [188]. Another possibility is to load the atoms into a magnetic trap, which was the strategy pursued by the Munich (now Singapore) team [192], by the Amsterdam team [120, 200] and by us. The first approach is technically simpler, but the number of the trapped atoms depends greatly on the interplay between the capture volume and the trap depth. Without gray molasses cooling, a considerable amount of laser power is needed to trap a significant amount of atoms from the MOT. On the other hand, magnetic traps have bigger trap volumes and trap depths, thus being able to collect the full atomic cloud. Usually these setups are more complex that the single beam optical dipole trap, but the resulting number of degenerate atoms is larger. In our apparatus we load the sub-Doppler cooled atomic cloud into a quadrupole magnetic trap. The transfer is preceded by a phase of optical pumping into magnetically-trappable state(s). The trapped cloud is then transported from the MOT chamber to a science glass cell. The transport is realized by dynamically changing the currents of a series of pairs of coils, thus displacing the magnetic trap center. This step allows to move the atomic cloud to a glass cell where the optical access and the vacuum quality are much more favorable than the MOT chamber. By performing evaporative cooling of the atomic cloud in the science cell we were able to obtain a quantum degenerate gas.

In this chapter the principles of operation of magnetic trapping will be reviewed, with a separate section for the optical pumping phase and the loading in the trap. In a second part the implementation of a magnetic transport will be motivated and explained. Technical details concerning the electromagnets of the apparatus are given in appendix 5.A. The evaporation in the magnetic trap will be presented in chapter 6.

5.1 Principles of magnetic trapping of neutral atoms

Zeeman effect

The coupling between a neutral atom and an external magnetic field is in general weak when compared with ions. For alkalis the main contribution to the magnetic moment $\boldsymbol{\mu}$ comes from the valence electron. The order of magnitude of the coupling of an electron to an external magnetic field is the Bohr magneton $\mu_B/h \approx 1.4\text{MHz/G}$. The magnetic interaction contribution to the atomic Hamiltonian is given by $V = -\boldsymbol{\mu} \cdot \mathbf{B}$, which is the so-called *Zeeman* term. Setting the quantification axis parallel to the magnetic field $\mathbf{B}$, then $V = -\mu B$, μ being the projection of the atomic magnetic moment on the direction of the field. In the classical framework, the magnetic moment precesses around the magnetic field direction with the Larmor frequency $\omega_L = \mu B/\hbar$. This frequency sets a timescale for which the movement of an atom in an inhomogenous magnetic field is adiabatic[1]. In the quantum framework the magnetic moment is quantified. In alkalis there are two ground-state hyperfine manifolds: $F = I \pm 1/2$. For weak magnetic fields $B \ll B_{hf} = h\Delta\nu_{hf}/2\mu_B$ (where $h\Delta\nu_{hf}$ is the energy difference between the two hyperfine manifolds[2]) the magnetic interaction energy is quantized and given by $E_m = m_F g_F \mu_B B$, where m_F is the magnetic quantum number and g_F the Landé factor [189]. For the particular case of the stretched states $m_F = \pm(I + 1/2)$, the coupling of the atom to the magnetic field is maximum and is purely electronic $E_m = \pm\mu_B B$. Consequently, for the $F = I + 1/2$ manifold one has $m_F g_F = m_F/(I + 1/2)$ for $|m_F| \leq F$. The *Breit-Rabi* formula generalizes this result for any value of the magnetic field B [189]. For the case of the excited state manifold, we refer the reader to section 2.3.3.

Principle of magnetic trapping

Due to the Zeeman effect, an inhomogeneous magnetic field $B = B(\mathbf{r})$ will induce a magnetic force on the atoms $\mathbf{F}_m \propto -\boldsymbol{\nabla} B$. Maxwell's equations prevent the existence of a local maximum of the magnetic field. As a consequence, magnetic traps

[1] When the adiabaticity condition is violated, the magnetic moment μ is not conserved and the so-called Majorana flips occur. This will be object of study in section 6.3.1.

[2] $B_{hf} \approx 459\text{G}$ for ^{40}K and $B_{hf} \approx 82\text{G}$ for ^{6}Li.

for neutral atoms rely on the fact that low field seeking atoms[3] are trapped around a magnetic field minimum. Since the coupling of neutral atoms to an external magnetic field is quite weak, as pointed out before, the trap depths achieved are usually small. However, after laser cooling the atomic ensemble to $\sim 100\mu$K, magnetic trapping is generally quite easy to implement[4]. For example to trap a cloud with $T = 1$mK one has to produce a field difference of ~ 150G (10mK$\hat{=}$150G, for the stretched states).

The simplest way of creating a magnetic trap is to have a pair of concentric loops of conducting wire separated by a gap with currents flowing in opposite directions. For symmetry reasons, the magnetic field produced by these rings is 0 at the center of the arrangement and increases (in absolute value) along every direction of space. The magnetic field 0 is the field minimum and atoms in low field seeking states will be attracted to it from every direction. Consider a system of oriented axis with origin in the trap center, as depicted in fig. 5.1.1. Since electric currents are counter-propagating, the system is anti-symmetric and the magnetic field is an odd function $B(-r) = -B(r)$. By Taylor-expanding the magnetic field $B(\mathbf{r})$ around its origin (the trap center) one can write $B_z \approx bz + \mathcal{O}(z^3)$, where b is the so-called *magnetic field gradient* and embodies the trapping strength. Using the second Maxwell law $\boldsymbol{\nabla} \cdot \mathbf{B} = 0$ one has immediately for the radial direction that $B_\rho \approx -b\rho/2 + \mathcal{O}(\rho^3)$. The magnetic field is then given by

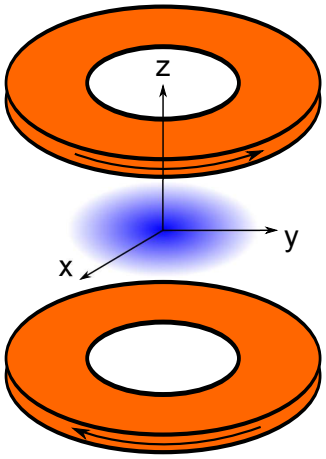


Figure 5.1.1: Scheme of an atomic cloud trapped by the magnetic field created by two coils. The curved arrows indicate the direction of current flow.

$$B(\mathbf{r}) = b(-x/2, -y/2, z) \tag{5.1.1}$$

up to the third order for this arrangement: the so-called *quadrupole* trap [131]. Notice

[3] $m_F g_F > 0$ in the small magnetic field approximation.
[4] In the historical case of Hydrogen, no laser cooling was implemented rendering magnetic trapping challenging [86]

that this field also obeys $\boldsymbol{\nabla} \times \mathbf{B} = 0$. Say that the distance between the rings is D and that their radius is R. It can be shown that the configuration $D = R$ has highest magnetic field gradient [129] and it is given by

$$b = \frac{48}{25\sqrt{5}} \frac{\mu_{\mathrm{m}} I}{R^2}, \tag{5.1.2}$$

where μ_{m} is the magnetic permeability and I is the current flowing through the wires. This particular configuration is called *anti-Helmholtz* and is very commonly used in cold atom experimental apparatus.

Trapping of neutral atoms in a quadrupole magnetic trap

The total potential felt by a magnetically trapped atom is given by the sum of the magnetic $\mu_{\mathrm{B}} b|B|$ and the gravitational mgz contributions

$$U(\mathbf{r}) = \mu_B b \sqrt{(x^2 + y^2)/4 + z^2} + mgz. \tag{5.1.3}$$

Here it is assumed that the atom is in the stretched state, but for the general case we can replace: $b \to (\mu/\mu_B)b$. It is also assumed that gravity is along the axial direction of the coils. The volume of the trap is given by

$$V_e = \int e^{-U(\mathbf{r})/k_{\mathrm{B}}T} d\mathbf{r} = \frac{32\pi\lambda^3}{(1-\gamma^2)^2}.$$

Here $\lambda = k_{\mathrm{B}}T/\mu_B b$ is the characteristic length of the magnetically trap cloud and γ is a gravity parameter $\gamma = b_g/b$, with $b_g = mg/\mu_{\mathrm{B}}$. For example, after loading the magnetic trap in the MOT chamber and compressing the trap, one has 3×10^9 atoms of ^{40}K at $T \approx 200\mu$K for a gradient of $b = 1.5$T/m, giving a central density of $n_0 = N/V_e \approx 4 \times 10^{12}\mathrm{cm}^{-3}$ and $\lambda \approx 0.20$mm.

Notice that by doing $x = y = 0$ in eq. 5.1.3 one gets $U(z) = \mu_B(b|z| + b_z z)$, meaning that gravity can be interpreted as a positive contribution to the magnetic gradient for $z > 0$ ($b \to b + b_g$) and a negative contribution for $z < 0$ ($b \to b + b_g$). In other words, gravity tilts the magnetic potential. However for most situations $\gamma^2 \ll 1$, which will be assumed unless explicitly stated.

By modifying the current I one can linearly vary the magnetic gradient b, thus changing the strength of the trap. This change is adiabatic if done slower than the timescale associated with the movement of the trapped atoms e.g. $\lambda/v_{\text{th}} = \lambda/\sqrt{8k_{\text{B}}T/\pi m}$, which is on the order of the (sub-)millisecond. In this case, the entropy is conserved. Since phase space density is conserved in a adiabatic process (for a fixed trap shape) one obtains readily that $n_0^{1/3}\Lambda \propto b/T^{3/2}$ is constant ($\Lambda^2 = 2\pi\hbar^2/mk_{\text{B}}T$ is the de Broglie wavelength). As a consequence, increasing the magnetic field gradient will increase the cloud temperature

$$T/T_0 = (b/b_0)^{2/3}. \tag{5.1.4}$$

This is intuitive since an increase in magnetic trapping energy will increase the kinetic energy to insure energy conservation. One other hand, the cloud size decreases $\lambda/\lambda_0 = (b/b_0)^{-1/3}$ and central density increases linearly $n/n_0 = b/b_0$.

Probing a trapped atomic cloud

The atomic cloud density profile of a classical gas in the magnetic trap is given by

$$n(\mathbf{r}) = n_0 e^{-U(\mathbf{r})/k_{\text{B}}T} = n_0 \exp\left\{-\frac{1}{\lambda^2}\sqrt{(x^2+y^2)/4+z^2}\right\}, \tag{5.1.5}$$

where $n_0 = N/V_e$ is the central atomic density and it now explicit that λ is the typical length of the trapped cloud [206]. Probing the density distribution of a magnetically trapped cloud using standard imaging procedures is not straightforward. In the presence of a magnetic field, the imaging transitions will be shifted due to the Zeeman effect. If one supposes that the imaging transition involves two stretched states, the Zeeman frequency shift will be of $\mu_{\text{B}}B(\mathbf{r})/h$, where $B(\mathbf{r})$ is the local magnetic field. This means that while the atoms in the center of the trap will be on resonance ($B(0) = 0$), the atoms from the edge will yield lower signal, as the absorption coefficient/fluorescence rate scales as $\mathcal{A} = 1/\left(1+(2\mu_{\text{B}}B(\mathbf{r})/\hbar\Gamma)^2\right)$. Furthermore, notice that the assumption that the imaging transition is between stretched states (and closed) is a simplification. In practice, since the magnetic moment of the atom is aligned with the local magnetic field direction, the coupling of the atom to the light

field has to be calculated locally. In spite of these difficulties, one can still obtain information if the Zeeman shift at the edge of the cloud is small compared to transition width $2\mu_B b\lambda/\hbar\Gamma \ll 1$. This can be improved by having a cloud of small temperature or just by decompressing the trap ($b\lambda \sim b^{2/3}$). For example, for $b = 2.5\mathrm{T/m}$ and $T = 100\mu\mathrm{K}$ the absorption at the cloud edge is only reduced by $1/3$. An obvious strategy to avoid these problems is to switch off abruptly the magnetic field and measure the density profile. This measurement is meaningful if done right after switching off the trap $t_{\mathrm{TOF}} \ll \lambda/\sqrt{k_B T/m}$, otherwise the trap density profile will be perturbed (see eq. 2.3.3). This condition gives $t_{\mathrm{TOF}} \ll 0.4\mathrm{ms}$ for the example above. This is very stringent condition, since it is close to the time scale of the magnetic field current electronic switches and of the exposure time for the image taking ($100\mu\mathrm{s}$). Moreover, in our apparatus the presence of metallic components build up Foucault currents that dissipate in $\tau \sim 2\mathrm{ms}$, making this experiment unfeasible. For $t_{\mathrm{TOF}} \gg \lambda/\sqrt{k_B T/m}$ we lose information about the *in situ* distribution and the atomic density profile is given by the Maxwell-Boltzmann law and one can accurately extract the number of atoms and the temperature. The remaining parameter is b, which can be estimated by measuring the coil geometry and using eq. 5.1.2.

Let us suppose that one could accurately image the magnetically trapped cloud. If x is the imaging axis, the integrated density profile is be given by

$$n_{2\mathrm{D}}(y,z) = n_0 \int \exp\left\{-\frac{1}{\lambda^2}\sqrt{(x^2+y^2)/4+z^2}\right\} dx,$$

which does not have analytical solution. By integrating the collected image numerically, say along the y axis, one has

$$n_{1\mathrm{D}}(z) = \int n_{2\mathrm{D}}(y,z)dy = \frac{N}{4\lambda}\left(1+\frac{|z|}{\lambda}\right)e^{-|z|/\lambda},$$

where it was used $n_0 = N/32\pi\lambda^3$. By fitting the integrated density profile with the previous function, one can directly get access to the atomic cloud size λ and the total number of atoms N.

5.2 Optical pumping and transferring atoms into the magnetic quadrupole trap

Optical pumping

After the molasses phase atoms are depolarized: they populate both hyperfine ground states and are randomly distributed in the m_F states. Before loading them into the magnetic trap, one performs an optical pumping phase in order to pump the atoms into trappable states (low-field seekers). This phase lasts 470μs: in the first 400μs an homogeneous magnetic field of $\sim$ 1G is quickly ramped and in the last 70μs a σ^+ polarized light pulse is applied into the atoms (50μs for ^{6}Li). The purpose of the (bias) magnetic field is to define a quantization axis, while the collinear σ^+ laser beam pumps atoms to increasing m_F state. The cycles of absorption/emission of photons induce heating $\sim E_R/k_B$ per cycle on average and for that reason it is important to have conditions such that that number of cycles is minimized[5]. A trick is to use an optical transition such that the target state is a dark state. For example, if ones drives a $F \rightarrow F' = F$ transition, once atoms are in the $m_F = F$ state they will not absorb any additional photons. Hence this state is dark and is protected against further heating. At the same time, the optical pumping stage has to have the smallest duration possible since atoms expand freely, decreasing their (phase space) density. This is a quite dramatic for ^{6}Li since it has a smaller mass.

One is interested in pumping both ^{40}K and ^{6}Li to their stretched states $F = m_F = I + 1/2$. For ^{40}K the optical pumping is done on the $F = 9/2 \rightarrow F' \rightarrow 9/2$ transition (of the D_2 line), in the presence of repumper light $F = 7/2 \rightarrow F' = 9/2$. For ^{6}Li the optical pumping is done in the $F = 3/2 \rightarrow F' = 3/2$ transition (of the D_1 line), which also has a dark state $m_F = 3/2$, in the presence of repumper light $F = 1/2 \rightarrow F' = 3/2$. In spite of the presence of the dark states, it is still important to keep the light power as low as possible since in practice light is not perfectly σ^+ polarized (n.b. in our setup the same MOT $\lambda/4$ plate is used for both ^{40}K and ^{6}Li) and, in the case of ^{40}K, off-resonant excitations to the energetically close $F' = 11/2$ excited state can be enhanced due to power broadening. When measuring atom number and temperature of the atoms captured in the magnetic trap, we observe that excessive

[5] E_R/k_B is $\approx 0.41\mu$K for ^{40}K and $\approx 3.5\mu$K for ^{6}Li.

laser power is detrimental. For ^{6}Li only the stretched state is magnetically trappable and stable against inelastic collisions [178], while for ^{40}K the condition is less stringent as different spin states can be trapped (see experiment of fig. 5.2.1). Fortunately, it happens that a mixture of spins of ^{40}K is rather stable [44]. Moreover, a mixture of spins of ^{40}K with ^{6}Li in the stretched state is also relatively stable [200], as it is going to be studied with more detail in section 6.3.2. In the end, in order to optimize the laser power during the optical pumping what we do in practice is: for ^{6}Li one wants to optimize collision rate ($\propto N/T^{5/2}$); for ^{40}K one needs a mixture of spins to perform evaporative cooling, so one optimizes the phase space density after the magnetic evaporation in the optical dipole trap [200] (cf. chapter 6). The optimal optical pumping parameters are indicated in table 5.2.1.

After the optical pumping phase we observe heating, mostly along the direction of the optical pumping beam. For ^{40}K the temperature along this axis increases by $\approx 45\mu$K, while for ^{6}Li it increases by $\approx 170\mu$K, which corresponds to a temperature increase of $110E_R/k_B$ and $50E_R/k_B$, respectively.

Transfer to the magnetic quadrupole trap

Once the atoms are pumped into stable low field states, they can be loaded into the magnetic trap. The optimal loading occurs in two phases. In the first one the magnetic field is ramped as fast as possible in order to confine the atoms. In the second one the magnetic field is ramped adiabatically to compress the trap and increase atomic density. In the first step, the quick ramp has to be such as the final magnetic field gradient stops the atoms from expanding, keeping the atomic density constant in time. In the second step, the magnetic field ramp is adiabatic. This ensures minimal loss of phase space density during the transfer. Say that σ is the average RMS radius of the atomic cloud after the optical pumping phase $\sigma = \sqrt{\langle r^2 \rangle}$ and that the RMS size of a magnetically trapped cloud is $\approx \lambda$. If there was a single very fast ramp of the magnetic field gradient then $\lambda \ll \sigma$ and the atomic cloud would be out of equilibrium: the atoms would oscillate in the magnetic trap, rendering a hot cloud after dissipation of the excessive energy. If there was a single slow ramp of the gradient, then the atoms would have time to expand before being trapped, decreasing density, and resulting in a size $\lambda > \sigma$ which would correspond to a hotter cloud ($\lambda \propto T$). Again, in the ideal

case, the gradient has to be rapidly ramped to $\lambda \approx \sigma$ so that the atoms are trapped and in equilibrium. Then, the gradient can be adiabatically ramped up in order to enhance density/collision rate without any loss in phase space density. In our experiment $\sigma \approx 1.5$mm and $T = 20\mu$K after the ^{40}K molasses, corresponding to a very low gradient of $b = 0.02$T/m, two orders of magnitude smaller than the highest value achieved in this setup. Experimentally we observe that changing the ramping time of the gradient does not have a great impact on the density of the atoms, except for very slow ramps ($\tau \sim 10 - 100$ms). Very fast ramps ($\tau \lesssim 1$ms) are not possible in our apparatus due to Foucault currents in the MOT chamber. These currents might prevent us from achieving optimal loading, but it turns out that the loss in phase space density is small.

The typical numbers measured in the magnetic trap are indicated in table 5.2.1. The loading efficiency is quite good: the ratio between the detected number of trapped atoms and the number of atoms before ramping the magnetic field is 1 for ^{40}K and ≈ 0.9 for ^{6}Li.

When releasing the atoms from the trap and performing a time-of-flight measurement of the thermal speed of the atomic ensemble we find that its value is not isotropic. The cloud is not in thermal equilibrium, but we take the liberty to assign a "temperature" (not in the thermodynamical sense) for two directions of the measurement: vertical (the optical pumping direction) and horizontal. In the case of ^{6}Li, the vertical temperature is higher than the horizontal one, probably due to the severe heating caused by the optical pumping. This heating is more dramatic for ^{6}Li than for ^{40}K due to its large recoil energy. In order to reduce this effect we tried to perform the optical pumping with two balanced contra-propagating beams, thus compensating the net momentum kick of several recoils. This strategy did not yield a clear improvement in the temperature anisotropy. In contrast with the case of ^{6}Li, ^{40}K exhibits a higher temperature in the horizontal direction. This might be due to the reduced heating caused by the optical pumping and a small horizontal mispositioning of the molasses relative to the magnetic field center. This difference in position is of $\approx d = 300\mu$m, which a sudden ramp of the magnetic trap would make the cloud oscillate horizontally and corresponds to $E/k_{\mathrm{B}} = \mu_{\mathrm{B}}(b/2)d/k_{\mathrm{B}} \approx 150\mu$K. This value gives an upper bound for the heating caused by the misalignment, which might be more severe for ^{40}K than for ^{6}Li due to the difference in mass (and inertia). Nevertheless, we observed that by

letting the atoms collide in the trap the temperature differences decreased. After a waiting time of $\approx$ 0.5s the two gases of ^{40}K and ^{6} Li were practically thermalized. A more detailed study will be presented in section 6.7.2.

Finally, the lifetime of the magnetically trapped cloud in the MOT chamber was determined to be (16.5 ± 0.6)s. This value was achieved after carefully isolating the atoms from any source of resonant photons by means of the installation of mechanical shutters and switching AOMs off. These photons are detrimental as they depolarize the atoms into non trapped states (a few photon flux is sufficient to quickly deplete the trap). The measured lifetime did depend on the atomic species and we concluded that it is limited by collisions of the trapped atoms with atoms from residual background gas.

Probing the spin composition of trapped atomic cloud

Finally, one would like to determine the spin-composition of the trapped gas. While for ^{6}Li only the stretched state $|F = 3/2, m_F = 3/2\rangle$ is simultaneously trappable and collisional stable [178], for ^{40}K several Zeeman states of the $F = 9/2$ manifold can be trapped and their mixture is long-lived [44]. To probe the spin-composition of a ^{40}K mixture, one can decompress the magnetic trap down to a point at which the vertical magnetic force exerted on a certain spin component is weaker than gravity. By measuring the atom loss, one can determine the number of atoms that fell and their magnetic moment (spin). Using this strategy one can discriminate the different spin species and determine their populations. For $F = I + 1/2$, atoms with Zeeman state m_F will fall from the trap when

$$b \lesssim (F/m_{\mathrm{F}}) b_g. \tag{5.2.1}$$

An example of such an experiment is shown in fig. 5.2.1. In this experiment a cloud at $T \sim 120\mu$K is magnetically trapped in the science cell with $b = 2.5$T/m. The current flowing in the coils is then linearly reduced to a final value I in 400ms and after a wait time of 700ms the trap is recompressed and the remaining atom number measured after a time-of-flight. One observes that there is a series of steps, each one corresponding to a different spin state: for $I < 2.75$A no atom is detected, for 2.75A $<$

$I < 3.5$A only $m_F = 9/2$ is present, for 3.5A $< I <$ 5A both $m_F = 9/2$ and $m_F = 7/2$ are present and for $I >$ 5A three spin-states are detected $m_F = 9/2, 7/2, 5/2$. The different spins can be identified by their magnetic moment: $3.5A \approx 2.75A \times 9/7$ and $5A \approx 2.75A \times 9/5$, as predicted by eq. 5.2.1. These values allow us to determine the trapping gradient of these pairs of coils: $b_g/2.75\text{A} = 25.5 \times 10^{-3}\text{T}/(\text{m}\cdot\text{A})$, which is compatible with the value estimated from the geometry of our coils using the Biot-Savart law $25.0 \times 10^{-3}\text{T}/(\text{m}\cdot\text{A})$.

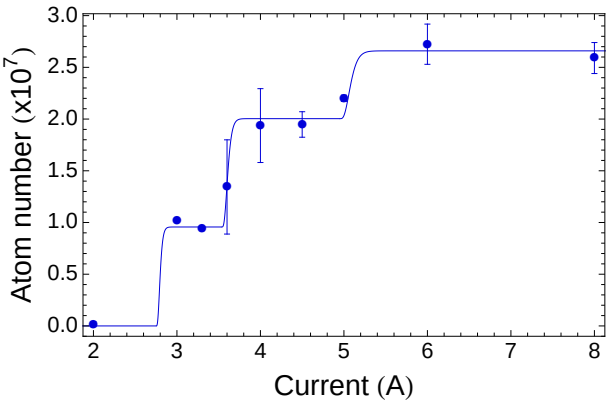


Figure 5.2.1: Spin-composition analysis by ramping down the magnetic confinement. See description in the main text.

Let us finish the analysis of this experiment by deriving the function used for the fit in fig. 5.2.1. The behavior assumed in the previous paragraph was the one corresponding for a cloud with $T = 0$: a series of step functions. For finite temperature T the cloud increases its size while the trap is being decompressed $\lambda \sim b^{-1/3}$ and atoms might hit the cell/chamber walls and be lost. In section 6.5.2 it will be shown that if atoms with energy $E > E_{\text{cut}}$ are removed for the trap, the fraction of remaining atoms is given by $P(9/2, \eta_{\text{cut}}) = \Gamma(9/2, \eta_{\text{cut}})/\Gamma(9/2, \infty)$, with $\eta_{\text{cut}} = E_{\text{cut}}/k_B T$ and $\Gamma(n, \eta) \equiv \int_0^\eta x^{n-1} e^{-x} dx$ being the incomplete Gamma function. In this particular problem $E_{\text{cut}} = \mu_B(m_F/F)(b - (F/m_F)b_g)L$, where L is the distance between the trap center and the obstacle where the atoms are adsorbed. On the other hand

$k_B T = k_B T_0 (b/b_0)^{2/3}$ for an adiabatic opening (see eq. 5.1.4). So one has finally:

$$\frac{N(b)}{N_0} = \sum_{m_F>0}^{F} f_{m_F} P\left(\frac{9}{2}, \frac{((m_F/F)b - b_g)}{b^{2/3} b_0^{1/3}} \frac{L}{\lambda_0}\right) \theta(b - (F/m_F) b_g), \tag{5.2.2}$$

where $\lambda_0 = k_B T_0/\mu_B b_0$ is the initial cloud size, N_0 the total atom number, f_{m_F} is the fraction of atoms in the m_F state in the sample (with $\sum_{m_F>0}^{F} f_{m_F} = 1$) and $\theta(x)$ is the Heaviside function. In the limit $L \gg \lambda_0$ one gets a sum of step functions, while for hotter clouds the steps are smeared out. Notice that it is assumed that the cloud size is at all moments much smaller than the dimensions of the coils, otherwise the linear approximation for the magnetic field breaks down and one has to take into account higher order terms. In other words, the size of the chamber/cell has to be smaller than the size of the coils $L \ll R$ (cf. eq. 5.1.2). Equation 5.2.2 is fitted to the experimental data and plotted in fig. 5.2.1. The agreement of the theory to the data is quite good.

This technique can in principle be used to determine the spin composition of magnetically trapped atoms or to purify a mixture of spins by removing the unwanted ones. However, in our setup we found out that when performing this experiment the sample is depolarized. The reason for this unexpected depolarization is still not clear. We speculate that the magnetic field ramp down is not sufficiently slow to be adiabatic for $b \sim b_g$, because the oscillation period is rather large $\lambda/v_{th} \sim b^{-2/3}$.

	^{40}K	^{6}Li
I_{pump}	$1.0 I_{sat}$	$0.1 I_{sat}$
I_{rep}	$24 I_{pump}$	$12 I_{pump}$
δ_{pump}	2.0Γ	$\sim 3\Gamma$
δ_{rep}	0.3Γ	δ_{rep}
N ($\times 10^9$)	3.0 (100%)	1.0 (90%)
T_H/T_V (μK)	240/180	230/320
PSD	$\sim 3 \times 10^{-5}$	$\sim 4 \times 10^{-6}$

Table 5.2.1: Summary of the optical pumping parameters and loaded number of atoms, temperature and phase space density (PSD) in the compressed magnetic trap in the MOT chamber $b = 1.5$T/m (after waiting time of 0.5s). The values refer to the single-species operation.

Summary

In the preceding sections we presented the principles of magnetic trapping and we studied the trapping of an atomic cloud in a magnetic quadrupole. By optically pumping the atoms into magnetically trappable states, one can load the magnetic trap and adiabatically compress it in order to enhance density. In table 5.2.1 we summarize the main parameters of the optical pumping phase and of the magnetically trapped clouds.

5.3 Magnetic transport

The majority of the experiments with utracold atomic gases comprises a mechanism that displaces the atomic cloud from the MOT region into a science cell. There are two main reasons to do this. The first one is that in the MOT region the optical access is reduced, for instance due to the presence of the optics for the creation of the MOT in all directions of space. The second is that background residual pressure is usually not good enough in the MOT region to perform evaporative cooling in a magnetic trap, due to the proximity to the atomic sources. By implementing differential pumping stages one can have a much improved vacuum quality in a separate region. There are essentially two classes of transport methods for cold gases: optical and magnetic.

The optical method consists in trapping the atomic cloud in the focus of a tightly focused laser beam and to displace it to the desired region [36, 81] (cf. section 7.1 for the working principle of an optical dipole trap). Up to now all experiments relied on an optical setup mounted on an electronically controlled air bearing stage. Recently Léonard et al. [111] reported on an optical transport of a distance of 28cm, using a fixed optical setup, featuring a lens with electrically tunable focal distance. This solution has the advantage of not including the cumbersome and expensive air bearing stage.

The magnetic method consists in simply displacing the magnetic field center. This can be done by installing the anti-Helmholtz coils in a movable stage. Another option is to have a set of pairs of coils and, by dynamically changing the current on each coil pair, the atoms can be transported from coil pair to coil pair. The advantage of the first method is its simplicity, but it requires an important compromise in terms of optical

accessibility due to the moving coil mount. Moreover, since this mount is usually metallic, it can create unwanted magnetic fields such as Foucault currents.

In this experiment we have chosen to implement a magnetic transport composed of pairs of coils in the anti-Helmholtz configuration [72]. The total distance is 64cm and the transport has an "L" shape. An important part of the first year of the thesis of the author were dedicated to the implementation, optimization and debugging of this device. This setup is already well described in the thesis of Salez [171], but there are some updates worth mentioning. In this section we will start by reviewing the basic principles of the magnetic transport and in the second to report on the present configuration and performance. This section with conjunction with ref. 171 should give a complete description of the magnetic transport implemented in the apparatus.

5.3.1 Working principle

The principle of the magnetic transport is to change the position of the magnetic trap center in space and time, so that atoms adiabatically follow it, while keeping the atomic cloud confined. The transport comprises two linear sections: one from the *MOT chamber* to the *elbow* and another from the *elbow* to the *science cell*, in an "L" shape (see fig. 5.3.3). We consider the transport to be done along one dimension, comprising two segments, since atoms stop at the elbow. Let us suppose that the magnetic field minimum is at some position x_0 along that dimension. Since all coil pairs are in the anti-Helmholtz configuration, the trap will be linear and therefore will be characterized by the gradients in each direction of space: b_x, b_y and b_z, that is $\mathbf{B} = (b_x(x - x_0), b_y y, b_z z)$. We take by convention x to be the longitudinal direction (the transport direction), z to be the vertical (gravity) direction and y the transversal direction. These gradient values are not independent, since they have to obey Maxwell's law

$$\boldsymbol{\nabla} \cdot \mathbf{B} = b_x + b_y + b_z = 0. \tag{5.3.1}$$

For this reason, we reason in terms of the transversal gradient b_y and the aspect ratio $A = b_x/b_z$. So, for every instant of time, there are three parameters to impose in order to have a well defined trap: the trap position x_0, the transversal gradient b_y and the aspect ratio A. These three parameters can independently be controlled with three pairs of coils with electric currents I_1, I_2 and I_3. In other words, for a fixed set of three pairs

of coils and for a continuous set of transport parameters $P(x_0) = (x_0, b_y(x_0), A(x_0))$, one can always find a continuous set of solutions $I(x_0) = (I_1(x_0), I_2(x_0), I_3(x_0))$ that satisfy $CI = P$, where C is the matrix of conditions which depends only the geometric properties of the coils. Having calculated the solutions $I(x_0)$ for every position of the trap center x_0, in a second stage one imposes a dynamical function for the movement of the trap center $x_0(t)$. The current that must be fed to each coil pair n as a function of time is simply $I_n(x_0(t))$.

Switching points

In practice, a magnetic transport along a linear segment is composed of several coil pairs in the anti-Helmholtz configuration, approximately equidistant and with some superposition. At every instant of time only three coils have current flowing, say I_1, I_2 and I_3, as argued above. As the atomic cloud moves in the direction of coil 3, the influence of coil 1 decreases and current I_1 decreases with distance x_0 accordingly (see fig. 5.3.1). At some *switching point* $x_0 = x_{\text{sw}}$ we will have $I_1(x_{\text{sw}}) = 0$ and at this

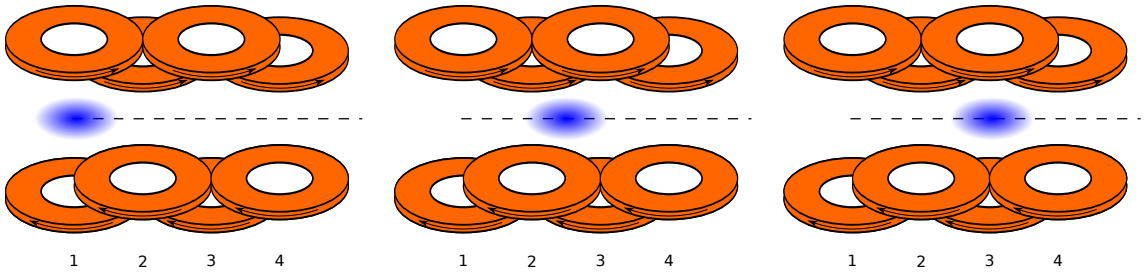


Figure 5.3.1: By dynamically changing the current of three coil pairs one can displace the center of the magnetic trap and its confinement strength, thus transporting an atomic cloud. In the second image the atomic cloud is in the geometrical center of coil pairs 2 and 3, which corresponds to a *switching point*. Here both the currents of coil pair 1 and 4 must be 0 and consequently the aspect ratio of the trap is defined by the geometry of coil pairs 2 and 3. For prior (later) positions the current in coil pair 1 (4) will be positive, respectively.

point coil 4 must be switched on. Let us study more carefully this switching point. At this point the equation $CI = P$ becomes

$$\tilde{B}_2 I_2 + \tilde{B}_3 I_3 = 0 \quad A = \frac{\tilde{b}_{x,2} I_2 + \tilde{b}_{x,3} I_3}{\tilde{b}_{z,2} I_2 + \tilde{b}_{z,3} I_3} \quad b_y = \tilde{b}_{y,2} I_2 + \tilde{b}_{y,3} I_3,$$

where $\tilde{B}_n$ ($\tilde{b}_n$) is a magnetic field (gradient) produced by coil n per unit of current, respectively, evaluated at x_{sw}. Inserting the first equation in the other ones one gets

$$A = \frac{\tilde{b}_{x,2} + \tilde{b}_{x,3}(-\tilde{B}_2/\tilde{B}_3)}{\tilde{b}_{z,2} + \tilde{b}_{z,3}(-\tilde{B}_2/\tilde{B}_3)} \quad I_2 = \frac{b_y}{\tilde{b}_{y,2} - \tilde{b}_{y,3}\tilde{B}_2/\tilde{B}_3} \quad I_3 = \frac{-\tilde{B}_2}{\tilde{B}_3} I_2.$$

The first equation imposes a relation between the aspect ratio and the switching point $A(x_{sw})$, while the two others are straightforward: they give the currents as a function of b_y and x_{sw}. As an example, in fig. 5.3.2 we plot the function $A(x_{sw})$ for the transport coil pairs T_1 and T_2 , playing the role of coils 2 and 3 respectively (cf. schemes 5.3.3 and 5.3.4 and table 5.A.2). It can be seen that for a given aspect ratio, there are always two switching points, except for one case. To get a deeper insight into this curve, let us think of the case in which coils 2, 3 and 4 are on (that is with I_2, I_3 and I_4 all positive) and that the cloud center performs a backward movement. Like for the forward movement, there will be a switching point at which coil 4 switches off $I_4 = 0$, which is not necessarily the same point as the switching point for coil 3. This is well illustrated in fig. 5.3.2: the left branch $x_{sw} < 14.1$cm corresponds to the switching points of coil 3, while the right branch corresponds to a switch off of coil 4. If the aspect ratio was chosen to be $A = -0.3$, coil 3 would turn off at $x_{sw,1} \approx 12.7$cm ($I_3 = 0$), while only at $x_{sw,2} \approx 15.3$cm would coil 4 turn on. There would exist solutions of the $CI = P$ equation for $x_{sw,1} < x_0 < x_{sw,2}$, but with negative I_3 or I_4 values, which is not

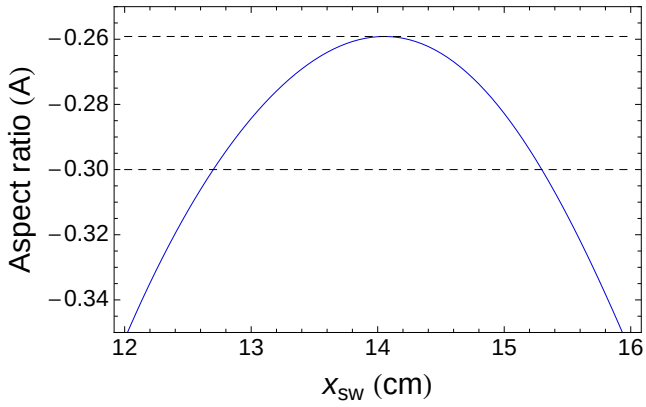


Figure 5.3.2: Calculation of the aspect ratio as a function of the switching point x_{sw} for the T_1 and T_2 coils.

possible in our setup.

In conclusion, avoiding negative currents imposes another condition to the problem, which fixes the aspect ratio and the (single) switching point: in this case, $A = -0.259$ for $x_{\mathrm{sw}} = 14.1\mathrm{cm}$. These solutions have to be found numerically by maximizing the function $A(x_{\mathrm{sw}})$ for every pair of pairs of coils. Notice that the numerically calculated switching point x_{sw} corresponds to the average position of coils T_1 and T_2, which is expected due to symmetry.

In the thesis of Salez [171] the aspect ratio was fixed to $A = -0.3$ and the resulting negative currents were clipped. This gave rise to uncontrolled variations of the gradients (see discussion in sections 4.4.1, 4.4.2 and 4.4.3 of that thesis).

5.3.2 Optimization and performance

The choice of transporting an atomic cloud comes with the price, which is a decrease in phase space density. This can be translated into a loss of atoms or heating during the transport, which must be minimized. Atoms can be lost mainly in two processes: collision and adsorption in the walls of the vacuum tubes and spilling due to insufficient trap depth. Heating arises when the changes in the trap geometry during transport are not adiabatic. In this section we will evaluate the present efficiency of the transport. Details concerning the coils used for transport, the water cooling mechanisms, the used power supplies and the electronics can be found in appendix 5.A and ref. 171.

The trap geometry constraints (aspect ratio A and transversal gradient b_y) and the result of the calculation of the respective currents for each coil pair are plotted in fig. 5.3.5[6] and are going to be discussed in the following paragraphs.

The starting condition of the magnetic transport is the trapping in the MOT coils and here the aspect ratio (cf. top left plot) is $A(0) = -0.5$, naturally[7]. The black dots in the aspect ratio plot show the other points of the transport at which the aspect

[6] These plots can be compared with the "old sequence", as shown in figs. 4.4, 4.3 and 4.15 of ref. 171, respectively.

[7] This is simply a result of the cylindrical symmetry of the system and Maxwell's equations, see eq. 5.1.1.

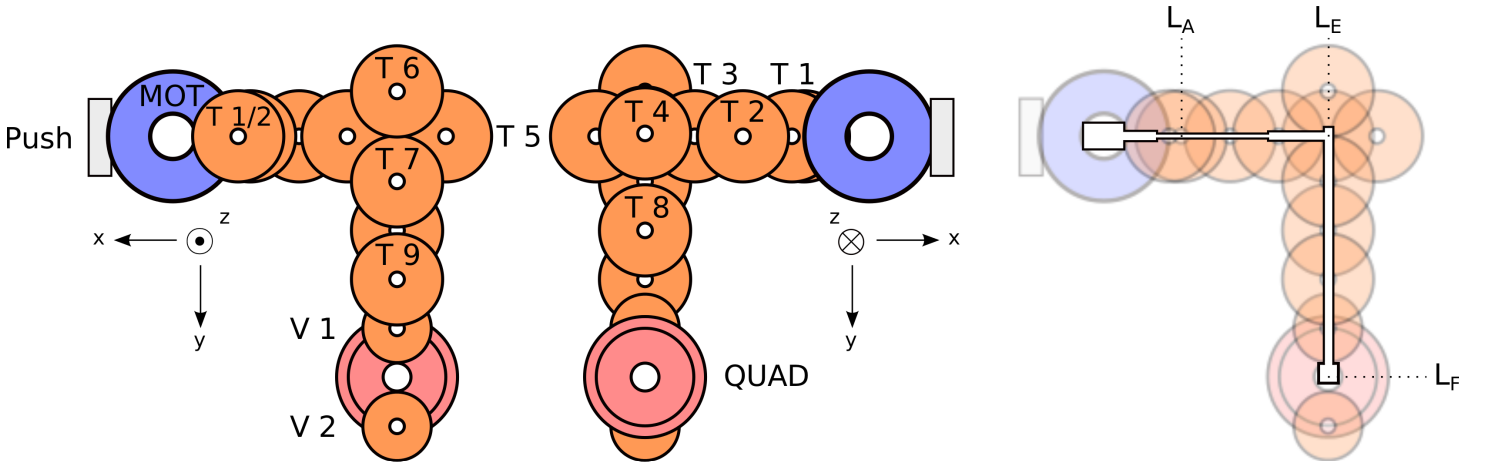


Figure 5.3.3: Scheme of the upper transport coils seen from above (left) and below (center). Vacuum chamber (right): $L_A = 10.7$cm, $L_E = 30.95$cm (elbow) and $L_F = 64.7$cm (science cell).

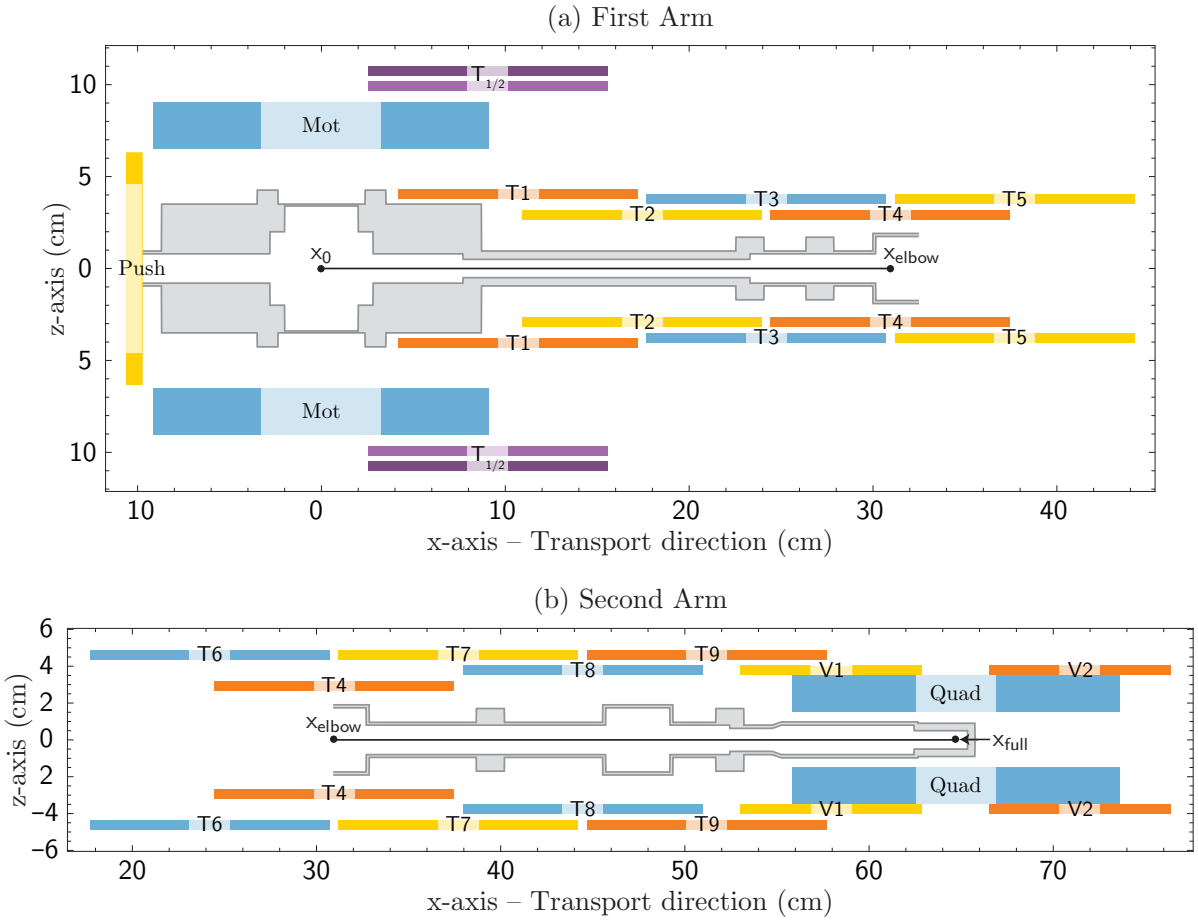


Figure 5.3.4: Scheme of the transport coils and the vacuum chamber seen from the side ($y = 0$). Here $x_{\text{elbow}} \equiv L_{\text{E}} = 30.95\text{cm}$ and $x_{\text{full}} \equiv L_{\text{F}} = 64.7\text{cm}$ (scheme from ref. 183).

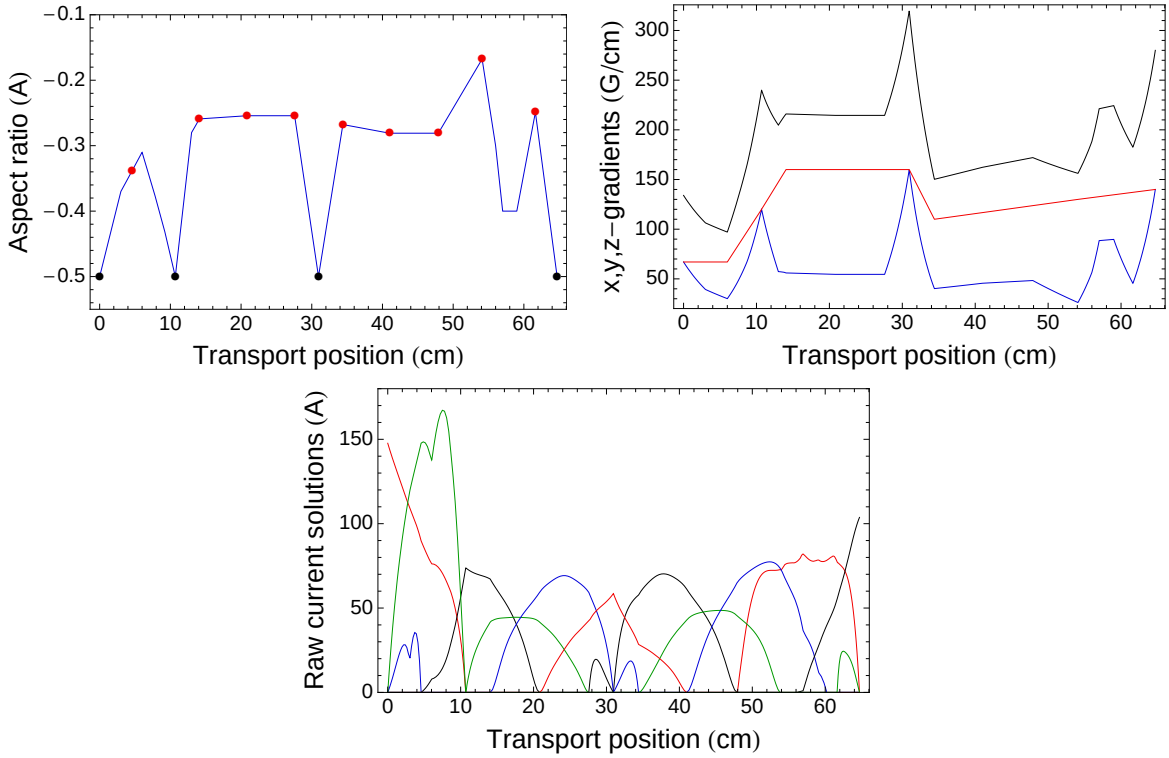


Figure 5.3.5: Aspect ratio $A = b_x/b_z$ (top left), absolute value of the magnetic field gradients (top right: b_x in blue, b_y in red, b_z in black) and calculation of the current for each coil pair (bottom: caption in the main text) as a function of the position of the trap center in the transport.

ratio is also $A = -0.5$. Apart from the starting position where the cloud is trapped by the MOT coils, the cloud is trapped by the T_1 coils at $L_A = 10.7$cm, by the T_4 coils at the elbow $L_E = 30.95$cm and by the Quad coils at the end of the transport $L_F = 64.7$cm. The red dots show the switching points and their corresponding aspect ratios, calculated as discussed in the previous section. The resulting constraints are basically an interpolation between the previous conditions, except at the injection region ($x_0 < L_A$) and at the arrival to the science cell ($\sim 50\text{cm} < x_0 < L_F$). Here the aspect ratio must be carefully tuned in order to optimize the trap depth in the longitudinal direction, since it can be very low. This optimization is vital, otherwise there can be severe atom spilling, caused by inertia for instance[8].

In the top right graph of fig. 5.3.5 the absolute value of the magnetic field gradients

[8] See discussions in sections 4.3.1 and 5.3.4 of ref. 171.

is plotted as a function of the position in the transport (in this thesis we convention the axial/vertical gradient b_z to be positive and the remaining gradients b_x and b_y to be negative). As mentioned before we impose b_y and consequently the remaining gradients can be calculated from the aspect ratio $A = b_x/b_z$ definition and Maxwell's law:

$$b_x = \frac{-Ab_y}{1+A} \quad b_z = \frac{-b_y}{1+A}.$$

Having fixed the trap geometry (aspect ratio and transversal gradient) as a function of the trap position in the transport and having all the geometrical parameters of the coils, one can now use equation $CI = P$ to calculate the current for each coil pair as a function of the trap position in the transport. The calculation result is given in the bottom plot of fig. 5.3.5. In red it is plotted in this order: the MOT coils, T_4 and V_1; in green $T_{1/2}$, T_2, T_8 and V_2; in blue the Pushing coil, T_3, T_6 and T_9; and in black T_1, T_5, T_7 and the Quad coils. The complete geometric properties of these coils are given in ref. 171, except for the Quad coils which are in appendix 5.A.1. Notice that coils T_5, T_6 and V_2 have inverted current direction.

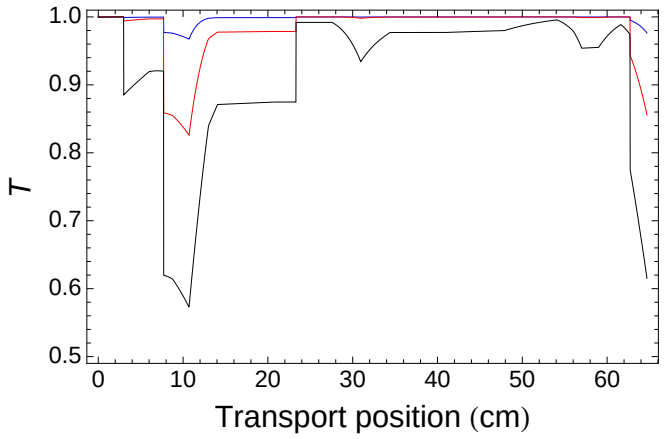


Figure 5.3.6: Fraction of atoms which are left after cropping in the vacuum tube at the position x_0 of the transport for $T_0 = 300\mu$K (blue), for $T_0 = 300\mu$K and a misalignment of 1.5mm in the y direction (red) and for $T_0 = 600\mu$K (black). T_0 is the temperature in the initial magnetic trap.

One of the reasons for losing atoms during the transport is their adsorption in the walls of the transport tube, as mentioned before. This is particularly important at the level of the transport injection due to the presence of a tube of diameter 10mm

for differential pumping (7.7cm $< x_0 <$ 23.31cm) and the entrance of the science cell at the end of the transport, which has the same diameter (see fig. 5.3.3 and 5.3.4). Having fixed all the trap constraints in the previous paragraphs one can calculate the cropping in the transport $\mathcal{T}$ in the following way

$$\eta(x_0) = \frac{\mu_B b_y(x_0) R_y(x_0)}{k_B T(x_0)} \quad \mathcal{T}(x_0) = P(9/2, \eta(x_0)).$$

$\mathcal{T}(x_0)$ is the fraction of atoms which are left after cropping in the vacuum tube at the position x_0 of the transport. $R_y(x_0)$ is the local radius of the transport tube and $P(n, \eta)$ is the normalized incomplete Gamma function, already mentioned in section 5.2. Moreover $T(x_0)$ is the local temperature given by the adiabatic relation 5.1.4:

$$T(x_0) = T_0 \prod_{i=x,y,z} (b_i(x_0)/b_{i,0})^{2/9},$$

where T_0 and $b_{i,0}$ are the parameters in the MOT chamber. Notice that to calculate the cropping we neglect the contribution in the z direction since this gradient is always larger than the one in the y direction (see fig. 5.3.5). The result of the calculation of $\mathcal{T}$ is given in fig. 5.3.6: it shows that the injection in the transport $x_0 \sim$ 11cm and the entry in the science cell $x_0 \sim$ 64cm are the regions where most adsorption losses will occur. For a cloud with $T_0 = 300\mu$K the loss will be of $\sim$ 3%, while for $T_0 = 600\mu$K the loss will be of $\sim$ 43%. On the other hand, for $T_0 = 300\mu$K and a misalignment of the transport of 1.5mm in the y direction, the loss will increase to $\sim$ 17%. The temperatures in the initial trap for ^{40}K and ^{6}Li are in the range $200 - 300\mu$K so we expect a good transmission. This validates the constraints imposed to the magnetic transport. The experimental results will be shown in a following paragraph.

The last step in the definition of the transport sequence is to impose the dynamics of the movement of the magnetic trap center $x_0(t)$ (see fig. 5.3.7). These dynamics are divided in three parts: first, from the MOT region to L_A (blue), second, from L_A to the elbow L_E (red) and third, from the elbow L_E to the science cell L_F (black). In order to have a smooth function for each transport segment, we have chosen that the velocity and the acceleration must be 0 for both ends of each segment. As a consequence, the velocity function is a polynomial of degree 4 in time. The reason to separate the

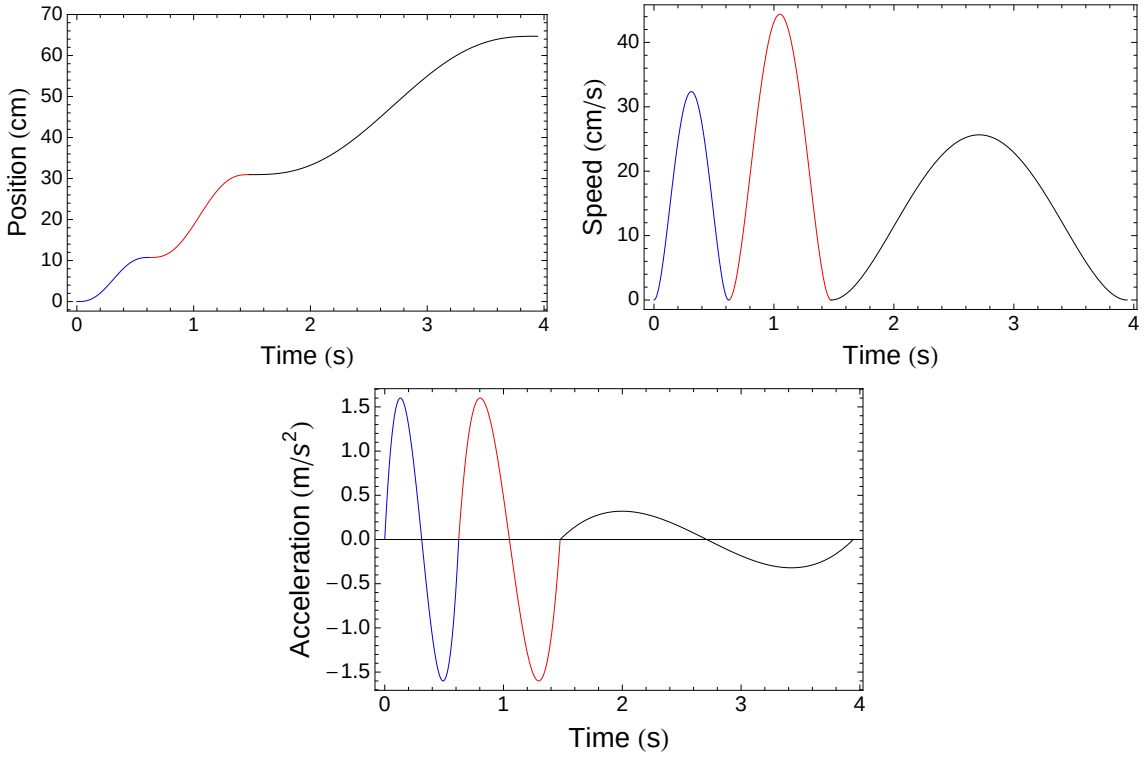


Figure 5.3.7: Position of the magnetic trap center (top left), velocity (top right) and acceleration (bottom) as a function of the transport time. In blue is the first transport segment (from the MOT cell to L_A), in red the second (from L_A to the elbow L_E) and in black the third (second transport arm: from the elbow L_E to the science cell L_F).

first transport arm (from the MOT to the elbow) in two segments is due to the region around $\lesssim L_A$ (the transport injection) which is problematic for two reasons. The confinement in the longitudinal direction is weak (low trap depth) and it corresponds to the entry in the transport tube, which has a diameter of 10mm (where adsorption losses can be dramatic). With this approach, both the velocity and the acceleration of the cloud are small around the injection region. The choice of the maximal acceleration is a compromise with the lag felt by the atomic cloud. In our conditions lag should be smaller than 1mm[9], which is small compared with the typical cloud longitudinal size $2\lambda_x \sim 10$mm. The final duration for each segment of the transport was optimized subsequently, being 1s for $x_0 < L_A$, 1.3s for $L_A < x_0 < L_E$ and 3s for $L_E < x_0 < L_F$, yielding a total duration of the magnetic transport of 5.3s.

[9]See fig. 5.4 of ref 171.

Back-and-forth experiment

In order to diagnostic the magnetic transport, we did a "back-and-forth" experiment, in which atoms were transported from the initial trap into a certain transport position and then transported back to the beginning. This allows us to directly measure the relative atom loss and temperature increase in the path travelled by the atoms. This is a powerful diagnostic method in the absence of direct imaging along the transport axis.

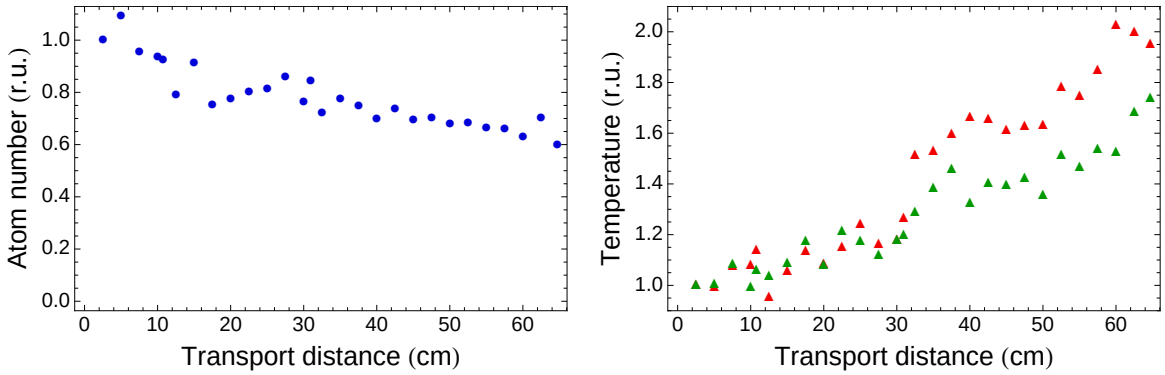


Figure 5.3.8: Efficiency of the magnetic transport determined by the "back-and-forth" experiment for ^{40}K. Measured atom number (left) and temperature (right: T_{hor} in red and T_{vert} in green) as a function of the probed transport distance. The initial temperature is $\approx 200\mu$K. Notice that in this experiment the distance travelled by the atoms is twice the probed transport distance.

The back-and-forth experiments were performed with ^{40}K and the results are plotted in fig. 5.3.8. They show that the atom number is continuously reduced down to 60% of its initial value, meaning that one can estimate the efficiency for a one-way travel as $\sim \sqrt{0.6} \approx 78\%$ (assuming that the losses are similar in both ways). Before the differential pumping tube, that is for $x_0 < 7.7$cm, the lifetime in the magnetic trap is ≈ 16.5s, limited by the background pressure, while at the elbow $L_{\mathrm{E}} = 30.75$cm it is ~ 130s. The transport time from the MOT chamber to $x_0 = 7.7$cm takes 1s and so the effect of the residual background pressure is negligible.

Concerning temperature, it can be measured by the standard time-of-flight technique. The values in the initial trap were already measured $T_0 \approx 200\mu$K and are shown in table 5.2.1. The temperature after a back-and-forth travel is plotted in the

right graph of fig. 5.3.8. It was observed an increase of the temperature in both the horizontal and the vertical directions, being more important in the horizontal one. One can identify important heating occurring around $x_0 = 32$cm (beginning of the second section of the transport) and at the arrival in the science cell $x_0 > 60$cm. In the remaining regions there is a slope of gradual heating. After the complete back-and-forth experiment from the initial trap to the science cell and back the measured temperatures were $T_{\text{hor}} = 550\mu$K and $T_{\text{vert}} = 457\mu$K. Notice that the observed heating depends on the duration of the transport. The results presented here concern a total transport duration of 5.3s, which is a trade-off between heating and experimental repetition time.

The origin of the gradual heating might come from modeling imperfections of the magnetic transport, resulting in the production magnetic field that is not the same as the calculated one. These imperfections might shake the magnetic trap diabatically resulting in heating. Another cause for modeling imperfections is the induction of Foucault currents in the transport water cooling plates, whose (dynamic) contribution to the magnetic field is not taken into account. Furthermore, at every switching point, there is the switching of two MOSFETs (one off, another on) in order to make the current flow from one transport coil pair to another. It might be that this abrupt switching disturbs the atomic cloud, even if one expects there should be no current flowing in the coils during the switching. A way to improve this is to implement a solution with 4 power supplies.

Let us now estimate the effect of the misalignment of the transport assembly. In the first section of the transport there is no possibility of imaging the atomic cloud. Nevertheless, by transporting the cloud to a certain transport position x_0 and then adiabatically decompressing the trap, one can measure the *effective* radius of the transport tubbing $R(x_0)$ (see end of section 5.1). We interpret the difference between the measured effective radius and the real radius of the transport tube as a misalignment and we determined it as $\approx$ 1mm for $x_0 = 9$cm (see fig. 5.13 of ref. 171). In the second section of the transport one can image the cloud and measure its distance to the transport tubbing. In fig. 5.3.9 it is plotted the distance between the atomic cloud (the magnetic field center) and the center of the circular constriction of 10mm of diameter

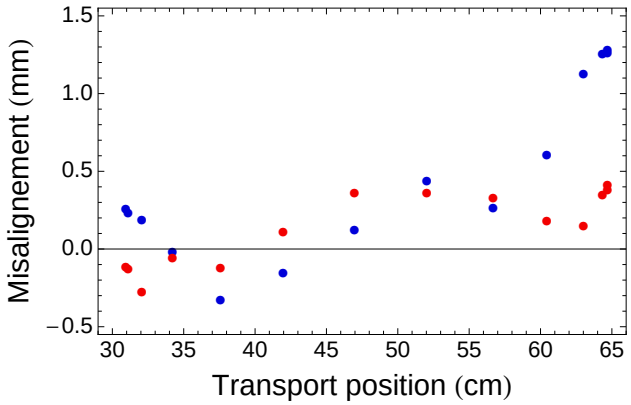


Figure 5.3.9: Transversal distance between the magnetic field center and the center of the science cell for the second portion of the magnetic transport. In blue is the x direction and in the red the z direction, as defined in section 2.2.3.

at the science cell entrance[10]. The misalignment is smaller than 0.5mm in both axis between the elbow and $x_0 = 60$cm and it is probably due to imperfections in the relative positioning of the transport coils. For $x_0 > 60$cm one sees that the cloud is displaced horizontally by $\approx$ 1mm, which might be due to a misalignment of the final quadrupole coils relative to the transport plate. Fortunately, this displacement is not associated with atom loss nor important heating (see fig. 5.3.8).

Concerning ^{6}Li, we expect its solo transport efficiency to be smaller than the one of ^{40}K, since its initial temperature is bigger. However, in the presence of ^{40}K the cloud of ^{6}Li thermalizes to a smaller temperature, which should improve the transport efficiency. Moreover, we expect that heating during transport to be less important for ^{6}Li due to its smaller inertia.

5.4 Conclusions

In this chapter we reviewed the principle of magnetic trapping, we studied the particular case of the quadrupole trap and we explained how to fully experimentally characterize a trapped atomic cloud. In order to transfer atoms from the molasses to the magnetic trap an optical pumping phase is required in order to pump all the atoms into trappable Zeeman state(s). We show that we were able to transfer 100%

[10]For an engineering drawing of the science cell see fig. C.1 of ref. 166

of the ^{40}K atoms and 90% of the ^{6}Li atoms from the molasses into the magnetic trap. The optimized parameters of the optical pumping phase and the characterization of the magnetically trapped clouds are summarized in table 5.2.1.

In order to transport the atomic cloud from the MOT chamber into the science cell, in which the background pressure and the optical access is improved, we designed a magnetic transport composed of a series of pairs of coils. By dynamically changing the current of each coil pair we are able to move the trap center and transport the atomic cloud. The magnetic transport sequence transports the atoms from the MOT chamber to the science cell, covering a distance of $\approx$ 65cm in 5.3s. We estimate that 80% of the atoms reach the science cell, limited by spilling and adsorption in the tubbing of the apparatus. The measured averaged atom number fluctuations of ^{40}K are $\approx$ 9% at this point. After transport, we observe a temperature increase of $\sim$ 50%, yielding a loss in phase space density of factor $N/T^{9/2} \sim 1/7$, mainly due to heating. One could decrease heating by increasing the transport time, but we find that the achieved compromise between phase space density loss and experimental repetition rate to be satisfactory. This concludes the optimization and the characterization of the magnetic transport, which has a good performance compared to other solutions [36, 72, 81, 135].

Appendix 5.A Electromagnets

5.A.1 Description of the coils

In this apparatus there are several electromagnetic coils present, which were designed to produce magnetic fields with different purposes.

The Zeeman slower and its compensation coil (named *anti-Zeeman*), that slow the ^{6}Li atomic jet, and the four racetrack coils, that produce the ^{40}K 2D-MOT, were already described in refs. 166, 171. The first ones are made with hollow tubbing through which tap water can flow, while the latter are let permanently switched on since heating is not significant.

In the MOT chamber there is the MOT coil pair that creates the magnetic field gradient for the MOT and the magnetic trapping of the atoms. There is also a pair of coils for the optical pumping (SP), that have low impedance in order to quickly ramp an homogenous magnetic field. For the magnetic transport we use the MOT coils, the pushing coil, two pairs of coils called $T_{1/2}$ (inner and outer), a series of pair of coils $T_1, T_2, \ldots, T_5$ for the first section (in T_5 current flows in the opposite direction), and $T_4, T_6, \ldots, T_9, V_1, V_2$ and Quad (in T_4 and V_2 current flows in the opposite direction). We refer the reader to ref. 171 for details about the coils and below for the Quad coils. The most relevant parameters of these coils are listed in table 5.A.2.

The power supplies used to feed current to the coils are listed in table 5.A.1. According to the suppliers, the Delta Elektronika have specified current stability of 10^{-4}, the TDK-Lambda 3×10^{-4} and the High Finesse $< 10^{-5}$ (typical bandwidth 5Hz-1MHz).

We implemented a security system that monitors the temperature of several of the coils used in the experiment (via thermistances glued to them) and shuts down all the power supplies when the measured temperature value is above a certain safe set point. Flowmeters measure the water flux through the cooling elements and warns the security system if the water flux is not sufficient, resulting again in the switch off of all power supplies.

The apparatus also has magnetic field compensation coils. Three large coils were installed $\approx$ 80cm from the MOT chamber, in each direction of space, in order to compensate for stray fields and optimize the functioning of the gray molasses. Their

shape is squared with side $\ell = 1$m and each coil has 54 turns. There are switched using MOSFETs (see next section for details concerning the switching electronics) and are only on during the gray molasses phase. Two other coils were installed ≈ 45cm from the science cell. Their shape is squared with side $\ell \approx 35$cm and each coil has 70 turns. They are also switched using MOSFETs. For the vertical axial direction the *outer coils* in the Helmholtz configuration are used, as explained in the following section.

Code	Model
Blue	Delta Elektronika SM 45-140
Delta SP	Delta Elektronika SM 1540-D
Orange	Delta Elektronika SM 45-70D
Yellow	Delta Elektronika SM 45-70D
Annexe	Delta Elektronika SM 30-200 (2x in series)
Genesis	TDK-Lambda GEN 50-200
White	Delta Elektronika SM 15-400
HighFinesse	High Finesse 30A/15V

Table 5.A.1: Code for the power supplies.

Coil(s)	Position (cm)	Axial field	Power supply	Cooling
MOT	0	0.91G/A/cm	Blue	Hollow wires
SP	0	4.8G/A	Delta SP	None
Pushing	-9.86	$(0.16 - 0.73\text{cm}^{-1})$G/A	**Yellow**	
$T_{1/2}$ (inner/outer)	9.05	0.37G/A/cm	Annexe	Cooling plate
		0.29G/A/cm	Genesis	
T_1	L_A =10.7	3.3G/A/cm	Orange	Transport cooling plate
T_2	17.45	5.5G/A/cm	**Yellow**	
T_3	24.2	3.7G/A/cm	Blue	
T_4	L_E =30.95	5.5G/A/cm	Orange	
T_5	L_E+6.75	−3.7G/A/cm	**Yellow**	
T_6	L_E−6.75	−2.6G/A/cm	Blue	
T_7	37.7	2.6G/A/cm	**Yellow**	
T_8	44.45	3.7G/A/cm	Blue	
T_9	51.2	2.6G/A/cm	Orange	
V_1	57.95	2.8G/A/cm	**Yellow**	
V_2	71.45	−2.8G/A/cm	Orange	
Quad	L_F =64.7	2.7G/A/cm	Blue	Hollow wires

Table 5.A.2: Coils present in the experiment, their position in the transport (0 is the MOT chamber and 64.7cm is the science cell positions), main components of the produced field calculated at the center of the coil pair (for the pushing coil it was calculated at the center of the MOT coils), the corresponding power supply and cooling mechanism. The water cooling the transport cooling plate is stabilized to 17°C by a chiller, while for the other systems the water comes from the tap. Hollow wires allow direct cooling with water. See ref. 171 for more details.

Quad coils

The Quad coils are composed of two pairs of concentric coils: the *inner coils* and the *outer coils* (see scheme of fig. 5.A.1). For the magnetic transport they are connected in the anti-Helmholtz configuration and have the same current flowing. They are made of hollow copper wires with squared cross section $4 \times 4\text{mm}^2$, through which water flows from the chiller which stabilizes water temperature to 17°C. These coils were wound by the company Oswald[11] and were impregnated in epoxy for mechanical stability. The inner coils have 4 layers of 12 windings each and their mean radius is 44mm. The outer coils have 4 layers of 4 windings each and their mean radius is 80.5mm. The mount for the Quad coils is made of glass-fibre-reinforced polyamide 66[12] and it fixes the position of the coils by clamping them against to the transport mount (see fig. 5.A.2). The electromagnetic properties of the quadrupole coils are listed in table 5.A.3 and the electronic connections are shown in a scheme in fig. 5.A.3.

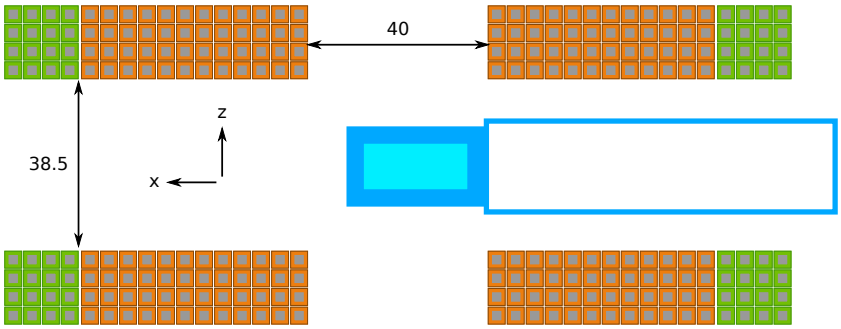


Figure 5.A.1: Scheme of the cross-section of the science cell and the Quad coils: inner pair (in orange) and outer coils (in green). Each square represents the cross-section of the hollow copper wire $4 \times 4\text{mm}^2$.

The Quad coils were mounted in such a away that the inner coils have an important positive curvature. Indeed, the distance between the inner coils exceeds their radius and so the axial magnetic field they produce is not homogenous. The field produced by these coils can be written as $B_z = B_0 + \frac{1}{2}B''z^2 + \mathcal{O}(z^4)$ and $B_\rho = -\frac{1}{4}B''\rho^2 + \mathcal{O}(\rho^4)$,

[11] Oswald Elektromotoren GmbH

[12] This is a plastic with good stability, both short-term (strength and stiffness) and long-term (fatigue and creep). It is used for several applications, such as auto parts such as mirror housing brackets or clutch pedals [12]. This material was also used for the coil mount of the experiment in Innsbruck.

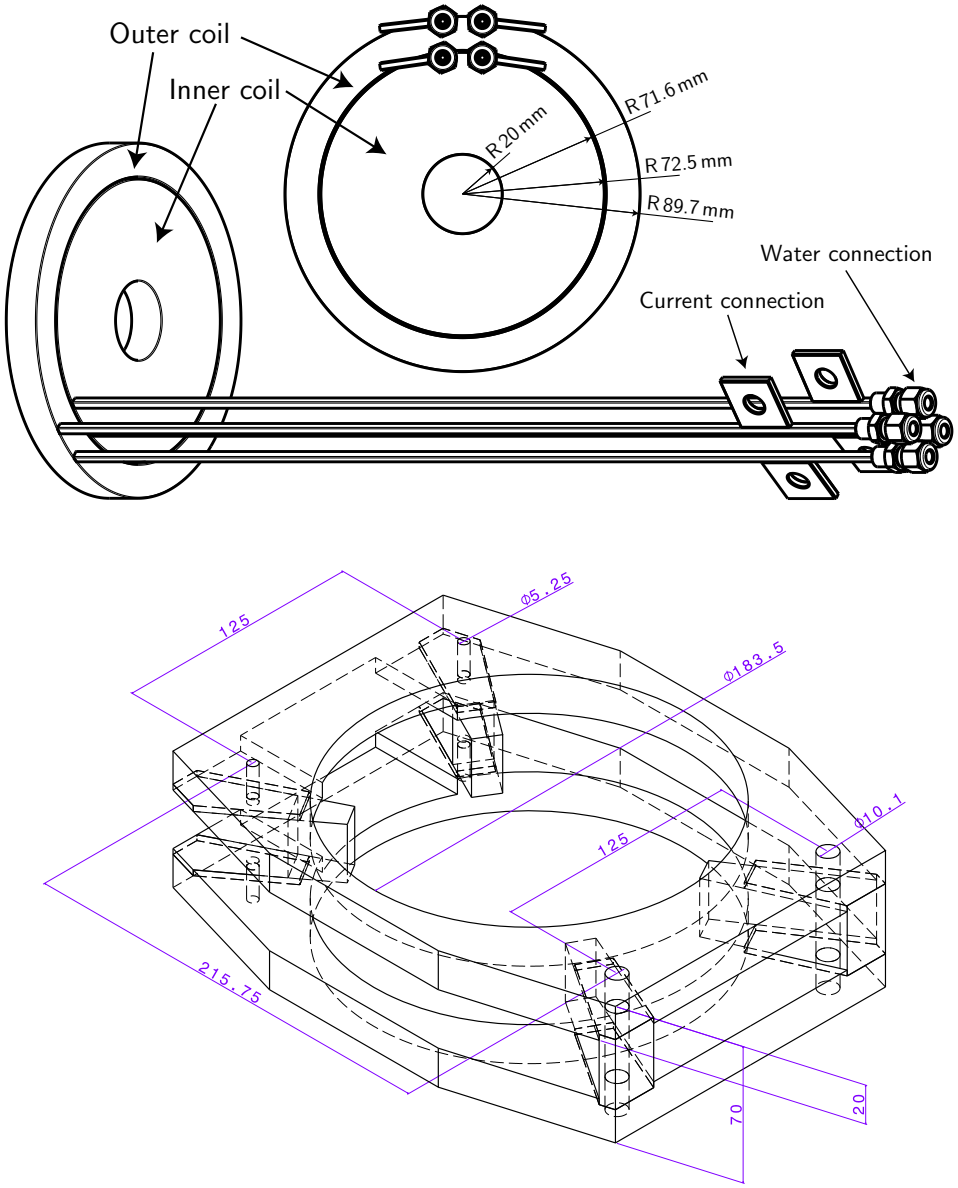


Figure 5.A.2: Engineering drawing of the quadrupole coils (top) and their mount (bottom). The quadrupole coils are made of two concentric coils: *inner* and *outer* and are made of hollow copper wire impregnated in epoxy. The mount is made of glass-fibre-reinforced polyamide 66 and clamps the coils into the magnetic transport cooling plate. Scheme in the top is from ref. 183.

where B'' is the field curvature. An atom in a high field seeking state will be harmonically trapped in the transversal direction $\hat{\rho}$ with trapping frequency

$$\omega_\rho^2 = \frac{\mu_B B''}{2m}.$$

For example, for $B_0 = 200$G in the *inner* coil $\omega_\rho/2\pi = 5.2$Hz for ^{40}K and $\omega_\rho/2\pi = 13$Hz for ^{6}Li (stretched states). The outer coils have a negative curvature and so they can trap low field seekers. For $B_0 = 200$G in the *outer* coil $\omega_\rho/2\pi = 7.0$Hz for ^{40}K and $\omega_\rho/2\pi = 18$Hz for ^{6}Li (stretched states). Since the curvatures of the two coil pairs have different sign, we can tune the curvature by distributing the current between them.

Inner coils	Axial field	
H	$B_0 = 8.00$G/A	$B'' = 0.61$G/A/cm^2
AH	2.5G/A/cm	

Outer coils	Axial field	
H	$B_0 = 2.089$G/A	$B'' = -0.29$G/A/cm^2
AH	0.24G/A/cm*	

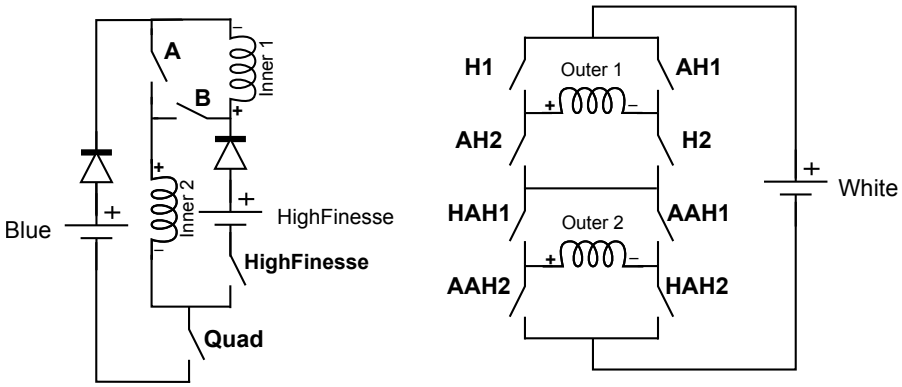
Table 5.A.3: Field produced by the inner and the outer coils in the Helmholtz (H) or anti-Helmholtz (AH) configurations. All values were experimentally determined, except for the one marked with an asterisk *.

5.A.2 Electronics

In order to quickly switch on or off the current flowing in a coil, we installed a system of MOSFETs[13] and IGBTs[14]. They can be controlled using the TTL channels of the digital cards[15]. Between the cards and the switching electronic devices we installed optocoupler circuits[16] in order to isolate and protect the digital cards and avoid ground loops of current. Individual MOSFETs are installed for each coil pair listed in table

[13] IXFN 200N10
[14] Mitsubishi Electric CM600HA-24A
[15] National Instruments PXI-6533
[16] As explained in the thesis of Salez [171].

5.A.2, except for the MOT coils and the Quad coils (inner and out) for which IGBTs were used. This allows individual control of each pair of coils, in contrast with the *switch box* reported in ref. 171, which was removed from the apparatus. The source of each MOSFET is always connected to the ground of the respective power supply and each MOSFET is protected using varistors[17]. The IGBTs are also protected using varistors and their circuit is showed in fig. 5.A.3. The Quad coils are installed in such a away that we can change the configuration of the inner and the outer coils (Helmholtz or anti-Helmholtz). Diodes[18] were installed to ensure that current is flowing in the desired direction in the electronic circuits[19] and to protect the power supplies.



Outer coils	H	Inv H	AH	Inv AH
HH	1	0	0	1
AH	0	1	1	0
H/AH	1	0	1	0
AAH	0	1	0	1

Figure 5.A.3: Electronic schematics of the inner coils (left) and the outer coils (right), with the relevant power supplies, IGBTs (named in bold) and diodes. When the current is flowing in the direct direction of a coil, the magnetic field produced in the science cell is in the (positive) z direction. Table with the code for the IGBTs logics for the different magnetic field field configurations of the outer coils: Helmholtz (H), anti-Helmholtz (AH) and inverted currents.

[17] Vishay 07K14 for the gate and Vishay S20K320 for the drain
[18] Vishay 400U120D
[19] Dynex DFM600BXS12-A000

6 Evaporative cooling in a plugged magnetic quadrupole trap

6.1 Introduction

With the discovery of sub-Doppler cooling techniques, alkali cold gases became serious candidates to achieve Bose-Einstein condensation in the early 90s. However, optical cooling strategies alone were proven insufficient to reach this goal at that time. Indeed, phase space density could reach at best $\sim 10^{-3}$, being limited by light induced collisions in particular. In order to go further up in phase space density, the technique of evaporative cooling was adapted from early experiments with spin-polarized Hydrogen [125] to alkali gases [99]. This strategy can be used when the atomic gas is trapped in a conservative trap. The main idea behind evaporative cooling is to selectively remove the most energetic atoms from the trap, while the remaining atoms rethermalize into a cloud with smaller temperature. This method was proven to be very efficient: at the expense of some atom loss, the phase space density (PSD) can increase very fast. Evaporative cooling is still at present the standard method to achieve quantum degeneracy[1].

This chapter will be mainly devoted to the study and the experimental realization of evaporative cooling of ^{40}K in a plugged magnetic quadrupole trap. In a first part we will describe the elastic (section 6.2) and inelastic collisions (section 6.3) between Potassium atoms. We will conclude that for ^{40}K the s-wave and the p-wave channels have both important contributions to the elastic collision rate and that inelastic Majorana losses can be suppressed with an optical plug. In section 6.4 we will study the evaporation dynamics of this system, by extending the standard analytical treatment [33] to a momentum-dependent scattering cross-section and by evaluating the individual contributions of the s-wave and the p-wave channels. In a second part we will

[1] A remarkable exception is the case of Strontium, for which it was recently reported laser cooling to quantum degeneracy [190].

start by introducing the experimental techniques used in this thesis for evaporative cooling in a plugged trap (section 6.5). In section 6.6 we will present and discuss the experimental results of the evaporative cooling and demonstrate that with this technique we can enhance the phase space density of the atomic sample. In the following chapter 7, we will show that by performing evaporative cooling to $T = 100\mu$K in the plugged magnetic quadrupole trap ($b = 2.5$T/m), we can efficiently load an optical dipole trap (where the degenerate gas will be produced).

Finally we will address in section 6.7 the cooling of ^{6}Li. Since there is only one atomic state that is simultaneously magnetically trappable and stable, collisions can only take place via the p-wave channel. As for ^{6}Li p-wave collisions are suppressed below $\sim$ 6mK [100], the gas is collisionless in our experimental conditions. In order to cool down ^{6}Li we rely on interspecies collisions with ^{40}K [176] (sympathetic cooling). We will show that by performing evaporative cooling on ^{40}K we cool a small sample of ^{6}Li in a plugged magnetic trap and we can load it into an optical dipole trap.

6.2 Cold elastic collisions

The performance and the dynamics of evaporative cooling crucially rely on elastic collisions between atoms. Due to the Pauli exclusion principle, *indistinguishable* fermions can only collide via the p-wave channel. These collisions are suppressed at very low temperatures due to the rotational p-wave barrier[2]. For *distinguishable* fermions the scattering cross-section is finite at very low temperatures $\sigma = 4\pi a^2$, where a is the *scattering length*. In turns out that at finite temperatures p-wave collisions can dominate over the s-wave ones. In this section we will determine the thermally-averaged scattering cross-section of ^{40}K for the s-wave and the p-wave channels. We will show that for $T \gtrsim 100\mu$K the scattering cross-section for p-wave collisions is more important than its s-wave counterpart.

It follows from basic scattering theory [106, 155, 206] that one can write the scattering cross section in the following way

$$\sigma(k) = \int d\Omega \, |f(\theta)|^2 \quad \sigma(k) = \int d\Omega \, |f(\theta) \pm f(\pi - \theta)|^2 \,. \tag{6.2.1}$$

[2]We do not consider here the exceptional case of dipolar interactions [2].

The expression at left is valid for the scattering of *distinguishable* particles, while the one at right takes into account the symmetry properties of *indistinguishable* particles. Here k is the wavenumber of the relative motion[3]. The function $f(\theta)$ is the *scattering amplitude* and it can be expanded in partial waves using the Legendre polynomials P_ℓ as follows

$$f(\theta) = \sum_{\ell=0}^{\infty} (2\ell+1) f_\ell P_\ell(\cos\theta) \quad f_\ell = \frac{1}{k\cot\eta_\ell - ik}.$$

Here η_ℓ is the *phase shift* and depends directly on the properties of the molecular scattering potential. For a finite-range potential, the partial scattering amplitudes are $f_\ell \sim k^{2\ell}$ in the limit of low energies[4] [106, eq. 132.8]. In consequence, the scattering cross section is dominated by the s-wave ($\ell = 0$) scattering at low temperature. This can be interpreted as the repulsive effect of the rotational barrier $\ell > 0$. In the particular case of indistinguishable fermions, the scattering cross section decreases with decreasing temperature, since they can not scatter in the s-wave channel due to the Pauli exclusion principle.

The Boltzmann equation relates the scattering cross section with the collision rate in a trapped gas, which is a fundamental quantity in the study of evaporative cooling. For an atomic cloud in thermal equilibrium, one can calculate the thermally-averaged scattering cross section

$$\sigma(T) = \frac{\langle v\sigma\rangle}{\bar{v}_\mu} = \frac{2}{\bar{v}_\mu}\left(\frac{\Lambda_\mu}{2\pi\hbar}\right)^3 \int d^3\mathbf{p}\,(p/\mu)\,\sigma(p) e^{-p^2/2\mu k_B T}, \tag{6.2.2}$$

where $p = \hbar k$, $\bar{v}_\mu = \sqrt{4k_B T/\pi\mu}$ is the thermal speed of the reduced-mass particle and $\Lambda_\mu^2 = \pi\hbar^2/\mu k_B T$ its thermal wavelength [206]. For a single-component gas the collision rate is given by

$$\boxed{\gamma_{\text{coll}} = \frac{1}{\sqrt{2}} n_0 \sigma(T) \bar{v}_{\mu=m/2} \frac{V_{2e}}{V_e},} \tag{6.2.3}$$

with $V_e = \int d^3\mathbf{r} \exp\{-U(\mathbf{r})/k_B T\}$ being the reference trap volume, $V_{2e} = \int d^3\mathbf{r} \exp\{-2U(\mathbf{r})/k_B T\}$ being a "two-particle overlap volume" and $n_0 =$

[3] For a collision of energy E between particles with reduced mass μ, $E = \hbar^2 k^2/2\mu$.
[4] To be accurate, for a potential varying as r^{-n}, this result is only valid for $\ell < (n-3)/2$ [106, 155].

N/V_e the central atom density in the trap. $V_{2e}/V_e = 1/2^\delta$ for a power-law trap potential $V(r) \sim r^{3/\delta}$ and $\delta = 0$ for an homogeneous gas. For a multiple component gas the collision rate is twice as big [206].

The remaining part of this section is divided into two parts and has the objective of evaluating the thermally-averaged scattering cross section for ^{40}K atoms. In the first part we will study the s-wave scattering between distinguishable particles. In the second one we will analyze the case of the p-wave scattering between two indistinguishable fermions.

6.2.1 S-wave collisions

For distinguishable particles, one can obtain the low energy scattering cross section by expanding eq. 6.2.1. The contribution of the s-wave channel is given by

$$\sigma(k) = \frac{4\pi a^2}{\left(1 - r_e a k^2/2\right)^2 + a^2 k^2},$$

where a is the s-wave scattering length and r_e is the effective range [206]. For bosonic particles there is a supplementary factor of 2 in the cross section due to constructive interference in the scattering. By modeling the molecular potential with a long-range van der Waals attraction $U(r) = -C_6/r^6$ and a hard-core short-range cut off, one can obtain

$$r_e \approx a_6 \left(1.39473 - 4/3\,(a_6/a) + 0.63732\,(a_6/a)^2\right) \quad a_6 = (2\mu C_6/\hbar^2)^{1/4},$$

where μ is the reduced mass of the colliding particles [59] [155, section 5.3]. The thermally-averaged collision rate can be calculated by plugging this result into eq. 6.2.2

$$\frac{\sigma(T)}{\sigma(0)} = \int_0^\infty \frac{x e^{-x}}{\left(1 - \alpha(T)x\right)^2 + \beta(T)x} dx \quad \begin{cases} \alpha(T) = \pi r_e a/\Lambda_\mu^2 \\ \beta(T) = 2\pi a^2/\Lambda_\mu^2 \end{cases}$$

with $\Lambda_\mu^2 = \pi\hbar^2/\mu k_B T$.

As discussed before, the s-wave scattering length encapsulates information concerning the low-energy scattering of particles via their molecular potentials. For this

reason it is a function of the contributions of the triplet and the singlet potentials (and the magnetic field). Atoms in their stretched states ($F = I + 1/2$ and $m_F = \pm F$) only scatter through the triplet channel, which greatly simplifies the problem[5]. In general, a multi-channel calculation is needed. The triplet s-wave scattering lengths for the scattering of ^{40}K with the different Potassium isotopes are [56]

isotope	a_t (a_0)
40/40	169.67(24)
39/40	−1985(69)
40/41	97.39(9)

Although the mixture ^{39}K-^{40}K is apparently very favorable, it turns out that for collisions at increasing energy (temperature) the scattering cross section decreases very fast. Due to the negative value of the scattering length, it will eventually cross 0, yielding a minimum of the thermally-averaged scattering cross section (Ramsauer-Townsend effect). For temperatures around $\sim 400\mu$K the scattering cross sections for all atom combinations are similar (see fig. 6.2.1). For simplicity we decided to perform evaporative cooling in a mixture of states of ^{40}K.

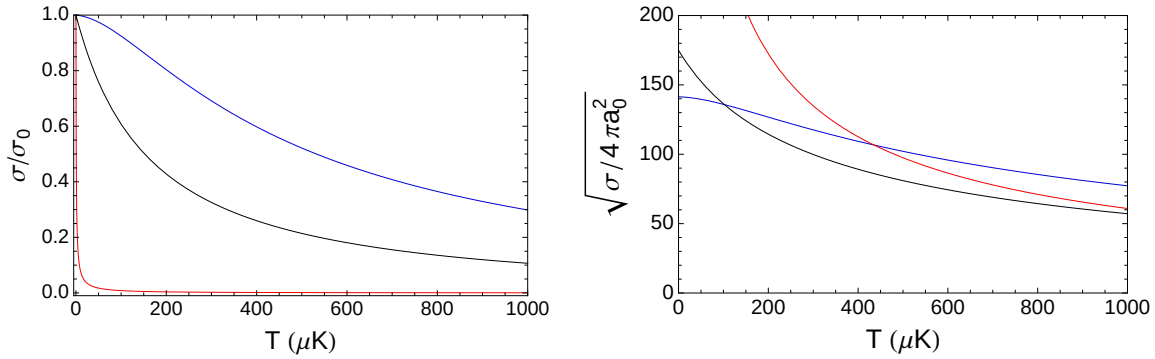


Figure 6.2.1: $\sigma(T)/\sigma(T=0)$ (left) and $a(T)/a_0 \equiv \sqrt{\sigma(T)/4\pi a_0^2}$ (right) as a function of temperature for ^{40}K-^{40}K (black), ^{39}K-^{40}K (red) and ^{40}K-^{41}K (blue) collisions.

[5]For ^{40}K one is usually interested in the states $m_F = \pm 9/2$ and $m_F = \pm 7/2$ of the $F = 9/2$ manifold. For simplicity, one neglects the singlet channel contribution of state $m_F = \pm 7/2$ at low magnetic field. Experimental data show that this is in an accurate simplification [41].

6.2.2 P-wave collisions

For indistinguishable fermions, the p-wave $\ell = 1$ contribution dominates at low energy

$$\sigma(k) = 2\pi(6|f_1|)^2 \int_0^{\pi/2} \cos^2\theta \sin\theta d\theta = 24\pi|f_1|^2.$$

The p-wave phase shift can be approximately be given by an expansion to the second order

$$k^3 \cot\eta_1 \approx -1/\mathcal{V} + k^2/\mathcal{R}_1,$$

where $\mathcal{V}$ is an interaction effective volume and $\mathcal{R}_1$ an interaction effective range [106]. The p-wave scattering length is given by $\mathcal{V} = a_1^3$, since by definition $\lim_{k\to 0} k^{2\ell+1} \cot\eta_\ell = -1/a_\ell^{2\ell+1}$.

By doing $x = p^2/2\mu k_B T = k^2\lambda^2$, with $\lambda = \hbar/\sqrt{mk_B T}$ (for the equal-mass problem), in eq. 6.2.2 one gets

$$\sigma(T) = \int_0^\infty \sigma(k = \sqrt{x/\lambda^2}) x e^{-x} dx.$$

Plugging in the low-energy expansion for p-wave one obtains

$$\frac{\sigma(T)}{4\pi a_0^2} = 6\int_0^\infty \frac{x e^{-x}}{x/\tilde{\lambda}^2 + (-\tilde{\lambda}^2/x\tilde{\mathcal{V}} + 1/\tilde{\mathcal{R}}_1)^2} dx,$$

where a_0 is the Bohr radius and the tilded variables are now adimensional (e.g. $\tilde{\mathcal{R}}_1 = \mathcal{R}_1/a_0$). In particular, by taking the low and high temperature limits, one gets the following scalings:

$$\frac{\sigma(T)}{4\pi a_0^2} \overset{\tilde{\lambda}\gg 1}{=} 36\tilde{\mathcal{V}}^2/\tilde{\lambda}^4 \propto T^2 \quad \frac{\sigma(T)}{4\pi a_0^2} \overset{\tilde{\lambda}\ll 1}{=} 6\tilde{\lambda}^2 \propto 1/T.$$

Fitting this result to the scattering cross-section data set kindly provided to us by John Bohn for ^{40}K in the stretched state[6], one gets

$$\mathcal{V} \approx (111 a_0)^3 \quad \mathcal{R} \approx 280 a_0.$$

[6] John Bohn computed the scattering cross-section by doing a full coupled scattering calculation. The results were subsequently adjusted to fit the data of the Boulder experiments (see details in ref. 41). Here the raw data is used, without adjusted parameters.

The results are presented in fig. 6.2.2 and they show that this approach is good for $T < 600\mu K$. For higher temperatures, a higher order term is needed to the p-wave phase shift expansion

$$k^3 \cot \eta_1 \approx -1/\mathcal{V} + k^2/\mathcal{R}_1 + k^4\mathcal{R}_2$$

and in that case the fitting parameters are

$$\mathcal{V} \approx (111a_0)^3 \quad \mathcal{R}_1 \approx 390a_0 \quad \mathcal{R}_2 \approx 15a_0.$$

The fit to the data is quite good, validating the model for p-wave collisions. In fig. 6.2.2 we observe the expected $\sim T^2$ behavior of the scattering cross-section at low temperature, which peaks around $T_\mathrm{p} \approx 200\mu$K. This peak value for the p-wave scattering is consistent with the estimation $k_\mathrm{B}T_\mathrm{p} = \hbar^2/mr_e^2 \approx k_\mathrm{B} \times 0.4$mK, where r_e is the effective range of the van der Waals potential [100]. Comparing with the s-wave scattering cross-section, we observe that p-wave scattering dominates for $T > 100\mu$K. Moreover, we also conclude that the scattering cross-section depends on the temperature. The scattering cross-section for a ^{40}K gas was experimentally measured and reported in ref. 41 and matches well the results of this section. In section 6.4 we will study the influence on evaporation dynamics of a non-constant scattering cross-

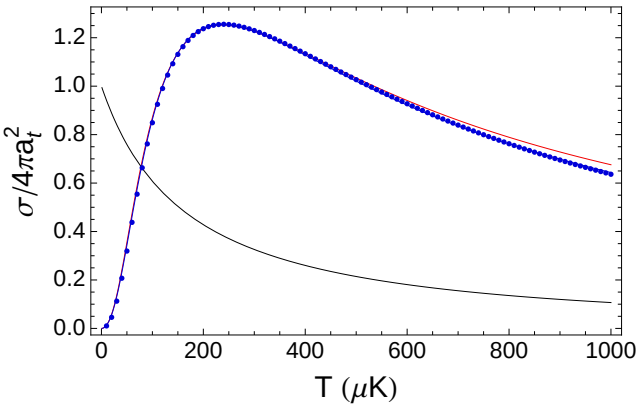


Figure 6.2.2: p-wave contribution $\sigma(T)/4\pi a_t^2$ for ^{40}K as a function of temperature, with $a_t = 170a_0$. Red curve is the fit with two parameters model and the blue with three. Data was kindly provided by John Bohm. Black curve is the s-wave case for comparison.

section in the s-wave and p-wave channels.

6.3 Loss mechanisms

The efficiency of evaporative cooling depends directly on the ratio between elastic collisions and inelastic losses $r = \Gamma_{\text{inel}}/\Gamma_{\text{coll}}$. In order to optimize the performance of the evaporation one must minimize this ratio r. The collision rate Γ_{coll} depends on the elastic scattering cross-section studied in the previous section and on the experimental parameters (density and temperature). This section is devoted to the study of two different loss mechanisms that contribute to Γ_{inel} and hinder cooling: Majorana flips and spin-exchange collisions. In addition, a trapped cold atomic gas also collides with the residual background gas. The total rate of inelastic losses Γ_{inel} will be the sum of all the mentioned contributions.

6.3.1 Majorana losses

The loss process resulting from a Majorana spin flip can occur in a magnetically trapped atomic cloud. As seen in section 5.1, the simplest way of creating a magnetic trap is to have a pair of coils with currents flowing in opposite directions. This configuration has the inconvenient of having a trap center where the magnetic field is null and, as a consequence, the direction of the magnetic field changes abruptly in its vicinity. If an atom crosses this region in a time much smaller than the inverse Larmor frequency $\omega_{\text{L}} = \mu_{\text{B}} B/\hbar$, its magnetic moment can not adiabatically follow the local direction of the magnetic field. As a consequence, in the frame of the local magnetic field, the atom can flip its spin from a low-field seeker into a high-field seeker and be expelled from the trap. It is difficult to do a full analytical/quantitive account of this process, but from the previous considerations one can estimate that the Majorana atom loss rate should scale as

$$\Gamma_{\text{m}} = C\frac{\hbar}{m\lambda^2} \quad \lambda = \frac{k_{\text{B}}T}{\mu_{\text{B}}b},$$

where b is the magnetic gradient of the axial/strong direction, λ is the typical cloud size and C is a geometrical adimensional constant [156]. There are different published

values for this constant C, differing up to a factor of 10, making the precise quantification of Majorana losses difficult [115, 156]. Recently, two other groups argued that since Majorana flips also induce a temperature increase, the decay rate of the number of atoms Γ_m observed in experiments is actually not constant in time, because it is a function of temperature. By describing Majorana losses with a simple system of coupled equations

$$\frac{\dot{N}}{N} = -\Gamma_m \quad \frac{\dot{T}}{T} = \frac{4}{9}\Gamma_m$$

they propose to measure the Majorana heating rate instead of the atom losses, since it is exactly solvable

$$T(t) = T_0\sqrt{1 + t/\tau} \quad \frac{1}{\tau} = \frac{8}{9}\Gamma_m(T_0). \tag{6.3.1}$$

With this improved model, the constant C seems not to depend strongly on the choice of the atom, since the ^{87}Rb and the ^{23}Na values are found to be similar $C = 0.040$ [51, 84].

Majorana losses make the task of evaporative cooling to very low temperatures in a linear magnetic trap impossible: not only there is atom loss, but also heating, being both increasingly dramatic for lower temperatures $\Gamma_m \propto 1/T^2$. There are essentially two classes of strategies to avoid this problem. The first one is to construct a magnetic trap with a non-zero field minimum, such as the top trap [156] or the Ioffe-Pritchard trap [161]. The second is to use an optical force. This last class has two different approaches: the use of a repulsive potential in the trap center (optical plug) that decreases the atomic density [39] or the use of an attractive potential close to the trap center (hybrid trap) to protect the coldest atoms from Majorana flips [115]. In our experiment we use a combination of these two and we observe suppression of the Majorana losses (see section 6.5.4).

6.3.2 Spin-exchange collision rate

When two atoms collide they can exchange angular momenta. In the presence of a magnetic field, changing m_F states can result in a net energy gain due to the Zeeman shift, which can be turned into kinetic energy during a spin-changing collision. Spin-

exchange collisions in a magnetic trap have as consequences the depolarization of the atomic cloud, heating and atom loss.

For ^{40}K atoms in the $F = 9/2$ manifold it was found that spin-mixtures are quite stable [44]. On one hand, there are no hyperfine spin-exchange collisions due to the inverted hyperfine structure. In consequence, the mixture of $|F = 9/2, m_F = 9/2\rangle$ and $|9/2, 7/2\rangle$ is stable. On the other hand, it was experimentally observed that the Zeeman state-exchange collisions have a very low rate. For example, DeMarco [44] determined $K_2 = 1.0 \times 10^{-14}\text{cm}^3/\text{s}$ as an upper bound for the rate of the reaction $|9/2, 7/2\rangle + |9/2, 5/2\rangle \rightarrow |9/2, 9/2\rangle + |9/2, 3/2\rangle$. In the same reference it is reported that a theoretical multi-channel calculation performed by John Bohn is consistent with the experimental measurement.

6.4 Evaporation dynamics

In the previous sections we studied the elastic and the inelastic collision processes at finite temperature. We concluded that inelastic losses can be neglected if the Majorana flips are inhibited. Moreover, we observed that there are two channels that contribute to the elastic collisions at finite temperature: s-wave and p-wave. The purpose of this section is to study and quantify the cooling effect of these elastic collisions when the trap depth is decreased.

The basic principle of evaporative cooling was already explained in the introduction of this chapter. By decreasing the trap depth of a conservative trap, energetic atoms resulting from elastic collisions can leave the trap. This results in a net kinetic energy loss for the remaining atoms or, in other words, in a temperature decrease. In consequence, evaporative cooling depends crucially on the elastic collisions. To study the dynamics of evaporation one usually takes the scattering cross section σ as being constant [33, 99]. In the case of ^{40}K, we concluded at the end of section 6.2 that this is hardly a good approximation (see fig. 6.2.2). The scattering cross-section is only constant for distinguishable spins at very low temperatures. For increasing temperature, the s-wave cross-section decreases and the p-wave cross-section increases, peaking around $T_p \approx 200\mu$K. For $T > 100\mu$K we observed that the p-wave scattering cross-section dominates over the s-wave counterpart. In order to get some insight on the corrections induced by a momentum dependent scattering cross section on the

evaporation dynamics, we will extend the calculations done in ref. 33. At the end of the section, we will compare the obtained results with the experiments.

6.4.1 Evaporation rate

Let us start by considering a thermal gas ($n_0\Lambda^3 \ll 1$) with temperature T trapped in a potential $U(r)$ with depth ϵ_c. In this situation a particle with energy $\epsilon > \epsilon_c$ will escape the trapping potential and be lost. One assumes that particles explore all the phase space and that the evaporation dynamics is slow enough such that at all times the particle energy distribution can be given by a *truncated* Boltzmann distribution $f(\epsilon) = n_0\Lambda^3 e^{-\epsilon/k_BT}\theta(\epsilon_c - \epsilon)$, where $\Lambda^2 = 2\pi\hbar^2/mk_BT$. Notice that n_0 and T refer to the non-truncated distribution: in the cut distribution $f(\epsilon)$, n_0 is no longer the central density and T is not a temperature in the thermodynamical sense. Indeed, the central density is given by $n(0) = n_0 P(3/2, \eta)$,[7] where $\eta = \epsilon_c/k_BT$. For a magnetic quadrupole trap $U(\mathbf{r}) = \mu_B b\sqrt{\rho^2/4 + z^2}$ one has $n_0 = N/32\pi\lambda^3$ with $\lambda = k_BT/\mu b$.

Let us consider two particles with energies (momenta) ϵ_1 ($\mathbf{p}_1$) and ϵ_2 ($\mathbf{p}_2$) that scatter with cross-section $\sigma(\mathbf{q})$ and then depart with energies (momenta) ϵ_3 ($\mathbf{p}_3$) and ϵ_4 ($\mathbf{p}_4$). The total momentum is $\mathbf{P} = \mathbf{p}_1 + \mathbf{p}_2 = \mathbf{p}_3 + \mathbf{p}_4$ and the exchanged momentum $\mathbf{q} = (\mathbf{p}_2 - \mathbf{p}_1)/2$ and $\mathbf{q}' = (\mathbf{p}_4 - \mathbf{p}_3)/2$ (with $q = |\mathbf{q}| = |\mathbf{q}'|$). In order to determine the rate at which particles evaporate $\dot{N}_{\text{evap}}$ one has to calculate the scattering events such that the final energies are $\epsilon_3 < \epsilon_c$ and $\epsilon_4 > \epsilon_c$ (without loss of generality)

$$\begin{aligned}\dot{N}_{\text{evap}} &= -\int_{\epsilon_c}^{\infty} \rho(\epsilon_4)\dot{f}(\epsilon_4)d\epsilon_4 \qquad (6.4.1)\\ &= -\frac{1}{h^6 2m}\int d\epsilon_1 d\epsilon_2 d\epsilon_3 d\epsilon_4 \left(f(\epsilon_1)f(\epsilon_2) - f(\epsilon_3)f(\epsilon_4)\right) d^3\mathbf{r}d^3\mathbf{P}dqq^3dudu'\sigma(q,u')\\ &\quad \prod_{i=i}^{4}\delta(p_i^2/2m + U(\mathbf{r}) - \epsilon_i).\end{aligned}$$

Here the Boltzmann equation and the ergodicity hypothesis were used [33, 121]. In the second line $\sigma(q,u')$ is the *differential* scattering cross-section and u (u') is the cosine

[7] Here $P(n,\eta) = \int_0^\eta u^{n-1}e^{-u}du / \int_0^\infty u^{n-1}e^{-u}du$ is the normalized incomplete Gamma function and it will be properly introduced in section 6.5.2.

of the angle between **P** and **q** (**q**′).

This calculation was performed for both the s-wave and the p-wave cases and we refer the reader to appendix 6.A for details. The result for the evaporation rate is

$$\Gamma_{\text{evap}} \equiv -\frac{\dot{N}_{\text{evap}}}{N} = \Gamma_{\text{coll}} e^{-\eta} \frac{V_{\text{evap}}}{V_e} = \Gamma_{\text{coll}} e^{-\eta} \mathcal{I}_0(\eta) f_N \equiv \Gamma^0_{\text{evap}} f_N.$$

Here $V_e = \int d\mathbf{r} \exp\{-U(\mathbf{r})/k_B T\}$ is the reference volume and $\Gamma_{\text{coll}} = n_0 \sigma_0 \bar{v}$ (this quantity should not be confused with the *collision rate* already shown in eq. 6.2.3) with $n_0 = N/V$ and $\bar{v} = \sqrt{8 k_B T/\pi m}$. $\Gamma^0_{\text{evap}} = \Gamma_{\text{coll}} e^{-\eta} \mathcal{I}_0(\eta)$ is the standard result for the evaporation rate with constant scattering cross section $\sigma_0 = 4\pi a^2$ with

$$\mathcal{I}_0(\eta) = \eta - 11/2 \; P\left(11/2, \eta\right) / P\left(9/2, \eta\right)$$

for a quadrupole potential [33]. The corrections due to the momentum-dependent cross section are included in the corrective term f_N, which can be numerically calculated and is plotted in fig. 6.4.1. It shows that the assumption of a constant s-wave scattering cross section largely overestimates the evaporation rate. It also shows that the p-wave contribution is non-negligible down to $T \sim 50\mu$K.

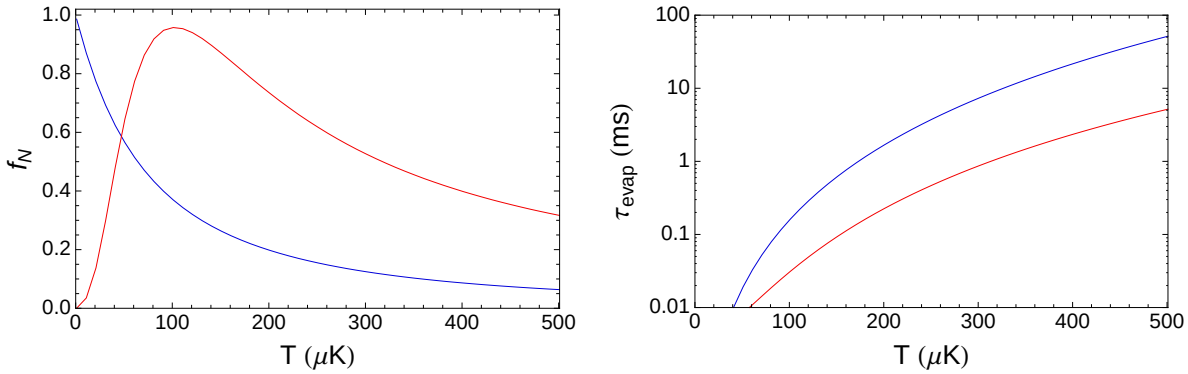


Figure 6.4.1: (Left) Corrective factor f_N of the evaporation rate induced by a momentum-dependent scattering cross section for $\eta = 8$. Blue curve is the s-wave case and the red curve is the p-wave case. The two curves have the same normalization: $f_N = 1$ refers to the situation of a constant s-wave scattering cross section. (Right) Evaporation time $\tau_{\text{evap}} = 1/\Gamma_{\text{evap}}$ for 10^9 Potassium atoms for $\eta = 8$ and $b = 2.5$T/m.

6.4.2 Evaporation dynamics

In the previous section the evaporation rate $\Gamma_{\text{evap}} = -\dot{N}_{\text{evap}}/N$ was calculated. Now it will be interesting to investigate how the number of trapped atoms and the temperature evolve as a function of time in a trap with constant η, taking into account the corrections calculated in the previous section. This will be done by extending the theory laid out in ref. 33. Imposing the conservation of energy and total number of particles, one obtains a set of rate equations for energy E, number of trapped particles N and temperature T:

$$\begin{aligned}
\frac{\dot{E}}{E} &= \frac{\dot{N}}{N} + \frac{\dot{T}}{T} \\
\frac{\dot{N}}{N} &= -\Gamma^0_{\text{evap}} f_N - \Gamma_{\text{inel}} + \tilde{\xi}\frac{\dot{T}}{T} \\
\frac{\dot{E}}{E} &= -\frac{\eta + \tilde{\kappa}}{\tilde{c}}\Gamma^0_{\text{evap}} f_E - \Gamma_{\text{inel}} + \tilde{\xi}\frac{\dot{T}}{T}\frac{\eta}{\tilde{c}}.
\end{aligned}$$

The first equation comes from the relation $E = \tilde{c} N k_B T$ and the two other ones from the sum of the contributions of evaporation, inelastic processes and spilling[8] to the balance of particles and energy. In these equations the tilde quantities are functions of η alone and are defined in ref 33. The $f_E(\eta)$ function is the analog of the f_N correction for the momentum-dependent scattering cross section correction of the energy lost due to evaporation

$$\begin{aligned}
\mathcal{I}^E(\eta) &= \frac{1}{P(9/2,\eta)}\frac{1}{2\sqrt{2\pi}}\int_0^{\eta} d\eta_3 \int_{\eta_3}^{\eta} d\eta_2 e^{-\eta_2} \int_{\eta_3-\eta_2}^{0} d\eta_1 e^{-\eta_1}(\eta_1+\eta_2-\eta_3) \\
&\qquad \int_0^{\eta_3} d\eta_x \int d\eta_q \tilde{\sigma}_s(\eta_q) \frac{\eta_x^2}{\sqrt{\eta_1+\eta_2+\eta-\eta_q-2\eta_x}} \\
f_E(\eta) &= \mathcal{I}^E(\eta)/\mathcal{I}^E_0(\eta).
\end{aligned}$$

[8] In order to maintain $\eta = \epsilon_c/k_B T$ constant during evaporation, ϵ_c must decrease at the same pace as temperature. As a consequence, some atoms (and energy) are lost due to the decrease of the trap depth. These so-called *spilling* losses are detrimental to evaporation, since there is no cooling of the remaining atoms in the trap, in contrast to evaporation.

The previous results can be used to write a differential equation for a quantity denoted as x proportional to the collision rate

$$\dot{x} = (A - B)x^2 - rx. \tag{6.4.2}$$

Here $r = \Gamma_{\text{inel}}/\Gamma_{\text{coll}}$ and A and B are functions of η and the corrective factors for momentum-dependent scattering f_E and f_N

$$A = \frac{\delta\tilde{\alpha} - 1}{1 - \tilde{\alpha}\tilde{\xi}} e^{-\eta}\mathcal{I}_0(\eta) f_N \quad B = A\frac{\tilde{\alpha}/2}{\delta\tilde{\alpha} - 1} \quad \tilde{\alpha} = \frac{(\eta + \tilde{k})f_E/f_N - \tilde{c}}{\tilde{c} + ((\eta + \tilde{k})f_E/f_N - \eta)\tilde{\xi}}.$$

Notice that f_N and f_E are functions of temperature and thus depend on x in a non-trivial manner. In order to proceed the investigation one has to rely on the numerical solving of the differential equation 6.4.2. For simplicity, we make $f_N(T) \sim f_N(T_0)$ and $f_E(T) \sim f_E(T_0)$ to have an upper bound of the sought result. In this case the differential equation has analytical solution

$$x = \frac{e^{-rt}}{1 - (1 - e^{-rt})\frac{A-B}{r}}, \tag{6.4.3}$$

which has the same form as the simple case of constant scattering cross section [33]. This result shows that there is a certain characteristic time for which the denominator

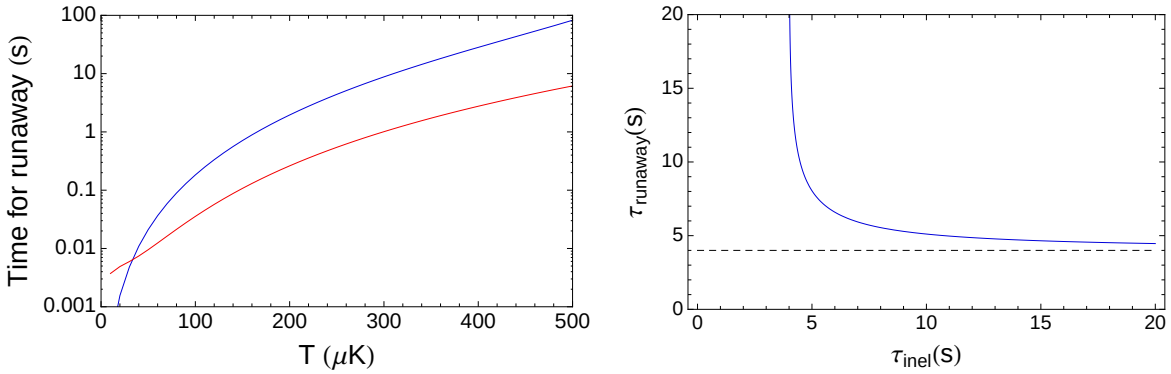


Figure 6.4.2: Runaway time for an evaporation with 10^9 Potassium atoms for $\eta = 8$ and $b = 2.5\text{T/m}$. (Left) Blue curve is the s-wave case two distinguishable spins and the red curve is the p-wave case of indistinguishable fermions. (Right) Runaway time as a function of the inelastic collision time for $\Gamma_{\text{coll}} = 100\,\text{s}^{-1}$.

is zero and the collision rate diverges. This value is the runaway time:

$$\tau = -\frac{1}{r\Gamma_{\text{coll}}} \ln\left(1 - \frac{r}{A-B}\right),$$

which becomes simply $\tau = 1/\Gamma_{\text{coll}}(A-B)$ for $r = \Gamma_{\text{inel}}/\Gamma_{\text{coll}} \ll 1$. The runaway time is plotted in fig. 6.4.2 and it shows the calculation for the s-wave and the p-wave cases. In the experiments reported in section 6.6 we measure $\tau \sim 9$s, for an evaporation with $\eta \approx 8$ starting at $T \approx 350\mu$K with $N = 1.5 \times 10^9$ atoms. We would expect the runaway time to be smaller by roughly one order of magnitude due to the dominant contribution of the p-wave collisions, but this is not observed in our experiments. One possible explanation is an hypothetical inaccuracy of the theoretical data used to model the p-wave scattering cross-section for $T \sim 300\mu$K, as there are no experimental measurements to verify it [41]. Nevertheless, we experimentally observe efficient evaporative cooling in the plugged magnetic quadrupole trap.

It is important to discuss the validity of the approximation $r \ll 1$. To be more precise, r must be compared to $A - B$, which is a function of η. For the case $\eta = 8$, then $A_0 - B_0 \sim 400$ and as a consequence $r < 400$ in order to have runaway evaporation. For $\Gamma_{\text{coll}} \sim 100\,\text{s}^{-1}$ one must have $\tau_{\text{inel}} > 4$s, which is largely the case for the experiments reported in this thesis.

In this section we did a theoretical study of the evaporation dynamics considering the case of s-wave and p-wave momentum-dependent collisions. We evaluated their respective corrective factors to the evaporation rate and we calculated the runaway time for fast evaporative cooling of ^{40}K. This concludes the theoretical analysis of the evaporative cooling. In the following section we shall present the techniques and the experimental results.

6.5 Experimental techniques

In the experiments reported in this chapter, the atoms are confined in a quadrupole magnetic trap. The principles of magnetic trapping and the properties of this trap were already discussed in chapter 5. By exciting magnetically trapped atoms using hyperfine transitions into states which are expelled from the trap (high-field seekers), one can remove atoms from the trap. Due to the linear Zeeman shift induced by the

magnetic trap, the resonance frequency of the atom-removal transitions depends on the position of the atoms in the trap. Using this fact, one can use hyperfine transitions to extract atoms with a chosen energy. This technique allows to tune the trap depth of a magnetic trap simply by manipulating the frequency of the exciting electromagnetic wave. The used hyperfine transitions are in the microwave (MW) range for ^{40}K and in the radio-frequency (RF) range for ^{6}Li and will be object of study in the first part of this section.

In the second part of this text, the optical plug will be described. As mentioned before, the purpose of the optical plug is to inhibit the inelastic losses caused by Majorana flips. We will measure the Majorana heating rate and show that it is highly suppressed in the presence of the plug. These two "experimental techniques" will be essential for performing evaporative cooling, which will be described in the following section 6.6.

6.5.1 Radio-frequency and micro-wave sources

In order to address magnetically trapped ^{40}K and ^{6}Li atoms independently one must use the individual hyperfine transitions, instead of the "usual" Zeeman transitions. These transitions excite trapped low-field seekers into repelled high-field seekers. In the case of ^{40}K the $|9/2,9/2\rangle \rightarrow |7/2,7/2\rangle$, the $|9/2,7/2\rangle \rightarrow |7/2,7/2\rangle$ and the $|9/2,5/2\rangle \rightarrow |7/2,7/2\rangle$ transitions are used, while for ^{6}Li only $|3/2,3/2\rangle \rightarrow |1/2,1/2\rangle$ is relevant since in a magnetic trap there is only one stable and trappable state. The frequency of those transitions as a function of energy can be calculated using the Breit-Rabi formula and are plotted in fig. 6.5.1. The addressing of these transitions depends on the polarization of the incident electromagnetic radiation, respective to the local direction of the magnetic field. In the quadrupole trap the field direction varies over space and the surfaces with constant energy have an ellipsoidal shape. In consequence, coupling will occur in two pole-like regions.

The RF/MW signals for evaporation are produced by two independent Agilent synthesizers which can be programmed via LAN by the control computer. They are

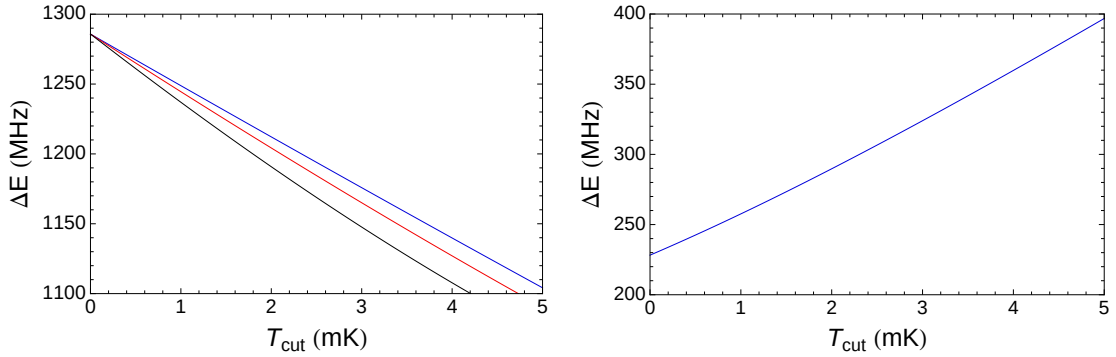


Figure 6.5.1: Transition frequencies as a function of energy cut $\epsilon_{\text{cut}} = k_B T_{\text{cut}}$. ^{40}K in the left (MW transitions to the $|7/2, 7/2\rangle$ state from $|9/2, 9/2\rangle$ (blue), $|9/2, 7/2\rangle$ (red) and $|9/2, 5/2\rangle$ (black)) and ^{6}Li in the right.

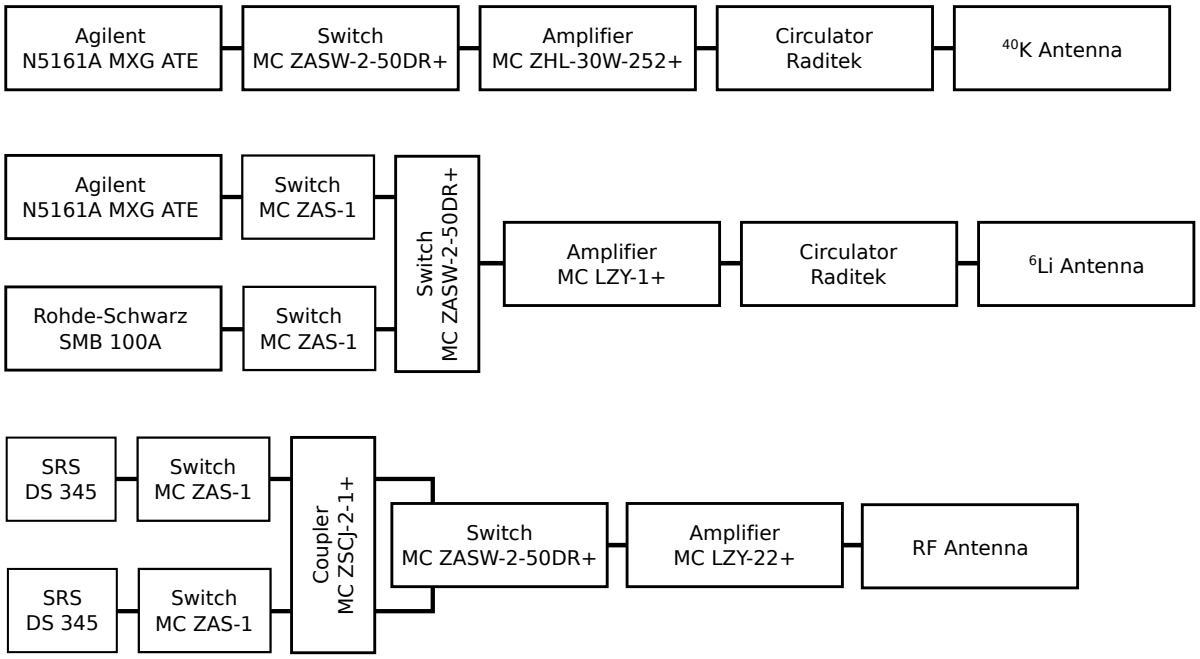


Figure 6.5.2: Scheme of the RF/MW electronics for evaporation in the magnetic trap and spin manipulation. MC stands for Mini Circuits. The antennae are described in appendix 6.B.

both connected to fast switches and amplified. On the output there is a circulator[9], whose transmission port is connected to the antennae (placed close to the science cell with the axis perpendicular to the z direction) and whose reflection port is connected to a high power -40dB attenuator and a 50Ω termination[10]. These circuits are schematized in fig. 6.5.2 and include electronics used for other manipulations of the atomic states (such as the adiabatic passage described in section 7.5.3). Details concerning the construction of the antennae can be found in appendix 6.B.

6.5.2 Probing density and energy distributions in a magnetic trap

A useful and precise way of "tomographically" probe the atom cloud in a magnetic trap is to use RF/MW radiation, as the hyperfine transitions are narrow compared to the optical ones. An experiment that we performed was to eliminate from the trap all atoms with energy superior than $\epsilon_{\text{cut}} = k_B T_{\text{cut}}$ and to measure the number of remaining atoms. This quantity can easily be calculated knowing that the density of states is given by a law of the type $\rho(\epsilon) \propto \epsilon^{1/2+\delta}$ for a power law trap $V(r) \sim r^{3/\delta}$. The number of atoms remaining in the trap after a cut to energy ϵ_{cut} is

$$\frac{N(\epsilon_{\text{cut}})}{N_0} = \frac{\int_0^{\epsilon_{\text{cut}}} \epsilon^{1/2+\delta} e^{-\epsilon/k_B T}}{\int_0^{\infty} \epsilon^{1/2+\delta} e^{-\epsilon/k_B T}} \tag{6.5.1}$$

Introducing the incomplete gamma function $\Gamma(n,\eta) \equiv \int_0^{\eta} x^{n-1} e^{-x} dx$ and defining $\eta_{\text{cut}} = \epsilon_{\text{cut}}/k_B T = T_{\text{cut}}/T$ one gets $N(\eta_{\text{cut}})/N_0 = \Gamma(3/2+\delta, \eta_{\text{cut}})/\Gamma(3/2+\delta, \infty) \equiv P(3/2+\delta, \eta_{\text{cut}})$. For a linear trap we have $\delta = 3$ and thus $N_{\text{cut}} = N_0 P(9/2, \eta_{\text{cut}})$.

An example of such measurement can be found in fig. 6.5.3. The cloud temperature can be determined with this technique and in contrast with the TOF technique it does not depend on the magnification of an optical system (see section 2.3.1). At low temperature $T \approx 100\mu$K we see that both methods agree very well. At higher temperature it is difficult to measure the temperature by TOF.[11]

[9] The circulator for MW is RADC-800-2000M-S23-10/100WR Fwd-b and for RF is Raditek RADC-225-400MHN23-150WR-f4.

[10] Mini Circuits BW-40N100W+ and Minicircuits KARN-50+

[11] The small size of the science cell requires using small values of time-of-flight for a hotter cloud. We

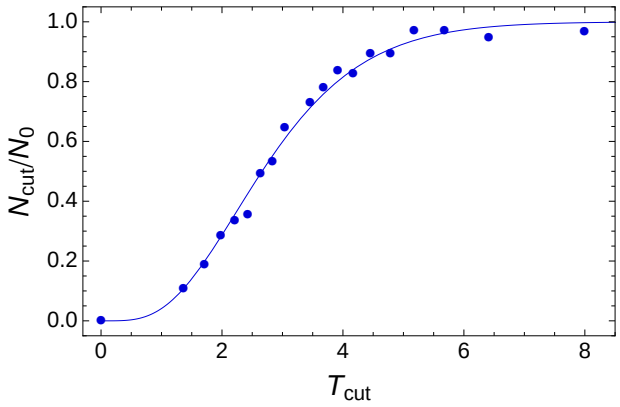


Figure 6.5.3: Using MW to eliminate K atoms from a linear magnetic trap to a certain energy $k_B T_{\text{cut}}$. The dots are data from single experiments and the curve is a fit of equation 6.5.1. The temperature obtained from the fit is $T = 640\mu$K for a trap gradient of $b = 2.2$T/m in the science cell.

Another useful experiment is to probe the flux of atoms through a RF/MW shell of a certain energy ϵ_{cut}. This can be done experimentally by switching on the RF/MW knife at a fixed frequency for a time interval short enough so that the energy distribution is not perturbed significantly (but still long enough compared to the oscillation time of the atoms in the trap). The cut knife defines a surface $\mathcal{S}$ in such a way that $U(\mathbf{r}) = \epsilon_{\text{cut}}$ with $\mathbf{r} \in \mathcal{S}$. Let us calculate the loss of atoms due to spin flips in this surface $\mathcal{S}$ during a short time. This quantity is proportional to the atomic flux through the surface $\phi = S \int f(\mathbf{r},\mathbf{p})|v_\perp| d^3\mathbf{p}$ with $\mathbf{r} \in \mathcal{S}$, where S is the area of $\mathcal{S}$, $v_\perp$ is the component of the atomic speed normal to the surface and $f(\mathbf{r},\mathbf{p})$ is the atomic distribution function in the surface. This function is simply the Maxwell-Boltzmann distribution $f(\mathbf{r},\mathbf{p}) = \mathcal{N}\exp[-H(\mathbf{r},\mathbf{p})/k_B T]$, where $H(\mathbf{r},\mathbf{p}) = p^2/2m + V(\mathbf{r})$ is the Hamiltonian of the system and $z = n(0)\Lambda^3$. Let us start by calculating the flux integral

$$\begin{aligned}\int f(\mathbf{r},\mathbf{p})|v_\perp| d^3\mathbf{p} &= 2\pi \int d\cos\theta \int p^2 dp \left(\frac{p}{m}|\cos\theta|\right) \mathcal{N}\exp[-H(\mathbf{r},\mathbf{p})/k_B T] \\ &= \frac{2\pi}{m}\mathcal{N}\int p^3 e^{-(p^2/2m+\epsilon_{\text{cut}})/k_B T} dp = \pi m \mathcal{N}(2k_B T)^2 e^{-\eta_{\text{cut}}}.\end{aligned}$$

observe that the eddy currents resulting from switching of the magnetic trap significantly perturb the absorption imaging measurements.

Here $\eta_{\text{cut}} = \epsilon_{\text{cut}}/k_B T$. Concerning the surface area S, one can easily calculate it using the formula for the surface of an ellipsoid. It gives $S = 2\pi 5.52 \ell_{\text{cut}}^2$ with $\ell_{\text{cut}} = \epsilon_{\text{cut}}/\mu_B b = \eta_{\text{cut}}\lambda$, where b is the strong axis magnetic gradient and $\lambda = k_B T/\mu b$ is the size of the cloud along that axis.

This result can be used to calculate the atom loss due to the knife cut. The atom loss is $\Delta N = \mathcal{P}\phi\delta t$, where δt is the duration of the RF/MW pulse and $\mathcal{P}$ the probability of a spin-flip when an atom crosses $\mathcal{S}$ (it is supposed constant[12]). Finally one obtains

$$\Delta N \;=\; \mathcal{P}\delta t 2\pi 5.52 \eta_{\text{cut}}^2 \lambda^2 \pi m \mathcal{N} \left(2k_B T\right)^2 e^{-\eta_{\text{cut}}}$$

and using $\mathcal{N} = N\Lambda^3/V_e h^3$ one gets the desired result

$$\frac{\Delta N}{N} = \alpha \mathcal{P} \frac{\sqrt{k_B T/m}}{\lambda/\delta t} \eta_{\text{cut}}^2 e^{-\eta_{\text{cut}}}, \quad \alpha = \frac{5.52}{8\sqrt{2\pi}} \approx 0.275.$$

This expression fits very well with the experimental results (see fig. 6.5.4).

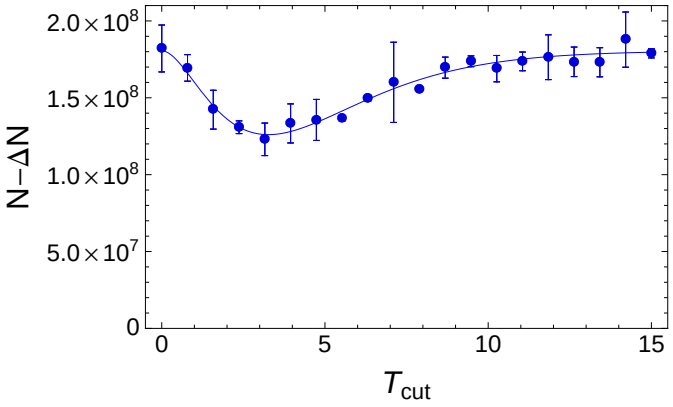


Figure 6.5.4: Atom flux experiment for a ^{40}K cloud in the compressed trap $b = 5.25\text{T/m}$. The fit gives $T = 1.64\text{mK}$ and $\alpha\mathcal{P}\frac{\sqrt{k_B T/m}}{\lambda/\delta t} = 0.556$, hence $\mathcal{P} = 15.1\%$.

6.5.3 Optical plug

In order to efficiently perform evaporative cooling in a quadrupole trap, Majorana losses must be suppressed. Indeed, it was already shown in section 6.3.1 that the exis-

[12] $\mathcal{P}$ is actually an averaged probability, since there are only flips in the poles of the surface $\mathcal{S}$

tence of a magnetic field zero induces inelastic losses and heating of the cloud, which are aggravated with the decrease of temperature due to the consequent increase of density. To inhibit this effect, a laser beam with a repulsive force was focused into the magnetic field zero. In the region close to the new bottom of the trap the confinement is harmonic.

A Verdi[13] single mode laser is used for this purpose, since its wavelength $\lambda = 532$nm is blue detuned respective to the strong D transitions of both ^{6}Li and ^{40}K. The laser beam passes through an AOM[14] and 7W of power are focused into a waist of $\approx 20\mu$m into the atomic cloud along y-axis (see figure in section 2.2.3 for a full scheme). The optical components such as lenses and mirrors are made of fused silica in order to prevent thermal lensing due to high power. By aligning the laser beam in the center of a quadrupole magnetic trap, the potential at the center will be shifted by U_0 and the trap bottom will be harmonic. The calculated parameters are indicated in table 6.5.1. For details concerning the optically plugged magnetic trap see ref. 51.

	^{6}Li	^{40}K
U_0 (mK)	0.78	0.80
$\omega_b/2\pi$ (kHz)	4.1	1.6
$\omega_{b/2}/2\pi$ (kHz)	3.0	1.2

Table 6.5.1: Parameters for the plugged trap: the maximum light shift (U_0) and the trapping frequencies for the strong and weak direction of the quadrupole trap.

For diagnostic purposes a leak from a dichroic mirror of the plug beam was aligned into a 4-quadrant photodiode[15]. By imaging the focus of the plug into the 4-quad PD, one can follow the slow drift of the beam. These drifts can be corrected by acting on piezo-actuators mounted on a mirror close to the science cell[16]. A LabView routine was implemented in order to place the plug beam in a certain reference position (measured by the 4-quad PD), by actuating on the piezo-actuators, when prompted. The "fast" pointing noise was studied by measuring the position of the plug in the 4-quad PD for $\sim$ 3min with different sampling intervals. The root mean squared av-

[13] Coherent Verdi V10 (10W)
[14] AA Opto-electronic MCQ110-A2-VIS
[15] Newport Model 2901
[16] Newport AG-M100N

erage displacement is of $\sim 1\mu$m (much smaller than the waist) and when measuring the noise spectrum we did not observe resonant behavior.

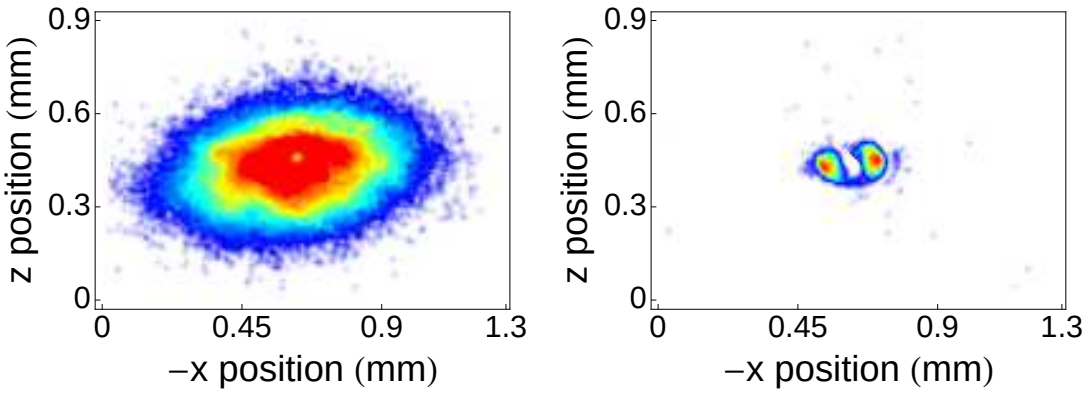


Figure 6.5.5: Absorption imaging along the axis of the plug of a ^{40}K atomic cloud in the magnetic quadrupole. On the left side a cloud with $T = 95\mu$K was released from the magnetic trap for 2ms in the presence of the plug. On the right side is an image *in situ* of a cloud resulting from a MW cut down to $T_{\text{cut}} = 100\mu$K. This last picture is used to position the plug in the center of the trap.

6.5.4 Study of the plugged magnetic quadrupole trap

To determine the importance of losses during evaporation, a study was performed by holding the cloud in the quadrupole trap with gradient $b = 2.5\text{T/m}$. In a first series of measurements, the optical plug was absent in order to quantify the importance of the Majorana losses. For the atomic cloud arriving at the science cell ($T = 325\mu$K) the lifetime was determined from a exponential fit to be ≈ 70s. By performing evaporative cooling down to $T \approx 75\mu$K, the lifetime decreased to (5.2 ± 0.3)s in the absence of the plug, as expected. A systematic study of the Majorana heating was performed by determining the temperature by free expansion after a variable hold time (blue circles in fig. 6.5.6). The Majorana heating is given by eq. 6.3.1, which we reproduce here

$$T(t) = T_0\sqrt{1 + t/\tau} \quad \frac{1}{\tau} = C\frac{8}{9}\frac{\hbar}{m\lambda_0^2} \quad \lambda_0 = \frac{k_B T_0}{\mu_B b}.$$

This expression is plotted for $T = 75\mu$K as a blue dashed line in fig. 6.5.6. One can see that the observed heating (blue circles) is more severe than predicted. By

fitting the experimental data with eq. 6.3.1 one gets $C = 0.16 \pm 0.02$, about 4 times larger than reported for ^{87}Rb by Dubessy et al. [51]. This increased heating could be due to nature of ^{40}K (e.g. the atomic ground-state structure $F = 9/2$). In the presence of the plug we observe a strong suppression of the Majorana heating (red circles in fig. 6.5.6). By fitting the previous equation to the experimental data we obtain $C = 0.02 \pm 0.02$ (red curve)[17]. In these experiments the initial central density in the trap was of $n_0 = 6 \times 10^{12}\text{cm}^{-3}$.

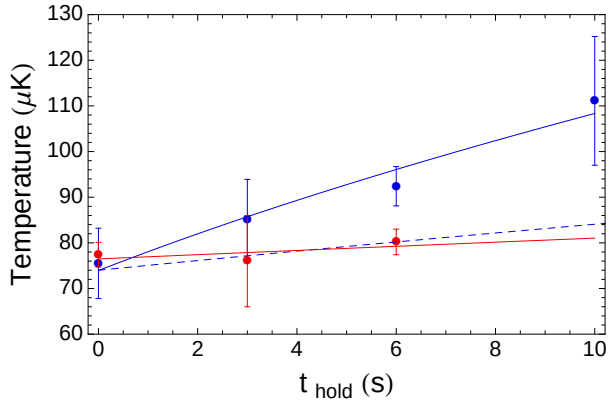


Figure 6.5.6: Cloud temperature as a function of hold time in the unplugged (blue dots) and plugged (red dots) magnetic quadrupole trap. The dashed blue line is the expected heating using the result of ref. 51, the blue (red) line is the fit to the experimental data for the unplugged (plugged) trap.

6.6 Evaporation in the plugged trap

After the atomic cloud being magnetically transported to the science cell, we perform evaporative cooling in order to achieve quantum degeneracy. This happens in two stages: first we perform cooling in the plugged magnetic quadrupole trap and second in an optical dipole trap. In this section we report the first cooling stage, which is optimized in order to maximize the initial collision rate in the optical dipole trap, so that the subsequent step is efficient. Evaporative cooling of ^{40}K in a quadrupole trap is realized by doing a microwave (MW) frequency ramp in the presence of the optical

[17] We have chosen to suppress one experimental data point $T = (93 \pm 15)\mu$K at $t_{\text{hold}} = 10$s from the plot, due to its high experimental uncertainty.

plug, as described in the previous section 6.5. The transfer and evaporation in the optical dipole trap will be the subject of chapter 7.

In this experiment, a linear ramp of microwave from $T_{\mathrm{cut}} = 3.7\mathrm{mK}$ to $T_{\mathrm{cut}} = 0.70\mathrm{mK}$ is done in 5s, cooling a cloud of 1.5×10^9 atoms at $320\mu\mathrm{K}$ into a cloud of 1.5×10^8 atoms at $95\mu\mathrm{K}$, in a quadrupole trap with a gradient of $b = 2.5\mathrm{T/m}$ in the strong direction. After an adiabatic opening of the magnetic trap 2.8×10^7 atoms were detected in the optical dipole trap at $45\mu\mathrm{K}$. The temperature measurements of the cloud in the quadrupole trap were performed by using the MW cut technique introduced in section 6.5.2. The MW ramp for the temperature measurement was performed in 350ms, then the magnetic trap was ramped down to 10% of its initial value, it was switched off and the remaining number of atoms determined by absorption imaging. The ramping down of the field was performed in order to decrease the effect of eddy currents, which perturb the atom counting. This strategy was validated at low temperature $\sim 100\mu\mathrm{K}$ by comparing it with the standard measurement of the cloud expansion speed, performed at long time-of-flight values ($t \geq 5\mathrm{ms}$), a regime in which there are negligible eddy current effects. The measured atom number and the temperature are plotted as function of the evaporation time in fig. 6.6.1. From the log-log plot of temperature and the atom number one can deduce experimentally the exponent $\alpha = d\ln T/d\ln N \approx 0.55$, meaning that one has to lose ≈ 2 orders of magnitude in atom number to win an order of magnitude in temperature. For the phase space density coefficient $\Gamma = -d\ln \mathrm{PSD}/d\ln N$, one has $\Gamma = 9\alpha/2 - 1 \approx 1.45$, showing that this evaporation is not very efficient (usually $\Gamma \approx 3$ for a ^{87}Rb experiment). We did not observe improvement by increasing the evaporation time. On the other hand, this evaporation sequence is quick and optimizes loading of the optical dipole trap for subsequent cooling.

To estimate the order of magnitude of the collision rate, we take a constant scattering cross-section $\sigma = 4\pi(170a_0)^2$, which is not a bad approximation between $T = 100 - 300\mu\mathrm{K}$ (see fig. 6.2.1). The collision rate in a quadrupole trap is $\gamma_{\mathrm{coll}} = n/8\sqrt{2}\sigma_s\sqrt{8k_{\mathrm{B}}T/\pi m}$, with $n = (N/2)/32\pi\lambda^3$. The evolution of the collision rate during the evaporation is depicted in fig. 6.6.1 and it increases over time, showing that we approach the runaway regime. The data was fitted to the model of eq. 6.4.3 for the lossless case $r \ll 1$, which gives $\gamma_{\mathrm{coll}}(t) = \gamma^0_{\mathrm{coll}}/(1 - t/\tau_{\mathrm{div}})$, where $\gamma^0_{\mathrm{coll}} \approx 37\mathrm{Hz}$

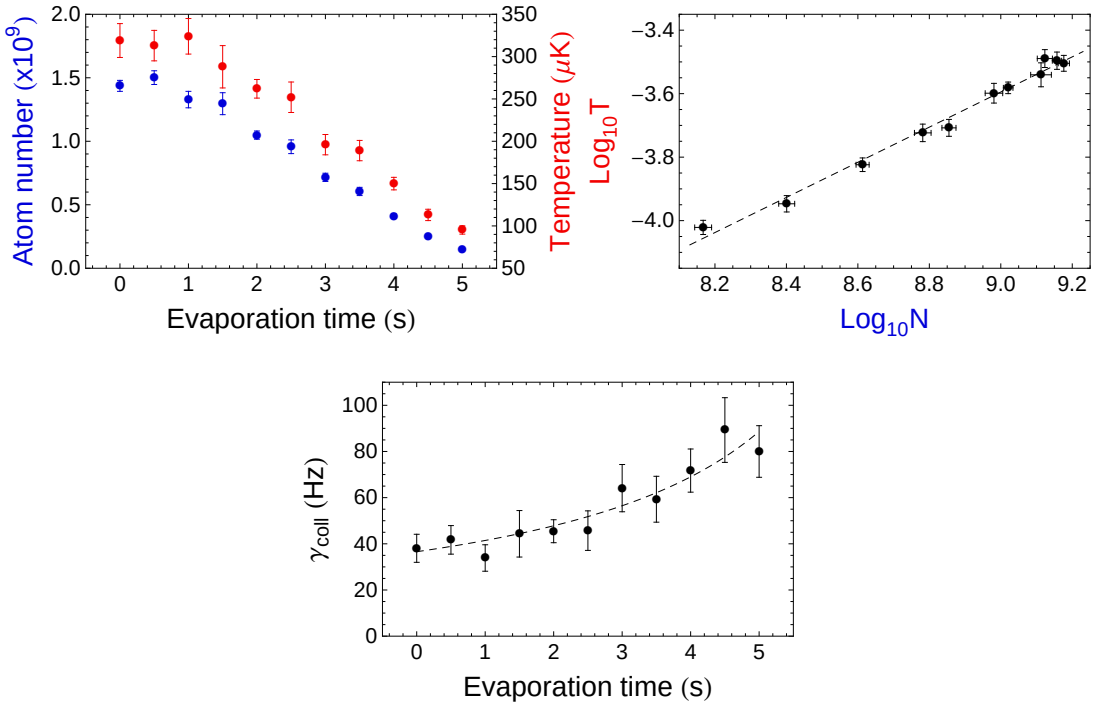


Figure 6.6.1: Atom number and temperature as a function of evaporation time (top left) and log-log plot of temperature as a function of atom number (top right). Collision rate as a function of evaporation time (bottom).

is the initial collision rate and $\tau_{\mathrm{div}} \approx 8.5$s is the runaway time. Since the lifetime in the trap is $\tau_{\mathrm{inel}} \sim 70$s, we can estimate $r = 1/\gamma^0_{\mathrm{coll}}\tau_{\mathrm{inel}} \sim 1/2600$, which is largely sufficient to consider the evaporation lossless.

We have shown in this section that we are able to cool down a gas of ^{40}K and increase its collision rate and phase space density by performing evaporative cooling in an plugged magnetic quadrupole trap. We will show in the following chapter that we can load about $\approx 3 \times 10^7$ atoms into an optical dipole trap with $T \approx 45\mu$K. Subsequent evaporative cooling in this trap will allow us to to observe a quantum degenerate gas.

6.7 Sympathetic cooling of ^{6}Li

^{6}Li only has one state which is simultaneously magnetically trappable and stable against spin-exchange collisions [178], which is the stretched state $|F = 3/2, m_F = 3/2\rangle$. Due to fermionic nature of ^{6}Li and the strong suppression of collisions below $T_p = 6$mK by the $\ell = 1$ (p-wave) rotational barrier [100], it is not possible to cool down this species on its own in a magnetic trap. Instead, we use a sympathetic cooling technique [100, 176]. This strategy consists in cooling another species, in our setup ^{40}K, and let ^{6}Li gradually thermalize with the coolant. The technique crucially relies on interspecies collisions.

In this section we will evaluate the thermalization rate of a trapped gas of ^{6}Li with ^{40}K in the same magnetic quadrupole trap and compare it with experiments realized in the MOT chamber. In a second part we will present preliminary results on the sympathetic cooling of ^{6}Li with ^{40}K. Finally we will discuss inter-species inelastic losses due to spin-exchange collisions.

6.7.1 Thermalization of a gas of ^{6}Li with ^{40}K

The reported triplet scattering length for ^{6}Li-^{40}K collisions is $a_t = 63.5a_0$ [212]. When calculating the thermally-averaged scattered cross-section $\sigma_{LiK}(T)$ (see eq. 6.2.2), we conclude that its dependence with temperature is very weak (see left plot in fig. 6.7.1).

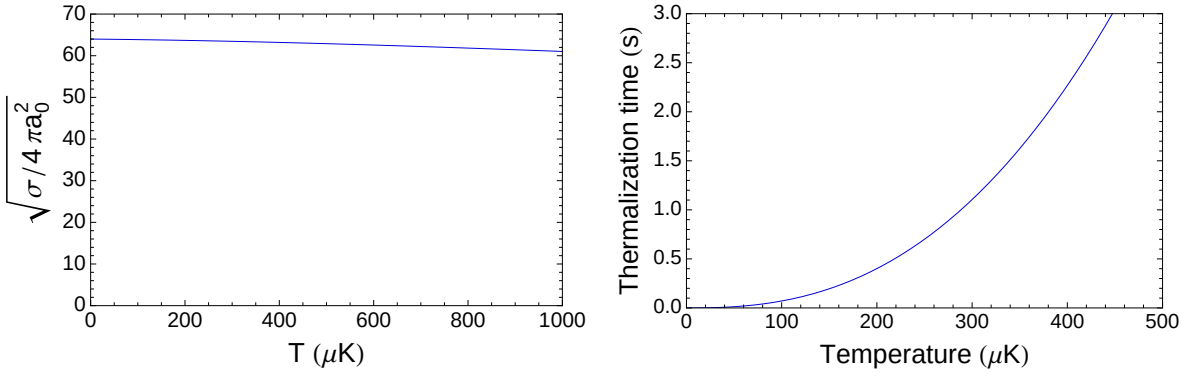


Figure 6.7.1: (Left) Thermally-averaged scattered cross-section for ^{6}Li-^{40}K collisions. (Right) Thermalization time for ^{6}Li in the presence of 3×10^9 Potassium atoms in a quadrupole magnetic trap $b = 1.35$T/m.

The collision rate for inter-species collisions is given by the expression

$$\gamma_{\text{coll}} = \sqrt{2} n \bar{v} \sigma_{\text{LiK}} \frac{V_{2e}}{V_e},$$

where $\bar{v} = \sqrt{4 k_B T / \pi \mu}$ and $V_{2e}/V_e = 1/8$ in a quadrupole trap[18] [206]. Using this result one can calculate the thermalization rate $1/\tau_{\text{th}}$ between the two species. Assuming that one has a majority gas (^{40}K in our case) and a minority gas (^{6}Li), that is $N_{\text{K}} \gg N_{\text{Li}}$, which are at the same temperature T, for a small perturbation in temperature $\delta T/T \ll 1$ the gases will re-thermalize with rate

$$\frac{1}{\tau_{\text{th}}} = \frac{\xi}{2\,(\delta + 3/2)} \gamma_{\text{coll}},$$

with $\xi = 4\mu/M$ being a mass mismatch term and δ the scaling of the power-law trap potential $V(r) \sim r^{3/\delta}$. A point worth stressing is that for a single species in an homogenous trap ($\xi = 1$ and $\gamma = 0$) it takes 3 collisions to thermalize $\tau_{\text{th}} = 3/\gamma_{\text{coll}}$. However for a linear trap it takes 9 collisions for a single species gas ($\xi = 1$ and $\delta = 3$) and ≈ 20 for a heterospecies ^{6}Li-^{40}K gas ($\xi \approx 0.454$ and $\delta = 3$). In the right panel of fig. 6.7.1 we calculate the thermalization rate of ^{6}Li with a gas of 3×10^9 atoms of ^{40}K in a quadrupole magnetic trap of the MOT chamber $b = 1.35\text{T/m}$.

6.7.2 Thermalization experiments in the MOT chamber

When describing the loading of atoms in the magnetic quadrupole trap in the MOT chamber, we observed that the trapped clouds were not in thermal equilibrium (cf. summary in table 5.2.1). Indeed, the measured "temperature" was not isotropic. By measuring the temperature of a magnetically trapped ^{6}Li cloud as a function of hold time (in the absence of ^{40}K), we observed that the temperature anisotropy did not reduce up to $\approx$ 5s of waiting time in the trap (see fig. 6.7.2). Notice that ^{6}Li is polarized in single state (the stretched state) and is collisionless, due to its fermionic character and the p-wave barrier. Nevertheless, we (naïvely) expected that the ensemble of the single atom trajectories would mix together, resulting in an energetically isotropic gas, since in the magnetic quadrupole trap all the trapping directions are coupled

[18] Notice the factor 2 for distinguishable particles.

together[19]. It turns out that this intuition is wrong. By running a simple numerical simulation of the movement of a single particle in the trap it was observed that the temperature anisotropy did not decrease, as we observed in experiments.

In another set of experiments, we trapped ^{6}Li together with ^{40}K and observed the full thermalization of the gases. After a hold time of $\tau \approx 1.5$s in the trap, the temperatures of each gas were isotropic and approximately the same. The reason for this behavior is the possibility of interspecies collisions $\sigma_{^6\mathrm{Li}^{40}\mathrm{K}} \approx 1.4 \times 10^{-12}\mathrm{cm}^2$, which allows energy redistribution. The observed thermalization time-scale is close to the calculation of the preceding section (see fig. 6.7.1).

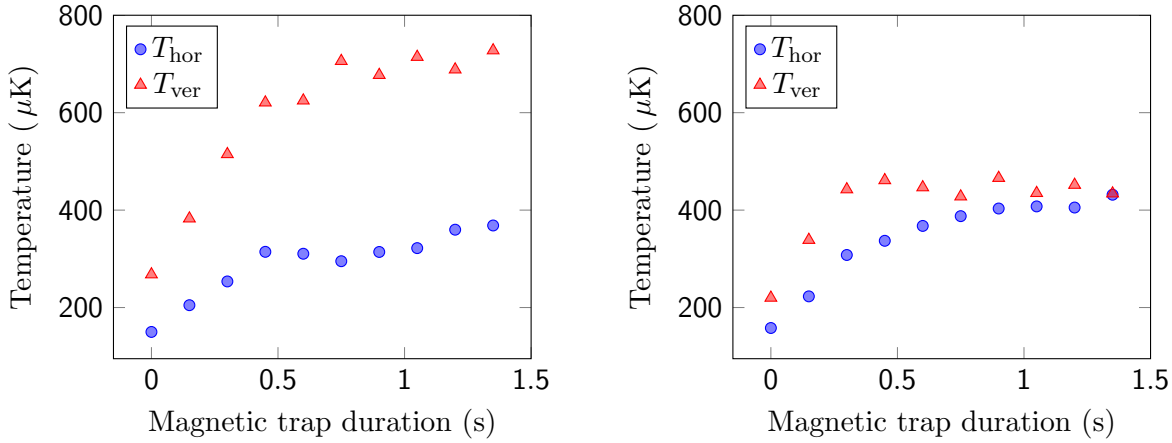


Figure 6.7.2: Study of the thermalization of a ^{6}Li cloud in a magnetic quadrupole trap. The magnetic gradient is ramped to $b = 1.35\mathrm{T/m}$ in 450ms. (Left) Absence of ^{40}K: no thermalization is observed. (Right) Presence of ^{40}K: we observe full thermalization in ≈ 1.5s. (figures from ref. 183).

6.7.3 Sympathetic cooling of ^{6}Li

In the previous paragraphs we evaluated and experimentally demonstrated the thermalization of a gas of ^{6}Li by a reservoir of ^{40}K. This opens the door for sympathetic cooling of ^{6}Li while performing evaporative cooling of ^{40}K.

[19] This contrasts with the case of the harmonic trap: since the trap directions are separable, the motion of a collisionless gas in each direction is independent.

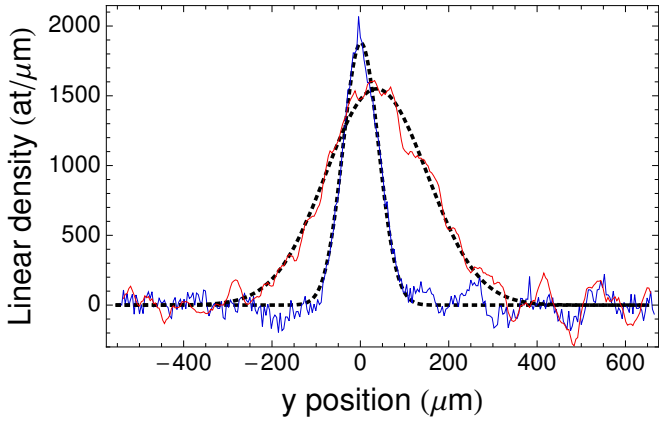


Figure 6.7.3: Integration of a double absorption image of a mixture of ^{6}Li (4.5×10^5 atoms at $T = 38\mu$K in red) and ^{40}K (1.9×10^5 atoms at $T = 31\mu$K in blue) simultaneously loaded in an optical dipole trap after 0.5ms of time-of-flight. Dashed lines are gaussian fits.

Preliminary studies showed that we were able to cool a cloud of $\approx 2 \times 10^6$ atoms ^{6}Li to $T \approx 60\mu$K in the plugged quadrupole trap in the science cell. We observed that the presence of the optical plug was crucial. In its absence, cooling was very inefficient due to the strong Majorana losses. In the presence of the optical plug, the measured lifetime of the ^{6}Li cloud at low temperature was $\approx$ 20s. In order to cool ^{6}Li we observed that it was required to have a small initial sample of $\sim 10^7$ atoms in the science cell. This was achieved by detuning away the ^{6}Li Zeeman slower in order to have a smaller magneto-optical trap (MOT) and consequently less atoms reaching the science cell. For large samples of ^{6}Li, we observed that cooling was inefficient.

By ramping down the magnetic field gradient at the end of the evaporation we were able to load the optical dipole trap (this procedure will be described in detail in section 7.3). We observed the trapping of 4.5×10^5 atoms of ^{6}Li at $T \approx 38\mu$K (PSD$\approx 5 \times 10^{-4}$) and 1.9×10^5 atoms of ^{40}K at $T \approx 31\mu$K (PSD$\approx 7 \times 10^{-5}$) in the optical dipole trap (see fig. 6.7.3). This preliminary result is very promising and leaves room for further optimization.

6.7.4 Spin-exchange interspecies collision rate

When sympathetically cooling ^{6}Li in the presence of ^{40}K, inelastic losses due to spin-exchange collisions can occur and they can be detrimental to the evaporation, as it

was already discussed in section 6.3.2. Collisions between stretched states are immune to this effect, since the angular momentum of these states is maximum. A spin-exchange collision between these states would violate the conservation of angular momentum and so they do not occur. On the other hand, other spin states of ^{40}K may coexist in the trap, such as $|F = 9/2, m_F = 7/2\rangle$ and $|F = 9/2, m_F = 5/2\rangle$. Collisions with atoms of ^{6}Li in the stretched state may exchange the spins. At the present, we did not find a clear sign of spin-exchange reactions between ^{6}Li and ^{40}K in our experimental conditions. However, it is important to estimate its magnitude, since these reactions could be relevant in future experiments.

The rate of the spin-exchange reaction $|i\rangle \rightarrow |f\rangle$ is given by

$$\frac{dn_{\mathrm{Li},i}}{dt} = \frac{dn_{\mathrm{K},i}}{dt} = -\frac{dn_{\mathrm{Li},f}}{dt} = -\frac{dn_{\mathrm{K},f}}{dt} = -K_2 n_{\mathrm{Li},i} n_{\mathrm{K},i},$$

where n is the density of ^{6}Li or ^{40}K atoms in the initial (i) or final (f) state. The two-body scattering rate K_2 for spin exchange is given by:

$$K_2 \;=\; 4\pi(a_s - a_t)^2 v'_{\mathrm{rel}} \left|\langle f \left|\mathbf{s}_{\mathrm{Li}} \cdot \mathbf{s}_{\mathrm{K}}\right| i\rangle\right|^2,$$

where in turn $v'_{\mathrm{rel}} = \sqrt{\frac{2}{\mu}\left(E_{\mathrm{kin}} + \Delta E_{\mathrm{mag}}\right)}$ is the relative speed between the atoms after collision (with $E_{\mathrm{kin}} = 3/2 k_B T$ for a trapped gas and ΔE_{mag} is the variation in magnetic energy due to change in spin) [155]. The scattering lengths for ^{6}Li-^{40}K in the singlet and triplet channel are a_s and a_t, respectively and $\mathbf{s}$ is the electron spin operator. This expression includes only the contribution of the exchange interaction, which should be the dominant one. The dipolar-dipolar interaction is another inelastic mechanism with exchange of spins, but it will not be treated here.

Let us start by considering the reaction $|i\rangle = |\mathrm{K}, 9/2, 7/2\rangle + |\mathrm{Li}, 3/2, 3/2\rangle \rightarrow |f\rangle = |\mathrm{K}, 9/2, 9/2\rangle + |\mathrm{Li}, 1/2, 1/2\rangle$. The spin-exchange matrix element can be calculated and is $\langle f \left|\mathbf{s}_{\mathrm{Li}} \cdot \mathbf{s}_{\mathrm{K}}\right| i\rangle = \sqrt{2/3}/12$. Since the final state of ^{6}Li is not trapable, we will observe a decay of the total atom number of ^{6}Li

$$\frac{dN_{\mathrm{Li}}}{dt} = -\langle K_2 n_{\mathrm{Li}} n_{\mathrm{K}}\rangle = -\int d^3\mathbf{r}\, K_2 n_{\mathrm{Li}} n_{\mathrm{K}}.$$

Taking the known dependence of the atomic density in a quadrupole trap (eq. 5.1.5),

we can obtain an expression for the decay time τ of the ^{6}Li sample

$$\frac{1}{\tau} = \frac{\pi}{4}(a_s - a_t)^2 \sqrt{\frac{3k_BT}{\mu}} n_{K,0} \left|\langle f \left|\mathbf{s}_{\mathrm{Li}} \cdot \mathbf{s}_{\mathrm{K}}\right| i\rangle\right|^2 \int u^2 du \sqrt{1 + 2u_{\mathrm{hf}}/3 + \alpha u/3} e^{-u},$$

where the replacement $u = 2r'/\lambda$, with $\mathbf{r}' = (x/2, y/2, z)$ and $\lambda = k_BT/\mu_b b$ was made for the calculation. The volume of the trap is $V_0 = \int d^3\mathbf{r} e^{-U/k_BT} = 32\pi\lambda^3$. Also the assumption was made that the Zeeman shift of all the states is linear $\Delta E_{mag} = E_{\mathrm{hf}} + \alpha\mu_{\mathrm{B}} b r'$, with $\alpha = 7/9 + 4/3 = 10/9$ and $u_{\mathrm{hf}} = E_{\mathrm{hf}}/k_BT$. The result is plotted as a function of temperature in red in fig. 6.7.4. Neglecting the kinetic energy and the Zeeman shift one obtains $1/\tau n_{K,0} \approx 1.7 \times 10^{-14}\,\mathrm{cm}^{-3}\mathrm{s}^{-1}$.

Another possible spin-exchange reaction is $|i\rangle = |\mathrm{K}, 9/2, 7/2\rangle + |\mathrm{Li}, 3/2, 3/2\rangle \rightarrow |f\rangle = |\mathrm{K}, 9/2, 9/2\rangle + |\mathrm{Li}, 3/2, 1/2\rangle$. In this case ^{6}Li does not change of hyperfine manifold, but only of Zeeman state. The matrix element is $\langle f \left|\mathbf{s}_{\mathrm{Li}} \cdot \mathbf{s}_{\mathrm{K}}\right| i\rangle = \sqrt{3}/18$. The decay rate of ^{6}Li can also be calculated using the same procedure, yielding

$$\frac{1}{\tau} = \frac{\pi}{4}(a_s - a_t)^2 \sqrt{\frac{3k_BT}{\mu}} n_{K,0} \frac{\mathcal{I}}{108}.$$

Here $\mathcal{I} = \int u^2 du \sqrt{1 + \alpha u/3} e^{-u} \approx 2.395$, with $\alpha = 7/9 - 1/3 = 4/9$. The result of this calculation is plotted as a function of temperature in blue in fig. 6.7.4.

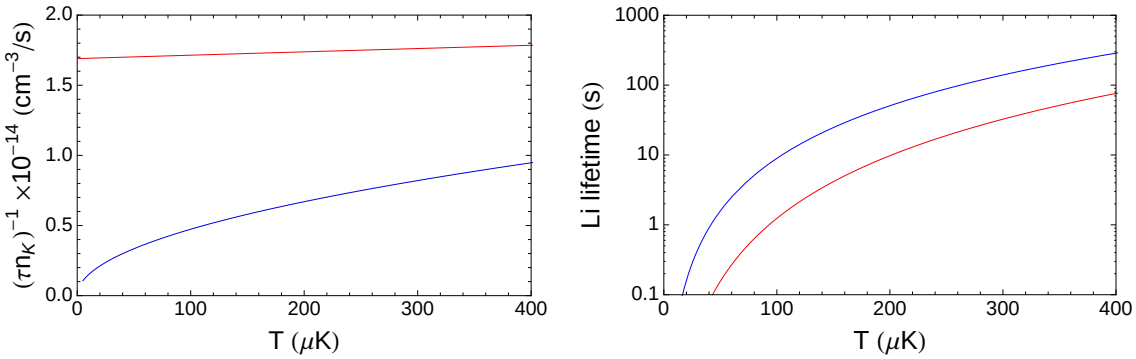


Figure 6.7.4: Spin-exchange losses as a function of temperature for the collisions: $|\mathrm{K}, 9/2, 7/2\rangle\,|\mathrm{Li}, 3/2, 3/2\rangle \rightarrow |\mathrm{K}, 9/2, 9/2\rangle\,|\mathrm{Li}, 3/2, 1/2\rangle$ (blue curve) and $|\mathrm{K}, 9/2, 7/2\rangle\,|\mathrm{Li}, 3/2, 3/2\rangle \rightarrow |\mathrm{K}, 9/2, 9/2\rangle\,|\mathrm{Li}, 1/2, 1/2\rangle$ (red curve). The lifetime of Lithium is plotted for 10^9 Potassium atoms in a magnetic trap with $b = 2.5\mathrm{T/m}$.

The hyperfine-changing spin-exchange collisions are the most likely process that changes the spin of ^{6}Li and induces losses. After a collision there is a gain in kinetic energy of h228.2MHz $\sim$ 11mK and ^{6}Li, being the lighter atom, takes most of this energy and is expelled from the trap. This is the dominant term of the loss rate, but we observe nevertheless a weak dependence on the internal state.

This study shows that spin-exchanging collisions rate can be small compared to the evaporation time-scale, which leaves a window open for sympathetic cooling in the presence of different spin states of ^{40}K. Notice that this study is not exhaustive as it does not comprise the calculation for other trappable spin states of ^{40}K (such as $|F = 9/2, m_F = 5/2\rangle$), nor other inelastic processes that we assumed to be less important. In ref. 200 it was observed that when evaporating a mixture of spins of ^{40}K in the presence of a cloud of ^{6}Li in a plugged magnetic trap, the density of ^{40}K stopped increasing for $n_K \gtrsim 10^{12}\text{cm}^{-3}$, contrasting with the case in which ^{6}Li was absent. In the experiments reported in the previous section 6.7.3, the density of ^{40}K was probably too small to observe any spin-exchange reactions ($n_K \approx 5 \times 10^{11}\text{cm}^{-3}$).

6.8 Summary

In this chapter we studied the evaporative cooling of ^{40}K in a magnetic quadrupole plugged trap. By describing the elastic and inelastic collision channels we were able to estimate the expected evaporation rate and the time for runaway evaporation. Experiments were done in the presence of an optical plug, which was shown to inhibit detrimental Majorana losses. Starting from a gas of ^{40}K with $N = 1.5 \times 10^9$ atoms at 320μK in a trap with gradient $b = 2.5\text{T/m}$, we obtain 1.5×10^8 atoms at 95μK after 5s of evaporation. This yields a gain of factor $\approx 2.4 \times 10^2$ in phase space density. These are good conditions to efficiently load an optical dipole trap, as it will be demonstrated in the following chapter 7. Subsequent evaporative cooling will result in a degenerate quantum gas.

We also discussed the cooling of ^{6}Li in the magnetic plugged trap, which is done by successive thermalization with the ^{40}K cloud in the trap, due to interspecies collisions (sympathetic cooling). At the end of the evaporative cooling sequence we were able to load 4.5×10^5 atoms of ^{6}Li at $T = 38\mu$K in the optical dipole trap.

Appendix 6.A Corrective factor for evaporation rate

In this section we calculate the integral of eq. 6.4.1 from section 6.4.1 for the s-wave and the p-wave cases:

$$\dot{N}_{\text{evap}} = -\frac{1}{h^6 2m}\int d\epsilon_1 d\epsilon_2 d\epsilon_3 d\epsilon_4 \left(f(\epsilon_1)f(\epsilon_2) - f(\epsilon_3)f(\epsilon_4)\right) d^3\mathbf{r} d^3\mathbf{P} dq q^3 du du' \sigma(q,u') \prod_{i=i}^{4} \delta(p_i^2/2m + U(\mathbf{r}) - \epsilon_i).$$

We refer the reader to the mentioned section for details concerning the notation and the context of the calculation.

To simplify the notation one defines an adimensional scattering cross-section $\sigma(q,u') \equiv \sigma_0\tilde{\sigma}(q,u')$ with $\sigma_0 = a_s^2$. In the following on shall analyze two different cases: the s-wave ($\tilde{\sigma}(q,u') = \tilde{\sigma}_s(q)$) and the p-wave ($\tilde{\sigma}(q,u') = \tilde{\sigma}_p(q)u'^2$).

S-wave scattering case

Let us start by integrating the angular variables

$$\int du \delta\left(\frac{p_1^2}{2m} + U(\mathbf{r}) - \epsilon_1\right)\delta\left(\frac{p_2^2}{2m} + U(\mathbf{r}) - \epsilon_2\right) = \frac{2m}{Pq}\delta\left(\epsilon_1 + \epsilon_2 - 2U(\mathbf{r}) - \frac{P^2}{4m} - \frac{q^2}{m}\right),$$

with an analogous result for u'. On the other hand, the integral in $\mathbf{P}$ is given by

$$\int \frac{d^3\mathbf{P}}{P^2}\delta\left(\epsilon_1 + \epsilon_2 - 2U(\mathbf{r}) - \frac{P^2}{4m} - \frac{q^2}{m}\right)\delta\left(\epsilon_3 + \epsilon_4 - 2U(\mathbf{r}) - \frac{P^2}{4m} - \frac{q^2}{m}\right) = \\ = \frac{4\pi\sqrt{m}\delta(\epsilon_1 + \epsilon_2 - \epsilon_3 - \epsilon_4)}{\sqrt{\epsilon_1 + \epsilon_2 - 2U(\mathbf{r}) - q^2/m}}.$$

For the integral in r, let us specialize to the linear trap case. This integral goes from 0 to the maximum position of the particle $\epsilon_3 = \mu b r_{max} = x_{max}$

$$\int d^3\mathbf{r}\frac{1}{\sqrt{\epsilon_1 + \epsilon_2 - q^2/m - 2U(\mathbf{r})}} = \frac{16\pi}{(\mu_B b)^3}\int_0^{x_{\max}} dx \frac{x^2}{\sqrt{\epsilon_1 + \epsilon_2 - q^2/m - 2x}}.$$

For the integral in q, one performs a simple replacement by introducing the exchanged energy $\epsilon_q = q^2/2m$

$$\int dq\tilde{\sigma}_s(q)q = \frac{m}{2}\int d\epsilon_q\tilde{\sigma}_s(q=\sqrt{2m\epsilon_q}).$$

Concerning the limits of the definite integrals, let us recall that the extracted particle has $\epsilon_4 \in [\epsilon_c, \infty[$ and the other particles have energies smaller than ϵ_c. Moreover, ϵ_3 is the smallest energy value $\epsilon_3 \leq \epsilon_i$, as consequence of energy conservation. Finally, fixing ϵ_3 and ϵ_2, one has $\epsilon_1 = \epsilon_4 + \epsilon_3 - \epsilon_2 < \epsilon_c + \epsilon_3 - \epsilon_2 < \epsilon_c$. For the integral in ϵ_q

$$\epsilon_q \lessgtr \frac{(p_3 \pm p_4)^2}{4m} = \frac{\epsilon_3}{2} + \frac{\epsilon_4}{2} - x \pm \sqrt{\epsilon_3 - x}\sqrt{\epsilon_4 - x},$$

where $\mathbf{p}_{3,4} = \mathbf{P}/2 \pm \mathbf{q}$. Using the previous results and integrating in ϵ_4

$$\begin{aligned}\dot{N}_{\text{evap}} &= -\frac{64\pi^2 m^{5/2}\sigma_0}{h^6(\mu_B b)^3}\int_0^{\epsilon_c} d\epsilon_3 \int_{\epsilon_c+\epsilon_3-\epsilon_2}^{\epsilon_c} d\epsilon_1 \int_{\epsilon_3}^{\epsilon_c} d\epsilon_2 f(\epsilon_1)f(\epsilon_2)\int_0^{\epsilon_3} dx \\ &\int d\epsilon_q\tilde{\sigma}_s(q)\frac{x^2}{\sqrt{\epsilon_1+\epsilon_2-q^2/m-2x}},\end{aligned}$$

where the limits for the ϵ_q integral were omitted for simplicity. Notice that for the integration domain of ϵ_4, $f(\epsilon_4) = 0$. Let us now adimensionalize the energy variables $\eta_i = \epsilon_i/k_BT$ and introduce the energy distributions

$$\dot{N}_{\text{evap}} = -\frac{64\pi^2 m^3\sigma_0}{h^6}\lambda^3\left(n_0\Lambda^3\right)^2(k_BT)^3\left(\frac{k_BT}{m}\right)^{1/2}\times\mathcal{F}(\eta_c)$$

where $\mathcal{F}(\eta_c)$ was defined to simplify the notation

$$\mathcal{F}(\eta_c) = \int_0^{\eta_c} d\eta_3\int_{\eta_3}^{\eta c} d\eta_2 e^{-\eta_2}\int_{\eta_c+\eta_3-\eta_2}^{\eta_c} d\eta_1 e^{-\eta_1}\int_0^{\eta_3} d\eta_x\int d\eta_q\tilde{\sigma}_s(\eta_q)\frac{\eta_x^2}{\sqrt{\eta_1+\eta_2-\eta_q-2\eta_x}}.$$

The evaporation volume as defined in ref. 33 is given by

$$V_{\text{evap}} = -\frac{\dot{N}_{\text{evap}}}{n_0^2 4\pi\sigma_0\bar{v}e^{-\eta_c}} = \frac{16\pi m^3}{h^6}\lambda^3\Lambda^6(k_BT)^3\left(\frac{\pi}{8}\right)^{1/2}e^{\eta_c}\times\mathcal{F}(\eta_c)$$

with $\bar{v} = \sqrt{8k_BT/\pi m}$. Using now the fact that $\zeta_\infty(T) = 32\pi\lambda^3/\Lambda^3$ one gets

$$V_{\text{evap}} = \Lambda^3\zeta_\infty(T)\frac{1}{32\pi^2\sqrt{2\pi}}e^{\eta_c} \times \mathcal{F}(\eta_c)$$

To simplify again the notation, let us define $V_{\text{evap}}/V_e = \mathcal{I}(\eta \equiv \eta_c)$, where $V_e = \Lambda^3\zeta_\infty(T)P\left(\frac{3}{2}+\delta,\eta\right) = N/n_0$ is the reference volume. In the case of constant σ, that is of $\tilde{\sigma}_s(q) = 1$, one obtains

$$\mathcal{I}_0(\eta) = \eta - \left(\frac{5}{2}+\delta\right)P\left(\frac{5}{2}+\delta,\eta\right)/P\left(\frac{3}{2}+\delta,\eta\right).$$

Here δ is the trapping potential energy scaling exponent with position $U \sim r^{3/\delta}$ (e.g. $\delta = 3$ for the quadrupole potential). Defining the corrective term as $f_N(\eta) \equiv \mathcal{I}(\eta)/\mathcal{I}_0(\eta)$ one has $V_{\text{evap}}/V_e = \mathcal{I}_0(\eta)f_N(\eta)$. This corrective term f_N is plotted in blue in fig. 6.4.1 for ^{40}K.

P-wave scattering case

In this case the scattering cross-section depends on the out-going angle as $\tilde{\sigma}(q,u') = \tilde{\sigma}_p(q)u'^2$, but the modifications in the previous reasoning are straightforward. In the end it suffices to modify the integrand:

$$\tilde{\sigma}_s(\eta_q)\frac{\eta_x^2}{\sqrt{\eta_1+\eta_2-\eta_q-2\eta_x}} \to \frac{1}{4}\tilde{\sigma}_p(\eta_q)\frac{\eta_x^2}{(\eta_1+\eta_2-\eta_q-2\eta_x)^{3/2}}\frac{(\eta_1+\eta_2-2\eta_3)^2}{\eta_q}.$$

Appendix 6.B Construction of the antennae

In order to manipulate the atomic quantum state it is very useful to have at disposal a radio-frequency/microwave radiation source. For instance, to change the Zeeman state (or spin) of an atom at a certain magnetic field (range of 0-50 MHz) or the hyperfine state ($\sim$ 230MHz for ^{6}Li and $\sim$ 1.3GHz for ^{40}K, etc.). The oscillating electrical signal can be produced by a synthesizer (or a VCO), then amplified and delivered to an antenna, which converts the electric signal into electromagnetic radiation. In general, the response of the antenna depends strongly on the frequency of the signal. This is highly inconvenient for cold atom experiments, since one needs the antenna

to respond in a certain frequency range around the frequency of interest. The antennae are positioned close to the science cell with their axis orthogonal to the vertical z direction[20]. This chapter is devoted to the description of the antennae construction of the LiK experiment.

6.B.1 Potassium-40 hyperfine frequency (MW) antenna

In order to evaporate ^{40}K in a magnetic trap, the needed frequencies are in the range between $\sim$ 1.1GHz ($\sim$ 5mK depth) to 1.285GHz (resonance), in the microwave (MW) band, as showed in fig. 6.5.1. To have a performant antenna, it was decided to use a $\lambda/2$ 1-turn coil (diameter = 11.5 cm). When dealing with MW electrical currents flowing through a conductor one has to have in mind the skin effect. Indeed, in this frequency range $f = \omega/2\pi$ the current is only flowing in a small layer of thickness δ at the surface of the conductor

$$\delta = \sqrt{\frac{2\rho}{\omega\mu}} \approx 2\mu\text{m}.$$

Here ρ is the resistivity of the conductor and μ its magnetic permeability. In order to increase the radiative volume of the antenna we used Litz wire, which is a series of several thin copper wires put in parallel. For the ^{40}K antenna we used a multiplet of 400 wires of diameter 40μm.

In order to characterize the antenna, the $\lambda/2$ wire loop was connected to a bi-direction coupler and the power of the reflection port was measured[21]. By changing the frequency of the input signal it was observed a sharp decrease of the reflection at $\approx$ 1.5GHz, which was interpreted as a transmission resonance of the antenna. The next step was to displace this peak to the frequency region of interest. In a perfect LC circuit the resonance frequency is given by $\omega_0 = 1/\sqrt{LC}$. We thus tried to insert capacitors in parallel to the antenna in order to decrease the resonance frequency, with no success. Inspired by ref. 44 we tried instead to use the stub technique by inserting a T-connector and BNC cable with a loose end. It was indeed observed that the

[20] For atoms in an homogenous magnetic field, an antenna with its axis parallel to that field will excite π transitions only.
[21] Mini Circuits ZABDC20-182H-S+

resonance frequency shifted, whose displacement could be adjusted by changing the length of the loose BNC cable (this was done simply by cutting the cable and checking the position of the resonance).

In the plots below it is depicted the power measured at the reflection port of the coupler (assumed to have a constant response over the interest frequency range) minus the power measured at the input of the coupler. It is assumed that at the maximum value of reflection there is no transmission of power to the antenna, which is the worse case scenario.

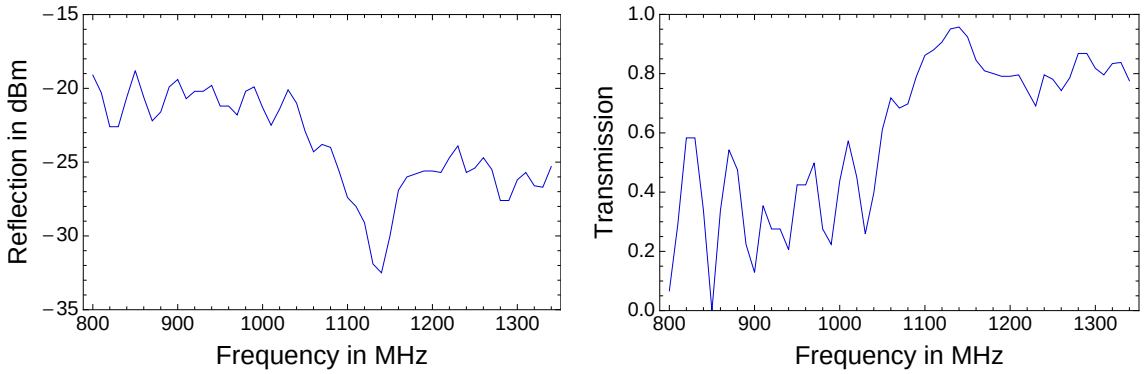


Figure 6.B.1: Characterization of the MW coil. Power reflected from the antenna as a function of the frequency (left) and calculation of the transmission coefficient (right).

6.B.2 Radio-frequency antenna

The RF antenna is typically used to change the spin populations in two different regimes. The first one is the low magnetic field $B \sim 10$G (corresponding to ~ 3MHz for ^{40}K) and the second is at high field $B \sim 200$G, where several interesting ^{40}K Feshbach resonances exist (roughly at 45 MHz).

The coil used for these purposes was done using a $2r = 0.5$mm diameter copper wire wound 10 times around a pen of diameter $2R = 11$mm. The inductance of this coil can be estimated using the formula for a set of coil loops:

$$L = \mu_0 R N^2 (\ln 8R/r - 2) \sim 2.2\mu\text{H}.$$

To directly measure the inductance, one used a directional coupler[22] with a frequency synthesizer as source and the coil as load. A fraction of the reflected wave (~10%) could be measured by using the coupling channel. By comparing the incoming and the reflected wave, the phase difference was measured as a function of the frequency of the synthesizer signal. The results were fitted with the argument of the reflection coefficient Γ

$$\Gamma = \frac{Z_2 - Z_1}{Z_1 + Z_2},$$

where $Z_1 = 50\Omega$ and $Z_2 = i\omega L + R$. The fit gave $L = 3.8\mu\text{H}$ and $R = 35\Omega$.[23]

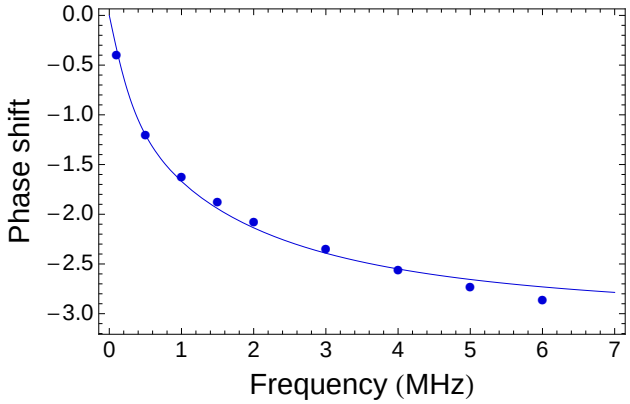


Figure 6.B.2: Measurement of the inductance of the coil. Phase difference between the incoming and the reflected wave in the coil as function of the signal frequency.

In order to have an efficient antenna one must *impedance match* it. This means that one has to change it in such a way that its impedance is 50Ω, as seen by the amplifier/synthesizer If this condition is met then there is no reflection $\Gamma = 0$. In practice things are often difficult: for starters, one can only impedance match for a certain frequency ω_0. The important figure of merit is $|\Gamma|^2$, which is the fraction of reflected power. To impedance match an *unbalanced L half section* filter was built. This is no more than a capacitor of capacitance C put in parallel with the coil and an inductor

[22] Mini Circuits ZDC-10-1+

[23] This resistance actually is a function of the frequency (cf. for DC $R = 0\Omega$), but was taken as constant for this simple fit.

of inductance L_2 in series with them. The impedance of this system is then

$$Z_2 = i\omega L_2 + \frac{1}{i\omega C + \frac{1}{R+i\omega L}}.$$

This function $|\Gamma|$ has a minimum when $\mathrm{Im}(Z_2) = 0$ and its depth and width as a function of the frequency $\omega/2\pi$ depend on the real part (if $R = 50\Omega$ then $|\Gamma|^2 = 0$ but the width of the resonance is small). Using available values for inductors and capacitors in the lab[24] $L_2 = 560$nH and $C = 27$pF were chosen, which give a resonance frequency of $\omega_0/2\pi = 44$MHz. At low frequency there is some transmission since $Z_2 \approx R$.

To measure the reflected power from the circuit the coupler technique was used again. The input and the reflected power were measured using the spectrum analyzer and the transmission power coefficient to the antenna circuit was calculated as $1 - 10^{-\mathrm{IN_{dBm}}+\mathrm{R_{dBm}}}$. There is good agreement between the measurement and the designed behavior.

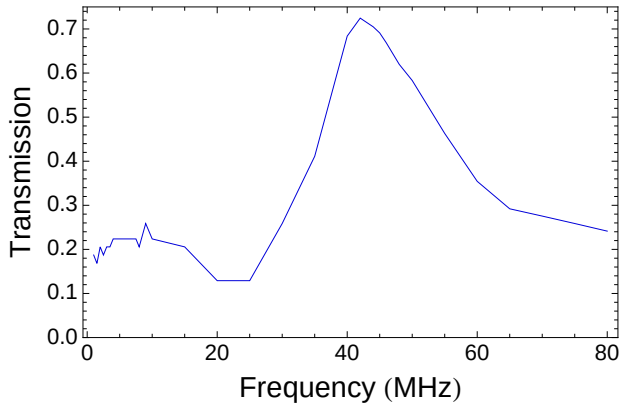


Figure 6.B.3: Power transmitted to the RF coil circuit as a function of frequency of the synthesizer.

[24] Note that most standard electronic components have a radical dependence on frequency. For this application components specified for "RF" were used (SMD mounting).

6.B.3 Lithium-6 hyperfine frequency (RF) antenna

When doing impedance matching, the use of lumped elements sometimes is not possible, e.g. due to power or frequency constraints. In these cases the stub technique is most useful, like it was done for the antenna for ^{40}K in the microwave range. To evaporate (or cut the velocity distribution) of ^{6}Li using hyperfine transitions, one is interested in the range between 228MHz (resonance) up to 400MHz. The transmission coefficient of this antenna was measured using a calibrated network analyzer[25].

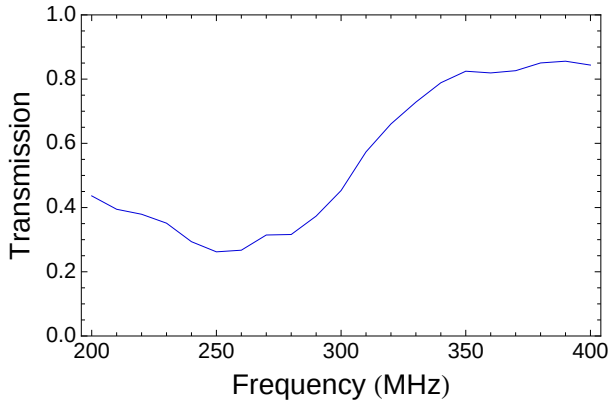


Figure 6.B.4: Power transmitted to the ^{6}Li RF antenna measured with the help of a network analyzer.

6.B.4 Stub technique

The idea of the stub technique is to change the impedance of a circuit by manipulating its geometry. Indeed, since the wavelengths for RF/MW antennae are macroscopic (cm to m) one can change the impedance by imposing conditions to the phase and modify the standing electric wave in the circuit. There are two basic building blocks to create stubs which are quite useful.

The first one is the introduction of a cable of length ℓ by means of a T adapter into the circuit (stub). This is equivalent to put an impedance Z_{stub} at that point of the circuit. This impedance is given by $Z_{\text{SC}} = iZ_0 \tan(\beta\ell)$ or $Z_{\text{OC}} = -iZ_0 \cot(\beta\ell)$, whether that cable is short circuited or open at the end, respectively. Here Z_0 is the

[25] Anritsu 37369C

characteristic impedance, typically 50Ω, and $\beta = \omega/v$ is the phase constant. This means that inserting a stub is equivalent of introducing an inductor or a capacitor in the circuit, depending on the chosen length.

The second one is the introduction of a cable of length ℓ in series with a load (Z_L). The total impedance of the system load+cable is given by

$$Z = Z_0 \frac{Z_L + iZ_0 \tan \beta\ell}{Z_0 + iZ_L \tan \beta\ell},$$

assuming that the impedance of the cable is Z_0.

By attaching a series of stubs and cables to an antenna coil one can "design" the impedance function just by manipulating the lengths of the cables.

7 Evaporative cooling in an optical dipole trap

In this chapter we will describe the loading and the evaporative cooling of a mixture of spins of ^{40}K in an optical dipole trap (ODT). We will start by reviewing the principles of optical trapping (section 7.1) and by presenting the experimental setup (section 7.2). These sections will be followed by a study of the transfer of the atomic cloud from the plugged magnetic quadrupole trap into the ODT (section 7.3). In section 7.4 we will discuss the axial confinement in an ODT. Experimental results of the evaporative cooling to quantum degeneracy will be presented and discussed in section 7.5, which includes a study of the adiabatic transfer of the atoms into the lower Zeeman states (section 7.5.3). In section 7.6 we will discuss the few remaining steps to cool a mixture of ^{6}Li-^{40}K to double quantum degeneracy.

7.1 Trapping in an ODT

An oscillating electromagnetic field can induce a change in the energy of the atomic levels due to its coupling with the atomic electric dipole. One can show that this energy shift is proportional to the light intensity (in the first order approximation). Therefore, by shinning an inhomogeneous laser beam to the atoms $I(\mathbf{r})$ (focusing a beam onto the atoms for example), one can induce a mechanical force $\propto -\boldsymbol{\nabla} I(\mathbf{r})$ to the atoms. This effect is relevant for a large laser detuning in order to have a small scattering rate and negligible heating. In the limit of a laser detuning much larger than the atomic fine structure, the atom can be seen as a simple two-level system. In this case, the light shift of the ground state and the photon scattering rate are [75]

$$U_{\mathrm{dip}}(\mathbf{r}) = -\frac{3\pi c^2}{2\omega_0^3}\left(\frac{\Gamma}{\omega_0-\omega}+\frac{\Gamma}{\omega_0+\omega}\right) I(\mathbf{r}) \tag{7.1.1}$$

$$\Gamma_{\mathrm{sc}}(\mathbf{r}) = \frac{3\pi c^2}{2\hbar\omega_0^3}\left(\frac{\omega}{\omega_0}\right)^3\left(\frac{\Gamma}{\omega_0-\omega}+\frac{\Gamma}{\omega_0+\omega}\right)^2 I(\mathbf{r}). \tag{7.1.2}$$

Here $\omega/2\pi$ is the laser frequency, $\omega_0/2\pi$ is the atomic transition resonance frequency and $\Gamma/2\pi$ its linewidth. An atomic cloud placed in the focus of a gaussian laser beam with power P, waist w (much larger than the cloud size) and negative (red) detuning $\omega - \omega_0 < 0$ will experience an attractive harmonic potential

$$U(\mathbf{r}) = \frac{1}{2}m\omega_{\mathrm{R}}^2\rho^2 + \frac{1}{2}m\omega_{\mathrm{Ax}}^2 x_{\mathrm{Ax}}^2$$

with depth $U_0 = U_{\mathrm{dip}}(0)$ with $I(0) = 2P/\pi w^2$ and

$$\omega_{\mathrm{R}} = \sqrt{\frac{4U_0}{mw^2}} \quad \omega_{\mathrm{Ax}} = \sqrt{\frac{2U_0}{mz_{\mathrm{R}}^2}}, \tag{7.1.3}$$

where $z_R = \pi w^2/\lambda$ is the Rayleigh length. These formulas were used to calculate the parameters of the ODT existing in our apparatus and are shown in table 7.2.1 of the following section.

The density profile of an atomic cloud in an optical dipole trap is given by a gaussian

$$n(\mathbf{r}) = \frac{N}{V_e}e^{-U(\mathbf{r})/k_{\mathrm{B}}T} = \frac{N}{V_e}\exp\left\{-\frac{\rho^2}{2\sigma_{\mathrm{R}}^2} - \frac{x_{\mathrm{Ax}}^2}{2\sigma_{\mathrm{Ax}}^2}\right\}, \tag{7.1.4}$$

with

$$V_e = (2\pi)^{3/2}\sigma_{\mathrm{R}}^2\sigma_{\mathrm{Ax}} \quad \sigma = \sqrt{\frac{k_{\mathrm{B}}T}{m\omega^2}}.$$

This allows to readily calculate other quantities such as the collision rate (see eq. 6.2.3)

$$\gamma_{\mathrm{coll}} = \frac{1}{2}n\sigma\bar{v},$$

with $n = (N/2)/V_e$ (for an equilibrated mixture of two spins), $\sigma = 4\pi a_t^2$ and $\bar{v} = \sqrt{8k_{\mathrm{B}}T/\pi m}$. In fig. 7.1.1 we show an absorption image of an atomic cloud in an ODT after time-of-flight[1], where we can observe the clear difference in the radial and axial confinement. See the corresponding caption for details.

As the trapped atoms are sitting at the maximum of laser intensity, it is important

[1] See section 2.3.1 for details concerning the time-of-flight technique.

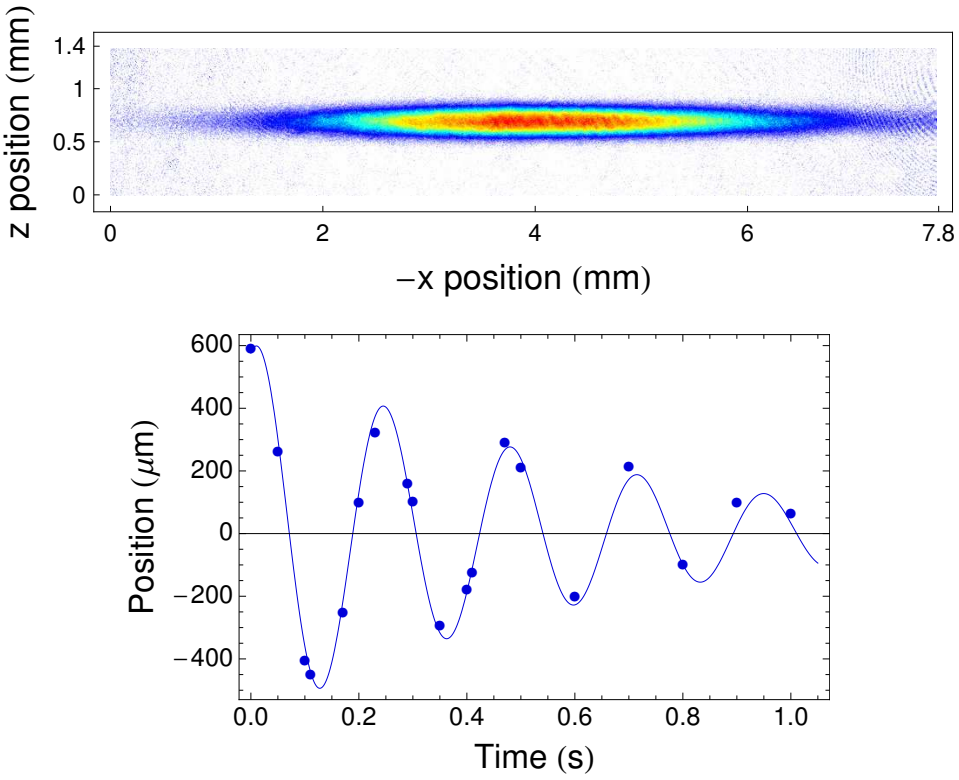


Figure 7.1.1: Characterization of an evaporatively cooled cloud of ^{40}K to $P = 1.1$W. (Top) Absorption image after 2ms of time-of-flight. (Bottom) Oscillations of the center of mass in the axial direction with $\omega_{\mathrm{Ax}}/2\pi = (4.26 \pm 0.03)$Hz (exponential damping with $\tau = (0.61 \pm 0.06)$s). The number of atoms is $N = 1.7 \times 10^7$, the temperature $T = 8.2\mu$K, the radial frequency $\omega_{\mathrm{R}}/2\pi = 880$Hz. This corresponds to a central density of $n = 1.2 \times 10^{13}\mathrm{cm}^{-3}$ and a phase space density of PSD$= 0.011$ (equivalent to $T/T_{\mathrm{F}} \sim 3$, assuming a balanced mixture of spins in the $|F = 9/2, m_{\mathrm{F}} = 7/2\rangle$ and the $|F = 9/2, m_{\mathrm{F}} = 9/2\rangle$ states).

to evaluate the heating caused by the scattering of photons from the trapping laser. Let us consider the case $\Delta = \omega - \omega_0 \ll \omega_0$, in which the so-called rotating wave approximation can be used. Using eqs. 7.1.1 and 7.1.2 we have the simple relation

$$\hbar\Gamma_{\mathrm{sc}} = \frac{\Gamma}{\Delta} U_{\mathrm{dip}}.$$

For a fixed optical potential U_{dip}, the scattering rate can be minimized by having a large detuning Δ. Since $U_{\mathrm{dip}} \propto I/\Delta$, this condition usually requires a large amount of laser power. In our case we use a laser beam with $\lambda = 1064$nm and power 10W

(see table 7.2.1), yielding $\Gamma_{sc,0}/2\pi \approx 0.56$Hz for ^{40}K. To evaluate the energy increase of the trapped atoms due to photon scattering, we follow the argument laid down in ref. 75. This quantity is given by

$$P_{heat} = 2E_{rec}\bar{\Gamma}_{sc},$$

where $E_{rec} = \hbar^2(2\pi/\lambda)^2/2m$ is the recoil energy and $\bar{\Gamma}_{sc}$ is a trap-averaged scattering rate. The heating power takes into account the longitudinal and the transversal contributions (hence the factor 2). Assuming that the atoms are at the bottom of the trap $k_B T \ll |U_0|$, we have $\hbar\bar{\Gamma}_{sc} \approx \Gamma|U_0|/|\Delta|$. On the other hand, since the mean total energy of a trapped atom is $E = 3k_B T$, we equate $P_{heat} = \dot{E}$, giving

$$\dot{T} = \frac{2\Gamma}{3}\frac{E_{rec}}{k_B}\frac{|U_0|}{\hbar|\Delta|}.$$

For the laser beam used in this apparatus, the heating due photon scattering events is $\dot{T} = 0.96\mu$K/s for ^{40}K and $\dot{T} = 2.4\mu$K/s for ^{6}Li (the main difference is due to the recoil energy). Notice that this heating rate was calculated for full power $P = 10$W and that it scales linearly with the laser power $\dot{T} \propto U_0 \propto P$. The degenerate gas is attained for $P \sim 100$mW and the residual heating of ~ 10nK/s is easily compensated by residual evaporation.

7.2 Experimental setup

After having performed evaporative cooling in the plugged quadrupole trap (chapter 6) the atomic cloud is transferred into an ODT for subsequent evaporation. This allows to explore the Physics with atomic interactions mediated by Feshbach resonances, which is difficult to study in magnetic traps since the atoms explore a low and inhomogeneous magnetic field. As discussed in the previous section 7.1, a red-detuned laser beam creates a negative light shift which is proportional to the light intensity. By focusing a red-detuned beam into an atomic cloud, the atoms will be attracted to its focus, which corresponds to the laser intensity maximum and the potential minimum. In this section we will describe the experimental realization of such an optical trap.

7.2.1 Laser setup

The optical dipole trap laser beam is produced by a Mephisto[2] which operates at $\lambda = 1064$nm in single frequency mode and displays very low power noise (cf. data-sheet of the manufacturer). The laser beam passes through an AOM[3] which is used to control the laser power (the zero order is rejected). This AOM is made of a large quartz crystal that allows laser beam diameters of 0.9mm to 2mm (active aperture of 2.5x2.5mm) and optical power densities up to 500 MW/cm^2 (1.4 kW/cm^2 in our setup). The response time is typically 0.2μs, limited by the diameter of the laser beam. The first order of the AOM is injected into a single-mode polarization-maintaining high power fiber, which is designed with a larger core to withstand larger laser power[4]. It was observed that for low power ($\sim$ 500mW) the fiber injection efficiency was of $\sim$ 85%, but for higher power the best achieved output was of 11W with 18W in the input of the fiber. The reason for the degradation of the injection efficiency is yet to be understood, but the fiber output power we reached was found to be sufficient. The input/output collimators were designed to be compatible with the high-power SMA 905 connector[5] and have focal distances of $f = 11$mm and $f = 30$mm, respectively. The output beam has a waist of $\approx$ 2.3mm and after a polarization beam splitter it is focused into the science cell using a $f = 200$mm lens[6]. To avoid eventual problems

	^{6}Li	^{40}K
P (W)	10	
w/z_R (μm/mm)	42/4.3	
U_0 (mK)	0.22	0.48
$\omega_R/2\pi$ (kHz)	4.2	2.4
$\omega_{Ax}/2\pi$ (Hz)	29	17

Table 7.2.1: Parameters for the optical dipole trap: available laser power P, beam waist w, Rayleigh length z_R, maximum light shift U_0 and trapping frequencies.

[2]Coherent Mephisto MOPA 25W
[3]AA Opto-Electronic MCQ80-A2.5-L1064-Z42-C47Bc
[4]NKT Photonics LMA-PM-10 2m length and $(8.6 \pm 0.5)\mu$m mode field diameter @1064nm, with a SMA 905 APC connector at the input (7°) and a SMA 905 PC connector at the output.
[5]Schafter+Kirchoff 60FC-SMA-T-4-A11-03 (input) and 60FC-SMA-0-M30-37 (output)
[6]Melles-Griot BFPL-200-UV

with optical interferences, the incidence of the beam is not normal with the cell wall, but of 10° with the normal (full scheme in section 2.2.3). The optical components such as lenses and mirrors are made of fused silica in order to prevent thermal lensing effects due to high power. The calculated optical dipole trap parameters are shown in table 7.2.1.

7.2.2 Laser power control with a logarithmic amplifier

The control (and stabilization) of the laser power on the atoms is made by measuring the power using a photodiode connected to a log circuit and by acting on the RF power delivered to the AOM. The log circuit[7] produces a voltage that is proportional to the logarithm of the current produced by the photodiode[8] [130, 154, 215], as shown in fig. 7.2.1. This trick allows to readily control the laser power in a range of more than 3 orders of magnitude using a commercial PID controller[9]. The output voltage of this PID acts on a RF power attenuator, which changes the laser power diffracted by the AOM. We will see in section 7.5 that evaporative cooling in the ODT is performed by reducing the laser power. This feedback system allows to readily execute convenient exponential ramps [144] simply by linearly ramping the set point of the PID.

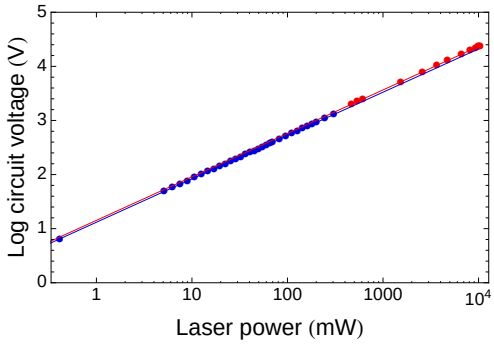


Figure 7.2.1: Voltage output of the log circuit as a function of the laser power measured at the entrance of the science cell. In blue measurement with photodiode (Thorlabs S121C) and in red measurement with bolometer (Thorlabs S350C). Both measurements show a logarithmic dependence $V = 0.804 \log_{10} P/P_0$ with slightly different offsets.

[7] Analog Devices AD8304
[8] Thorlabs SM05PD4A mounted InGaAs-Photodiode (FGA10)
[9] Stanford Research Systems SIM960

7.3 Loading of the ODT

7.3.1 Model

After the atom cloud is cooled in the plugged magnetic trap, as described in section 6.6 of the previous chapter, one can transfer it into the optical dipole trap (ODT). To have an optimized transfer, it is important to understand this process and to estimate at which point the evaporation should be stopped and the transfer be performed. The study of this problem will be the subject of this section.

If one neglects the effect of the optical plug, the potential of the combined quadrupole trap and the optical dipole trap is

$$U(\mathbf{r}) = \mu_B b\sqrt{(x^2+y^2)/4+z^2} - U_0 \exp\left\{-2(x^2+(z-z_0)^2)/w^2\right\} + mgz + E_0. \tag{7.3.1}$$

Here it is considered that the ODT is aligned along the y axis and that the confinement in this direction is predominantly magnetic $2\lambda \gg z_R$, with $\lambda = k_B T/\mu_B b$. The ODT is not aligned with the center of the magnetic field, otherwise Majorana flips would be enhanced, but it is at a distance of z_0 from the magnetic quadrupole center. In the experiments of this thesis $z_0 \approx -100\mu$m. E_0 is calculated such as that at the trap minimum $U(\mathbf{r}_{\min}) = 0$. The study of this potential is done in detail in ref. 115.

One possibility for the transfer is to abruptly switch off the magnetic field confinement and in this case the loading fraction can be estimated in the following way. For high temperature $\lambda \gg w$ one can neglect the spatial dependence of the ODT and the potential is simply given by $U(\mathbf{r}) = k_B T\sqrt{(x^2+y^2)/4+z^2}/\lambda - U_0 + mgz$. Its corresponding volume is

$$V_0 = \int d^3\mathbf{r} \exp\{-U(\mathbf{r})/k_B T\} = 32\pi\tilde{\lambda}^3 e^{-U_0/k_B T}, \tag{7.3.2}$$

where $\tilde{\lambda} = \lambda/(1-(b_g/b)^2)^{2/3}$ with $b_g = mg/\mu_B$ being the effective size of the magnetic trapped cloud in the presence of gravity[10]. If the magnetic trap is suddenly

[10] $b_g \approx 0.070$T/m for ^{40}K and $b_g \approx 0.011$T/m for ^{6}Li.

switched off, the atomic cloud in the ODT region has transversal area $\pi w^2/2$ and axial length $2 \times 2\lambda$ (the radius of the magnetically trapped cloud is 2λ in the y direction). Neglecting the effect of gravity $\tilde{\lambda} \approx \lambda$, an upper bound for the transferred fraction of atoms is

$$\frac{N_{\mathrm{ODT}}}{N} \sim \frac{w^2}{16\lambda^2} e^{U_0/k_{\mathrm{B}}T} e^{-z_0/\lambda},$$

where the term $e^{-z_0/\lambda}$ takes into account the displacement of the ODT relative to the magnetic quadrupole center[11]. According to this result, the transferred fraction is $\sim 0.71\%$ for $T = 325\mu$K (without evaporative cooling) and $\sim 50\%$ for $T = 95\mu$K (after evaporative cooling). This means that evaporative cooling is necessary to achieve a good transfer performance. Experimentally it is observed that the transfer efficiency at low temperature is smaller than the value predicted by this simple model. The main reason is that the high temperature approximation fails since $\lambda \approx 50\mu$m is not much bigger than the waist $w = 42\mu$m, as it is assumed for this model.

Instead of an abrupt switch off of the magnetic field, let us study the adiabatic ramping down of the field. To have a precise prediction let us take into account the full potential given by eq. 7.3.1, as it was done in ref. 115. The volume of the trap V_0 can be calculated by numerically integrating the full potential given by eq. 7.3.1, which is a function of temperature and magnetic field gradient b. By defining the partition function $\zeta = V_0/\Lambda^3$, with $\Lambda^2 = 2\pi\hbar^2/mk_{\mathrm{B}}T$ being the de Broglie wavelength, and calculating the free energy per particle $A = -k_{\mathrm{B}}T \ln \zeta$, one can deduce the entropy per particle $S/N = -\partial A/\partial T$, the phase space density per particle $\mathrm{PSD}/N = 1/\zeta$ and the collision rate

$$\gamma_{\mathrm{coll}}/N = (1/\sqrt{2})\bar{v}\sigma/(V_0 2^{\delta}) \tag{7.3.3}$$

with $\bar{v} = \sqrt{8k_B T/\pi m}$ being the thermal speed[12]. The results of this calculation are plotted in fig. 7.3.1 and the details are described in its caption. In the plot of the trap volume one sees at high temperature the behavior set by eq. 7.3.2 (the trap is essen-

[11] In other words, the atomic density at the position of the ODT is $N/V_0 e^{-z_0/\lambda}$

[12] At high temperature the trap is linear ($\delta = 3$) but at low temperature it is harmonic ($\delta = 3/2$). For the plot of the collision rate it was taken the average of the two cases to simplify $1/2^{\delta} \to 0.24$, that is $\Gamma_{\mathrm{coll}}/N = (0.24/\sqrt{2})\bar{v}\sigma/V_0$. For an exact calculation, the integral $V_{2,0} = \int d^3\mathbf{r} \exp\{-2U(\mathbf{r})/k_{\mathrm{B}}T\}$ has to be evaluated.

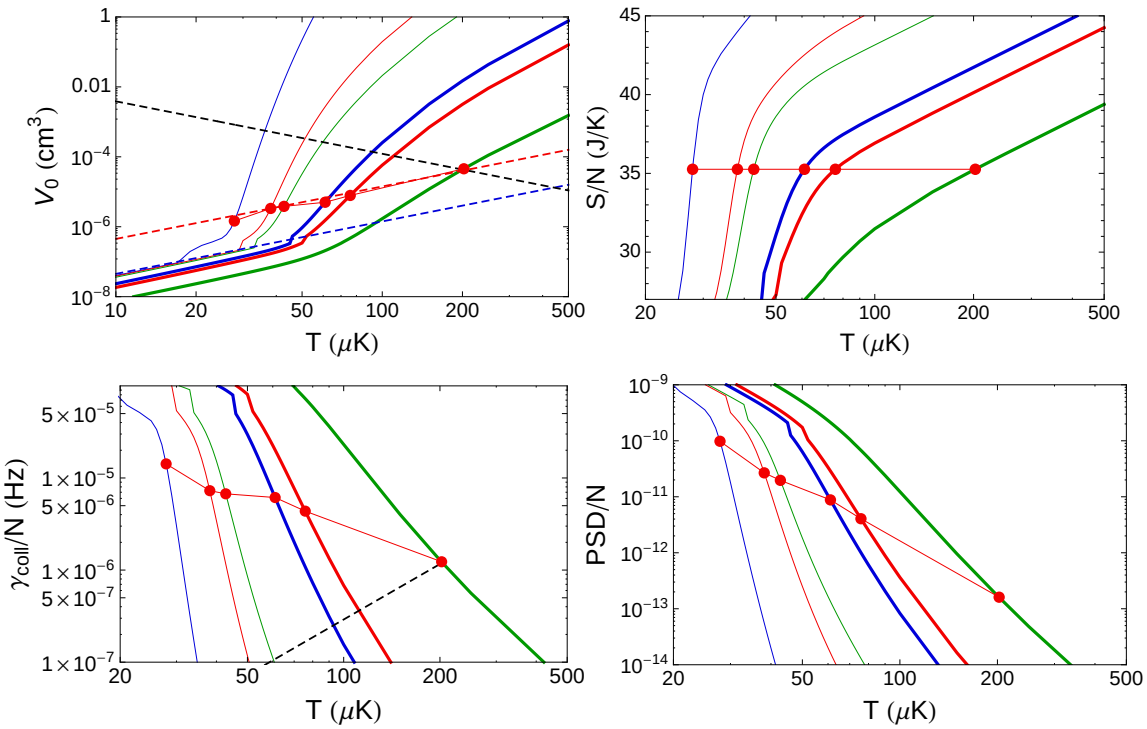


Figure 7.3.1: Solid lines: numerical calculation of the trap volume V_0 (top left), the entropy per particle (top right), the collision rate per particle (bottom left) and the phase space density per particle (bottom right) as a function of temperature. The calculation is performed for different values of the magnetic gradient $b = 2.5\mathrm{T/m}$ (thick green), $b = 0.5\mathrm{T/m}$ (thick red), $b = 0.3\mathrm{T/m}$ (thick blue), $b = 0.1\mathrm{T/m} \approx 1.42 b_g$ (thin green), $b = 0.08\mathrm{T/m} \approx 1.14 b_g$ (thin red), $b = 0.0703\mathrm{T/m} \approx 1.00 b_g$ (thin blue). Red dots: adiabatic evolution of a cloud at $T = 200\mu\mathrm{K}$ in a trap with gradient $b = 2.5\mathrm{T/m}$ ramped to $b \approx b_g$. The dashed lines are explained in the text.

tially magnetic) and at low temperature one sees the power law behavior expected for the quadratic trapping of the ODT ($V_0 \propto T^{3/2}$). Notice that in this limit the trapping is actually *hybrid*: the transversal confinement is optical and the axial is magnetic. The trap volume can be calculated in the low temperature limit and is plotted as a blue dashed line for $b = b_g$, while the red dashed line is $10V_{\mathrm{ODT}}$.

Let us consider the *adiabatic* ramping down of the magnetic field gradient[13] starting from $T = 200\mu$K and $b = 2.5$T/m. For each value of gradient considered in the numerical calculations, the result of the adiabatic opening is represented with a red dot. For instance, one can verify in the plot of entropy that the adiabatic opening does not change the entropy, as expected, but decreases temperature. The trap volume decreases approximately as a power law, opposite to the case of a pure magnetic quadrupole in which the volume increases in an adiabatic opening $V_0 \propto b^{-1}$ (black dotted line in the trap volume plot). One can also see that the trap volume is close to $10V_{\mathrm{ODT}}$ (red dashed line) and so 10% of the total atoms are expected to be loaded in the ODT after the adiabatic opening. Due to the fact that the trap volume decreases during the opening, the collision rate *increases*, as one can see in the corresponding plot (the black dashed line is the purely magnetic case). Finally, the plot of the phase space density (PSD) shows that there is an important increase of this variable. One might expect that the PSD should be constant in a adiabatic process, but this is not the case if the *geometry* of the trap changes [206]. This is sometimes called the dimple effect [208].

7.3.2 Experimental results

At the end of the evaporation in the plugged trap there are about 1.5×10^8 atoms at 95μK for a gradient of 2.5T/m (PSD$= 0.2 \times 10^{-3}$). By ramping down the magnetic gradient to $\lesssim b_g$ in 400ms the number of atoms loaded in the ODT is 2.8×10^7 and their temperature is 45μK (PSD$= 5 \times 10^{-3}$). The measured averaged shot-to-shot atom number fluctuations are $\approx 3\%$ at this point. Although the captured fraction is 1/5, the PSD increased by a factor of 25 due to the dimple effect. The density in the optical dipole trap is of $n_{\mathrm{ODT}} = N_{\mathrm{ODT}}/V_0 \approx 6.5 \times 10^{13}\mathrm{cm}^{-3}$. One could increase

[13] This means that the time scale for changing the magnetic field gradient has to be longer than $\sim V_0^{1/3}/\bar{v}$

the waist of the optical dipole trap and transfer at lower temperature, thus decreasing density without sacrificing in PSD. However, we decided to keep the waist unchanged, since in the case of the mixed evaporation we expect the density of ^{40}K to be lower and ^{6}Li has half of the trap depth of ^{40}K for $\lambda = 1064$nm light. We also observed that the optical plug has not a dramatic effect for ^{40}K. When evaporating in the magnetic quadrupole without the plug, the number of atoms loaded in the optical dipole trap decreases by only 40%. The position of the ODT respective to the magnetic quadrupole trap center was found by optimizing the number of loaded atoms. In fig. 7.3.2 we plot the number of trapped atoms as a function of the position of the ODT in the z direction. We observe that atoms are lost close to the magnetic field center due to Majorana spin flips. The optimal position was $z_0 \approx -100\mu$m, in accordance with the reasoning laid down in this section [115].

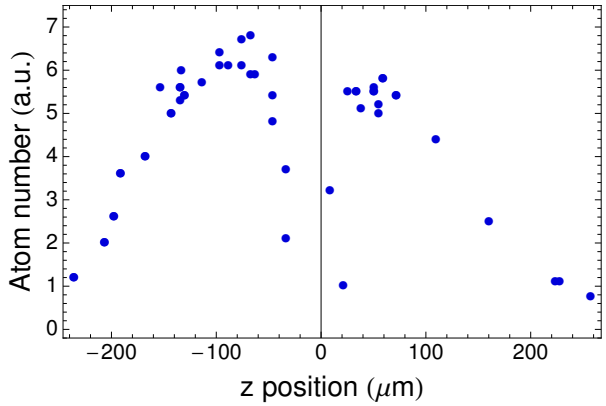


Figure 7.3.2: Number of atoms trapped in the ODT (arbitrary units) as a function of the laser beam position in the z direction.

For the mixed evaporation in the magnetic quadrupole trap, we observe that the presence of the plug is vital, as ^{6}Li suffers from more important Majorana losses. By performing sympathetic cooling of a sample of $\approx 2 \times 10^6$ ^{6}Li atoms down to 60μK, we were able to load 4.5×10^5 atoms in the optical dipole trap (see section 6.7.3 for details).

In conclusion, we have studied the loading of an atomic cloud into an optical dipole trap (ODT) by adiabatically decreasing the magnetic field gradient of the initial trap. We are able to load 2.8×10^7 atoms of ^{40}K at 45μK in the ODT, yielding a supplementary gain in PSD of factor 25 compared to the initial trap due to the dimple effect. These are excellent conditions to start evaporative cooling of ^{40}K in the ODT. In the following section we will discuss the axial confinement, before reporting the experimental results concerning evaporative cooling.

7.4 Axial confinement

Evaporative cooling in an ODT is performed by decreasing the laser power, which decreases not only the trap depth $U_0 \propto P$, but also the trapping frequencies $\omega \propto \sqrt{P}$. In the optimal case, evaporation dynamics have to be slower than all other time constants of the system. While γ_{coll} and $\omega_{\text{R}}/2\pi$ are of the order of kHz, $\omega_{\text{Ax}}/2\pi$ is smaller ($\sim$ 10Hz for the maximal power, see table 7.2.1). This frequency becomes too low in the last stages of the evaporation, where the atoms might have to take several seconds to oscillate in the axial direction. In order to circumvent this problem a additional confinement must be introduced in this direction. Two strategies were employed during this thesis: optical and magnetic.

The optical technique consists in crossing the optical dipole trap beam with a second laser beam. This beam has the same wavelength as the first one, but orthogonal polarization. Since the power of this beam is constant throughout the evaporation, the axial confinement it produces does not change while evaporating. In our apparatus the main optical dipole trap beam (ODT1) is aligned along the x-axis, while the axial confinement beam (ODT2) is aligned along the y-axis (see fig. 2.2.3 for a scheme). The frequency difference between the two laser beams is of 160MHz, imposed by the AOMs. The power of ODT2 is stabilized using a circuit analogous to the one described in section 7.2. This arrangement imposes the following confinement frequencies

$$\omega_x = \omega_{\text{R},2}, \quad \omega_y = \omega_{\text{R},1}, \quad \omega_z = \sqrt{\omega_{\text{R},1} + \omega_{\text{R},2}}.$$

The properties of ODT2 are listed in table 7.4.1. Figure 7.4.1 shows an absorption

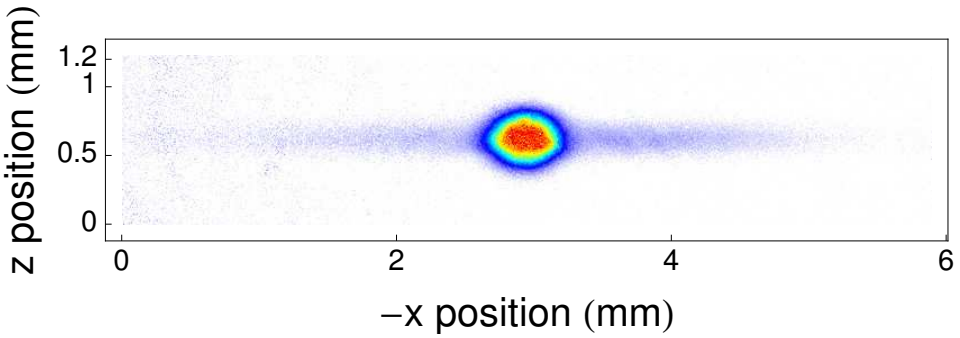


Figure 7.4.1: Absorption image after the loading in the crossed dipole trap and 6ms of time-of-flight. The number of atoms in the "dimple" is $N = 4.8 \times 10^6$, the temperature $T = 1.28\mu$K, the axial frequency $\omega_{\mathrm{Ax}}/2\pi = 24.5$Hz and radial frequency $\omega_{\mathrm{R}}/2\pi = 400$Hz. This corresponds to a central density of $n = 7 \times 10^{13}\mathrm{cm}^{-3}$ and $T/T_{\mathrm{F}} \approx 0.7$ (assuming a balanced mixture of spins in the $|F = 9/2, m_{\mathrm{F}} = 7/2\rangle$ and the $|F = 9/2, m_{\mathrm{F}} = 9/2\rangle$ states), T_{F} being the Fermi temperature.

	^{6}Li	^{40}K
P (W)	4.8	
w (μm)	340	
U_0 (μK)	1.6	3.5
$\omega_{\mathrm{R}}/2\pi$ (Hz)	44	25
$\dot{T}$ (nK/s)	18	7.0

Table 7.4.1: Parameters for the axial confinement laser beam (ODT2): the maximum light shift (U_0), its radial trapping frequency and heating rate.

image of the crossed dipole trap (ODT1+ODT2) taken along the axis of ODT2 (compare with fig. 7.1.1). One sees a very dense region where the laser beams cross and fainter wings along the horizontal direction. These wings are due to a fraction of atoms that have energy higher than the depth of ODT2, consequently not trapped in the crossing region.

Optical confinement solves the problem of the weak confinement along the axial direction and enhances collision rate. However, this can be cumbersome since it adds more degrees of complexity, such as the alignment of the crossing beams. Magnetic confinement does not have this problem. By confining the atoms magnetically in the axial direction and optically in the radial direction we create an *hybrid trap*. In our system we tested two kinds of hybrid traps: the *gradient confinement* and the *magnetic*

curvature.

The gradient confinement scheme is inspired by the hybrid trap reported by Lin et al. [115] and discussed in section 7.3. By having a magnetic quadrupole field with center above the ODT (distance z_0) the magnetic field felt by the atoms trapped along the ODT (aligned along the x axis) is

$$B(x, y = 0, z = z_0) = b\sqrt{x^2/4 + z_0^2}.$$

For low-field seeking atoms the resulting potential will be attractive. Neglecting the influence of the ODT in the axial confinement, the potential energy contribution in the axial direction is

$$U(x) = \mu_B b z_0 \sqrt{1 + x^2/4z_0^2},$$

for an atom in the stretched state. If the cloud size σ_x is much smaller than z_0, the trap has an harmonic shape with frequency

$$\omega_x^2 = \frac{\mu_B b}{4 m z_0}.$$

Notice that one can adjust this frequency by changing the magnetic gradient b. Another possibility is to introduce an homogenous field B_0. If this field is in the vertical (z) direction, the distance of the ODT to the center of the magnetic quadrupole field can be changed: $z_0 \to z_0 + B_0/b$.

In principle this strategy can only be used for $b < b_g = mg/\mu_B$, so that evaporated atoms from the ODT are not trapped in the quadrupole magnetic trap and fall due to gravity. We found out that higher magnetic field gradients can also be used, provided that a MW knife is present. This knife is placed at $B \lesssim bz_0$ in order to excite atoms evaporated from the ODT into high-field seeking states.

The magnetic curvature scheme relies on the fact that the *inner coils* in the science cell (which create the field for Feshbach resonances) are not in the Helmholtz configuration[14]. The field they produce has a non-zero quadratic term (curvature) of the Taylor expansion around the atoms position. A coil pair which is more distanced than the Helmholtz condition creates an attractive harmonic potential in the transversal

[14] See section 5.A.1 for details concerning the inner coils.

direction for the high-field seeking states with frequency

$$\omega_x^2 = \frac{\mu_B B''}{2m},$$

where B'' is the magnetic field curvature $B_z \approx B_0 + \frac{1}{2}B''z^2$. For ^{40}K, this frequency is given by $\omega_x/2\pi \approx 0.37\sqrt{B_0/1\text{G}}$. For ^{6}Li the corresponding frequency is 2.6 times bigger. For the pertinent Feshbach resonances $B \sim 200$G, the frequencies are $\omega_x/2\pi \approx 5.2$Hz for ^{40}K and $\omega_x/2\pi \approx 13$Hz for ^{6}Li. One might think that the magnetic field inhomogeneity responsible for trapping the atoms is incompatible with the Feshbach resonance study, which requires an homogenous field. It turns out that this variation is small. Indeed, if the magnetic field difference between the edge $x = \sigma_x$ of the cloud and its center is ΔB, then

$$E(\sigma) = \mu_B \Delta B = \frac{1}{2}m\omega_x^2\sigma_x^2 = \frac{1}{2}k_B T,$$

simply because it is the Zeeman shift that traps the atoms. Consequently, the magnetic field difference over the two edges of the cloud is $2\Delta B = k_B T/\mu_B$, which is $\Delta B \approx 15$mG for a cloud with $T = 1\mu$K. In a deep degenerate Fermi gas we have $E(\sigma) = \mu_B \Delta B = E_F$. For a cloud with $N = 10^6$ per spin state and $\bar{\omega}/2\pi = (5 \times 20^2)^{1/3}$, $2\Delta B \approx 3.3$mG. These values are much smaller than the width of ^{40}K-^{40}K ($\Delta \approx 7$G) and ^{6}Li-^{40}K ($\Delta \approx 1$G) Feshbach resonances [120, 198]. For very stringent applications, the axial confinement has to be done optically and the *outer* coils can be used to decrease the magnetic curvature.

In the experiments reported in this thesis the confinement in the axial direction is done optically, but magnetic confinement also gave satisfactory results. We managed to obtain a Fermi gas with $T/T_F \approx 0.5$ in the hybrid trap.

7.5 Evaporative cooling to quantum degeneracy

7.5.1 Introduction

In order to perform evaporative cooling in a optical dipole trap one has to reduce the laser power, which will directly decrease the trap depth $U_0 \propto P$. A full treatment of

the evaporation dynamics in the ODT will not be performed in this manuscript. On one hand, the typical temperature in the optical dipole trap is $\ll 50\mu$K and scattering occurs mainly in the s-wave channel, which is approximately temperature independent in this regime (see fig. 6.2.2). On the other hand, since the trapping is harmonic and, consequently, the atomic density profile is gaussian (see eq. 7.1.4), calculating analytically the evaporative dynamics is a simpler task (than the quadrupole trap case for example). For these two reasons, we refer the reader to refs. 33, 78, 99, 121 for studies concerning the evaporative cooling dynamics in a harmonic trap.

In the case of evaporation in an ODT, reducing the laser power (to reduce the trap height) also decreases the confinement. Indeed, the trapping frequencies depend on the laser power $\omega \propto \sqrt{P}$ (see eq. 7.1.3). The evaporation dynamics in this time-dependent trap was thoroughly studied by O'Hara et al. [144]. They derive the scaling laws for an evaporation with fixed $\eta = U_0/k_B T$ and the corresponding dynamics. They conclude that while the phase space density is enhanced, the atom density and collision rate decrease due to deconfinement.

7.5.2 Experimental results

In this section we describe the experimental results of the evaporative cooling of a mixture of spins of ^{40}K in an optical dipole trap. We assume in this experiment that atoms are distributed in the $|F = 9/2, m_F = 9/2\rangle$ and the $|F = 9/2, m_F = 7/2\rangle$ states (possibly there are some atoms in the $|F = 9/2, m_F = 5/2\rangle$ state), which are the states present in the plugged magnetic trap. We can control this mixture by performing imperfect optical pumping before loading the magnetic trap in the MOT chamber [200]. The populations of each state can be probed using the Stern-Gerlach technique described in section 7.5.3.

The first step of evaporation occurs in the single beam optical dipole trap in the presence of a vertical homogeneous guiding magnetic field. This step lasts for 5.5s and the laser power is exponentially decreased of a factor of ≈ 56. In a second stage, the optical axial confinement beam is switched on in 1.5s and, in a last step, the laser power is exponentially further decreased by a factor of ≈ 5.6 in 8s. These steps result in a quantum degenerate gas of $\approx 1.5 \times 10^5$ atoms per spin with $T/T_F \approx 0.17$.

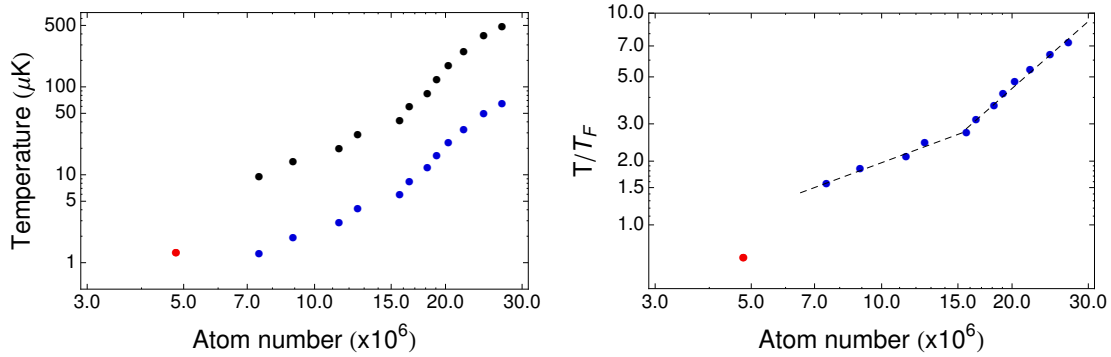


Figure 7.5.1: Evaporative cooling in the single beam ODT. On the left we plot the temperature (blue) and the calculated trap depth (black) as a function of the total atom number in the ODT. On the right we plot the T/T_F value as a function of the total atom number. The red dot refers to the loaded crossed dipole trap.

In figure 7.5.1 we show the measured temperature and the calculated value of T/T_F as a function of the number of trapped atoms N during the first stage of evaporation (in the single ODT). $T_F = \hbar\bar{\omega}(3N)^{1/3}$ is the Fermi temperature if we assume that the N atoms are equally distributed in two spin-states ($\bar{\omega}$ is harmonic average of the trap frequencies). This is the more appropriate degeneracy parameter for a Fermi gas[15]. We observe that in the evaporation sequence the atom number decreases by less than one order of magnitude, while the temperature decreases of factor ≈ 50. The plot of the T/T_F value in fig. 7.5.1 reveals two regimes of evaporative cooling, which are signaled with dashed lines. A first one with higher evaporation efficiency $\Gamma \approx 5.4$ and second with less efficiency $\Gamma \approx 2.3$, where $\Gamma = -d\ln \mathrm{PSD}/d\ln N = 3\, d\ln(T/T_F)/d\ln N$. Using the scaling laws derived in ref. [144], these two evaporation regimes correspond to $\eta \approx 8.6$ and $\eta \approx 5.8$, which are close to the values calculated using the estimation of the trap depth. The smaller efficiency of the second regime of evaporation might be caused by the loose axial trapping, which reaches $\omega_{Ax}/2\pi \approx 2$Hz at the end of this evaporation step.

By smoothly ramping up the power of the ODT2, the axial confinement laser beam, there is a further increase in PSD. The atom loss observed here is due to the fact that not all atoms from initial trap are loaded into the crossed dipole trap (see fig.

[15] In this thesis we have defined PSD$= n_0\Lambda^3$, n_0 being the central atomic density. For an equilibrated mixture of two spins we have the simple relation PSD$= 1/\left(3(T/T_F)^3\right)$.

7.4.1). In the crossed dipole trap we measure $N = 4.8 \times 10^6$ atoms at 1.28μK, yielding $T/T_F = 0.7$. The measured averaged shot-to-shot atom number fluctuations are $\approx 3\%$ at this point.

7.5.3 Transfer to the lower Zeeman states

In order to explore the rich Physics that emerges from tuning the interaction strength by means of a Feshbach resonance we prepare the atoms in the appropriate Zeeman states, before proceeding with further evaporative cooling. In the case of the resonance at $B_0 = 202.1$G the relevant states are $m_F = -9/2$ and $m_F = -7/2$ of the $F = 9/2$ manifold [120, 164]. Since at this point of the cooling sequence the majority of the atoms are in the positive states $m_F = 9/2$ and $m_F = 7/2$, a stage-preparation stage will be performed. This is done using consecutive adiabatic passages between the subsequent Zeeman states by means of a RF (radiofrequency) field.

The adiabatic passage is a well known technique in Atomic Physics to transfer atoms from one state to another [97, 100]. Two atomic states with a certain energy difference $\hbar\omega_0$ can be coupled to each other by means of electromagnetic radiation of frequency ω. In our case study, a RF field couples to the atomic magnetic dipole moment[16]. Let the strength of the coupling be given by the Rabi frequency Ω_R and the detuning be $\Delta = \omega - \omega_0$. By adiabatically sweeping the frequency of the radiation from negative detuning $-\Delta \gg \Omega_R$, to the coupling regime $|\Delta| \sim \Omega_R$ and then to positive detuning $\Delta \gg \Omega_R$, one can transfer an atom from a pure state a to another pure state b. The probability of transfer is given by

$$P_{a\to b} = 1 - \exp\left\{-\frac{\pi\Omega_R^2}{2|\partial_t\Delta|}\right\},$$

which is the Landau-Zener result for a two-level avoided crossing. For a perfect adiabatic passage $\Omega_R \gg \sqrt{|\partial_t\Delta|}$, the transfer is complete. The full analytical treatment of the adiabatic passage in ref. 189 (section 5.3.1).

The case of the $F = 9/2$ manifold of ^{40}K is slightly more complicated than the simple two-level system since it is a 10-level system . To solve the general case one has to

[16] This is the reason why transitions with $\Delta F = 0$ are allowed. This is not the case of transitions driven by light, for which the coupling with the atomic electric dipole moment is involved.

find the eigenstates of this problem, which involves diagonalizing a 10×10 matrix. By using the Breit-Rabi formula one can calculate the energy spacings between the different Zeeman states for a given bias field B_0. We chose to perform the adiabatic passage for a relatively high field of $B_0 = 19.2$G. In this regime, the transitions between the Zeeman states are of the order of 6MHz and they are not degenerate. For example, for $m_F = 9/2 \rightarrow m_F = 7/2$ the resonance is at $\omega_0/2\pi \approx 6.213$MHz, while for $m_F = 7/2 \rightarrow m_F = 5/2$ it is $\omega_0/2\pi \approx 6.151$MHz. The difference in frequencies is of 61kHz, while the estimated Rabi frequency is of the order of $\Omega_R \sim 10$kHz. In the low Rabi frequency regime the 10-level problem reduces to 9 practically independent adiabatic passages (see left plot in fig. 7.5.2). So, starting from a pure state of $m_F = 9/2$ one can chose the target Zeeman state by tuning the final frequency of the sweep. For lower field B_0 (or higher Rabi frequency), the dressed states are a more complex mixture of the Zeeman states during the sweep and selectivity is not possible.

In our experiment we perform the RF sweep using the setup already presented in fig. 6.5.2. The antenna was impedance matched and characterized as described in section 6.B.2. We perform a linear RF sweep from 6.5MHz to 5.5MHz in 10ms, yielding

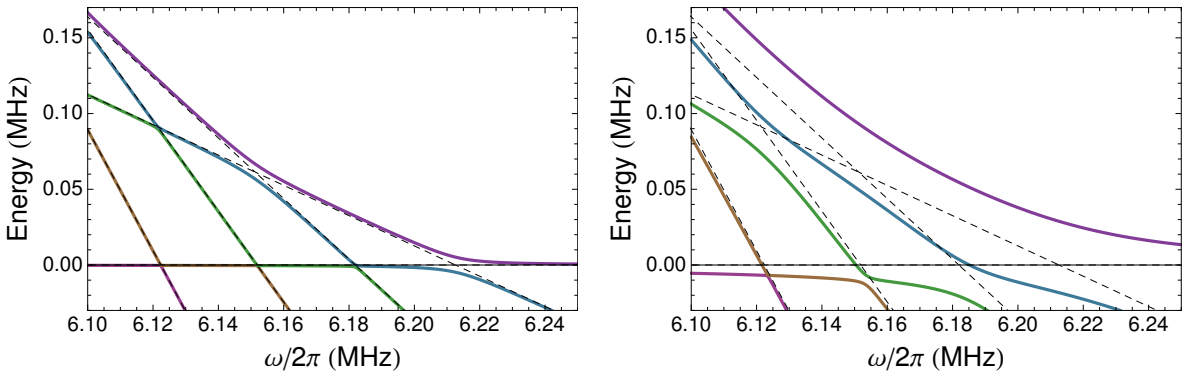


Figure 7.5.2: Calculation of the eigen-energies of the atomic Zeeman states of the $F = 9/2$ manifold for $B_0 = 19.2$G, dressed with RF radiation with frequency $\omega/2\pi$ and Rabi frequency Ω_R (abridged plot). Color code: purple for $m_F = 9/2$, blue for $m_F = 7/2$, green for $m_F = 5/2$, yellow for $m_F = 3/2$ and pink for $m_F = 1/2$. For the plot at the left $\Omega_R/2\pi = 5$kHz we observe 2 independent avoided crossings, while at the right $\Omega_R/2\pi = 25$kHz the state mixing is more rich. Dashed lines are the energies of the bare Zeeman states.

$\sqrt{|\partial_t \Delta|}/2\pi \approx 1.6$kHz. In order to distinguish the populations in each Zeeman states we perform a Stern-Gerlach experiment. By switching off the optical trap and applying a constant magnetic field, atoms will expand and experience a constant magnetic force that depends on their magnetic moment. Using this Stern-Gerlach technique we can separate the different spin components of an atomic cloud. An example of experiment is presented in fig. 7.5.3. It shows that initially both the $m_F = 9/2$ and the $m_F = 7/2$ states are populated (with some residue of $m_F = 5/2$), while after applying the RF sweep the atoms and transferred into their symmetric state with very good efficiency.

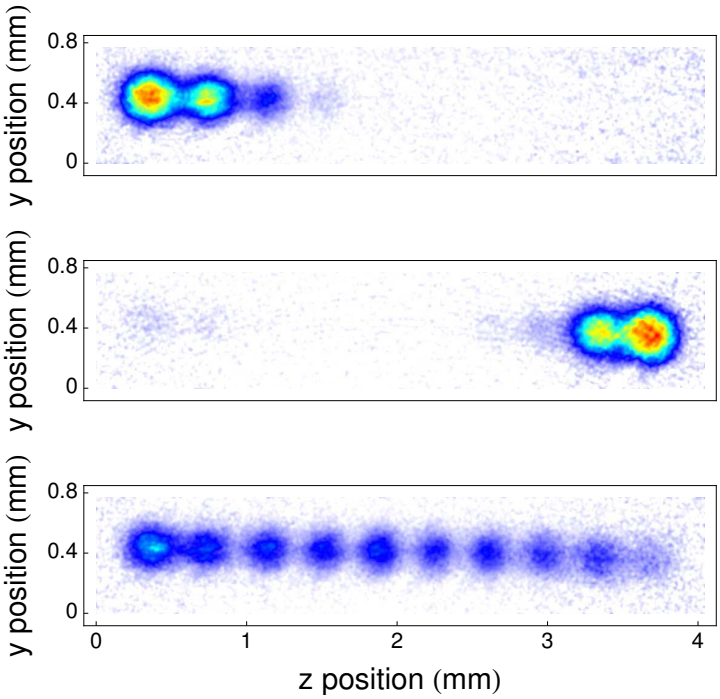


Figure 7.5.3: Adiabatic passage performed at constant magnetic field 19.2G. The RF field is swept from 6.5MHz to 5.5MHz in 10ms. The images are absorption pictures taken in the direction of the optical dipole trap after the Stern-Gerlach experiment. In the top is the result without applying the RF sweep, in the middle with the RF sweep and in the bottom is the result of applying 10 back-and-forth frequency sweeps in 10ms. The bottom image displays the 10 states of the $F = 9/2$ manifold: $m_F = 9/2$ is the first one at left and $m_F = -9/2$ is last one at right.

7.5.4 Degenerate Fermi gas

As the evaporative cooling continues and the trapped gas goes deeper in the quantum regime, the standard time-of-flight technique we use for measuring the temperature stops being valid. This strategy consists in measuring the average speed of the atomic cloud, which for a classical Maxwell-Boltzmann distribution is proportional to $\sqrt{k_B T/m}$. However, a Fermi gas at low temperature saturates in the Fermi-Dirac distribution and the average speed of the atomic cloud is some function of $v_F = \sqrt{2k_B T_F/m}$. In order to determine the temperature of the Fermi gas, the atomic density profile must be measured. For a Fermi-Dirac distribution the density profile in a harmonic trap is given by

$$n(\mathbf{r}) = n_0 \frac{\mathrm{Li}_{3/2}\{-\zeta e^{-\sum_i \frac{x_i^2}{2\sigma_i^2}}\}}{\mathrm{Li}_{3/2}\{-\zeta\}}, \tag{7.5.1}$$

where n_0 is the peak density, $\mathrm{Li}_n(z) = \sum_{k=1}^{\infty} z^k/k^n$ is the Polylogarithm (or Jonquière) function and ζ is the fugacity $-\mathrm{Li}_3(-\zeta) = (T/T_F)^{-3}/6$. The density distribution after time-of-flight t_{TOF} is simply re-scaled: $\sigma_i^2 = \sigma_{i,0}^2(1+\omega_i^2 t_{TOF}^2)$, which is a particular result for harmonic trapping. This distribution smoothly interpolates between the gaussian classical distribution $T/T_F \gg 1$ and the zero temperature distribution

$$n(\mathbf{r}) = n_0 \left(1 - \sum_{i=x,y,z} \frac{x_i^2}{R_{F,i}^2}\right)^{3/2},$$

where $R_{F,i}^2 = 2E_F/m\omega_i^2$ are the Fermi radii. Details concerning these results can be found in the thesis of DeMarco [44], in ref. 92 (section 2.3) and in ref. 100 (section 3.3). Notice that these results are only valid in the very weakly interacting regime $k_F a \ll 1$. In the regime of strong interactions $k_F a \sim 1$ other thermometry strategies must be used [122, 136, 137].

After loading the atomic cloud in the crossed dipole trap we evaporate for 8s by decreasing the power of the ODT1 by a factor of 5.6. In order to have access to the single spin density profile we perform imaging at high magnetic field bias (see section 2.3.3). In this regime we can selectively image the different spin components of the

cloud. By fitting the density profile of the atoms in the $m_F = -9/2$ state with eq. 7.5.1, we obtain a temperature of $T/T_F \approx 0.17$ (see fig. 7.5.4). If only the wings of the density profile are fitted with the Maxwell-Boltzmann gaussian distribution, the curve deviates from the data in the central region and we get an independent measurement of the temperature (which is not consistent with the Fermi-Dirac fit). We have therefore obtained a degenerate Fermi gas in the weak interactions regime $k_F a \approx 0.07$. The number of atoms in the $m_F = -9/2$ state is 1.5×10^5 and the cloud temperature is 70nK ($T_F \approx 0.41\mu$K). In the $m_F = -7/2$ state we have roughly the same number of atoms at the same temperature.

This result is the second main achievement of the thesis. We have obtained a deeply degenerate Fermi quantum gas with a quite large number of atoms in the $m_F = -9/2$ and the $m_F = -7/2$ states. In order to study a degenerate gas in the strongly interacting regime it suffices to further increase the magnetic field to the Feshbach resonance $B_0 = 202.1$G. For a degeneracy parameter below $T_c/T_F \approx 0.19$ at resonance, we should be able to observe the transition to a strongly interacting Fermi superfluid [100].

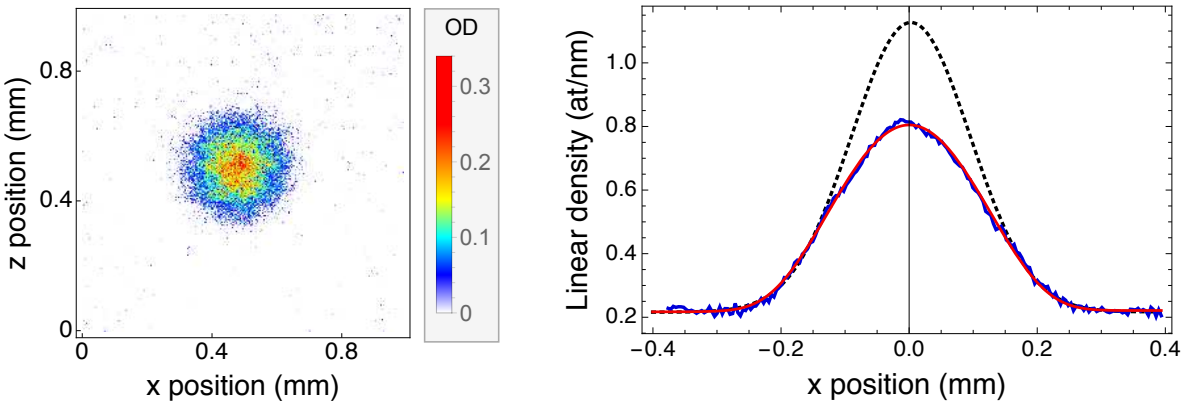


Figure 7.5.4: (Left) Absorption image of a quantum degenerate gas of ^{40}K atoms in the $m_F = -9/2$ state after 20ms of time-of-flight. The slight asymmetry is due to the trap aspect ratio. (Right) Integrated density profile data. (blue), Fermi-Dirac distribution fit (red curve) and Maxwell-Boltzmann distribution fit of the wings (black dashed curve). From the Fermi-Dirac fit one obtains $T/T_F \approx 0.17$, $N = 1.5 \times 10^5$ and $T \approx 70$nK.

7.6 Cooling of the ^{6}Li-^{40}K mixture

If we restrict ourselves to binary mixtures, there is only one demonstrated strategy to cool the ^{6}Li-^{40}K mixture in an optical dipole trap (ODT), at the present. The idea is to trap a mixture of spins of ^{6}Li in the $F = 1/2$ manifold and perform evaporative cooling in the ODT near the Feshbach resonance between the $|F = 1/2, m_F = \pm 1/2\rangle$ states ($B_0 \sim 832$G [216]). This allows to enhance the collision rate and have a very efficient evaporative cooling for ^{6}Li. ^{40}K in small numbers has been cooled by successive thermalization with the ^{6}Li gas (sympathetic cooling) [188].

In our setup we would like to investigate another route that could potentially lead to larger and balanced samples of quantum degenerate ^{40}K and ^{6}Li atoms. For the ODT used in this apparatus the trap depth for ^{6}Li is roughly half of the one of ^{40}K ($\lambda = 1064$nm), as shown in table 7.2.1. If the two species have the same temperature then $\eta_{Li} \sim \eta_K/2$. In consequence, the evaporation rate of ^{6}Li is enhanced by a factor $e^{-\eta_{Li}}/e^{-\eta_K} \approx e^{\eta_K/2}$ compared to ^{40}K (e.g. for $\eta_K = 8$, this factor would be $e^{\eta_K/2} \approx 55$), as shown in eq. 7.B.1 (in appendix 7.B). Another effect is the fact that in a binary interspecies collision the ^{6}Li atom takes most of the kinetic energy due to its smaller mass. Since the interspecies and the ^{40}K intraspecies (between different spin states) collision rates are of the same order of magnitude, the evaporation rate of ^{6}Li is much larger that the evaporation rate of a spin mixture of ^{40}K, leading to a fast loss of ^{6}Li atoms from the trap.

A first way to circumvent this problem would be to enhance the intraspecies collision rate of a spin mixture of ^{40}K atoms by means of a Feshbach resonance. By evaporating ^{40}K at the same rate as ^{6}Li, one may be able to find a window of parameters for which both species would evaporatively cool. In figure 7.6.1 we plot the result of a calculation of the evaporation rates of ^{40}K and ^{6}Li for an ODT laser power $P = 1$W and 10^7 trapped atoms of ^{40}K at $k_B T = U_0/10$. This calculation confirms that the evaporation rate of ^{40}K with $a = 170a_0$ (dashed blue line) is much smaller than the evaporation rate of ^{6}Li (red line). Increasing the scattering length to $a = 1500a_0$, the evaporation rate of ^{40}K (blue solid line) is twice faster than of the one of ^{6}Li for $\eta_K \approx 6.3$. In conclusion, we should be able to control the double evaporation dynamics by tuning this scattering length.

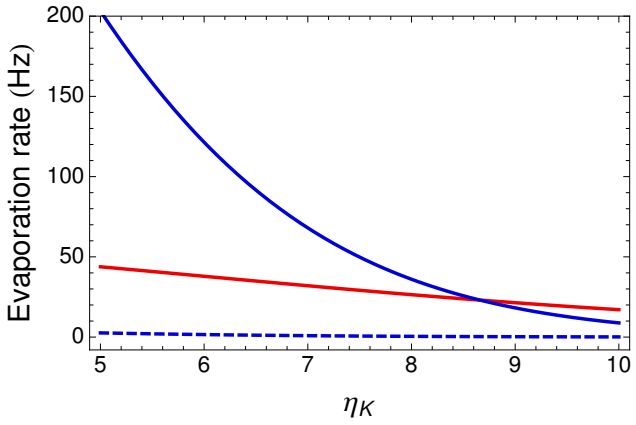


Figure 7.6.1: Calculation of the evaporation rate in an optical dipole trap for $P = 1\text{W}$ and 10^7 atoms of ^{40}K in two spin states at temperature $T = U_{0,\text{K}}/\eta_{\text{K}}$. In red is the evaporation rate for ^{6}Li due to collisions with ^{40}K, calculated using eq. 7.B.1. In blue is the evaporation rate for ^{40}K due to intraspecies collisions for $a = 170a_0$ (dashed line) and $a = 1500a_0$ (solid line). The interspecies contribution is negligible for a similar number of ^{6}Li atoms.

A second possible strategy is to perform two independent evaporations of ^{40}K and ^{6}Li, each in a balanced mixture of spin states. This is possible provided that the intraspecies collision rate is much higher than the interspecies one. This regime can be achieved by simultaneously enhancing the collision rate for both atomic species and perform fast evaporative cooling. For the case of ^{40}K we could use the resonance already mentioned in section 7.5.3 at $B_0 = 202.1\text{G}$. At this magnetic field value the scattering cross-section between ^{6}Li atoms in the states $|F = 1/2, m_{\text{F}} = 1/2\rangle$ ($|1\rangle$, the Zeeman state with lowest energy) and the $|F = 3/2, m_{\text{F}} = -3/2\rangle$ ($|3\rangle$, the Zeeman state with the third lowest energy) is enhanced since $a_{\text{Li}} \approx -800a_0$ [25, 149]. At the end of the evaporation, we would let the two samples thermalize via interspecies collisions.

In conclusion, we have discussed two promising alternative strategies to cool a mixture of ^{6}Li and ^{40}K with balanced numbers of atoms. The first strategy is to perform double evaporative cooling, relying on interspecies collisions for ^{6}Li and enhanced collisions between two spin states for ^{40}K. This evaporation regime would be attained when the evaporation rates of the two species are identical. The second strategy is to perform doubly *independent* evaporative cooling, relying on collisions between two spin states for both ^{6}Li and ^{40}K. If the evaporation rate for each species

is faster than the interspecies thermalization rate, the evaporations are independent. These two strategies will experimentally be investigated in the near future.

7.7 Conclusions

In this chapter we have presented the optical dipole trap and studied its loading from a plugged magnetic quadrupole trap. We managed to transfer 2.8×10^7 atoms of ^{40}K at 45μK in the ODT. We showed that we were able to evaporate a mixture of spins of ^{40}K in an ODT down to quantum degeneracy. We measured a degeneracy parameter of $T/T_{\mathrm{F}} \approx 0.17$ for 1.5×10^5 atoms in the $|F = 9/2, m_{\mathrm{F}} = -9/2\rangle$ state and similar parameters for the $|F = 9/2, m_{\mathrm{F}} = -7/2\rangle$ state. This chapter paves the way to obtain a strongly interacting Fermi superfluid and a mixture of degenerate Fermi gases in the near future.

Appendix 7.A Gravitational sag

In the introductory analysis performed in section 7.1 the gravitational force was neglected. It can actually have a dramatic effect in the ending steps of the evaporative cooling sequence in an optical dipole trap. The potential energy along the vertical (z) direction is given by

$$U(z) = \frac{1}{2}m\omega_z^2 z^2 + mgz = \frac{1}{2}m\omega_z^2(z - z_0)^2 + \frac{1}{2}m\omega_z^2 z_0^2,$$

with $z_0 = -g/\omega_z^2$. This simple manipulation reveals that gravity induces a sag of the atomic cloud of z_0, along the vertical direction. This calculation is valid as long as the gravitational sag is smaller than the waist of the ODT $|z_0| \ll w$. In the case of the ODT1 laser beam, $\omega_z/2\pi \gg \sqrt{g/w}/2\pi \approx 77$Hz. For the degenerate gas reported in this thesis $\omega_z/2\pi \approx 160$Hz, yielding a sag of $z_0 \approx -9.7\mu$m, smaller than the waist of ODT1. If this were not the case, the atomic cloud would sag to the edge of the laser beam, where the trap depth and the confinement are smaller. We observed this effect in some experiments and we compensated it by introducing a magnetic field gradient of $b = b_g = mg/\mu_B$ in the vertical direction, which exactly compensates gravity for the stretched states. In the presence of a bias field $B_0 \gg \sigma_z b$, this strategy can be used for both the high-field and the low-field seeking states, by reversing the sign of the gradient (or the direction of the bias).

Gravitational sag can be an issue when evaporating a mixture of ^{6}Li and ^{40}K, since these atoms will sag differently. At the ending steps of evaporative cooling one has to prevent the two atomic clouds from decoupling spatially, otherwise thermalization cannot be assured.

Appendix 7.B Evaporation rate of a double atomic gas with interspecies collisions

Let us consider two trapped gases with different masses without the possibility of having intraspecies collisions (e.g. two polarized Fermi gases at a temperature low enough so that p-wave collisions are inhibited). If the trap has a finite depth then collisions between the two gases can induce evaporation. The purpose of this section

section is to calculate the rate of this evaporation.

By following the reasoning of references [33, 121], already sketched above in section 6.4.2, and assuming that the scattering cross-section is constant the calculation is straightforward. The main difference is to properly define the total momentum $\mathbf{P} = \mathbf{p}_1 + \mathbf{p}_2$ and the exchanged momentum $\mathbf{q} = \mu_{12}(\mathbf{p}_1/m_1 - \mathbf{p}_2/m_2)$. The evaporation rate of particles 2 by collisions with particles 1 is:

$$\begin{aligned} \Gamma_{\text{evap}} &= n_1 \sigma_{12} \bar{v}_{12} e^{-\eta_2} \frac{V_{\text{evap}}}{V_{e,2}} \\ \frac{V_{\text{evap}}}{V_{e,2}} &= \left(\frac{m_2}{2\mu_{12}}\right)^{3/2} \frac{\zeta_{\infty,1}(T)}{\zeta_{\infty,2}(T)} \frac{\eta_1 P(3/2+\delta,\eta_1) - (5/2+\delta) P(5/2+\delta,\eta_1)}{P(3/2+\delta,\eta_2)}, \end{aligned} \tag{7.B.1}$$

with $\bar{v}_{12} = \sqrt{8kT/2\mu\pi}$. This result was used to evaluate the evaporation rate of ^{6}Li and ^{40}K in an optical dipole trap (see fig. 7.6.1).

8 Conclusions and outlook

This thesis has reported the design, construction and characterization of an experimental apparatus capable of creating a deep degenerate Fermi gas of ^{40}K with relatively large atom numbers. The discovery of an efficient sub-Doppler cooling scheme for ^{40}K was determinant to achieve the quantum regime. This cooling mechanism was readily adapted and implemented to the case of ^{6}Li and operated simultaneously with ^{40}K. This apparatus features an efficient magnetic transport from the MOT chamber to the science cell, which was optimized in the course of this thesis. A mixture of ^{40}K atoms in two spin states was evaporatively cooled first in a plugged magnetic trap and then in an optical dipole trap to quantum degeneracy. This thesis has also reported the sympathetic cooling of ^{6}Li in the plugged trap and loading into the optical dipole trap.

The described apparatus is on the brink of being able to produce strongly interacting superfluids of ^{40}K and strongly interacting fermionic mixtures of ^{40}K and ^{6}Li. These systems have plenty of exciting experimental possibilities. At the end of this chapter we will present some experiments to be realized with the described apparatus in the near future.

8.1 Summary of the results

The first step to create ultracold gases is to trap and cool atoms in a magneto-optical trap (MOT). In this thesis we described the implementation of a double-species MOT that simultaneously traps and cool atoms of fermionic ^{6}Li and ^{40}K with large numbers. Losses due to light-induced collisions were minimized to $\sim 10\%$ by optimizing the trap parameters (low magnetic field gradient and low repumper power). With this apparatus we were able to create excited ^{6}Li^{40}K* molecules by photoassociation and to determine their binding energies. This experiment give us insight over the interspecies molecular potentials, opening the door for the creation of dipolar

molecules in their rovibrational ground-state via the Raman adiabatic passage technique (STIRAP). These molecules have a strong long-range and anisotropic dipole-dipole interaction, leading to novel many-body phenomena.

One of the core results of this thesis is the report of a novel cooling scheme, which is able to cool both ^{40}K and ^{6}Li to the sub-Doppler regime. This scheme is based on the gray molasses technique, which relies on Sisyphus cooling and on velocity selective coherent population trapping (VSCPT) in dark dressed states. We implemented gray molasses in a $F \rightarrow F' = F - 1$ transition for ^{40}K and in a $F \rightarrow F' = F$ transition for ^{6}Li on the atomic D_1 lines. We observed that by adding repumper light in the Raman condition with the cooling light, thus forming a Λ system, the cooling effect of the gray molasses was enhanced. For both fermionic atoms we achieved sub-Doppler temperatures and the determined phase space densities are the highest reported in the literature for laser cooling of ^{40}K and ^{6}Li.

We successfully implemented a magnetic transport that is able to transfer the cold atomic cloud from the MOT chamber to a science cell. This cell has the advantage of having very low residual background pressure for future experiments and improved optical access for the realization of experiments. The optimization of the magnetic transport was described in this thesis and yielded a loss in phase space density of just a factor of 7, mainly due to heating.

We have described the evaporative cooling of a mixture of spin states of ^{40}K in a quadrupole magnetic trap in the presence of an optical plug. We demonstrate that this plug efficiently suppresses Majorana losses in this trap, which otherwise would hinder cooling. In order to understand and quantify the evaporation dynamics, we performed a theoretical study taking in consideration a momentum-dependent scattering cross-section for elastic collisions in the s-wave and p-wave channels. We also present results on the sympathetic cooling of ^{6}Li by ^{40}K in the plugged magnetic trap.

We performed a study of the adiabatic transfer of an evaporatively cooled atomic cloud from a magnetic quadrupole trap into an optical dipole trap. We showed experimentally that we are able to achieve an efficient transfer (20%), in accordance with the theoretical predictions. The loading into the optical dipole trap is accompanied by an enhancement of the phase space density due to the dimple effect. Subsequent evaporation in the optical dipole trap, loading into a crossed beam optical trap and further evaporation is able to create a relatively large quantum Fermi gas of 1.5×10^5

atoms of ^{40}K in the $|F = 9/2, m_F = -9/2\rangle$ state with $T/T_F \approx 0.17$, mixed atoms in the $|F = 9/2, m_F = -7/2\rangle$ state with similar parameters. This is the first quantum degenerate gas of ^{40}K reported in France and it should reveal a superfluid fraction in the strongly interacting regime, attained via a known Feshbach resonance at $B_0 = 202.1$G. Concerning ^{6}Li, we have shown sympathetic cooling by ^{40}K and efficient loading into the optical dipole trap. We pave the way to reach double quantum degeneracy by describing potential strategies to cool the mixture.

The constructed apparatus is able to create quantum degenerate gases with a fairly high repetition rate ($T = 45$s) and has a good short and long term stability. The scheme of fig. 8.1.1 illustrates the pathway to cooling a gas of ^{40}K to the quantum regime. In the very short term we believe that it will be able to create strongly interacting mixtures of ultracold ^{6}Li and ^{40}K. In the following section we present some exciting novel experiments that could be realized with this apparatus.

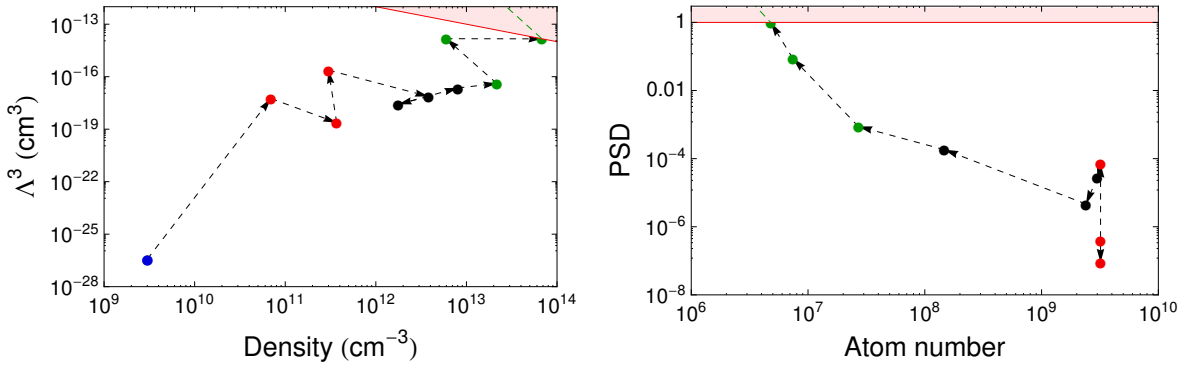


Figure 8.1.1: Pathway to quantum degeneracy of a ^{40}K gas: background pressure in the 2D-MOT chamber (blue), laser cooling (red: MOT, compressed MOT and D_1 gray molasses cooling), magnetic trapping (black: loading, magnetic transport and evaporation) and optical trapping (green: loading and evaporation). The red line shows the border from the classical to the quantum regime (pink region) PSD$= n_0\Lambda^3 = 1$, where n_0 is the atomic central density and Λ is the thermal de Broglie wavelength.

8.2 Perspectives

Since the apparatus built in this thesis is able to produce ultracold samples of ^{40}K, a first experiment that could be realized with the Fermi superfluid is the measurement of the superfluid gap Δ_{gap} across the BEC-BCS crossover. There are two experimental protocols proposed by Scott et al. [180]. The first one is to quench the superfluid by changing the scattering length faster than h/Δ_{gap} (which can be done by quickly ramping the magnetic field across a Feshbach resonance). This excitation will make the (superfluid) order parameter oscillate with frequency given by $2\Delta_{gap}/\hbar$. The second protocol is to induce forced oscillations of the order parameter by modulating the interactions and measuring the resonance frequency. In the theoretical proposal it is suggested that the projection technique to the molecular BEC side [92, 100, 165, 218] could be used to directly measure the order parameter and its oscillations. Notice that these oscillations of the order parameter have an interesting similarity with the famous "Higgs amplitude mode" from condensed matter and high energy physics [54, 153].

Another research direction that we could follow is the study of the ^{6}Li-^{40}K Fermi gas in mixed dimensions. To create such a system we intend to selectively trap ^{40}K in a one-dimensional optical lattice at $\lambda = 808$nm, relatively close to the ^{40}K atomic resonance, but far detuned from the ^{6}Li transitions. If the typical energies of the ^{40}K cloud (E_F, k_BT and the interaction energy) are much smaller than the inter-level energy spacing of the lattice ($\hbar\omega_z$), the behavior of the ^{40}K is two-dimensional [159]. Since ^{6}Li is not be affected by this potential, its behavior is three-dimensional. In appendix 8.A we describe the already prepared optical lattice for ^{40}K.

The first step would be to study the effect of the mixed confinement on the interspecies Feshbach resonance. A related study was performed in a ^{87}Rb-^{40}K Bose-Fermi mixture, in which the lighter species was confined in 2D [105]. When the interspecies Feshbach resonance is tuned, it is predicted that this system has a rich many-body phase diagram [142]. Another interesting angle is to study the interactions between different 2D planes of ^{40}K mediated by the ^{6}Li 3D gas [141]. A calculation was performed in our group by D. Suchet regarding the transmission of a mechanical perturbation throughout the 2D layers of ^{40}K mediated by the excitation and absorption of phonons in a superfluid of ^{6}Li. For the BEC of ^{6}Li-^{6}Li molecules this effect

should be accessible in an experiment. Another direction would be the observation of non-Efimovian ^{6}Li-^{40}K-^{40}K trimers, which could be created in this mixed dimensional system and are predicted to be stable [113, 114]. Moreover, exciting analogies could be made with string theory [140] and eventually some collective excitations in the heterogeneous neutron star crust, such as the "Lasagna" mode [46].

Another direction would be to use the optical lattice to study the behavior of an interacting Fermi gas in two-dimensions. There are already some experimental results on this subject, namely by the group of M. Köhl [13, 14, 57, 62, 63, 102, 103, 204], C. Vale [52, 147], Turlapov [123], M. Zwierlein [186] and S. Jochim. However, several important open questions remain including the Berezinsky–Kosterlitz–Thouless transition to a superfluid phase.

Appendix 8.A Optical lattice for ^{40}K

The chosen wavelength for the selective potential for ^{40}K was $\lambda = 808$nm, which offers a good compromise between selectivity and heating due to photon scattering.

The setup[1] uses a commercial laser diode that lases at $\lambda = 808$nm and emits up to 150mW of laser power[2]. This laser diode is installed in a homemade mount with a grating in the Littrow configuration, which should reduce the laser linewidth to < 1MHz[3]. The light emitted from this extended-cavity passes through an optical isolator for protection of the diode and injects a tapered amplifier[4]. After a second optical isolator, the laser beam is diffracted by an AOM, which is used to electronically control the laser power, filtered[5] and injected into a single-mode polarization maintaining fiber. This system is able to deliver up to 500mW at the output of the fiber. Some power outputted by the laser diode is used to verify the laser wavelength and the single mode operation. The filter was installed to remove the spectral components due to fluorescence emission by the TA , namely the ones resonant with the

	^{40}K	^{6}Li
U_0 (μK)	39	6.4
$\dot{T}$ (μK/s)	0.19	0.053
$\omega_z/2\pi$ (kHz)	157	165
$T_z = \hbar\omega_z/k_B$	7.5	7.9
$\omega_\rho/2\pi$ (Hz)	381	437
T_F (μK)	1.8	-
$E_F/\hbar\omega_z$	0.24	-
E_r/k_B (μK)	0.37	2.4
U_0/E_r	105	2.7
Tunnel time	61s	6μs

Table 8.A.1: Calculated parameters for an optical lattice resulting from the retro-reflection of a laser beam with $\lambda = 808$nm, power $P = 150$mW and $w = 80\mu$m waist. For the estimation of the Fermi energy, we assume that 5×10^3 atoms are trapped in each lattice site.

[1] The described setup was aligned and tested by M. Rabinovich.
[2] Axcel Photonics M9-808-0150
[3] To further decrease the linewidth the laser can be locked to an external Fabry-Pérot cavity.
[4] Eagleyard Photonics TA-EYP-TPA-0808-01000-4006-CMT04-0000
[5] Semrock LL01-808-12.5

atoms. Preliminary tests showed trapping of ^{40}K atoms by a single laser beam.

In order to have a lattice potential, a retro-reflection configuration will be implemented. The resulting parameters of the lattice are given in table 8.A.1 for both ^{40}K and ^{6}Li. For the chosen laser beam parameters, ^{40}K can be quasi-2D trapped in the lattice sites, while ^{6}Li will hop from lattice site to lattice site $\tau_{\text{tunnel}} \sim 6\mu$s. ^{6}Li will behave effectively as 3D trapped particle, with a renormalized mass of $m^* \approx 1.22 m_{\text{Li}}$ in the lattice direction.

Index

2D-MOT diagnose problems, 51

A

Antennae construction, 193
AOM frequencies, 31
Atomic transitions, 30

B

Back-and-forth experiment, 146
Baking-out of the transport section, 28
Beat ^{6}Li D_1 offset lock, 101

C

Coils parameters, 153

G

Getter strip, 26
Gray molasses ^{6}Li level scheme, 98
Gray molasses ^{40}K level scheme, 87
Gray molasses parameters, 102

I

Imaging systems, 37

L

Laser detunings, 30
Laser table ^{6}Li, 46
Laser table ^{40}K, 45
Lifetime of the magnetic trap in science cell, 180
Lifetime of the magnetic trap in the elbow, 28
Lifetime of the magnetic trap in the MOT chamber, 26

M

Magnetic transport scheme, 141
Magnetic trap parameters, 134
Magnification of imaging systems, 37
Molasses paper, 105
MOT paper, 55

O

Optical setup around science cell, 32

P

Pixelfly and imaging specifications, 33

Q

Quad coils electronics, 157
Quad coils parameters, 154

R

Resolution of imaging systems, 37

V

Vacuum manifold, 24

Z

Zeeman slower clotting, 51

Bibliography

[1] S. Adhikari. *Superfluid Fermi-Fermi mixture: Phase diagram, stability, and soliton formation*. Physical Review A **76**, 053609 (2007).

[2] K. Aikawa, A. Frisch, M. Mark, S. Baier, R. Grimm, and F. Ferlaino. *Reaching Fermi Degeneracy via Universal Dipolar Scattering*. Physical Review Letters **112**, 010404 (2014).

[3] K. Aikawa. *All-optical selective formation of ultracold molecules in the rovibrational ground state*. PhD thesis (2011).

[4] J. Allen and A. Misener. *Flow of liquid Helium II*. Nature **141**, 75 (1938).

[5] F. Alzetto, R. Combescot, and X. Leyronas. *Atom-dimer scattering amplitude for fermionic mixtures with different masses: s-wave and p-wave contributions*. Physical Review A **86**, 062708 (2012).

[6] M. H. Anderson, J. R. Ensher, M. R. Matthews, C. E. Wieman, and E. A. Cornell. *Observation of Bose-Einstein condensation in a dilute atomic vapor.* Science **269**, 198–201 (1995).

[7] A. Aspect, E. Arimondo, R. Kaiser, N. Vansteenkiste, and C. Cohen-Tannoudji. *Laser cooling below the one-photon recoil energy by velocity-selective coherent population trapping*. Physical Review Letters **61**, 2–5 (1988).

[8] G. E. Astrakharchik, S. Giorgini, and J. Boronat. *Stability of resonantly interacting heavy-light Fermi mixtures*. Physical Review B **86**, 174518 (2012).

[9] M. Aymar and O. Dulieu. *Calculation of accurate permanent dipole moments of the lowest 1,3Σ^+ states of heteronuclear alkali dimers using extended basis sets.* The Journal of Chemical Physics **122**, 204302 (2005).

[10] S. Azizi, M. Aymar, and O. Dulieu. *Prospects for the formation of ultracold ground state polar molecules from mixed alkali atom pairs*. The European Physical Journal D **31**, 195–203 (2004).

[11] M. Baranov, C. Lobo, and G. Shlyapnikov. *Superfluid pairing between fermions with unequal masses*. Physical Review A **78**, 033620 (2008).

[12] BASF Corporation. *An advanced high modulus (HMG) short glass-fiber reinforced Nylon 6: Part II - mechanical performance*. Technical report (2003).

[13] S. Baur, E. Vogt, M. Köhl, and G. Bruun. *Collective modes of a two-dimensional spin-1/2 Fermi gas in a harmonic trap*. Physical Review A **87**, 043612 (2013).

[14] S. K. Baur, B. Fröhlich, M. Feld, E. Vogt, D. Pertot, M. Koschorreck, and M. Köhl. *Radio-frequency spectra of Feshbach molecules in quasi-two-dimensional geometries*. Physical Review A **85**, 061604 (2012).

[15] I. Bausmerth, A. Recati, and S. Stringari. *Chandrasekhar-Clogston limit and phase separation in Fermi mixtures at unitarity*. Physical Review A **79**, 043622 (2009).

[16] A. Behrle, M. Koschorreck, and M. Köhl. *Isotope shift and hyperfine splitting of the 4s-5p transition in Potassium*. Physical Review A **83**, 052507 (2011).

[17] C. Benvenuti, P. Chiggiato, P. Costa Pinto, A. Escudeiro Santana, T. Hedley, A. Mongelluzzo, V. Ruzinov, and I. Wevers. *Vacuum properties of TiZrV non-evaporable getter films*. Vacuum **60**, 57–65 (2001).

[18] I. Bloch, J. Dalibard, and S. Nascimbène. *Quantum simulations with ultracold quantum gases*. Nature Physics **8**, 267–276 (2012).

[19] D. Blume. *Few-body physics with ultracold atomic and molecular systems in traps*. Reports on progress in physics. Physical Society (Great Britain) **75**, 046401 (2012).

[20] D. Boiron, D. Meacher, P. Verkerk, and G. Grynberg. *Three-dimensional cooling of cesium atoms in four-beam gray optical molasses*. Physical Review A **52**, 3425–3428 (1995).

[21] D. Boiron, A. Michaud, P. Lemonde, Y. Castin, C. Salomon, S. Weyers, K. Szymaniec, L. Cognet, and A. Clairon. *Laser cooling of cesium atoms in gray optical molasses down to 1.1μK.* Physical review. A **53**, R3734–R3737 (1996).

[22] D. Boozer, H. Mabuchi, B. Lev, R. Miller, and L. Wilcut. *Ultra-High Vacuum Chambers*. **91125**, 1–16 (2005).

[23] S. N. Bose. *Plancks Gesetz und Lichtquantenhypothese*. Zeitschrift für Physik **26**, 178–181 (1924).

[24] J. Brantut, J. Clément, M. de Saint Vincent, G. Varoquaux, R. Nyman, A. Aspect, T. Bourdel, and P. Bouyer. *Light-shift tomography in an optical-dipole trap for neutral atoms*. Physical Review A **78**, 031401 (2008).

[25] A. Burchianti, ., G. Valtolina, J. a. Seman, E. Pace, M. De Pas, M. Inguscio, M. Zaccanti, and G. Roati. *Efficient all-optical production of large ^{6}Li quantum gases using D_1 gray-molasses cooling*. Physical Review A **90**, 043408 (2014).

[26] R. Casalbuoni and G. Nardulli. *Inhomogeneous superconductivity in condensed matter and QCD*. Reviews of Modern Physics **76**, 263–320 (2004).

[27] J. Catani, P. Maioli, L. De Sarlo, F. Minardi, and M. Inguscio. *Intense slow beams of bosonic Potassium isotopes*. Physical Review A **73**, 033415 (2006).

[28] P. Chiggiato and P. Costa Pinto. *Ti-Zr-V non-evaporable getter films: From development to large scale production for the Large Hadron Collider*. Thin Solid Films **515**, 382–388 (2006).

[29] C. Chin, R. Grimm, P. Julienne, and E. Tiesinga. *Feshbach resonances in ultracold gases*. Reviews of Modern Physics **82**, 1225–1286 (2010).

[30] S. Chu, L. Hollberg, J. Bjorkholm, A. Cable, and A. Ashkin. *Three-dimensional viscous confinement and cooling of atoms by resonance radiation pressure*. Physical Review Letters **55**, 48–51 (1985).

[31] C. Cohen-Tannoudji. *Cours de Physique Atomique et Moléculaire 1991-1992* ().

[32] C. Cohen-Tannoudji. *Cours de Physique atomique et moléculaire 1995-1996* (1996).

[33] C. Cohen-Tannoudji. *Cours de Physique atomique et moléculaire 1996-1997* (1997).

[34] G. Conduit, P. Conlon, and B. Simons. *Superfluidity at the BEC-BCS crossover in two-dimensional Fermi gases with population and mass imbalance*. Physical Review A **77**, 053617 (2008).

[35] L. Costa, J. Brachmann, A.-C. Voigt, C. Hahn, M. Taglieber, T. W. Hänsch, and K. Dieckmann. *S-wave interaction in a two-species Fermi-Fermi mixture at a narrow Feshbach resonance*. Physical Review Letters **105**, 123201 (2010).

[36] A. Couvert, T. Kawalec, G. Reinaudi, and D. Guéry-Odelin. *Optimal transport of ultracold atoms in the non-adiabatic regime*. EPL (Europhysics Letters) **83**, 13001 (2008).

[37] K. M. Daily and D. Blume. *Thermodynamics of the two-component Fermi gas with unequal masses at unitarity*. Physical Review A **85**, 013609 (2012).

[38] J. Dalibard and C. Cohen-Tannoudji. *Laser cooling below the Doppler limit by polarization gradients: simple theoretical models*. Journal of the Optical Society of America B **6**, 2023 (1989).

[39] K. Davis, M. Mewes, M. Andrews, N. van Druten, D. Durfee, D. Kurn, and W. Ketterle. *Bose-Einstein condensation in a gas of Sodium atoms*. Physical Review Letters **75**, 3969–3973 (1995).

[40] J. Deiglmayr, A. Grochola, M. Repp, K. Mörtlbauer, C. Glück, J. Lange, O. Dulieu, R. Wester, and M. Weidemüller. *Formation of ultracold polar molecules in the rovibrational ground state*. Phys. Rev. Lett. **101**, 133004 (2008).

[41] B. DeMarco, J. Bohn, J. Burke, M. Holland, and D. Jin. *Measurement of p-wave threshold law using evaporatively cooled Fermionic atoms*. Physical Review Letters **82**, 4208–4211 (1999).

[42] B. DeMarco and D. Jin. *Exploring a quantum degenerate gas of fermionic atoms*. Physical Review A **58**, R4267–R4270 (1998).

[43] B. DeMarco and D. S. Jin. *Onset of Fermi degeneracy in a trapped atomic gas*. Science **285**, 1703–1706 (1999).

[44] B. DeMarco. *Quantum behavior of an atomic Fermi gas*. PhD thesis (2001).

[45] B. J. DeSalvo, M. Yan, P. G. Mickelson, Y. N. Martinez de Escobar, and T. C. Killian. *Degenerate Fermi Gas of ^{87}Sr*. Physical Review Letters **105**, 030402 (2010).

[46] L. Di Gallo, M. Oertel, and M. Urban. *Collective excitations in the neutron star inner crust*. Physical Review C **84**, 045801 (2011).

[47] K. Dieckmann, C. A. Stan, S. Gupta, Z. Hadzibabic, C. H. Schunck, and W. Ketterle. *Decay of an ultracold Fermionic Lithium gas near a Feshbach resonance*. Physical Review Letters **89**, 203201 (2002).

[48] R. B. Diener and M. Randeria. *BCS-BEC crossover with unequal-mass fermions*. Physical Review A **81**, 033608 (2010).

[49] R. Drever, J. Hall, F. Kowalski, and J. Hough. *Laser phase and frequency stabilization using an optical resonator*. Applied Physics B **31**, 97–105 (1983).

[50] P. Duarte, R. Hart, J. Hitchcock, T. Corcovilos, T.-L. Yang, A. Reed, and R. Hulet. *All-optical production of a Lithium quantum gas using narrow-line laser cooling*. Physical Review A **84**, 1–4 (2011).

[51] R. Dubessy, K. Merloti, L. Longchambon, P.-E. Pottie, T. Liennard, A. Perrin, V. Lorent, and H. Perrin. *Rubidium-87 Bose-Einstein condensate in an optically plugged quadrupole trap*. Physical Review A **85**, 1–12 (2012).

[52] P. Dyke, E. D. Kuhnle, S. Whitlock, H. Hu, M. Mark, S. Hoinka, M. Lingham, P. Hannaford, and C. J. Vale. *Crossover from 2D to 3D in a Weakly Interacting Fermi Gas*. Physical Review Letters **106**, 105304 (2011).

[53] A. Einstein. *Quantentheorie des einatomigen idealen Gases*. Sitzungsberichte der Preußischen Akademie der Wissenschaften **3**, 18 (1925).

[54] M. Endres, T. Fukuhara, D. Pekker, M. Cheneau, P. Schauss, C. Gross, E. Demler, S. Kuhr, and I. Bloch. *The 'Higgs' amplitude mode at the two-dimensional superfluid/Mott insulator transition*. Nature **487**, 454–8 (2012).

[55] T. Esslinger, F. Sander, A. Hemmerich, T. W. Hänsch, H. Ritsch, and M. Weidemüller. *Purely optical dark lattice.* Optics letters **21**, 991–3 (1996).

[56] S. Falke, J. Friebe, and M. Riedmann. *Potassium ground-state scattering parameters and Born-Oppenheimer potentials from molecular spectroscopy*. Physical Review A (2008).

[57] M. Feld, B. Fröhlich, E. Vogt, M. Koschorreck, and M. Köhl. *Observation of a pairing pseudogap in a two-dimensional Fermi gas.* Nature **480**, 75–8 (2011).

[58] R. P. Feynman. *Simulating physics with computers*. International Journal of Theoretical Physics **21**, 467–488 (1982).

[59] V. Flambaum, G. Gribakin, and C. Harabati. *Analytical calculation of cold-atom scattering*. Physical Review A **59**, 1998 (1999).

[60] M. M. Forbes, E. Gubankova, W. V. Liu, and F. Wilczek. *Stability criteria for breached-pair superfluidity*. Phys. Rev. Lett. **94**, 17001 (2005).

[61] D. Fried, T. Killian, L. Willmann, D. Landhuis, S. Moss, D. Kleppner, and T. Greytak. *Bose-Einstein condensation of atomic Hydrogen*. Physical Review Letters **81**, 3811–3814 (1998).

[62] B. Fröhlich, M. Feld, E. Vogt, M. Koschorreck, M. Köhl, C. Berthod, and T. Giamarchi. *Two-dimensional Fermi liquid with attractive interactions*. Physical Review Letters **109**, 130403 (2012).

[63] B. Fröhlich, M. Feld, E. Vogt, M. Koschorreck, W. Zwerger, and M. Köhl. *Radio-Frequency spectroscopy of a strongly interacting two-dimensional Fermi gas*. Physical Review Letters **106**, 105301 (2011).

[64] T. Fukuhara, Y. Takasu, M. Kumakura, and Y. Takahashi. *Degenerate Fermi Gases of Ytterbium*. Physical Review Letters **98**, 030401 (2007).

[65] P. Fulde and R. A. Ferrell. *Superconductivity in a strong spin-exchange field*. Phys. Rev. **135**, A550–A563 (1964).

[66] U. Gavish and Y. Castin. *Matter-wave localization in disordered cold atom lattices*. Phys. Rev. Lett. **95**, 20401 (2005).

[67] M. E. Gehm. *Properties of 6 Li* (2003).

[68] I. Georgescu, S. Ashhab, and F. Nori. *Quantum simulation*. Reviews of Modern Physics **86**, 153–185 (2014).

[69] A. Gezerlis, S. Gandolfi, K. Schmidt, and J. Carlson. *Heavy-light fermion mixtures at unitarity*. Physical Review Letters **103**, 060403 (2009).

[70] S. Giorgini, L. P. Pitaevskii, and S. Stringari. *Theory of ultracold atomic Fermi gases*. Reviews of Modern Physics **80**, 1215–1274 (2008).

[71] V. Gokhroo, G. Rajalakshmi, R. K. Easwaran, and C. S. Unnikrishnan. *Sub-Doppler deep-cooled bosonic and fermionic isotopes of potassium in a compact 2D+ -3D MOT set-up*. Journal of Physics B: Atomic, Molecular and Optical Physics **44**, 115307 (2011).

[72] M. Greiner, I. Bloch, T. Hänsch, and T. Esslinger. *Magnetic transport of trapped cold atoms over a large distance*. Physical Review A **63**, 031401 (2001).

[73] M. Greiner, C. A. Regal, and D. S. Jin. *Emergence of a molecular Bose-Einstein condensate from a Fermi gas*. Nature **426**, 537–40 (2003).

[74] A. T. Grier, I. Ferrier-Barbut, B. S. Rem, M. Delehaye, L. Khaykovich, F. Chevy, and C. Salomon. *Λ-enhanced sub-Doppler cooling of lithium atoms in D_1 gray molasses*. Physical Review A **87**, 063411 (2013).

[75] R. Grimm, M. Weidemüller, and Y. Ovchinnikov. *Optical dipole traps for neutral atoms*. Advances in atomic, molecular, and optical physics **42**, 95–170 (2000).

[76] G. Grynberg and J.-Y. Courtois. *Proposal for a magneto-optical lattice for trapping atoms in nearly-dark states*. EPL (Europhysics Letters) **27**, 41 (1994).

[77] K. Gubbels, J. Baarsma, and H. Stoof. *Lifshitz point in the phase diagram of resonantly interacting ^{6}Li-^{40}K mixtures*. Physical Review Letters **103**, 195301 (2009).

[78] D. Guéry-Odelin. *Dynamique collisionnelle des gaz d'alcalins lourds: du refroidissement évaporatif à la condensation de Bose-Einstein*. PhD thesis (1998).

[79] H. Guo, C.-C. Chien, Q. Chen, Y. He, and K. Levin. *Finite-temperature behavior of an interspecies fermionic superfluid with population imbalance*. Physical Review A **80**, 011601 (2009).

[80] R. Gupta, C. Xie, S. Padua, H. Batelaan, and H. Metcalf. *Bichromatic laser cooling in a three-level system.* Physical Review Letters **71**, 3087–3090 (1993).

[81] T. Gustavson, A. Chikkatur, A. Leanhardt, A. Görlitz, S. Gupta, D. Pritchard, and W. Ketterle. *Transport of Bose-Einstein condensates with optical tweezers*. Physical Review Letters **88**, 020401 (2001).

[82] P. Hamilton, G. Kim, T. Joshi, B. Mukherjee, D. Tiarks, and H. Müller. *Sisyphus cooling of lithium*. Physical Review A **89**, 023409 (2014).

[83] R. Hanai, T. Kashimura, R. Watanabe, D. Inotani, and Y. Ohashi. *Excitation properties and effects of mass imbalance in the BCS-BEC crossover regime of an ultracold Fermi gas*. Physical Review A **88**, 053621 (2013).

[84] M.-S. Heo, J.-y. Choi, and Y.-i. Shin. *Fast production of large ^{23}Na Bose-Einstein condensates in an optically plugged magnetic quadrupole trap*. Phys. Rev. A **83**, 13622 (2011).

[85] H. Hess. *Evaporative cooling of magnetically trapped and compressed spin-polarized hydrogen*. Physical Review B **34**, 3476–3479 (1986).

[86] H. F. Hess, M. Hill, G. P. Kochanski, J. M. Doyle, N. Masuhara, D. Kleppner, and J. Greytak. *Magnetic trapping of spin-polarized atomic Hydrogen*. Phys. Rev. Lett. **59**, 672 (1987).

[87] T. Hodapp, C. Gerz, C. Furtlehner, C. Westbrook, W. Phillips, and J. Dalibard. *Three-dimensional spatial diffusion in optical molasses*. Applied Physics B **143**, 135–143 (1995).

[88] H. Hu, X.-J. Liu, and P. D. Drummond. *Phase diagram of a strongly interacting polarized Fermi gas in one dimension*. Physical Review Letters **98**, 070403 (2007).

[89] S. Inouye, M. Andrews, J. Stenger, H.-J. Miesner, D. M. Stamper-Kurn, and W. Ketterle. *Observation of Feshbach resonances in a Bose-Einstein condensate*. Nature **392**, 151–154 (1998).

[90] M. Iskin and A. L. Subasi. *Cooper pairing and BCS-BEC evolution in mixed-dimensional Fermi gases*. Physical Review A **82**, 063628 (2010).

[91] M. Jag, M. Zaccanti, M. Cetina, R. S. Lous, F. Schreck, R. Grimm, D. S. Petrov, and J. Levinsen. *Observation of a strong atom-dimer attraction in a mass-imbalanced Fermi-Fermi mixture*. Physical Review Letters **112**, 075302 (2014).

[92] D. Jin and C. Regal. *Fermi gas experiments*. In M. Inguscio, W. Ketterle, and C. Salomon, editors, *Ultra-cold Fermi Gases, Proceedings of the International School of Physics "Enrico Fermi", Course CLXIV, Varenna*, pages 1–52. (2006).

[93] S. Jochim, M. Bartenstein, A. Altmeyer, G. Hendl, S. Riedl, C. Chin, J. Hecker Denschlag, and R. Grimm. *Bose-Einstein condensation of molecules*. Science **302**, 2101–3 (2003).

[94] S. Jochim, M. Bartenstein, G. Hendl, J. Denschlag, R. Grimm, A. Mosk, and M. Weidemüller. *Magnetic field control of elastic scattering in a cold gas of fermionic Lithium atoms*. Physical Review Letters **89**, 273202 (2002).

[95] P. Kapitza. *Viscosity of liquid Helium below the λ-point*. Nature **141**, 74 (1938).

[96] A. Keshet and W. Ketterle. *A distributed, graphical user interface based, computer control system for atomic physics experiments*. The Review of scientific instruments **84**, 015105 (2013).

[97] W. Ketterle, D. Durfee, and D. Stamper-Kurn. *Making, probing and understanding Bose-Einstein condensates*. arxiv preprint cond-mat/9904034 **5** (1999).

[98] W. Ketterle. *Private communication* (2014).

[99] W. Ketterle and N. V. Druten. *Evaporative cooling of trapped atoms*. Advances In Atomic, Molecular, and Optical Physics **37**, 181–236 (1996).

[100] W. Ketterle and M. W. Zwierlein. *Making, probing and understanding ultracold Fermi gases*. In M. Inguscio, W. Ketterle, and C. Salomon, editors, *Ultracold Fermi Gases, Proceedings of the International School of Physics "Enrico Fermi", Course CLXIV, Varenna*, pages 95–288. (2008).

[101] C. Kohstall, M. Zaccanti, M. Jag, A. Trenkwalder, P. Massignan, G. M. Bruun, F. Schreck, and R. Grimm. *Metastability and coherence of repulsive polarons in a strongly interacting Fermi mixture.* Nature **485**, 615–8 (2012).

[102] M. Koschorreck, D. Pertot, E. Vogt, B. Fröhlich, M. Feld, and M. Köhl. *Attractive and repulsive Fermi polarons in two dimensions.* Nature **485**, 619–22 (2012).

[103] M. Koschorreck, D. Pertot, E. Vogt, and M. Köhl. *Universal spin dynamics in two-dimensional Fermi gases*. Nature Physics **9**, 405–409 (2013).

[104] T. Lahaye, C. Menotti, L. Santos, M. Lewenstein, and T. Pfau. *The physics of dipolar bosonic quantum gases*. Reports on Progress in Physics **72**, 126401 (2009).

[105] G. Lamporesi, J. Catani, G. Barontini, Y. Nishida, M. Inguscio, and F. Minardi. *Scattering in mixed dimensions with ultracold gases*. Physical Review Letters **104**, 153202 (2010).

[106] L. D. Landau and E. M. Lifshitz. *Course of Theoretical Physics - Vol 3 Quantum Mechanics - Nonrelativistic Theory*. (1977).

[107] M. Landini, S. Roy, L. Carcagní, D. Trypogeorgos, M. Fattori, M. Inguscio, and G. Modugno. *Sub-Doppler laser cooling of Potassium atoms*. Physical Review A **84**, 043432 (2011).

[108] A. I. Larkin and Y. N. Ovchinnikov. *Inhomogeneous state of superconductors*. Sov. Phys. JETP pages 20–762 (1965).

[109] J. Lawall, F. Bardou, B. Saubamea, and K. Shimizu. *Two-dimensional subrecoil laser cooling*. Physical Review Letters **73** (1994).

[110] J. Lawall, S. Kulin, B. Saubamea, and N. Bigelow. *Three-dimensional laser cooling of Helium beyond the single-photon recoil limit*. Physical Review Letters **75**, 4194–4197 (1995).

[111] J. Léonard, M. Lee, A. Morales, T. M. Karg, T. Esslinger, and T. Donner. *Optical transport of ultracold atoms using focus-tunable lenses*. arXiv preprint 1406.2336v1 (2014).

[112] P. Lett, R. Watts, C. Westbrook, W. Phillips, P. Gould, and H. Metcalf. *Observation of atoms laser cooled below the Doppler limit*. Physical Review Letters **61**, 169–172 (1988).

[113] J. Levinsen and D. Petrov. *Atom-dimer and dimer-dimer scattering in fermionic mixtures near a narrow Feshbach resonance*. The European Physical Journal D-Atomic, Molecular, Optical and Plasma Physics **65**, 67–82 (2011).

[114] J. Levinsen, T. G. Tiecke, J. T. M. Walraven, and D. S. Petrov. *Atom-dimer scattering and long-lived trimers in fermionic mixtures*. Phys. Rev. Lett. **103**, 153202 (2009).

[115] Y.-J. Lin, A. Perry, R. Compton, I. Spielman, and J. Porto. *Rapid production of ^{87}Rb Bose-Einstein condensates in a combined magnetic and optical potential*. Physical Review A **79**, 1–8 (2009).

[116] W. V. Liu and F. Wilczek. *Interior Gap Superfluidity*. Phys. Rev. Lett. **90**, 47002 (2003).

[117] W. V. Liu, F. Wilczek, and P. Zoller. *Spin-dependent Hubbard model and a quantum phase transition in cold atoms*. Physical Review A **70**, 033603 (2004).

[118] T. Loftus, C. Regal, C. Ticknor, J. Bohn, and D. Jin. *Resonant control of elastic collisions in an optically trapped Fermi gas of atoms*. Physical Review Letters **88**, 173201 (2002).

[119] M. Lu, N. Q. Burdick, and B. L. Lev. *Quantum Degenerate Dipolar Fermi Gas*. Physical Review Letters **108**, 215301 (2012).

[120] A. Ludewig. *Feshbach Resonances in ^{40}K*. PhD thesis (2012).

[121] O. Luiten and M. Reynolds. *Kinetic theory of the evaporative cooling of a trapped gas*. Physical Review A **53** (1996).

[122] L. Luo, B. Clancy, J. Joseph, J. Kinast, and J. Thomas. *Measurement of the entropy and critical temperature of a strongly interacting Fermi gas*. Physical Review Letters **98**, 1–4 (2007).

[123] K. Martiyanov, V. Makhalov, and A. Turlapov. *Observation of a two-dimensional Fermi gas of atoms*. Physical Review Letters **105**, 030404 (2010).

[124] M. M. Maska, R. Lemanski, C. J. Williams, and J. K. Freericks. *Momentum distribution and ordering in mixtures of ultracold light- and heavy-fermion atoms*. Physical Review A **83**, 063631 (2011).

[125] N. Masuhara, J. J. Doyle, J. J. Sandberg, D. Kleppner, T. Greytak, H. Hess, and G. Kochanski. *Evaporative cooling of spin-polarized atomic Hydrogen*. Physical Review Letters **61**, 935–938 (1988).

[126] D. McKay, D. Jervis, D. Fine, J. Simpson-Porco, G. Edge, and J. Thywissen. *Low-temperature high-density magneto-optical trapping of Potassium using the open 4S-5P transition at 405 nm*. Physical Review A **84**, 1–8 (2011).

[127] J. McNamara, T. Jeltes, A. Tychkov, W. Hogervorst, and W. Vassen. *Degenerate Bose-Fermi Mixture of Metastable Atoms*. Physical Review Letters **97**, 080404 (2006).

[128] H. J. Metcalf and P. van der Straten. *Laser cooling and trapping*. (1999).

[129] T. P. Meyrath. *Electromagnet design basics for cold atom experiments some theory of electromagnets exact field of a circular current loop*. Technical Report 1 (2004).

[130] T. P. Meyrath. *Experiments with Bose-Einstein condensation in an optical box*. PhD thesis (2005).

[131] A. Migdall, J. Prodan, W. Phillips, T. Bergeman, and H. Metcalf. *First observation of magnetically trapped neutral atoms*. Physical Review Letters **54**, 2596–2599 (1985).

[132] T. Mizushima, M. Ichioka, and K. Machida. *Fulde-Ferrell-Larkin-Ovchinnikov states in a superfluid Fermi gas*. Journal of Physics and Chemistry of Solids **66**, 1359–1361 (2005).

[133] G. Modugno, C. Benko, P. Hannaford, G. Roati, and M. Inguscio. *Sub-Doppler laser cooling of fermionic ^{40}K atoms*. Physical Review A **60**, R3373–R3376 (1999).

[134] D. Naik, A. Trenkwalder, C. Kohstall, F. M. Spiegelhalder, M. Zaccanti, G. Hendl, F. Schreck, R. Grimm, T. M. Hanna, and P. S. Julienne. *Feshbach resonances in the ^{6}Li-^{40}K Fermi-Fermi mixture: elastic versus inelastic interactions*. The European Physical Journal D **65**, 55–65 (2011).

[135] K. Nakagawa, Y. Suzuki, M. Horikoshi, and J. Kim. *Simple and efficient magnetic transport of cold atoms using moving coils for the production of Bose-Einstein condensation*. Applied Physics B **81**, 791–794 (2005).

[136] S. Nascimbène, N. Navon, K. J. Jiang, F. Chevy, and C. Salomon. *Exploring the thermodynamics of a universal Fermi gas.* Nature **463**, 1057–60 (2010).

[137] S. Nascimbène. *Thermodynamique des gaz de fermions ultrafroids*. PhD thesis (2010).

[138] D. Nath, R. K. Easwaran, G. Rajalakshmi, and C. S. Unnikrishnan. *Quantum-interference-enhanced deep sub-Doppler cooling of ^{39}K atoms in gray molasses*. Physical Review A **88**, 053407 (2013).

[139] K.-K. K.-K. Ni, S. Ospelkaus, M. H. G. de Miranda, A. Pe'er, B. Neyenhuis, J. J. Zirbel, S. Kotochigova, P. S. Julienne, D. S. Jin, and J. Ye. *A high phase-space-density gas of polar molecules*. Science **322**, 231–235 (2008).

[140] Y. Nishida. *Induced p-wave superfluidity in two dimensions: Brane world in cold atoms and nonrelativistic defect CFTs*. Annals of Physics **324**, 897–919 (2009).

[141] Y. Nishida. *Phases of a bilayer Fermi gas*. Physical Review A **82**, 011605 (2010).

[142] Y. Nishida and S. Tan. *Universal Fermi gases in mixed dimensions*. Physical Review Letters **101**, 1–4 (2008).

[143] Y. Nishida and S. Tan. *Confinement-induced Efimov resonances in Fermi-Fermi mixtures*. Physical Review A **79**, 060701 (2009).

[144] K. O'Hara, M. Gehm, S. Granade, and J. Thomas. *Scaling laws for evaporative cooling in time-dependent optical traps*. Physical Review A **64**, 051403 (2001).

[145] K. M. O'Hara, S. L. Hemmer, S. R. Granade, M. E. Gehm, and J. E. Thomas. *Measurement of the zero crossing in a Feshbach resonance of fermionic ^6Li*. Physical Review A **66**, 041401 (2002).

[146] M. Ol'shanii and V. Minogin. *Three-dimensional velocity-selective coherent population trapping of a (3 + 3)-level atom*. Optics communications **89**, 393–398 (1992).

[147] A. A. Orel, P. Dyke, M. Delehaye, C. J. Vale, and H. Hu. *Density distribution of a trapped two-dimensional strongly interacting Fermi gas*. New Journal of Physics **13**, 113032 (2011).

[148] G. Orso, L. Pitaevskii, and S. Stringari. *Equilibrium and dynamics of a trapped superfluid Fermi gas with unequal masses*. Physical Review A **77**, 033611 (2008).

[149] T. Ottenstein, T. Lompe, M. Kohnen, A. Wenz, and S. Jochim. *Collisional Stability of a Three-Component Degenerate Fermi Gas*. Physical Review Letters **101**, 203202 (2008).

[150] F. Papoff, F. Mauri, and E. Arimondo. *Transient velocity-selective coherent population trapping in one dimension*. Journal of the Optical Society of America B **9**, 321 (1992).

[151] M. Parish, F. Marchetti, A. Lamacraft, and B. Simons. *Polarized Fermi condensates with unequal masses: tuning the tricritical point*. Physical Review Letters **98**, 160402 (2007).

[152] S. J. Park, J. Noh, and J. Mun. *Cold atomic beam from a two-dimensional magneto-optical trap with two-color pushing laser beams*. Optics Communications **285**, 3950–3954 (2012).

[153] D. Pekker and C. M. Varma. *Amplitude / Higgs Modes in Condensed Matter Physics*. arxiv preprint 1406.2968 (2014).

[154] A. W.-C. Peng. *Quantum gas microscope with optical lattice*. PhD thesis (2010).

[155] C. Pethick and H. Smith. *Bose-Einstein Condensation in Dilute Gases*. (2002). ISBN 9780521846516.

[156] W. Petrich, M. H. M. Anderson, J. J. R. Ensher, and E. E. A. Cornell. *Stable, tightly confining magnetic trap for evaporative cooling of neutral atoms*. Physical Review Letters **74**, 3352–3355 (1995).

[157] D. S. Petrov, G. E. Astrakharchik, D. J. Papoular, C. Salomon, and G. V. Shlyapnikov. *Crystalline phase of strongly interacting Fermi mixtures*. Phys. Rev. Lett. **99**, 130407 (2007).

[158] D. S. Petrov, C. Salomon, and G. V. Shlyapnikov. *Weakly bound dimers of fermionic atoms*. Physical Review Letters **93**, 090404 (2004).

[159] D. Petrov, M. Baranov, and G. Shlyapnikov. *Superfluid transition in quasi-two-dimensional Fermi gases*. Physical Review A **67**, 031601 (2003).

[160] V. Popozuda. *Beijinho no ombro pro recalque passar longe* (2013).

[161] D. Pritchard. *Cooling Neutral Atoms in a Magnetic Trap for Precision Spectroscopy*. Physical Review Letters **51**, 1336–1339 (1983).

[162] E. Raab, M. Prentiss, A. Cable, S. Chu, and D. Pritchard. *Trapping of neutral sodium atoms with radiation pressure*. Physical Review Letters **59**, 2631–2634 (1987).

[163] A. Rapp, G. Zaránd, C. Honerkamp, and W. Hofstetter. *Color superfluidity and "Baryon" formation in ultracold Fermions*. Physical Review Letters **98**, 160405 (2007).

[164] C. A. Regal, M. Greiner, and D. S. Jin. *Lifetime of molecule-atom Mixtures near a Feshbach resonance in* ^{40}K. Physical Review Letters **92**, 083201 (2004).

[165] C. Regal. *Experimental realization of BCS-BEC crossover physics with a Fermi gas of atoms*. PhD thesis (2006).

[166] A. Ridinger. *Towards quantum degenerate Fermi mixtures : Photoassociation of weakly bound* $^{6}Li^{40}K$ *molecules*. PhD thesis (2011).

[167] A. Ridinger, S. Chaudhuri, T. Salez, U. Eismann, D. R. Fernandes, K. Magalhães, D. Wilkowski, C. Salomon, and F. Chevy. *Large atom number dual-species magneto-optical trap for fermionic ^6Li and ^{40}K atoms*. The European Physical Journal D **242**, 223–242 (2011).

[168] D. Rio Fernandes, F. Sievers, N. Kretzschmar, S. Wu, C. Salomon, and F. Chevy. *Sub-Doppler laser cooling of fermionic ^{40}K atoms in three-dimensional gray optical molasses*. EPL (Europhysics Letters) **100**, 63001 (2012).

[169] G. Ritt, G. Cennini, C. Geckeler, and M. Weitz. *Laser frequency offset locking using a side of filter technique*. Applied Physics B **79**, 363–365 (2004).

[170] A. Safavi-Naini, S. Rittenhouse, D. Blume, and H. Sadeghpour. *Nonuniversal bound states of two identical heavy fermions and one light particle*. Physical Review A **87**, 032713 (2013).

[171] T. Salez. *Towards quantum degenerate atomic Fermi mixtures*. PhD thesis (2011).

[172] G. Salomon, L. Fouché, P. Wang, A. Aspect, P. Bouyer, and T. Bourdel. *Gray-molasses cooling of ^{39}K to a high phase-space density*. EPL (Europhysics Letters) **104**, 63002 (2013).

[173] G. Salomon, L. Fouché, S. Lepoutre, A. Aspect, and T. Bourdel. *All optical cooling of ^{39}K to Bose Einstein condensation*. (2014).

[174] G. Sarma. *On the influence of a uniform exchange field acting on the spins of the conduction electrons in a superconductor*. Journal of Physics and Chemistry of Solids **24**, 1029–1032 (1963).

[175] J. Schoser, A. Batär, R. Löw, V. Schweikhard, A. Grabowski, Y. Ovchinnikov, and T. Pfau. *Intense source of cold Rb atoms from a pure two-dimensional magneto-optical trap*. Physical Review A **66**, 023410 (2002).

[176] F. Schreck, G. Ferrari, K. Corwin, J. Cubizolles, L. Khaykovich, M.-O. Mewes, and C. Salomon. *Sympathetic cooling of bosonic and fermionic lithium gases towards quantum degeneracy*. Physical Review A **64**, 011402 (2001).

[177] F. Schreck, L. Khaykovich, K. L. Corwin, G. Ferrari, T. Bourdel, J. Cubizolles, and C. Salomon. *Quasipure Bose-Einstein Condensate Immersed in a Fermi Sea*. Physical Review Letters **87**, 080403 (2001).

[178] F. Schreck. *Mixtures of ultracold gases: Fermi sea and Bose-Einstein condensate of Lithium isotopes*. PhD thesis (2002).

[179] U. Schünemann, H. Engler, R. Grimm, M. Weidemüller, and M. Zielonkowski. *Simple scheme for tunable frequency offset locking of two lasers*. Review of Scientific Instruments **70**, 242–243 (1999).

[180] R. G. Scott, F. Dalfovo, L. P. Pitaevskii, and S. Stringari. *Rapid ramps across the BEC-BCS crossover: A route to measuring the superfluid gap*. Physical Review A **86**, 053604 (2012).

[181] J. F. Sherson, C. Weitenberg, M. Endres, M. Cheneau, I. Bloch, and S. Kuhr. *Single-atom-resolved fluorescence imaging of an atomic Mott insulator.* Nature **467**, 68–72 (2010).

[182] Y.-I. Shin, C. H. Schunck, A. Schirotzek, and W. Ketterle. *Phase diagram of a two-component Fermi gas with resonant interactions.* Nature **451**, 689–93 (2008).

[183] F. Sievers. *Ultracold Fermi mixtures and simultaneous sub-Doppler laser cooling of fermionic ^{6}Li and ^{40}K*. PhD thesis (2014).

[184] F. Sievers, S. Wu, N. Kretzschmar, D. Rio Fernandes, D. Suchet, M. Rabinovic, C. V. Parker, L. Khaykovich, C. Salomon, and F. Chevy. *Simultaneous sub-Doppler laser cooling of fermionic ^{6}Li and ^{40}K: Theory and Experiment.* arXiv preprint 1410.8545 (2014).

[185] V. Smirnov, A. Tumaikin, and V. Yudin. *Stationary coherent states of atoms in a resonant interaction with elliptically polarized light. Coherent trapping of populations (general theory)*. Zh. Eksp. Teoret. Fiz **69**, 913 (1989).

[186] A. T. Sommer, L. W. Cheuk, M. J. H. Ku, W. S. Bakr, and M. W. Zwierlein. *Evolution of Fermion pairing from three to two Dimensions*. Physical Review Letters **108**, 045302 (2012).

[187] F. M. Spiegelhalder, A. Trenkwalder, D. Naik, G. Hendl, F. Schreck, and R. Grimm. *Collisional stability of ^{40}K immersed in a strongly interacting Fermi gas of ^{6}Li*. Physical Review Letters **103**, 223203 (2009).

[188] F. M. Spiegelhalder, A. Trenkwalder, D. Naik, G. Kerner, E. Wille, G. Hendl, F. Schreck, and R. Grimm. *All-optical production of a degenerate mixture of ^{6}Li and ^{40}K and creation of heteronuclear molecules*. Physical Review A **81**, 043637 (2010).

[189] D. A. Steck. *Quantum and atom optics* (2012).

[190] S. Stellmer, B. Pasquiou, R. Grimm, and F. Schreck. *Laser Cooling to Quantum Degeneracy*. Physical Review Letters **110**, 263003 (2013).

[191] T. B. Swanson, D. Asgeirsson, J. A. Behr, A. Gorelov, and D. Melconian. *Efficient transfer in a double magneto-optical trap system*. Journal of the Optical Society of America B **15**, 2641 (1998).

[192] M. Taglieber, A.-C. Voigt, T. Aoki, T. Hänsch, and K. Dieckmann. *Quantum Degenerate Two-Species Fermi-Fermi Mixture Coexisting with a Bose-Einstein Condensate*. Physical Review Letters **100**, 010401 (2008).

[193] M. Taglieber, A.-C. Voigt, F. Henkel, S. Fray, T. Hänsch, and K. Dieckmann. *Simultaneous magneto-optical trapping of three atomic species*. Physical Review A **73**, 011402 (2006).

[194] S. M. Tan. *A computational toolbox for quantum and atomic optics*. Journal of Optics B: Quantum and Semiclassical Optics **1**, 424–432 (1999).

[195] M. K. Tey, S. Stellmer, R. Grimm, and F. Schreck. *Double-degenerate Bose-Fermi mixture of strontium*. Physical Review A **82**, 011608 (2010).

[196] T. Tiecke, S. Gensemer, A. Ludewig, and J. Walraven. *High-flux two-dimensional magneto-optical-trap source for cold Lithium atoms*. Physical Review A **80**, 013409 (2009).

[197] T. G. Tiecke. *Properties of Potassium*. Technical report (2010).

[198] T. G. Tiecke, M. R. Goosen, A. Ludewig, S. D. Gensemer, S. Kraft, S. J. J. M. F. Kokkelmans, and J. T. M. Walraven. *Broad Feshbach resonance in the ^6Li $-^{40}$ K mixture*. Physical Review Letters **104**, 053202 (2010).

[199] T. G. Tiecke, M. R. Goosen, J. T. M. Walraven, and S. J. J. M. F. Kokkelmans. *Asymptotic-bound-state model for Feshbach resonances*. Physical Review A **82**, 042712 (2010).

[200] T. G. Tiecke. *Feshbach resonances in ultracold mixtures of the fermionic quantum gases ^6Li and ^{40}K*. PhD thesis (2009).

[201] A. Trenkwalder, C. Kohstall, M. Zaccanti, D. Naik, A. I. Sidorov, F. Schreck, and R. Grimm. *Hydrodynamic expansion of a strongly interacting Fermi-Fermi mixture*. Physical Review Letters **106**, 115304 (2011).

[202] A. G. Truscott, K. E. Strecker, W. I. McAlexander, G. B. Partridge, and R. G. Hulet. *Observation of Fermi pressure in a gas of trapped atoms*. Science (New York, N.Y.) **291**, 2570–2 (2001).

[203] J. Van Dongen, C. Zhu, D. Clement, G. Dufour, J. L. Booth, and K. W. Madison. *Trap-depth determination from residual gas collisions*. Physical Review A **84**, 022708 (2011).

[204] E. Vogt, M. Feld, B. Fröhlich, D. Pertot, M. Koschorreck, and M. Köhl. *Scale invariance and viscosity of a two-dimensional Fermi gas*. Physical Review Letters **108**, 070404 (2012).

[205] A.-C. Voigt, M. Taglieber, L. Costa, T. Aoki, W. Wieser, T. W. Hänsch, and K. Dieckmann. *Ultracold heteronuclear Fermi-Fermi molecules*. Physical Review Letters **102**, 020405 (2009).

[206] J. Walraven. *Elements of Quantum Gases: Thermodynamic and Collisional Properties of Trapped Atomic Gases*. (2006).

[207] J. Wang, H. Guo, and Q. Chen. *Exotic phase separation and phase diagrams of a Fermi-Fermi mixture in a trap at finite temperature*. Physical Review A **87**, 041601 (2013).

[208] T. Weber, J. Herbig, M. Mark, H.-C. Nägerl, and R. Grimm. *Bose-Einstein condensation of Cesium.* Science **299**, 232–5 (2003).

[209] M. Weidemüller, T. Esslinger, M. A. Ol'shanii, A. Hemmerich, and T. W. Hänsch. *A Novel Scheme for Efficient Cooling below the Photon Recoil Limit*. EPL (Europhysics Letters) **27**, 109 (1994).

[210] C. Weitenberg. *Single-Atom Resolved Imaging and Manipulation in an Atomic Mott Insulator*. PhD thesis (2011).

[211] F. Wilczek. *Quantum chromodynamics: Lifestyles of the small and simple*. Nature Physics **3**, 375–376 (2007).

[212] E. Wille, F. Spiegelhalder, G. Kerner, D. Naik, A. Trenkwalder, G. Hendl, F. Schreck, R. Grimm, T. Tiecke, J. Walraven, S. Kokkelmans, E. Tiesinga, and P. Julienne. *Exploring an ultracold Fermi-Fermi mixture: interspecies Feshbach resonances and scattering properties of ^{6}Li and ^{40}K*. Physical Review Letters **100**, 053201 (2008).

[213] C.-H. Wu, I. Santiago, J. W. Park, P. Ahmadi, and M. W. Zwierlein. *Strongly interacting isotopic Bose-Fermi mixture immersed in a Fermi sea*. Physical Review A **84**, 011601 (2011).

[214] S.-T. Wu, C.-H. Pao, and S.-K. Yip. *Resonant pairing between fermions with unequal masses*. Physical Review B **74**, 224504 (2006).

[215] X. Zhang. *Observation of quantum criticality with ultracold atoms in optical lattices*. PhD thesis (2012).

[216] G. Zürn, T. Lompe, A. Wenz, S. Jochim, P. Julienne, and J. Hutson. *Precise Characterization of ^{6}Li Feshbach Resonances Using Trap-Sideband-Resolved RF Spectroscopy*. Physical Review Letters **110**, 135301 (2013).

[217] M. Zwierlein, C. Stan, C. Schunck, S. Raupach, S. Gupta, Z. Hadzibabic, and W. Ketterle. *Observation of Bose-Einstein condensation of molecules*. Physical Review Letters **91**, 250401 (2003).

[218] M. Zwierlein, C. Stan, C. Schunck, S. Raupach, A. Kerman, and W. Ketterle. *Condensation of pairs of fermionic atoms near a Feshbach resonance*. Physical Review Letters **92**, 120403 (2004).

[219] M. W. Zwierlein, J. R. Abo-Shaeer, A. Schirotzek, C. H. Schunck, and W. Ketterle. *Vortices and superfluidity in a strongly interacting Fermi gas.* Nature **435**, 1047–51 (2005).